Title

Full Scale Cyclic Large Deflection Testing of Foundation Support Systems for Highway Bridges. Part I: Drilled Shaft Foundations

Permalink

https://escholarship.org/uc/item/5mt9q0m6

Authors

Stewart, Jonathan P
Taciroglu, Ertugrul
Wallace, John W
et al.

Publication Date

2007

UCLA

Structural & Geotechnical Engineering Laboratory

Full Scale Cyclic Large Deflection Testing of Foundation Support Systems for Highway Bridges.
Part I: Drilled Shaft Foundations

PRINCIPAL INVESTIGATOR
Jonathan P. Stewart
University of California, Los Angeles

CO-PRINCIPAL INVESTIGATORS
Ertugrul Taciroglu and John W. Wallace
University of California, Los Angeles

GRADUATE STUDENTS
Eric R. Ahlberg, Anne Lemnitzer, Changsoon Rha, and Payman Khalili-Tehrani
University of California, Los Angeles

STAFF OF NEES@UCLA
Steve Keowen, Robert L. Nigbor and Alberto Salamanca
University of California, Los Angeles

A report on research conducted under Grant No. 59A0247
from the California Department of Transportation

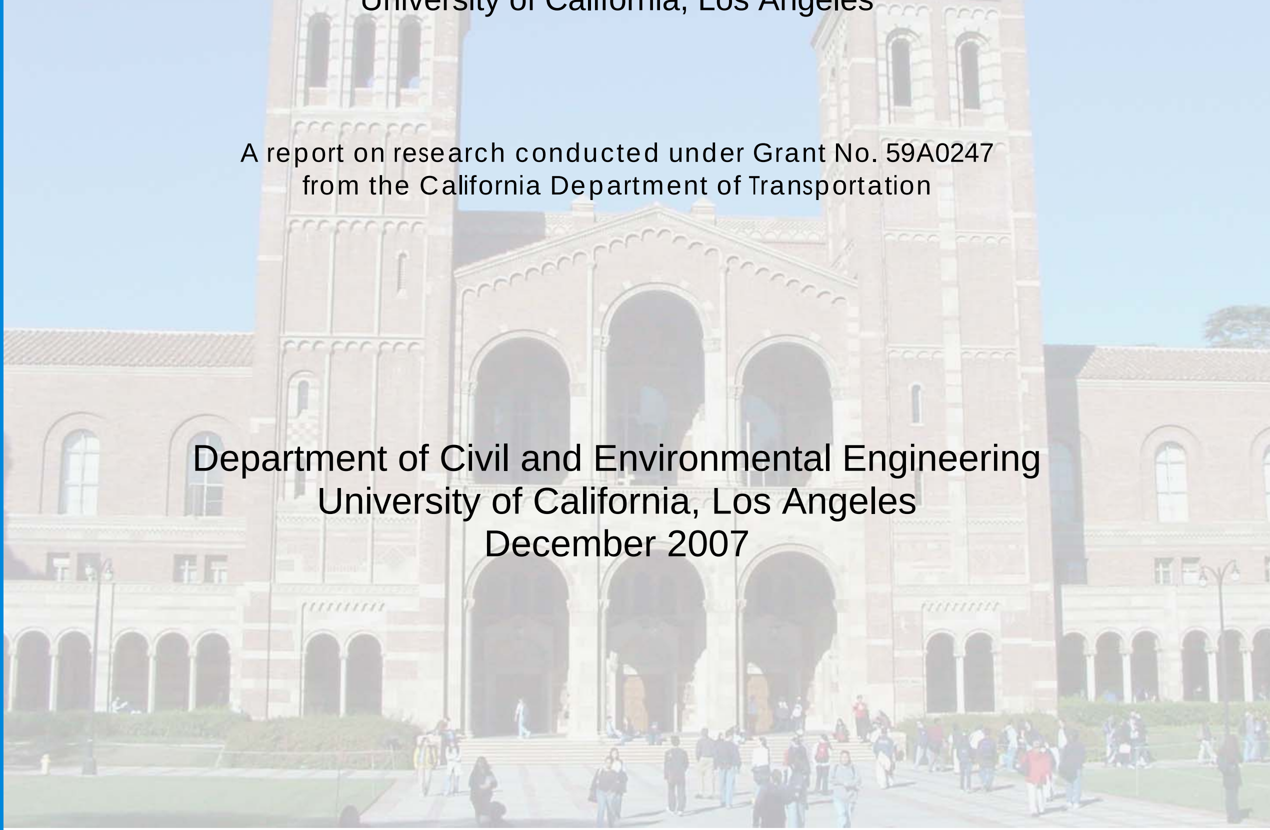

Department of Civil and Environmental Engineering
University of California, Los Angeles
December 2007

UCLA - SGEL
Report 2007/01

Full Scale Cyclic Large Deflection Testing of Foundation Support Systems for Highway Bridges. Part I: Drilled Shaft Foundations

PRINCIPAL INVESTIGATOR

Jonathan P. Stewart
University of California, Los Angeles

CO-PRINCIPAL INVESTIGATORS

Ertugrul Taciroglu and John W. Wallace
University of California, Los Angeles

GRADUATE STUDENTS

Eric R. Ahlberg, Anne Lemnitzer, Changsoon Rha, and Payman Khalili-Tehrani
University of California, Los Angeles

STAFF OF NEES@UCLA

Steve Keowan, Robert L. Nigbor and Alberto Salamanca
University of California, Los Angeles

A report on research conducted under Grant No. 59A0247
from the California Department of Transportation

Department of Civil and Environmental Engineering
University of California, Los Angeles
December 2007

Table of Contents

List of Figures

List of Tables

Acknowledgments

Support for this research was provided by the California Department of Transportation under Research Contract No. 59A0247 (and amendments thereto), which is gratefully acknowledged. We would like to acknowledge the valuable assistance and technical support of Caltrans staff in this project, particularly Anoosh Shamsabadi and Craig Whitten. George Cooke of GB Cooke Inc is recognized for his assistance in specimen construction and contract administration.

The authors gratefully acknowledge that this research was conducted with equipment purchased and integrated into the NEES@UCLA Equipment Site with support from NSF Cooperative Agreement CMS-0086596. The assistance provided by NEES@UCLA System Administrator Steve Kang and NEES System Integration team member Mr. Paul Hubbard is greatly appreciated.

Executive Summary

This research involved analysis and field testing of several foundation support components for highway bridges. Two classes of components were tested - cast-in-drilled-hole (CIDH) reinforced concrete piles (drilled shafts) and an abutment backwall. The emphasis of this document (Part I of the full report) is CIDH shafts.

CIDH shafts are among the most common support structures in highway construction. Typically, drilled shafts have simple, prismatic geometries; yet, they display a complex, inelastic response under applied loading. The two major factors that affect their behavior are the interaction between the shaft and surrounding soil media, and the material inelasticity of the shaft itself. In this report we document the results of two single shaft tests and one shaft group test. All specimens are two-feet diameter reinforced concrete drilled shafts that extend approximately 24ft below ground line. The single shaft specimens include one in a flagpole configuration extending 13.3ft above ground line and the other capped at the surface in a fixed-head configuration. The group test specimen had 9 individual shafts in a 3 by 3 configuration anchored at the ground surface (with a moment connection) in a reinforced concrete cap. The test site consists primarily of low plasticity alluvial clay that is expected to exhibit an undrained response to the cyclic lateral loading. The quasi static loading was applied with a hydraulic control system in displacement-control mode, with the full suite of loading taking several days to complete for each test. The test data have been reduced to provide complete load-deflection backbone curves for loading in both directions, curvature profiles at pre-yield deflection levels, hysteresis curves documenting the cyclic behavior of the shaft soil system at pre-yield displacements, *p*-*y* curves for the single shaft specimens, and group interaction factors for the group specimen.

Pre-test response predictions of the CIDH specimens were obtained via (1) a three dimensional finite element model, (2) a macro-element model, developed at UCLA, and (3) the so-called strain wedge model adopted from the literature. Simulation results were compared with each other and with field measurements. It was observed that all of the three numerical approaches yielded reasonably accurate predictions for these small diameter shafts. We provide *p*-*y* curves in the API format calibrated to the test data and show that those curves improve the accuracy of predictions relative to generic *p*-*y* curves in commonly used design guidelines published by the American Petroleum Institute (API).

The *p*-*y* curves obtained from the experiments are shown to differ from what would be predicted using standard API models, with the data indicating a stronger and stiffer response at shallow depths where the shaft-soil interaction is most pronounced. We also compare results of various tests to evaluate head fixity effects on *p*-*y* curves and the adequacy of the diameter effect built into API *p*-*y* guidelines.

1 INTRODUCTION

1.1. Introduction

Cast-In-Drilled-Hole (CIDH) shafts are a commonly used support element for bridges and highways in California. The lateral response of CIDH systems are controlled by the properties of the CIDH shaft and the soil that surrounds it. Effective design of these systems requires observation and analysis of the interaction between shaft and soil through full-scale field testing.

This document describes four of a sequence of five tests sponsored by the California Department of Transportation (Caltrans) and managed by the University of California, Los Angeles (UCLA). The first test – a six foot diameter shaft in a flagpole configuration – was completed in 2001 and the results are presented in Wallace et al. (2001). The tests that are the subject of this report consist of a two foot diameter flagpole specimen, a two foot diameter fixed-head specimen, a group of nine two foot diameter shafts, and an abutment wall.

1.2. Objectives and Scope

This report will present a detailed description of the planning of the tests, including predictive modeling, specimen construction and instrumentation, and test design. Detailed results from testing will also be presented, including reporting of test data; analysis of internal shaft behaviors, ultimately resulting in deflection and soil reaction profiles over the length of the shaft at different head displacements; and creation of p-y curves based on data gathered from testing. Finally, recommendations on how the results of these studies should be implemented into the design of CIDH shaft are discussed.

1.3 Organization of this Report

Because of the distinct nature of the CIDH shaft tests versus the wall test, these experiments are described separately. The wall test is described in its entirety in Chapter 6, including background and motivation, test data, and test interpretation. Information related to the CIDH tests is described in Chapters 2-5 and 7. Chapter 2 describes the specimen configurations, including structural details and geotechnical site conditions. Chapter 3 discusses pre-test blind predictions, including the analysis methods used in the predictions and the results of the simulations. Blind predictions of each test were an important component of this research program. Chapter 4 presents the tests results with a minimal level of implementation. The emphasis is on sensor performance, curvature profiles, and moment-curvature relationships for the shaft section. Chapter 5 provides relatively in-depth analysis of the CIDH shaft performance for the fixed-head test with the objective of developing p-y curves from the test data that can be compared to those typically used in engineering design practice. This report is concluded in Chapter 7, in which we investigate discrepancies between pre-test prediction and the test results.

2 TEST DESCRIPTION

2.1 Geotechnical Conditions

The site for the three tests described in this document is Caltrans-owned property at the interchange of I-405 and I-105 in Hawthorne, CA. The site has a mapped geology of Quaternary Alluvium, and the upper 50 ft of soil consists of mostly silty clays interspersed with relatively thin layers of silty sands.

In 2001, a large suite of geotechnical tests were performed at the site (Wallace, et al., 2001). Work performed included seismic cone penetration testing (SCPT), rotary-wash borings with standard penetration testing (SPT), down-hole suspension logging of shear wave velocities, pressuremeter testing (PMT), and test pit excavation mapping (See Figure 2.1). Laboratory testing of samples from the site included soil classification, consolidation testing, and unconsolidated-undrained triaxial testing. From this testing suite, the soil profile is described as (a more detailed description can be found in Wallace et al., 2001):

- (0 to ~5 ft) Rubble and fill
- (~5 to ~21 ft) Silty clay, PI ~15, 60% fines, lower-bound OCR from 3.5 to 5.9, 2 ft thick silty sand interbed at ~10 ft
- (~21 to ~24 ft) Medium- to fine-grained silty sand/sandy silt, PI ~12, 30% fines
- (~24 to ~48 ft) Silty clay, PI ~13 to ~14,
- (> ~48 ft) Medium sand, water bearing (water table is at ~48 ft)

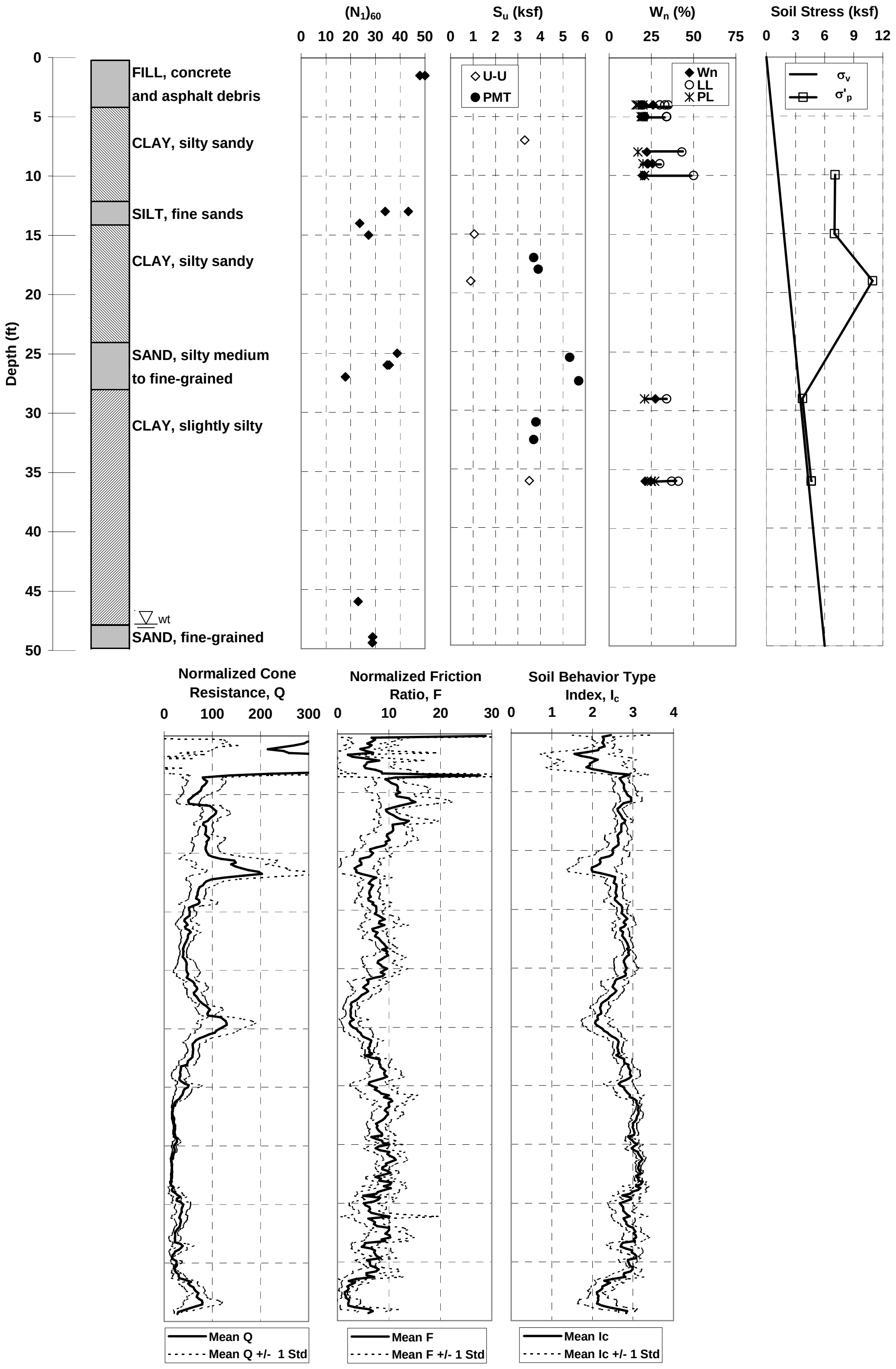

Figure 2.1. Site soil profile with field and laboratory results (Wallace, et, al. 2001).

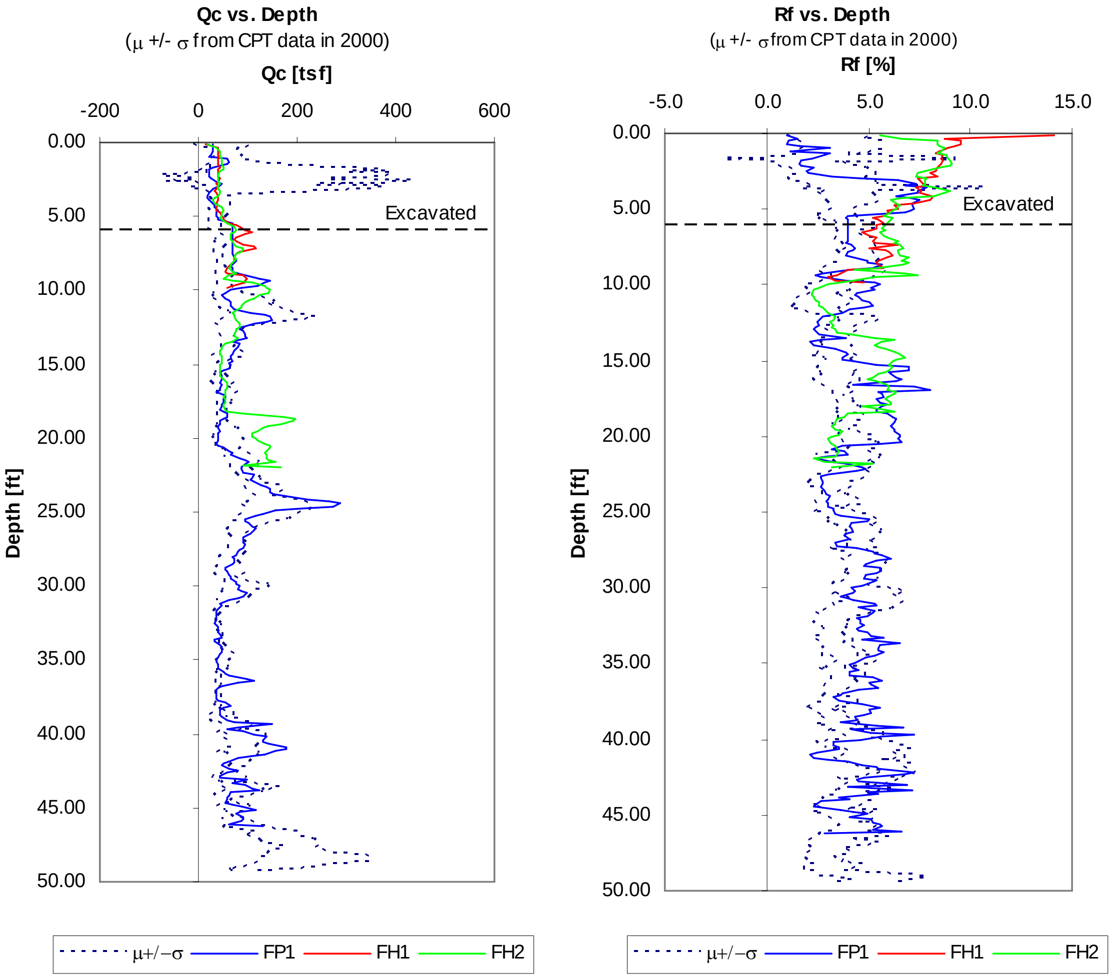

Figure 2.2. CPT profiles at flagpole (FP1) and fixed-head (FH1, FH2) test locations from 2005-06 and plus and minus one standard deviation (μ+/-σ) profiles from the suite of CPT tests done at the site in 2001.

Subsequent CPT soundings were performed in 2005 and 2006 at the locations of experiments performed as part of this study. These measurements confirmed that similar geotechnical characteristics exist at the present test locations as existed at the location of the previous experiment. Results of these tests, as well as plus and minus one standard deviation profiles from the suite of CPT tests done at the site in 2001, are shown in Figure 2.2. Due to rubble and fill near the surface of the flagpole and fixed-head test sites, the first six feet of soil was removed before testing. This soil is indicated by the horizontal dashed line in Figure 2.2 labeled “Excavated.”

2.2 Test Specimens

2.2.1 2ft Flagpole Specimen

The geometry of the 2ft flagpole specimen was dictated by scaling the 6ft flagpole test specimen by a geometric factor of 3. Thus, the diameter of the shaft is 2 ft and the height above ground is 13 feet 4 inches (the 6 ft flagpole height was 40 ft above ground). Below ground, the shaft extended 25 feet to ensure a “long-pile” failure in the shaft (compared to 48 ft for the 6 ft shaft). The shaft reinforcement was 8-#9 longitudinal bars and a 19-inch diameter, #5 spiral at a 4.5 inch pitch over the length of the shaft (See Figure 2.3).

The shaft was designed using a 4 ksi concrete mix; however, standard 6 x 12 in concrete cylinders tested according to ASTM C39 indicated a value of f'_c of between 5.2 ksi and 6.4 ksi with one cylinder having a value of 4.6 ksi (See Figure 2.4a). Nominal A706 Grade 60 reinforcement was specified for design, with coupon tests indicating a yield stress of approximately 71 ksi (See Figure 2.5).

Excavation and placement of the reinforcing cage began in October, 2004. Concrete was placed up to the ground surface, with the above ground portion of the continuous cage being cast three weeks later. As there was an extended period of time between the placement of the below ground and above-ground portions of the shaft, as well as limited access to the bottom of the above-ground formwork, construction jointing or debris problems at the interface could have occurred. Pictures of the installation of the specimen are shown in Figure 2.6.

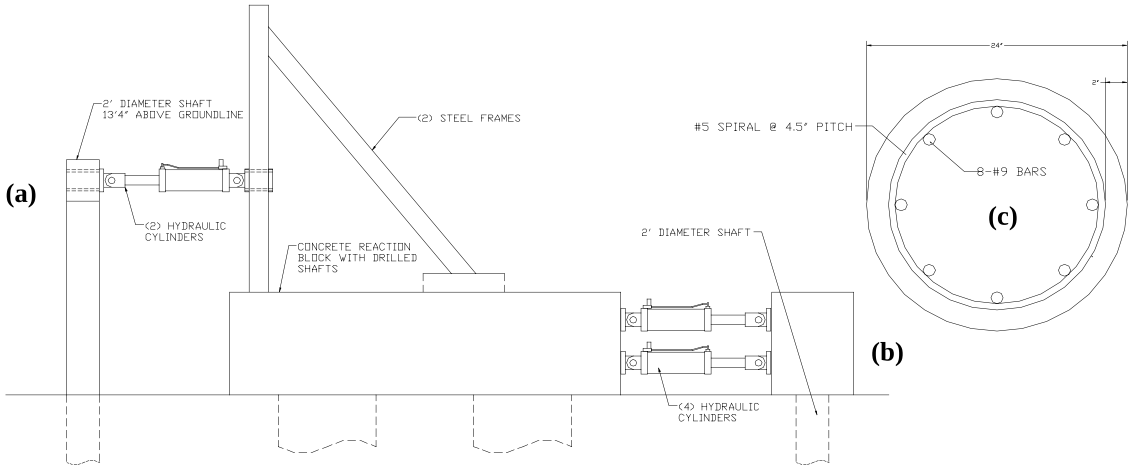

Figure 2.3. Schematic setups for (a) 2 ft flagpole and (b) fixed-head tests; (c) Shaft cross-sections

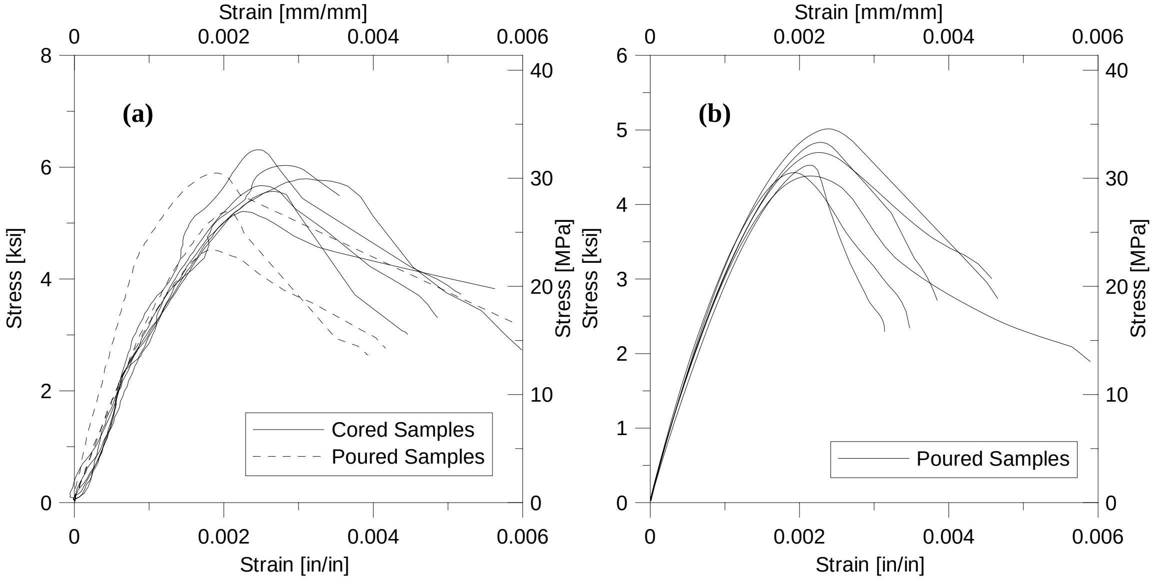

Figure 2.4. Concrete strengths for 2 ft (a) flagpole and (b) fixed-head tests

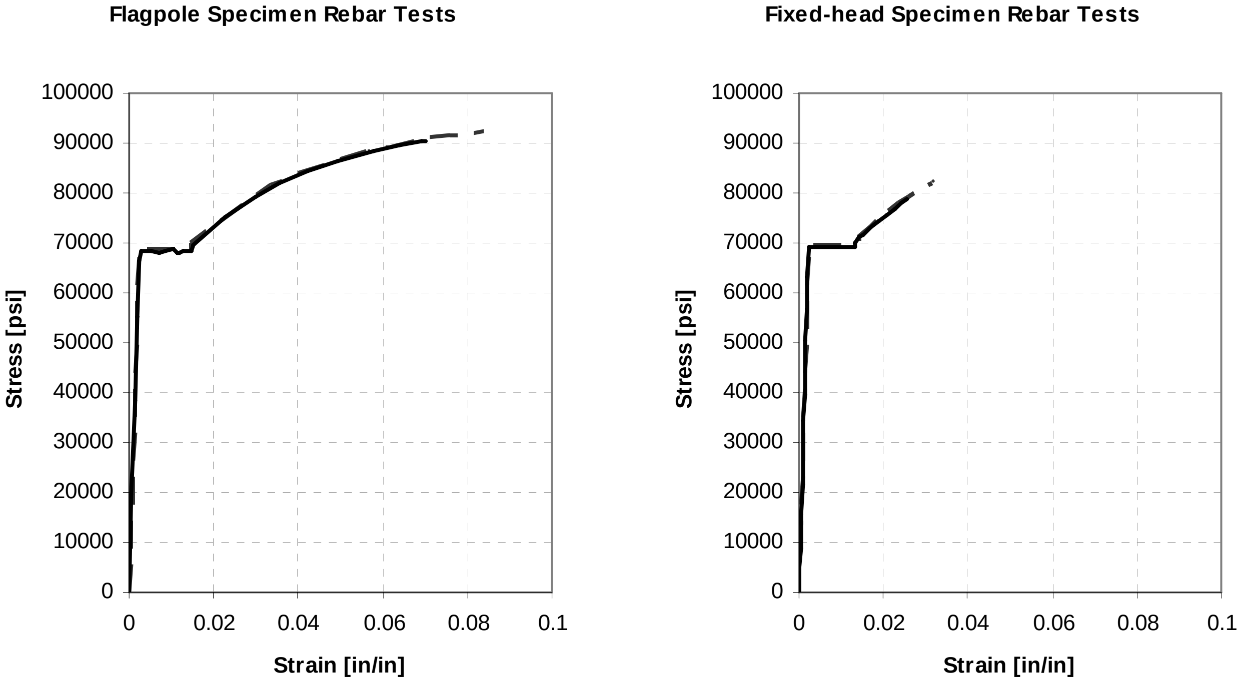

Figure 2.5. Steel reinforcement strengths for 2 ft flagpole and fixed-head tests

(a) (b)

Figure 2.6. Construction of (a) shaft below grade and (b) shaft and cap above grade.

2.2.2 2ft Fixed-head Specimen

The geometry, reinforcing, and materials of the 2ft fixed-head specimen were designed to be identical to that of the 2ft flagpole specimen, except to provide for a fixed-head (zero rotation) condition at the ground surface. The shaft extended 25 ft below ground, with reinforcing extending 6 ft above ground to be cast with the load application cap (See Figure 2.3). A 3 inch layer of Styrofoam was placed between the cap and soil during construction, and removed after construction, to avoid friction between cap and soil.

Results from 6 x 12 in. concrete cylinder tests conducted according to ASTM C39 are shown in Figure 2.4b. Testing of these samples indicated a specified concrete compressive strength of f'_c between 4.4 ksi and 5.2 ksi. Testing of longitudinal rebar samples indicated that the yield stress of the bars (f_y) was approximately 70 ksi.

Concrete for the fixed-head specimen reinforcing cage was cast in September, 2005, where as concrete for the cap was placed in October, 2005. Pictures of the completed cage installation and of concrete placement for the cap are shown in Figure 2.7.

(a) (b)

Figure 2.7. (a) Construction of shaft below grade and placement of Styrofoam at base of cap to provide gap between soil and cap; (b) construction of load application cap.

2.2.3 9-pile Group Specimen

The 9 Shaft Group Test specimen consists of nine reinforced concrete piles with a diameter of 2 feet (60.96 cm) supporting a concrete cap with dimensions of 18 feet in length, 16 ft in width and 6 ft in height. Lateral loading is applied to the test specimen using four actuators mounted between the pile cap and a large-capacity reaction block (described later), as shown in Figure 2.8.

The arrangement of the piles underneath the cap is depicted in Figure 2.8. The center-to-center spacing between each pile is 6 ft in both plan directions. All piles extend about 25 feet below ground and are equally reinforced as shown in Figure 2.8. Flexural (longitudinal) reinforcement consists of 8 - #7 bars placed over the full height of the pile, whereas transverse reinforcement consists of #4 spiral reinforcement extending along the full pile depth. Piles 7, 4 and 5, highlighted in Figure 2.8, are heavily instrumented.

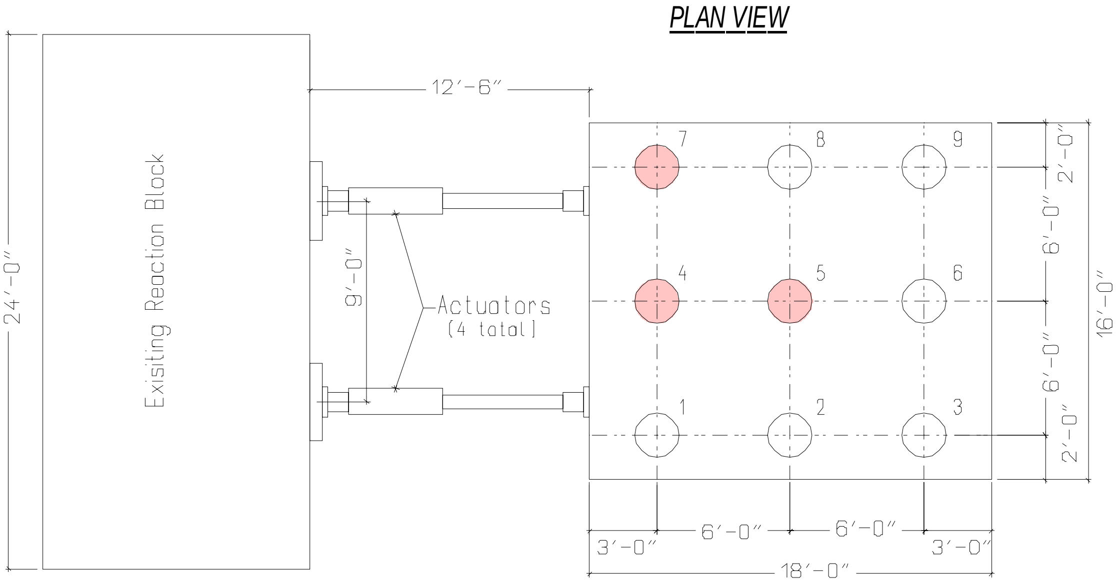

Figure 2.8. Plan View of 9-Pile Test Group Test

The pile cap and the 9 piles were constructed using normal weight concrete with a specified unit weight of 150 pcf with nominal (design) compressive strength (f'_c) of 4 ksi. Sample 6 x 12 in. cylinders for each pile as well as the pile cap were taken during the concrete placement and later tested to obtain the concrete compressive strength at 28-days and at test date. The in-situ compressive strength reached an average value of 4.57 ksi and the splitting tensile strength was measured to be 0.391 ksi. The stress -strain relationships from several cylinder tests are depicted below (Figure 2.9). Table 2.1 and Table 2.2 summarize the results obtained for the splitting and compressive tests on the 6 x 12 in. cylinders.

Table 2.1 Splitting Concrete Compressive Strength

Sample	Date	Pile	Load [kips]	tensile stress f_{ct} [ksi]
Truck 4/1	5/26/2006	P8	53.08	0.469
Truck 4/7	5/26/2006	P1	38.15	0.337
Truck 2/3	5/24/2006	P3	44.70	0.395
Truck 4/3	5/26/2006	P8	40.95	0.362
		ave:	44.22	***0.391***

Table 2.2 Concrete Compressive strength

Sample	***Date***	***Pile***	***max F'c*** [ksi]	***strain at failure*** [inch/inch]
6" slump Truck 1/2	24. Mai 2006	P5	4.846	0.00189
6" slump Truck 1/3	24. Mai 2006	P5	4.472	0.00188
6" slump Truck 1/5	24. Mai 2006	P9	4.824	0.00202
Truck 2/1	24. Mai 2006	P6, P3	4.893	0.00201
Truck 2/5	24. Mai 2006	P7	4.682	0.00186
Truck 3/5	26. Mai 2006	P4	4.201	0.00160
Truck 2/2	24. Mai 2006	P3	4.082	0.00188
		ave	**4.572**	**0.00188**

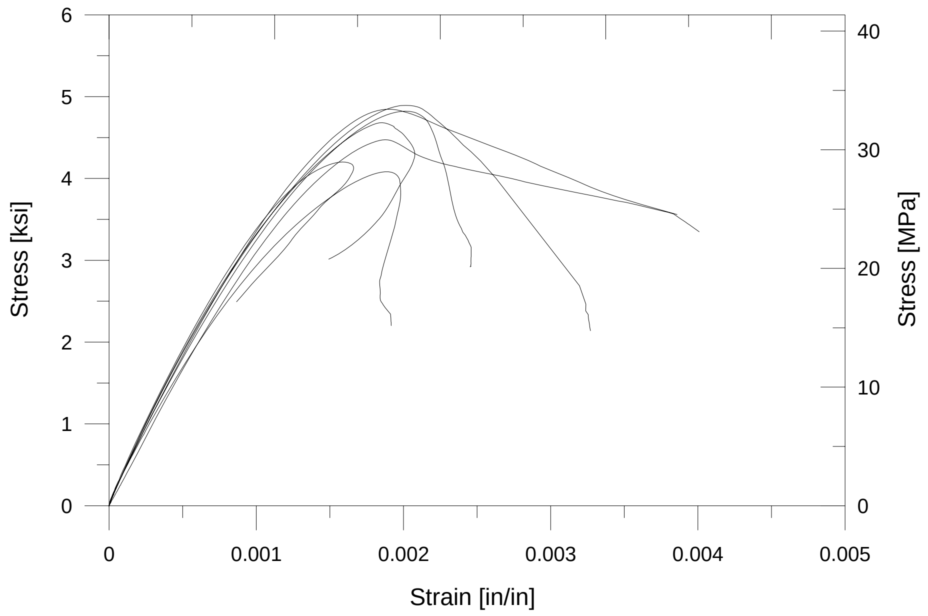

Figure 2.9. Cylinder compressive stresses

Reinforcement for each pile has nominal design strength of 60 ksi. Samples are being tested to obtain stress versus strain characteristics; however, the test results are not available at this time. The pile cap was reinforced with a top and bottom layers of #4 bars spaced at 12 inches, as well as two intermediate curtains of #4 reinforcing bars spaced at 12 in. on center reinforcement in N-S and E-W.

2.3 Instrumentation

Each shaft was instrumented with six types of sensors, including fiber-optic Fiber-Bragg gratings (FBGs), DC LVDT displacement sensors, longitudinal and transverse reinforcement strain gauges, diagonal DC LVDTs to measure shear deformations, inclinometers to measure rotation, pressure transducers and load cells to measure actuator loads, and string potentiometers and long-stroke AC LVDTs to measure displacement at the ground surface (See Figure 2.11).

The sensor layout for the specimens was determined by pre-test predictions of the shaft moment and shear profiles by Rha, et al. (2005). Based on those predictions, the flagpole shaft was expected to have significant flexural deformations (approaching yield) to a depth of 7 feet and significant shear deformations to a depth of 15 feet. Predictions for the fixed-head shaft indicated that significant flexural and shear deformations were expected to a depth of 10 feet. Sensor layouts were developed for the flagpole and fixed-head specimens and are shown in Figure 2.11. The sections below detail the instrumentation in the flagpole and fixed head shafts.

For the pile group test, three piles were instrumented (highlighted in Figure 2.8) with a total of 102 sensors per pile, consisting of 32 longitudinal strain gauges, 30 DC LVDT displacement sensors installed in vertical and diagonal configuration, 38 Fiber Bragg gratings in longitudinal direction and 2 tiltmeters to measure rotation. All 306 sensors were connected to a National Instruments data acquisition system and recorded during testing. An additional six external LVDTs (Figure 2.10) were installed on top and the sides of the pile cap to control the test and to monitor the displacement of the pile cap perpendicular to the applied load as well as the rotation of the pile cap. Within-shaft instrumentation for the three instrumented shafts was generally comparable to that for the fixed-head shaft.

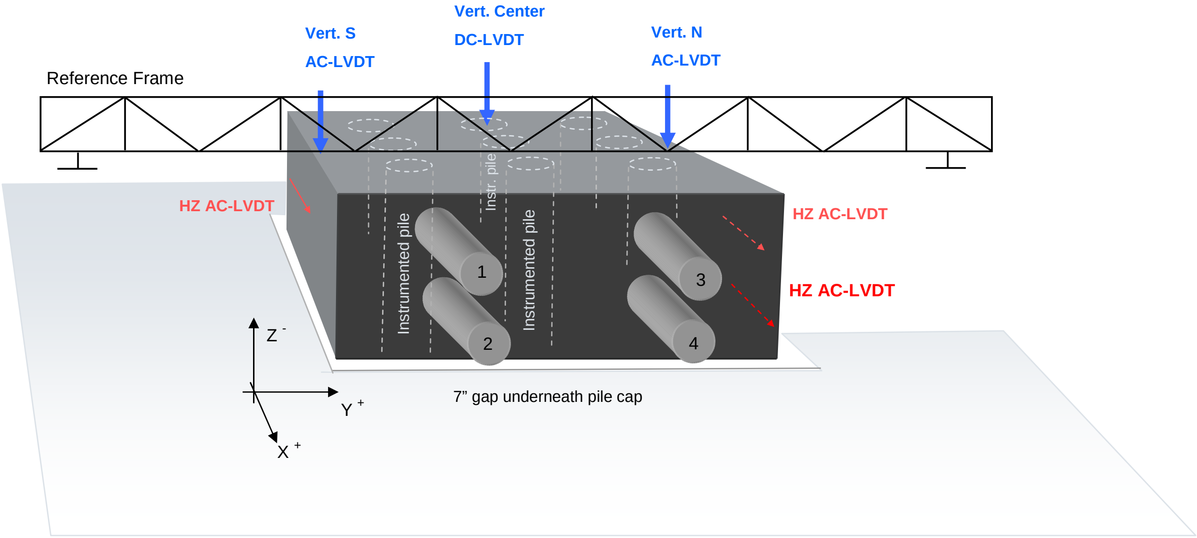

Figure 2.10. Sensors provided for control and monitoring cap movement

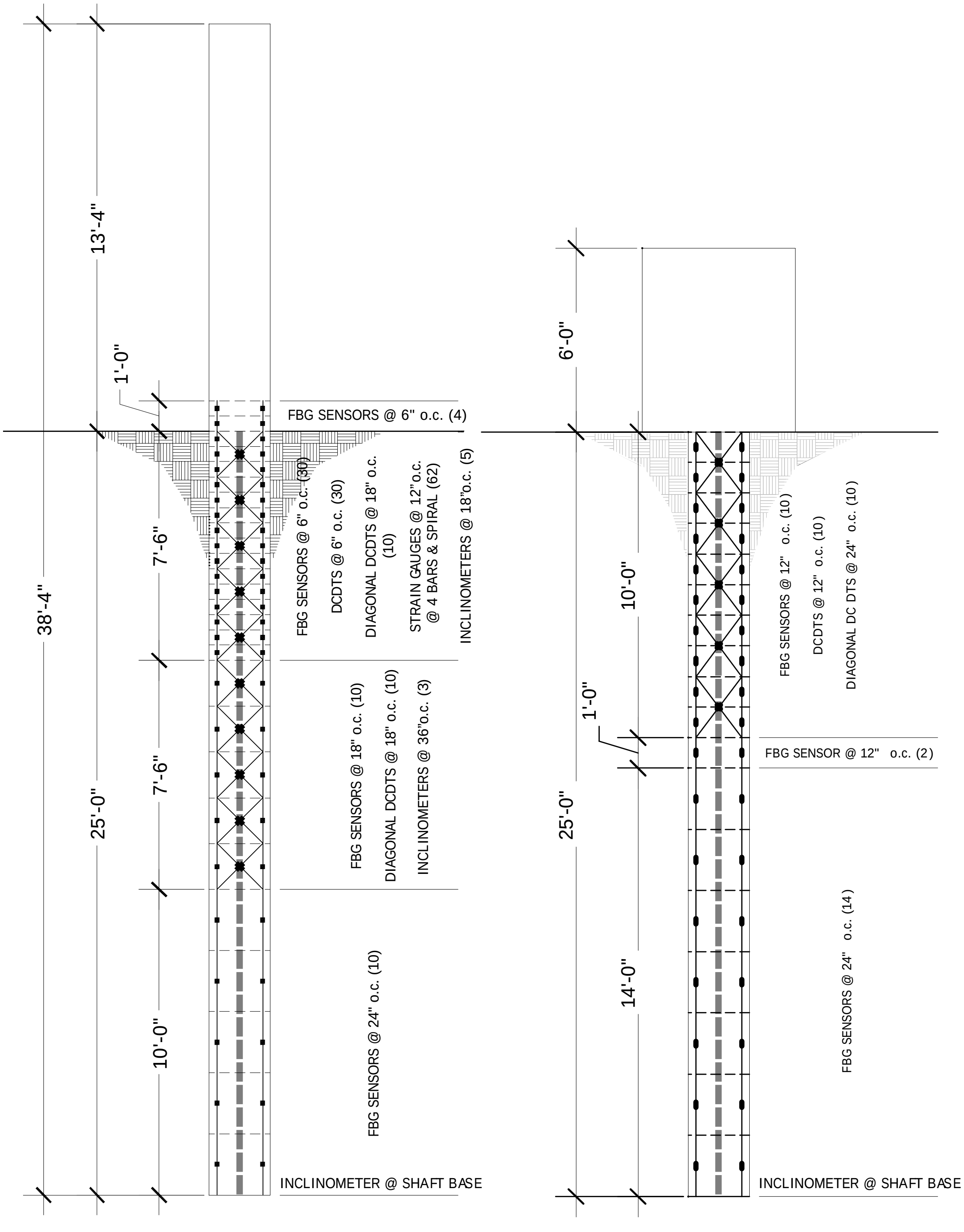

(a) **(b)**

Figure 2.11. Instrumentation layouts for the (a) 2 ft flagpole and (b) 2 ft fixed-head specimens

2.3.1 Fiber-Bragg Gratings (FBGs)

Fiber-optic FBGs, produced by Smartec SA (www.smartec.ch), were installed at 54 locations in the flagpole specimen and 36 locations in the fixed-head specimen. FBGs measure average axial concrete strain over a fixed gauge length by recording the shift in the wavelength of light reflected by the grating. The grating consists of a series of etchings in the core of a fiber-optic cable that reflect a very specific and narrow band of light wavelengths. The wavelength of the reflected light depends on the spacing of these etchings, and as the spacing changes with applied strain, the reflected wavelength changes proportionally.

The strain in the concrete specimen is transferred to the FBG via two stainless steel anchors at the ends of each sensor (Figure 2.12). The fiber is protected from the concrete environment by a plastic casing. The fibers are pre-tensioned to a tensile strain of ~0.5%, which allows the FBG to measure both tensile and compressive strains. With pre-tensioning, the FBGs can measure tensile strains up to about 1% to 1.5%. These sensors also have high resolution (1 microstrain), which allow for accurate strain measurements at low load and deformation levels, which is necessary for accurate assessment of *p-y* relations.

FBGs were placed in pairs normal to the cross-section of the shaft, at the vertical intervals indicted in Figure 2.11. These sensors were connected to a Micron Optics FBG-SLI swept-laser interrogator by a 48-channel switch provided by Smartec SA.

Figure 2.12. FGB housings and anchors shown installed on LVDT housings installed in flagpole specimen.

2.3.2 DC Linear Variable Differential Transducers (LVDTs)

Because the FBG sensors are destroyed when strained in tension beyond ~1.5%, LVDTs also were deployed to provide redundant measurements and to measure average strains in regions where relatively large axial deformations were expected. The LVDTs were placed in the same intervals as the FBGs (6, 18 and 24 inches in the flagpole specimen, and 12 and 24 inches in the fixed-head specimen). With a stroke capacity of +/-1 inch within the 6 inch gauge length, the LVDTs were capable of measuring strains up to 18%. The same LVDTs with 12 inch gauge lengths were able to measure strains up to 9%.

LVDTs were also placed diagonally (in the vertical loading plane) to measure shear deformations. These LVDTs, placed in an "X" pattern, were spaced at 18 inches from the ground surface to a depth of 15 feet in the flagpole specimen. In the fixed-head specimen, the "X" pattern was spaced at 24 inches to a depth of 10 feet (Figure 2.11).

To protect the LVDTs from the concrete environment, they were encased in protective housings that were anchored to the concrete with threaded steel rods. For the flagpole specimen, the protective housings were made with PVC and vinyl plastic. These materials were chosen due to the ease of sealing them against water intrusion and because standard pipe sizes and fittings allowed the housings to slide with relatively minimal force when the entire assembly is deformed. However, these PVC and nylon housings performed poorly on the diagonal elements during concrete placement and some were destroyed. For the fixed-head test, the housings were made using nested stainless steel tubes. Between anchor points, the two stainless steel tubes were nested to enable the larger tube to slide freely over the smaller tube during testing. To keep these tubes from moving during construction, however, the nested tubes were restrained using nylon-tipped set screws which secured the larger tube against the smaller tube. The nylon-tipped set screws kept the housings restrained during installation and construction, but were smooth enough to allow the tubes to slide when stressed during testing. The housings are shown in Figure 2.13.

(a) **(b)**

Figure 2.13. Diagonal LVDT housings made from (a) nylon for the flagpole test and made from (b) stainless steel for the fixed-head test.

2.3.3 Strain Gauges

Strain gauges were affixed on four longitudinal bars and on the reinforcing spiral at intervals of approximately 12 inches (Figure 2.11). These gauges were primarily provided in regions were strains exceeding yield were anticipated. Curvatures were also estimated from the longitudinal reinforcement strain gauge measurements.

The strain gauges were Texas Measurements (www.straingage.com) model YEF and YFLA gauges. The YEF gauges have plastic backings that allow them to measure strain at post-yield deformations. The gauges were affixed to the reinforcement using CN-Y adhesive and coated with M-Coat A, M-Coat B, and M-Coat J from Vishay Micromeasurements for water-proofing and protection. Uncoated and coated strain gauges installed on reinforcing bars are shown in Figure 2.14.

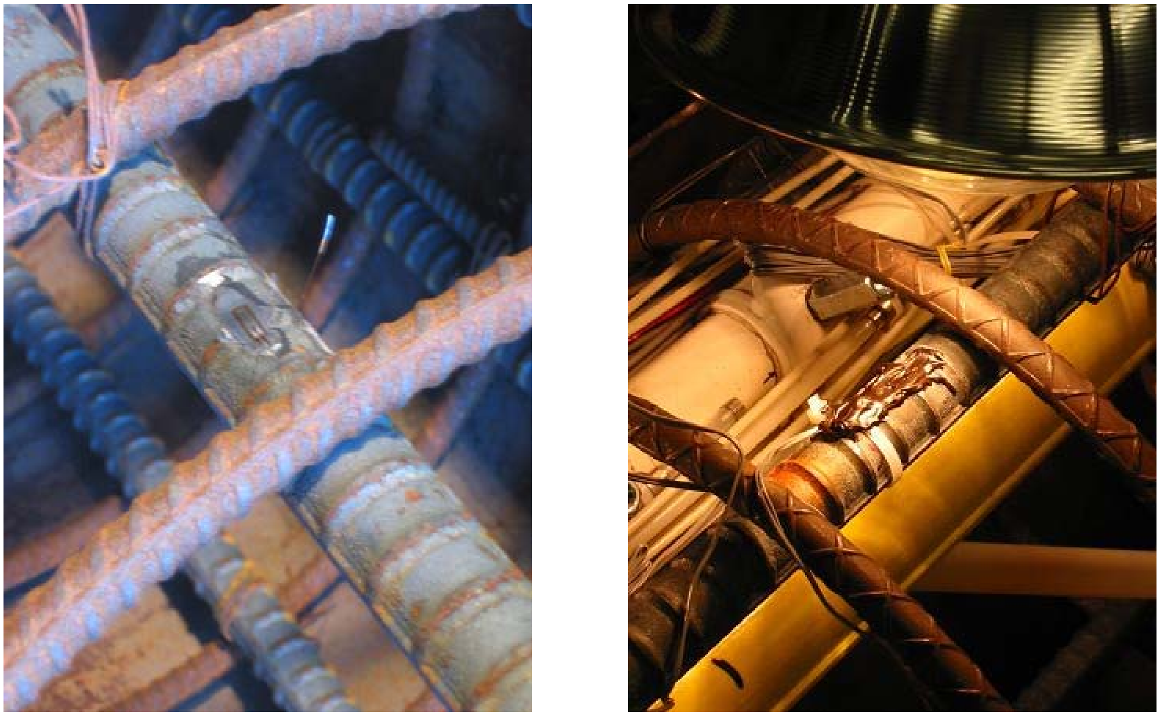

(a) (b)

Figure 2.14. Strain gauge (a) installed on rebar and (b) covered with final M-Coat J coating.

2.3.4 Inclinometers

Eleven Geokon (www.geokon.com) model 6300 inclinometers were installed within the flagpole and fixed head shaft to measure rotation. The locations of inclinometers are shown in Figure 2.11. Since inclinometers used have a minimum spacing of 18 inches, they were used primarily for verifying rotations inferred from curvatures measured from other instruments, rather than for producing curvature measurements themselves. An inclinometer at the base of each shaft was used to assess the tip rotation. The inclinometers are strung together using stainless steel tubes and suspended in a fiberglass tube from a cable attached to the top of the tube. The orientation of the inclinometer in the plane normal to the axis of the tube is maintained by wheels on the inclinometers that fit into grooves in the fiberglass tubing. An inclinometer and its fiberglass tube housing are shown in Figure 2.15.

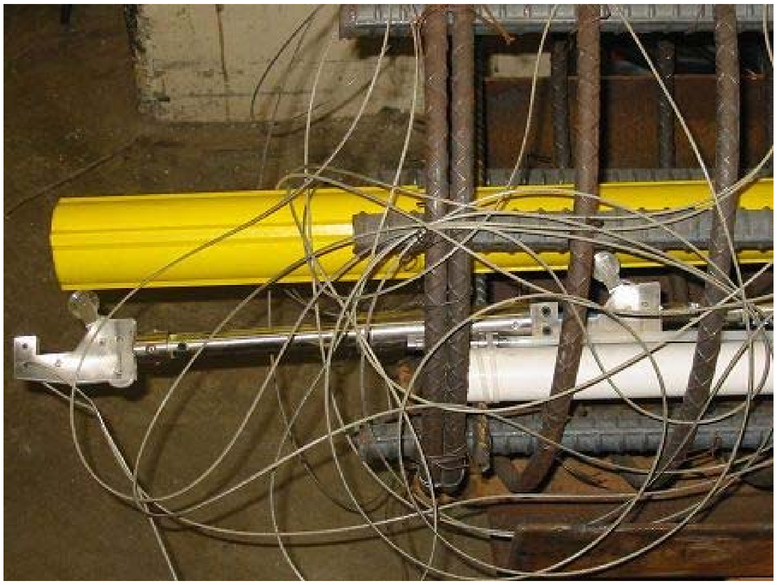

Figure 2.15. Inclinometers (silver) and fiberglass housing (yellow).

2.3.5 Load Measurements

For the flagpole test, pressure transducers were used to measure load applied from the hydraulic actuators. Two 5000 psi pressure transducers on each actuator were used to measure the pressure on both chambers of the hydraulic cylinder. By multiplying the pressure in each chamber by the area of the chamber and then by subtracting the loads in each chamber, the net load on the actuator can be deduced. Pre-test calibrations of the pressure transducers were conducted using a calibrated load cell to ensure proper measurement. Calculation of the net load in each actuator was carried out during post processing of the data since the hydraulics were not using load as a feedback signal.

For the fixed-head test, because loads were used as feedback signals, 400 kip capacity Interface load cells were attached to two UCLA cylinders used on the test. Load cells on the 1000 kip cylinders supplied by UC Berkeley were fabricated in-house and integrally attached to the cylinder rods. All load cells were checked for accuracy using resistor shunt calibrations and against a NIST traceable Lebow load cell from the UCLA structures lab.

2.3.6 Cap Displacement Measurements

String-pot displacement transducers were placed at the top of the flagpole shaft and near the ground surface to measure the displacement of the shaft relative to a fixed external reference point. The reference beam was placed far enough away from the shaft so as to not be influenced by the ground movement caused by testing. One sensor was placed at the centerline of the applied force to give an absolute measurement of the head displacement of the shaft, while three sensors were placed at 6 inch vertical intervals near the ground surface to measure displacement, rotation, and curvature of the shaft at that location. Unfortunately, one of the sensors at the ground surface was lost early in the test, which precluded determinations of curvature from external sources at the ground surface. The string pots are shown in Figure 2.16a.

Measurements of the motion of the fixed-head shaft cap were made using +/- 5 inch Transtek AC LVDTs attached to an external reference beam. The reference beam was a 2-foot diameter steel channel spanning across the site excavation pit. Four of the AC LVDTs measured the displacement of the cap behind each actuator and also served as displacement feedback signals for three of the actuators. The AC LVDTs were important for control and measurement of specimen displacement due to the small displacements required at the beginning of the testing sequence (four intermediate points before 0.0625 inches of displacement for the first displacement level). The sensors were calibrated and electrically stable to within 0.0001 inches. The AC LVDTs are shown in Figure 2.16b.

(a) (b)

Figure 2.16. (a) Flagpole specimen, reference frame and top string pot; (b) fixed-head reference frame and AC LVDTs.

2.4 Load Application System

2.4.1 Reaction System

To apply loads to the three specimens, a 24 ft long by 12 ft wide by 6 ft tall concrete block was installed at the site. The block is cast on top of two 6 ft diameter, 48 ft deep drilled shafts spaced 12 ft apart. The shaft-block system was designed to have a lateral load capacity of 3000 kips so as to handle demands from the 9-shaft group test. The block has attachment points on all sides for the hydraulic loading equipment.

For the 2 ft flagpole test, a steel reaction frame was attached to the reaction block to allow loads to be applied horizontally to the specimen at 13.33 ft above ground line. Two 450-kip, 36 in stroke actuators were attached between the specimen and the steel reaction frame (See Figure 2.3).

The 2ft fixed-head shaft required two 450-kip, 36 inch stroke actuators and two 1000-kip, 10 inch stroke actuators to be attached between the specimen cap and reaction block. The 1000-kip actuators were used because of the large force couple required to enforce the fixed-head boundary condition. The two 450-kip actuators were installed 4 ft above the ground surface, 6 ft apart, and the two 1000-kip actuators were installed 2 ft above the ground, 6 ft apart (See Figure 2.3).

Four 400 kip, 36” stroke actuators were installed between the reaction block and the cap of the 9 pile group to apply cyclical lateral displacement to the test specimen. The actuators were mounted 3.5 ft from the side edge of the pile cap; therefore, the actuators were spaced 9 ft apart in plan as shown in Figure 2.8. Vertically, the centerline of the top and bottom two actuators were mounted 2 ft from the top and bottom faces of the pile cap, with 2 ft between the top and bottom actuators, as shown in Figure 2.17.

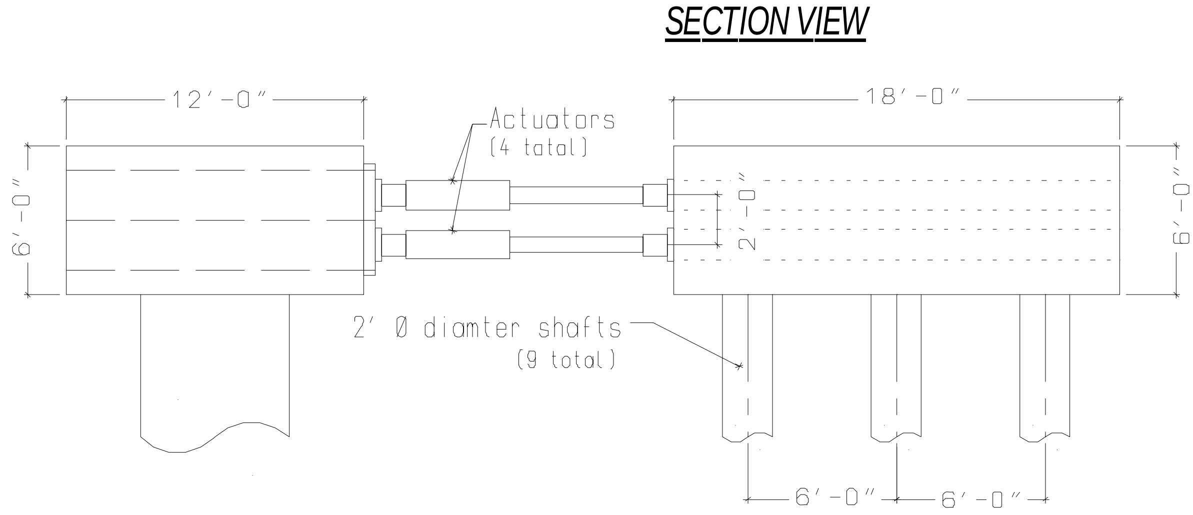

Figure 2.17. Section View of Pile Group Setup and Actuator Installation

2.4.2 Hydraulic Control System

The hydraulic actuators for all three tests were controlled electronically by an MTS Flextest GT controller. The controller can independently operate four actuators with displacement, force or calculated feedback. Hydraulic pressure is provided by a 20 gpm diesel pump and regulated by two, dual-channel hydraulic service manifolds.

The actuators for the 2 ft flagpole test were controlled on the displacement between attachment points (See Figure 2.18). Each actuator was programmed to displace the same relative amount, at the same constant rate. Because the actuators displaced equal amounts, there was no torsional rotation of the cap or shaft. Lateral displacement of the reaction system was monitored using a string pot attached between the specimen and a fixed, external reference frame, to enable calculation of the top lateral displacement of the flagpole. The displacements reported are corrected to remove the contribution of the reaction frame to lateral displacement.

The control system for the 2 ft fixed-head specimen required three actuators to be controlled on the absolute displacement of three points on the specimen cap, and the fourth to be controlled by calculation (See Figure 2.19). The fourth actuator was programmed to match the force of the actuator horizontally adjacent. The test could not use displacement control on all four actuators as this would create a one-degree indeterminate system (i.e., the four actuator displacements could be achieved with a non-unique set of forces in the actuators). The practical implication of this adverse situation was that the control system could ramp up the forces in the actuators until they rapidly reached their capacity, even though the net force on the system was very small.

Lateral displacements were applied to the 9-pile group using the same control equipment described for the single-pile fixed head test. Horizontal displacements were measured at three locations using LVDTs mounted between the pile cap and an external rigid reference frame (see Figure 2.10). The horizontal displacement measurements were used to monitor the horizontal cap displacement as well as to monitor and minimize (control to zero) the cap rotation (twisting). Control for the top two actuators was based on the absolute horizontal displacement, whereas the force in the bottom two actuators were controlled to be equal to the force in the actuator immediately above it. An alternative control scheme, where the force in the bottom two actuators was controlled to be twice the force in the top level actuators also was investigated. This scheme was investigated as a means to reduce the vertical cap rotation, which was measured using LVDTs mounted vertically between the rigid external frame and the cap, as shown on Figure 2.10. However, due to the large stiffness of the test specimen, this control approach could not be maintained beyond relatively low applied horizontal displacement levels because the load-capacity of the bottom actuators exceeded.

Figure 2.18. Flagpole test actuator configuration

Figure 2.19. Fixed-head test actuator configuration

2.5 Testing Protocol

2.5.1 2ft Flag-pole Test Displacement Levels

The test specimen was loaded pseudo-statically and cycled three times at each displacement level. Displacement levels were determined as fractions or multiples of the yield displacement predicted analytically (Rha, et al., 2005), and were chosen to fully capture the linear and post-yield portions of the backbone curve. The yield displacement predicted for the 2ft flagpole specimen was 2 inches and the displacement levels for the test are shown in Table 2.3. Displacements were held at all null, intermediate, and peak displacement stopping points for up to 3 minutes each to allow scanning of fiber-optic sensors as well as to record any important test observations. The number of stops for each displacement level cycle is also shown in Table 2.3.

2.5.2 2ft Fixed-head Test Displacement Levels

The testing regime for the 2 ft fixed-head specimen was determined using the same principles as the 2ft flagpole test, with a predicted yield displacement of 0.5 inches. The displacement levels for the test are shown in Table 2.3.

Table 2.3. Displacement levels for the 2 ft flagpole and 2 ft fixed-head tests

2 ft Flagpole Specimen (Predicted Yield Displacement, δ_y = 2 in)				
δ_y Multiplier	Displacement	Stops/Cycle		
		1	2	3
1/8	0.25 in	4	4	4
¼	0.5 in	4	4	4
½	1.0 in	4	4	4
¾	1.5 in	8	4	4
1	2.0 in	8	4	4
1-1/4	2.5 in	8	4	4
1-1/2	3.0 in	8	4	4
2	4.0 in	8	4	4
3	6.0 in	8	4	4
4	8.0 in	8	4	4
6	12.0 in	8	4	4
8	16.0 in	8	4	4

2 ft Fixed-head Specimen (Predicted Yield Displacement, δ_y = 0.5 in)				
δ_y Multiplier	Displacement	Stops/Cycle		
		1	2	3
1/8	0.0625	4	4	4
1/4	0.125 in	4	4	4
1/2	0.25 in	4	4	4
3/4	0.375 in	8	4	4
1	0.5 in	8	4	4
1-1/4	0.625 in	8	4	4
1-1/2	0.75 in	8	4	4
2	1.0 in	8	4	4
3	1.5 in	8	4	4
4	2.0 in	8	4	4
6	3.0 in	8	4	4
8	4.0 in	8	4	4

2.5.3 9-pile Group Test Displacement Levels

The displacement levels and the number of cycles at each displacement level applied to the cap of the 9-pile group are shown in Table 2.4. Up to a displacement level of 1.675 in., the specimen was pushed with the 4 hydraulic actuators as described in Table 2.4. However, evaluation of the test results indicated that some data for the external control and monitoring sensors were “clipped” at the 0.25, 0.375 and 0.5 in. displacement levels because of the gain settings for the sensors in the National Instrument system. Measurements from instrumentation within the three instrumented piles were not impacted, and recovery of the peak values for the “clipped” data is possible through the application of numerical approaches. For displacement levels exceeding 1.0 in., the pile cap was pushed, but could not be pulled, as the lateral strength of the 9-pile test specimens exceeded the tensile capacity of the actuators (piston area is reduced by the internal rod size). At the 1.675 in. displacement level, the compressive capacity of the actuators was reached. Three additional high-capacity actuators were installed (Fig. 2.9) to allow continuation of the test to higher displacement/load levels. For displacement levels beyond 1.675 in., displacements were applied to the pile cap using the four original actuators until the load capacity of these actuators was reached, and then the control of these four actuators was switched from displacement control to force control. With the load on the four original actuators held close the compressive capacity of these actuators, additional load was applied to the pile cap using the three additional high-capacity actuators to enable loading/displacing the pile cap beyond the 1.675 in. displacement level. Using this setup, the pile was pushed to an ultimate lateral displacement of 10 inches.

Table 2.4 9-Pile Group Applied Displacement History

Displacement levels for the 9 pile group		
Displacement [inch]	# of Cycles	Stops/Cycle
0.0200	1	1
0.0400	1	2
0.0625	3	4
0.0938	1	4
0.1250	1	4
0.1875	1	4
0.2500	3	4
0.3750	2	4
0.5000	4	4
0.6250	1	4
0.7500	2	4
1.0000	1	4
1.3500	1	4
1.5000	1	4
1.6750	1	4

3 PRE-TEST PREDICTIONS

3.1 Overview of Numerical Simulations

The numerical simulations provided in this chapter pertain to all of the 2ft-diameter pile—i.e., flagpole, fixed-head, and the 9-pile group—tests. These simulations provide blind-prediction results that are used for assessing the expected response of the test specimens prior to the actual tests, using various modeling and analysis tools. The simulation predictions are revisited in Chapter 7 where they are compared to the test results. The numerical simulations are carried out via three-dimensional Finite Element (FEM), *p-y* (using conventional API as well as "experimental" backbone curves), and Strain Wedge Methods (SWM). The computer programs used for each simulation are (*i*) a proprietary finite element analysis package ABAQUS (licensed to, and maintained by the UCLA Academic Technology Services) for FEM, (*ii*) the FrameLab program developed at UCLA (Taciroglu *et al.*, 2006) for the *p-y* method, and (*iii*) the SWM program (Ashour, 2002) for the Strain Wedge Method, respectively.

The primary numerical model for the 9-pile group simulations is a three-dimensional finite element model developed and analyzed using ABAQUS. The *p-y* model (with API backbone curves) implemented in FrameLab provides only single pile predictions, and herein they are extended to pile group predictions through the use of *p*-multipliers. For the Strain Wedge Method, the built-in features of SWM program for consideration of pile group effects are invoked in the analyses.

All of the numerical models share common features, such as a subset of the material parameters, descriptions of the specimen geometry as well as the loading; yet, they differ in the way these attributes are implemented in the aforementioned software packages.

3.2 Specimen Configurations

3.2.1 Flagpole Shaft

The diameter of the flagpole shaft is 2 ft. It is embedded in the soil by 25 ft, and extends above the ground line by 13.4 ft as illustrated in Figure 3.1(a). The shaft is reinforced with eight #9 longitudinal bars (thus, $\rho = A_s / A_g = (8 \times 1.0)/(\pi \times 12^2) = 0.0177$)[1] and with #5 hoops at 4.5-inch spacing (thus, $\rho_s = (4 \times 0.31)/(4.5 \times 19.5) = 0.0140$) as shown in Figure 3.1(c). The shaft-head is free and is subjected to a lateral load.

3.2.2 Fixed-head Shaft

The diameter of the fixed-head shaft is 2 ft and embedded in the soil by 25 ft. The shaft top is constrained by the pile cap at the ground line as illustrated in Figure 3.1(b). The reinforcement for this shaft is identical to that of the flagpole shaft.

3.2.3 Pile Group

The pile group specimen consists of nine 2-ft diameter piles with the arrangement shown in Figure 3.1(d). The piles extend 25 ft into the soil and the pile heads are constrained by the pile cap at the ground-line. The geometry of every pile within the group is identical to that of the fixed-head shaft shown in Figure 3.1(b). However, the reinforcements of the group shafts are lighter than that for the fixed-head shaft as indicated in Figure 3.1(c); as each shaft is reinforced with eight #7 longitudinal bars (thus, $\rho = (8 \times 0.6) / (\pi \times 12^2) = 0.01$) and with #4 spiral at 4-inch spacing (thus, $\rho_s = (4 \times 0.2) / (4 \times 19.5) = 0.0103$).

---

[1] For all shaft models, A_s and A_{sp} denote the area of longitudinal and hoop bars, respectively, A_g is the gross area of the shaft, s is the spacing of hoops, and D_c is the (out-to out) diameter of the hoop.

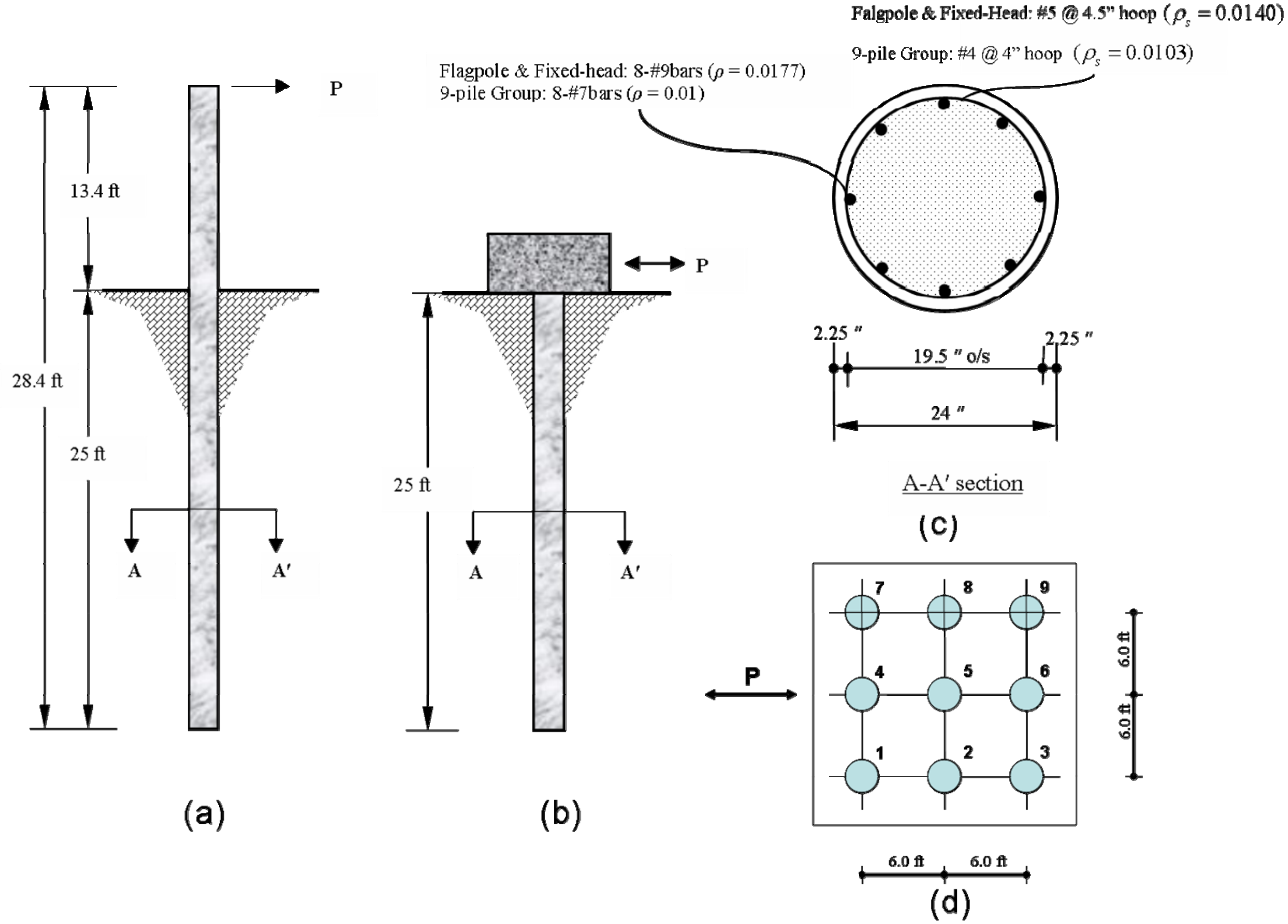

Figure 3.1. Configuration of the test specimens: Loading and geometry of the (a) flagpole shaft, and (b) the fixed-head shaft or the group piles; (c) Cross-sectional geometry and reinforcement of all specimens; (d) The plan view of the 9-pile group.

3.3 Three-dimensional Finite Element Models of the Specimens

3.3.1 Finite Element Models of the Concrete Shafts

The concrete shafts of all of the finite element models (i.e., flagpole, fixed-head, and 9-pile group) consist of two different types of solid (i.e., continuum) elements, and one type of truss element. The solid and the truss elements are used for modeling the concrete and the reinforcement, respectively. The cross-section of every shaft is divided into 16 solid finite elements. The inner 8 elements are 15-node quadratic triangular prisms (C3D15 in ABAQUS element library), and the outer 8 are 20-node quadratic bricks (C3D20 in ABAQUS element library) as illustrated in Figure 3.2(a). These solid elements (C3D20's and C3D15's) are converted automatically to appropriate variable-node element types (C3D27's that are brick elements with 21 to 27 nodes, and C3D15V's that are triangular prism elements with 15 to 18 nodes) if they are adjacent to a slave surface in a contact pair. The inner part of the cross-section is modeled using 15-node quadratic triangle prisms (C3D15) that are confined by the surrounding hoops (#5 at 4.5-inch spacing for flagpole and fixed-head shafts; #4 at 4-inch spacing for the group piles). The outer (unconfined concrete) part is modeled using 20-node quadratic bricks (C3D20). The longitudinal reinforcements (eight #9 bars for flagpole and fixed-head shafts; eight #7 bars for the group piles) are modeled using 3-node quadratic truss elements (T3D3 in ABAQUS element library). These elements are anchored at the interface points of the C3D15's and the C3D20's and thus, share the nodes with those elements as illustrated Figure 3.2(b). The length of the T3D3's vary from 1 ft to 3 ft, depending on their location along the length of the shaft.

In case of the flagpole shaft, the region of the shaft where highly nonlinear behavior is expected (i.e., -8 ft ~ + 5 ft of the ground line) is divided at every foot, whereas the rest of the shaft is divided at 1.66 ft or larger intervals. In total, the flagpole shaft is divided into 26 segments along the length, and each contains 16 solid, and 8 truss elements. Therefore, it is modeled using a total of 624 finite elements (208 each of C3D15's, C3D20's, and T3D3's).

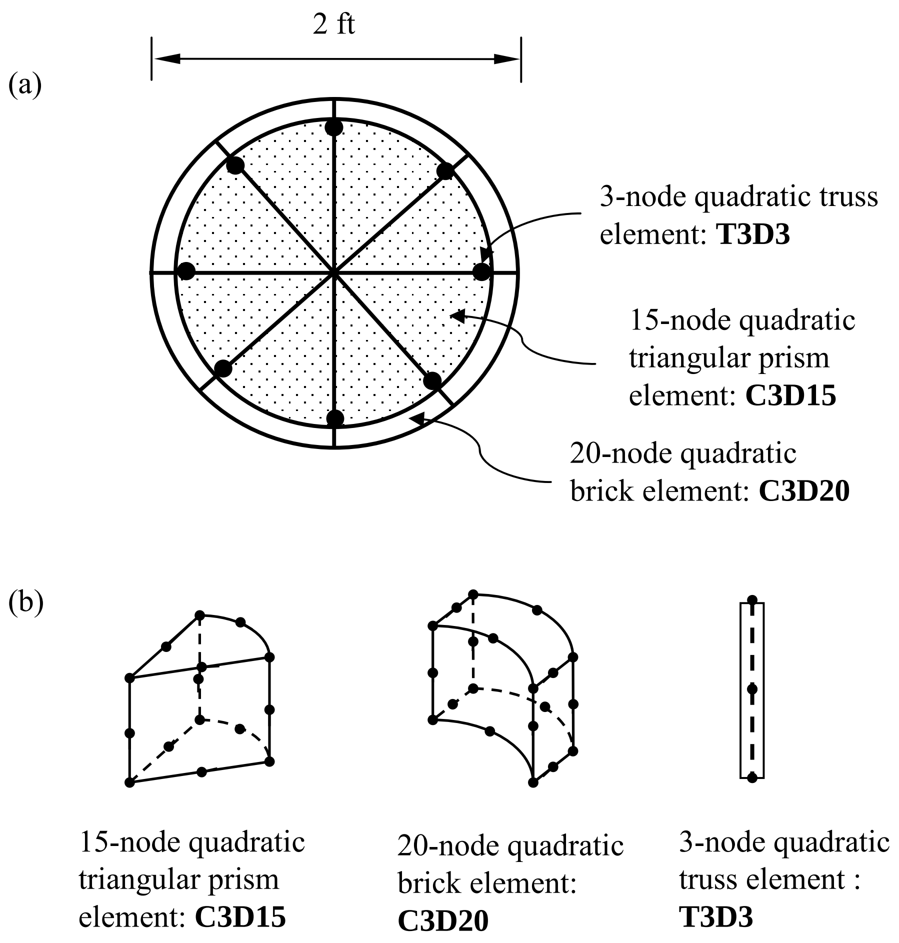

Figure 3. 2. Finite element models for all—i.e., flagpole, fixed head, or 9-pile group—shafts: (a) Shaft cross-section; (b) specific ABAQUS finite element types used.

In case of the fixed-head shaft and each of the 9-group piles, the shaft is divided at 3 ft increments, at the very bottom, to match the thickness of the surrounding soil layers, while the rest of the shaft is divided at 2 ft intervals or less. The region of the shaft where highly nonlinear behavior is expected (i.e., -8 ft depth and up to the ground line) is divided at every foot; whereas the lower part of the shaft is divided at every 2 ft. In total, each of these shafts is divided into 16 segments along the length, and each segment contains 16 solid, and 8 truss elements. Therefore the fixed-head shaft is modeled using a total of 384 finite elements (128 each of C3D15's, C3D20's, and T3D3's); and consequently, the total number of finite elements used for the shafts of the 9-pile group is $9 \times 384 = 3456$.

As the label implies, the top of the fixed-head shaft is fixed for rotation. For this shaft, we performed two sets of analyses: In case 1, we simultaneously prescribed a lateral displacement history and zero axial displacements at the top of the shaft, and in case 2, we simultaneously prescribed a lateral displacement history and zero axial loads at the top of the shaft. While the loading/boundary conditions in case 2 are the actual (field test) conditions, case 1 was studied to see the effects of axial loading/constraining on the shaft response.

For the 9-pile group, the boundary conditions for the all shaft heads are prescribed such that all of the nodes at the tops of the shafts have zero axial, and identical lateral displacements. Because the axial degrees-of-freedom were constrained at the shaft tops, lateral displacement (or load) induces axial stresses within the shafts.

3.3.2 Finite Element Models of the Soil Domains

The finite element models of the soil domain surrounding the shaft are *identical for the flagpole and fixed head shafts*. Both domains consist of 8-node linear brick elements (C3D8 in ABAQUS element library) and 8-node linear, one-way infinite elements (CIN3D8 in ABAQUS element library) are used as illustrated in Figure 3.3[2]. The total depth of soil mesh is 48 ft, thus the base-soil below the shaft is 23 ft thick. The base soil domain is divided into 5 layers of different thicknesses and the soil domain above the base-soil region is divided into 16 layers to match the number of layers of the shaft. Thus, a total of 21 soil layers are used in the vertical direction. The extent of the soil domain in the radial direction is chosen to be 11 times the shaft diameter (i.e., 22 ft). The soil domain is divided into 5 segments (of various lengths) along the radial direction. Each of these segments contains sixteen 8-node linear brick elements (C3D8). Therefore, a total of 1840 solid elements (1760 C3D8's and 80 C3D6's) are used to model the soil, including the area below the shaft. This is in addition to the 336 infinite elements (CIN3D8) that are used for modeling the remote soil domain.

---

[2] Note that this Figure 3.depicts the fixed-head shaft test specimen only. The finite element model of the soil domain for the flagpole shaft is identical to the one displayed in this figure.

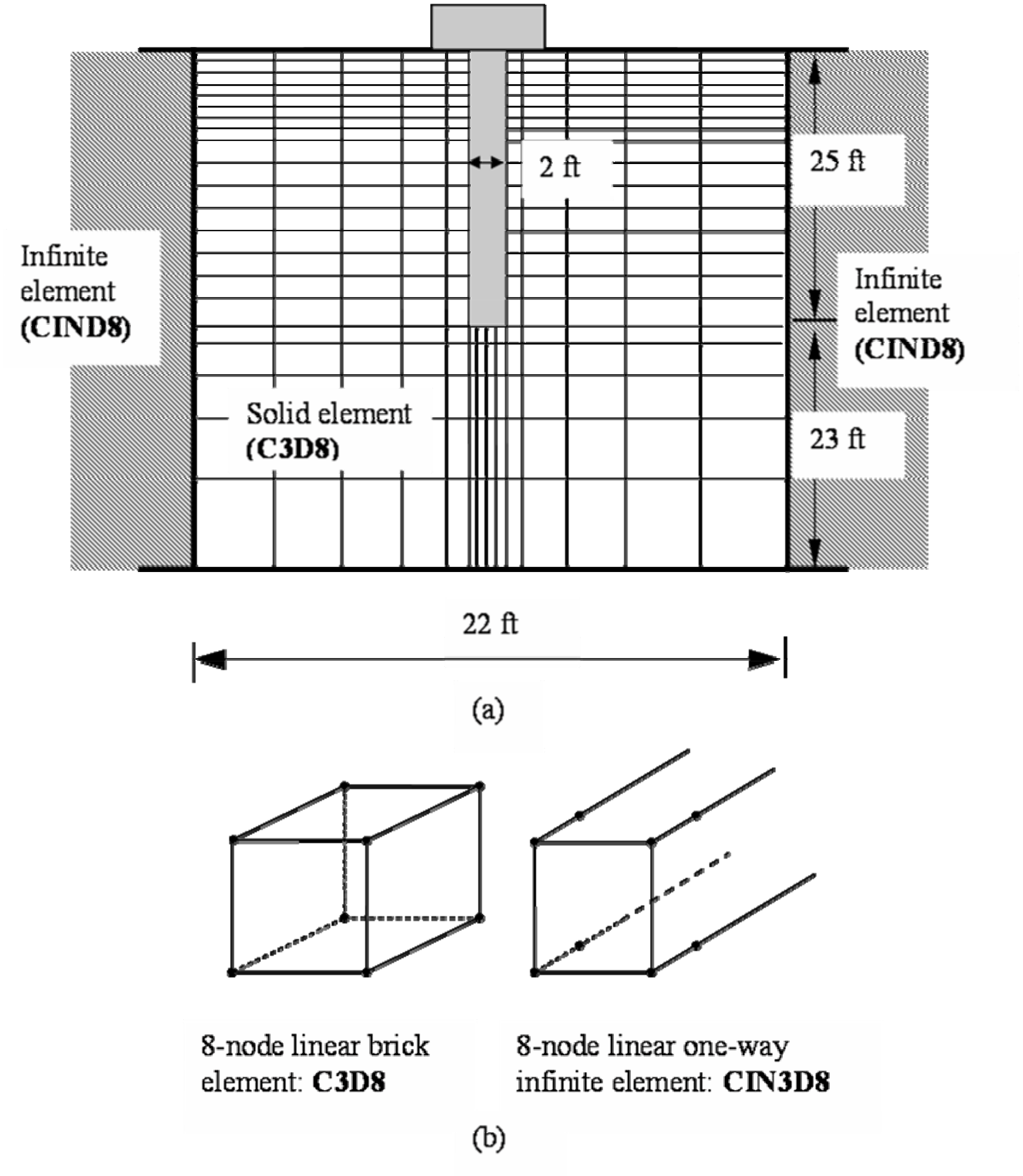

(a)

(b)

Figure 3.3. Finite element model of the soil domain for the fixed-head shaft: (a) Elevation view; (b) finite elements used.

The finite element model of the soil domain for the 9-pile group is shown in Figure 3.4. The soil domain near-pile zone, which is 6 ft by 6 ft in size in plan view, is modeled with a more refined mesh that matches the geometry of the shaft. Figure 3.5 displays the plan and elevation views of the global mesh for the pile group. The width and depth of the mesh is 50.5 ft and 40.0 ft, respectively; and there are nine pile zones. The domain outside of the pile zones is divided into a grid with variable spacing that ranges from 1.25 ft to 7.5 ft. The vertical grid lines are divided with 1 to 3 ft spacing (1 ft spacing is used where nonlinear behaviors are expected, and 3 ft spacing is used for the base soils).

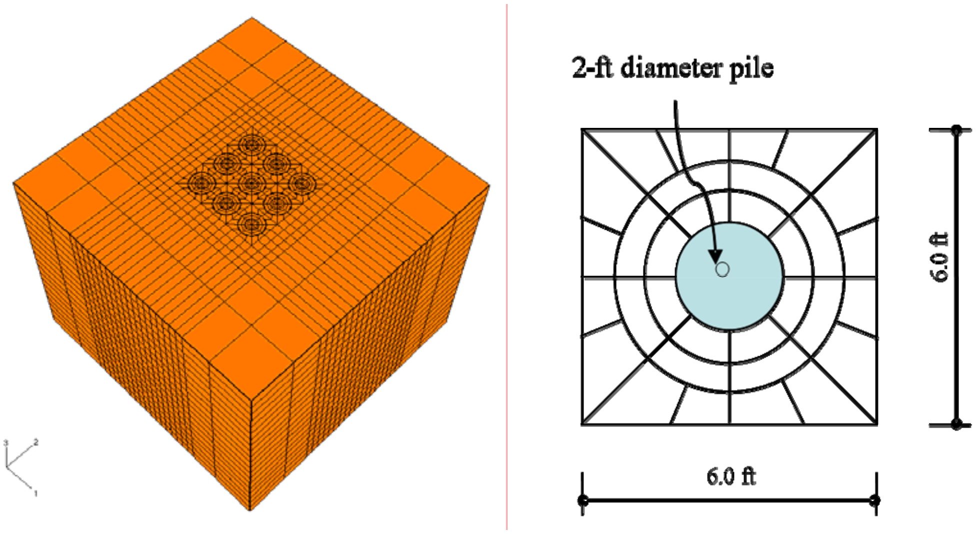

Figure 3.4. Isometric view of finite element model for the group pile (left), and plan view of the layout of soil elements near a pile (right).

For the 9-pile group, the soil elements surrounding the shaft are modeled with 8-node linear brick elements (C3D8 in ABAQUS element library). The total depth of soil mesh is 40 ft, thus the base-soil below the pile is 15 ft thick. The base soil domain is divided into 5 layers of equal thickness, and the soil domain above the base-soil region is divided into 16 layers to match the number of finite element layers for the piles. Thus, 21 soil layers are used in the vertical direction. The soil domain for each pile zone is divided into 32 segments within the 6 ft square (Figure 3.4). Each of these segments contains 21 8-node linear brick elements (C3D8) in the vertical direction. The bottom part of the pile consists of 16 6-node linear brick (C3D6) and 16 8-node linear brick elements (C3D8); and they have 5 layers along the vertical direction. Therefore, a total of 832 solid elements (752 C3D8's, and 80 C3D6's) are used to model the soil at each pile zone, including the area below the pile. The soil domain outside the pile zone consists of 228 segments and each segment contains 21 8-node linear brick elements (C3D8) in the vertical direction. As such, a total of 4788 solid elements (C3D8s) are used to model the soil outside the pile zones. Hence, the total number of finite elements used for meshing the soil domain of the 9-pile group specimen is 12,376 (11,556 C3D8s and 720 C3D6s).

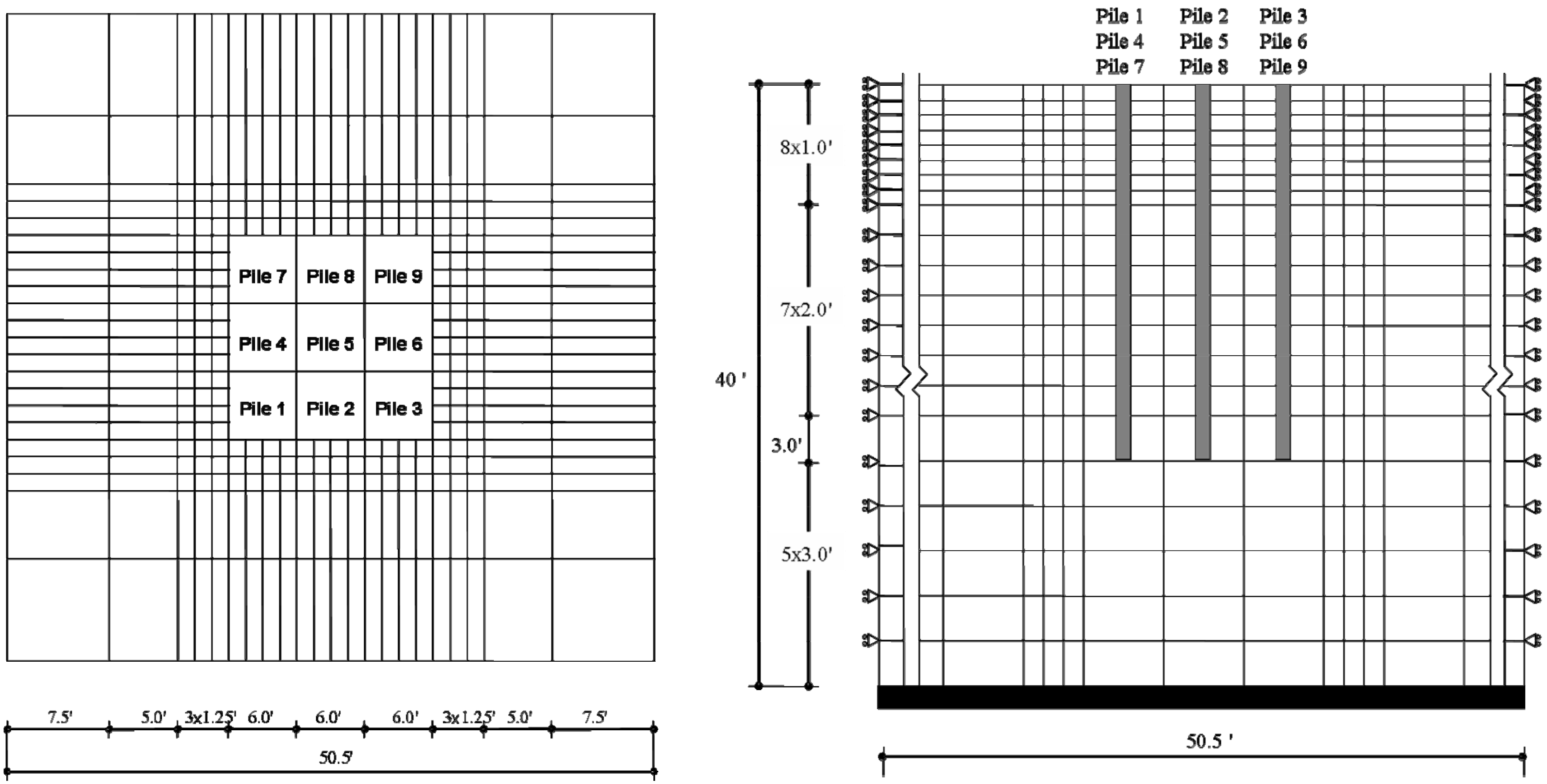

Figure 3.5. Plan (left) and elevation (right) views of the mesh layout for the 9-pile group.

3.3.3 Constitutive Models and Material Parameter Values

Concrete and Steel

The uniaxial compressive strength for concrete is assumed to be 4000 psi. The constitutive models for the concrete shaft have two different types: (a) confined and (b) unconfined. The constitutive relation for the confined concrete is based on the modified Kent-Park model (Park *et al.*, 1982), with a minor revision to take into account the circular geometry of the cross-section. The constitutive relations for confined and unconfined concrete are shown on Figure 3.6(a). The reinforcement for flagpole and fixed-head shafts is Grade-A615, #9 longitudinal bars, and the transverse reinforcement is Grade-A706, #5 spirals with 4.5-inch spacing along the height of the shafts; whereas the reinforcement of each shaft in the 9-pile group is Grade-A615, #7 longitudinal bars, and the transverse reinforcement is Grade-A706, #4 spirals with 4-inch spacing along the height of the shaft. The probable yield strength for the longitudinal bars is assumed to be 68 ksi, and hardening is considered. The nonlinear constitutive relation is approximated using a piecewise linear relationship as illustrated in Figure 3.6(b).

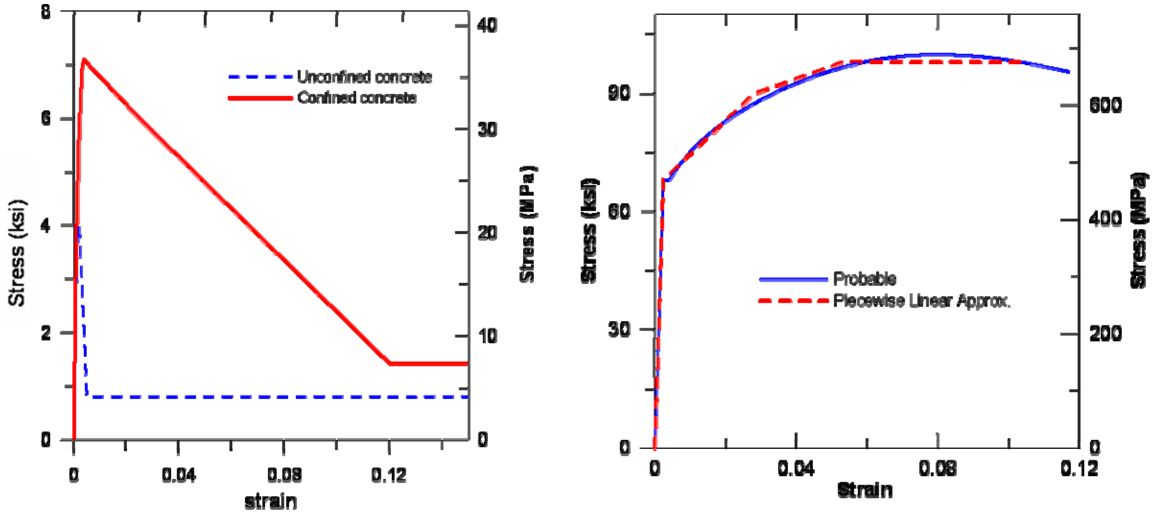

(a) (b)

Figure 3.6. Constitutive relationships for (a) concrete, and (b) steel.

Soils

The soil properties for all models are based on the earlier investigation for the 6ft-diameter flagpole shaft, as this test was carried out near the current test site (Janoyan *et. al*, 2001). The constitutive model for soil is the Mohr-Coulomb model as illustrated in Figure 3.7. In this model, yielding occurs when shear stress on any plane in the material reaches a certain limit value that depends linearly on the normal stress on the same plane, as shown in Figure 3.7(a) where material parameters, c, ϕ and σ_1, σ_3 denote the cohesion, the friction angle and the principal stresses, respectively. Figure 3.7(b) displays the Mohr-Coulomb failure criterion for general states of stress. The Young's moduli, which were obtained from the consolidation, pressuremeter, and shear wave velocity tests vary within a wide range; Thus, in the fixed-head shaft and pile group models both the maximum and minimum values are adopted for the simulation. In flagpole model different values of the Young's modulus were used for free-field soils and the soils in the vicinity of the shaft.

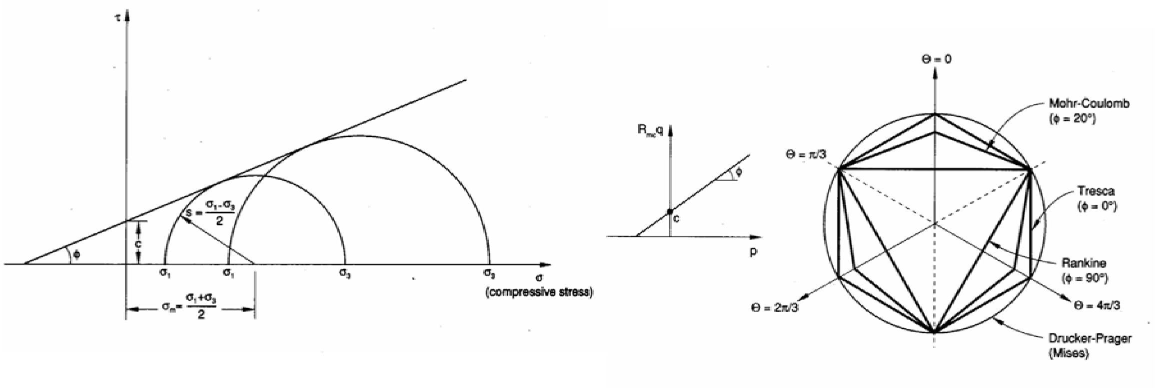

(a) (b)

Figure 3.7. Constitutive relationships for soil: (a) Mohr-Coulomb failure model; (b) Mohr-Coulomb yield surface in meridional and deviatoric planes.

The parameters used for defining the Mohr-Coulomb model in ABAQUS and their assigned values are:

γ = unit weight, 125 pcf

ν = Poisson's ratio, 0.3 (drained), 0.46 (undrained)

c, ϕ, ψ = cohesion, internal friction angle, and dilation angle (in degrees)

-40 ft $\le z \le$ -25 ft, c = 4700 psf, ϕ, ψ = 1° for base soil (clay)

-25 ft $\le z \le$ -22 ft, c = 150 psf, $\phi = 38^\circ$, $\psi = 12^\circ$ for surrounding soil (sand)

-22 ft $\le z \le$ 0 ft, c = 3900 psf, ϕ, ψ = 1° for surrounding soil (clay)

Note: $\phi_{clay} = 0^\circ$ leads to numerical instability so we use $\phi_{clay} = 1^\circ$.

E, Young's modulus for Fixed-head shaft and pile group models:

$8\text{x}10^6$ psf (upper limit) and $1\text{x}10^6$ psf (lower limit) for free field

4×10^6 psf (upper limit) and 5×10^5 psf (lower limit) within 1D distance.

E, Young's modulus for flagpole shaft model:

7×10^6 psf for free field, 4×10^6 psf within 1D distance.

3.4 Modeling with the *p-y* Approach

In this approach, the concrete shaft is modeled using the so-called fiber-based beam finite elements, and the response of soil is modeled using macroelements. Figure 3.8 depicts the overall *p-y* models for the (a) flagpole shaft, (b) fixed-head shaft and each of the shafts within the 9-pile group, (c) a macroelement of the soil, and (d) the cross-sectional fiber discretization of the shaft.

The macroelement (soil) models incorporate frictional forces and formation of gaps at the soil-pile interface as well as hysteretic behavior of the soil. The plastic envelope of the soil behavior is modeled via the, so-called, *p-y* approach. For flagpole and fixed-head shafts, two distinct sets of *p-y* curves that describe the soil behavior are used: (*i*) Curves—henceforth referred to as the "experimental" *p-y* curves—that we have developed and calibrated using the earlier full-scale field test results (Janoyan *et al.*, 2001); (*ii*) the standard *p-y* curves outlined in American Petroleum Institute's (API) guidelines for design of foundation piles for offshore platforms. Only the second set of *p-y* curves (i.e., the standard API *p-y* curves) were used in the modeling of the soil behavior for a fixed-head pile within the pile group. The analyses performed with the *p-y* approach are carried out with FrameLab, which is a structural analysis program developed at UCLA. This program has been verified extensively using other programs such as OpenSees, and with numerous benchmark problems (Taciroglu *et al.*, 2006).

The fiber models for all (i.e., flagpole, fixed-head and 9-pile group) shafts are the same (although with different boundary conditions as it will be discussed in the following section). For the group of piles in this approach, a single fixed-head pile was considered, which is identical to 2-ft diameter fixed-head test specimen. The group effect was considered through the use of "*p*-multipliers."

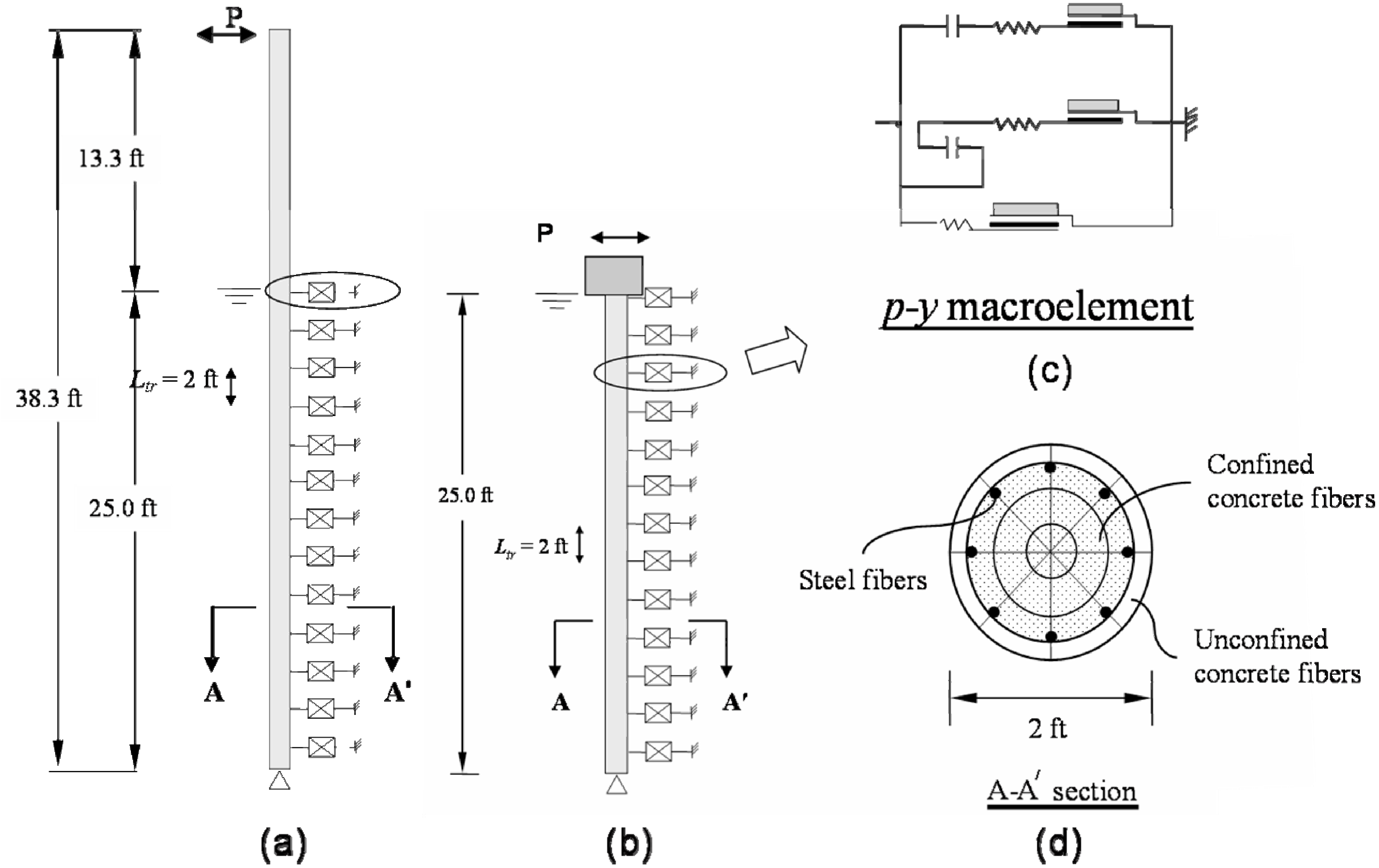

Figure 3.8. The p-y models for (a) the flagpole shaft, (b) the fixed-head shaft and each of the group piles. The shaft and the soil are modeled with (c) zero-length macroelements and (d) fiber-based beam finite elements.

3.4.1 The *p-y* Model Descriptions

In the *p-y* model, the concrete shaft is modeled using fiber-based beam elements. The cross-section consists of confined/unconfined concrete and steel as shown in Figure 3.8(d); and this discretization is similar to the three-dimensional finite element models described earlier. The cross-sectional elements in the *p-y* model, however, are the so-called "fibers," rather than continuum (solid) elements. The section is divided into 8 unconfined concrete, 24 confined concrete, and 8 steel fibers, as shown in Figure 3.8(d). The *p-y* macroelements are located at 2 ft spacing, thus there are 13 of them (below the ground). The macroelements are built by the parallel combination of a drag element, no-tension and no-compression elements, and an elastoplastic element (with a *p-y* backbone curve) as illustrated in Figure 3.8(c). These components represent the friction between the soil and the shaft, elastoplastic compressive soil reactions at leading and rear faces of the shaft, as well as the gaps that open and close under cyclic loading. A detailed explanation of the macroelements can be found elsewhere (see, for example, Taciroglu *et al.*, 2003; Rha *et al.*, 2004).

The boundary condition for the fixed-head shaft is shown in Figure 3.8(b). As previously mentioned, we have considered two sets of loading/boundary conditions at the top of the fixed-head shaft: In case 1, we simultaneously prescribed a lateral displacement history and zero axial displacements at the top of the shaft; and in case 2, we simultaneously prescribed a lateral displacement history and zero axial loads at the top of the shaft. While the loading/boundary conditions in case 2 are the actual (field test) conditions, case 1 was studied to see the effects of axial loading/constraining on the shaft response. For both cases, the shaft bottom is "pinned." The pinned boundary condition at the shaft bottom satisfies vertical equilibrium. The assumption is reasonable because the piles are long and displacements at the shaft bottoms have been observed to be negligible. The boundary condition for the shaft within the 9-pile group is slightly different: The shaft is again pinned at its bottom, but the shaft-top is rotationally constrained in order to model the fixity due to the massive pile cap. For the flagpole shaft, the top is free to rotate and has a prescribed lateral displacement/load.

3.4.2 The *p*-Multipliers to Account for Group Effects in the 9-pile group

The response of a pile group can be obtained from the *p-y* model for single pile by using the, so-called, *p*-multipliers. For closely spaced piles, Brown *et al.* (1987) proposed that the *p-y* curve for a pile in a group be obtained using *p*-multipliers to reduce all the *p* values on a single pile *p-y* curve. This concept has been further developed by Rollins and his collaborators. In this report, the *p*-multipliers have been obtained using the equations introduced by Rollins *et al.* (2006a, 2006b), given as:

First (lead) Row Piles: $$f_m = 0.26\ln\left(\frac{S}{D}\right) + 0.5 \le 1.0$$

Second Row Piles: $$f_m = 0.52\ln\left(\frac{S}{D}\right) \le 1.0$$

Third or Higher Row Piles: $$f_m = 0.60\ln\left(\frac{S}{D}\right) - 0.25 \le 1.0$$

where S and D denote the pile spacing and diameter, respectively. These equations reported to have resulted from a series of full-scale load tests performed on three different pile groups at various spacing and with up to five rows of piles (Rollins *et al.*, 2006a, 2006b). For our pile group specimen the pile spacing is three times the pile diameter so $S/D = 3$.

3.4.3 Material Properties

The shaft is modeled using the well-known fiber-based beam finite elements (Spacone *et al.*, 1996) to incorporate the hysteretic response of the reinforced concrete. The constitutive relationship for steel fibers used in the present study is by Filippou *et al.* (1983), which is an enhanced version of that by Menegotto and Pinto (1973) that includes isotropic strain hardening. The yield strength is assumed to be 68 ksi with 20% strain hardening. The constitutive relationship for (confined and unconfined) concrete is the cyclic model proposed by Mohd-Yassin (1994) who implemented a cyclic loading capability over the monotonic envelope of the modified Kent-Park model (Park *et al.*, 1982). Since only the pushover analysis is carried out, the constitutive relations for FEM shown in Figure 3.6(a) are used for the unconfined/confined concrete fibers as well. The uniaxial concrete compressive strength is assumed 4000 psi (same as that in the three-dimensional finite element model).

Two types of *p-y* envelope curves were considered for the inelastic response of the soil—namely, the standard API *p-y* curves (API, 1993; Matlock, 1970), and the "experimental" *p-y* curves. The experimental *p-y* curves used in this study were calibrated with the measured data from the earlier field-tests at UCLA on a 6ft-diameter shaft (Janoyan *et al.*, 2001). The "experimental *p*-y curves" were obtained with the following method:

1. First, the measured *p-y* curves from the earlier UCLA field-test on a 6ft-diameter shaft were converted to those for a 2ft-diameter shaft simply by scaling (multiplying) them with appropriate conversion factors. These factors were obtained by evaluating the ratio of ultimate resistance of soil for a 2 ft-diameter shaft over that of a 6ft-diameter shaft
2. The scaled curves obtained in step 1 were used to calibrate the parameters of a standard API curve (whose functional form was slightly modified to improve the accuracy of the regression). These new curves with the calibrated parameters, dubbed the "experimental *p*-y curves," were implemented in FrameLab to perform the prediction studies for the 2ft-diameter shaft.

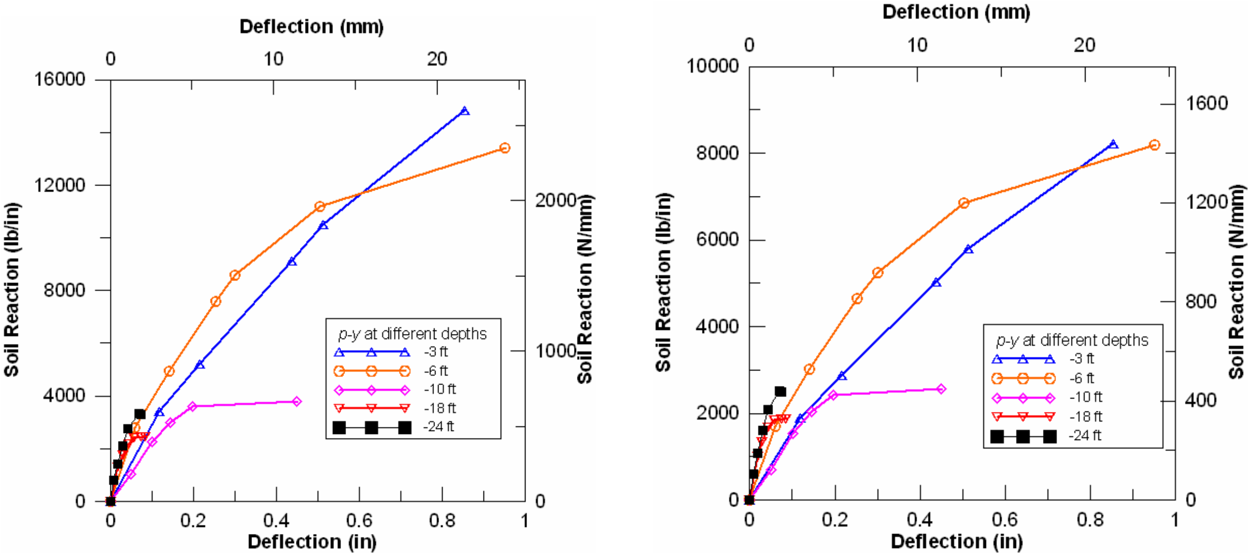

(a) (b)

Figure 3.9. The experimental p-y curves for (a) 6 ft, and (b) calibrated 2ft-diameter shafts.

The scaled (for the 2ft-diameter shaft) *p-y* data and the calibrated "experimental *p-y* curves" are displayed in Figure 3.9(a), (b), respectively. As mentioned above, for the formulation of experimental *p-y* curves, the exponential form defined in API guidelines has been employed with some modifications in parameters including an exponent value. Therefore, the experimental *p-y* curves were also parameterized using the undrained shear strength c, unit weight of the soil γ, pile/shaft diameter D, an empirical constant J, strain at one-half the maximum stress ε_c, and depth z similar to the standard API *p-y* curves. Although the functional form of the standard and the experimental curves are similar, the values of some of their coefficients (hence their predictions regarding the soil response) are different. The parameters used for both the API *p-y* curves and the experimental *p-y* curves are γ = 125 pcf, c = 3900 psf. On the other hand, the parameter J and ε_{50} were defined as 0.25 and 0.007 for API *p-y* curves, while they varied along depth z for the calibrated *p-y* curves. For the pile group only the standard API *p-y* curves were used for the modeling with the same set of parameters as stated above.

A new set of experimental *p-y* curves have been calibrated using the data gathered through the field test experiments on the 2ft-diameter piles. This new set of *p-y* curves will be introduced later in Chapter 5 of this report, accompanying the results of the FrameLab models, in which these new experimental *p-y* curves are used.

A full account of the FrameLab models can be found in Rha *et al.* (2004) or Taciroglu *et al.* (2003, 2006), and are omitted here for brevity.

3.5. Modeling with the Strain Wedge Approach

The Strain Wedge Model (Norris, 1986) provides an alternative analysis method of the response of piles embedded in soil. This approach combines the traditional one-dimensional beam on elastic foundation analysis and three-dimensional soil-pile interaction behavior. The original model has been extended by Ashour *et al.* (1998, 2002) and Ashour and Norris (2000) and now incorporates a Mohr-Coulomb representation of the soil strength. Formulation and implementation details of the strain wedge method can be found in Ashour *et al.* (2002).

The computer program “SWM,” which is developed by Ashour, is used for simulating all three experiments. This computer program has built-in features for consideration of pile groups; and these features were invoked in our analyses (as opposed to obtaining single pile responses from SWM, and subsequently using the *p*-multipliers to account for group effects).

3.5.1. Model Description

The geometry of passive failure wedge (Figure 3.10) is controlled by two factors—the mobilized effective stress friction angle of the soil (φ_m), and the depth of pile deflection under lateral load (*h*). For the calculation of soil reaction, the initial pile deflection pattern is assumed to be linear (being zero at depth *h* to a nominal value at the surface) and an iterative procedure is used for determining φ_m and *h* for a given head load. The strain wedge model consists of one constant segment of nonlinear concrete shaft, and three layers of soil (10 ft thick base-soil, 5ft thick sand, and 20ft thick clay).

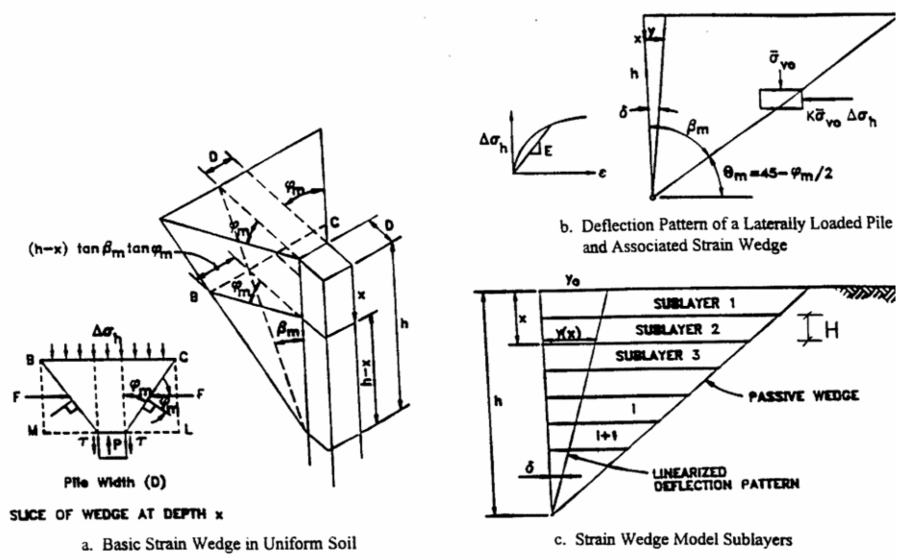

a. Basic Strain Wedge in Uniform Soil

b. Deflection Pattern of a Laterally Loaded Pile and Associated Strain Wedge

c. Strain Wedge Model Sublayers

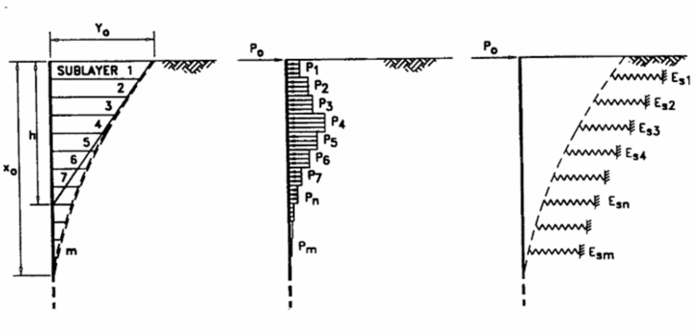

Figure 3.10. Strain wedge model by Ashour et al. (1998, 2000, 2002).

3.5.2 Material Properties

The shaft is modeled as a segment of (nonlinear) concrete pile in the SWM program. The uniaxial compressive strength of concrete and the yield stress of steel were designated as 4000 psi and 68 ksi, respectively. Unlike the fiber-based model used in FrameLab, the reinforcement input is based on the steel ratio. The longitudinal and transverse steel ratios for the shaft were chosen to be 0.01 and 0.022, as determined previously. The strain wedge model requires the following properties to establish the soil profile: Effective unit weight of soil (γ), effective angle of internal friction (φ), axial strain at 50 % of stress level (ε_{50}), and undrained shear strength for clay (c) in addition to the thicknesses of each of the soil layers. Therefore, soil properties used in previous models are identical to those used in this model; i.e., γ = 125 pcf, $\varphi = 1°$ for clay and $\varphi = 38^\circ$ for sand, c =3900 psf for clay and c=150 for sand, and $\varepsilon_{50} = 0.007$.

3.6 Pre-test Simulation Results

3.6.1 Flagpole Shaft

Flagpole Shaft Simulation Results with the Three-dimensional Finite Element Model

The simulation results presented here are obtained by prescribing a displacement history (displacement control) at the top of he shaft. The analysis proceeds until the top displacement reaches 8 inches. At this displacement value, severe convergence problems occurred[3], indicating a possible unstable behavior in the shaft due to the damage/yielding. Figure 3.11 displays the relationship between top displacement of the shaft and corresponding lateral load at the shaft top.

Following FEMA-356 (2000), the nonlinear relationship between the applied force and the displacement can be replaced with an idealized bilinear relationship using an effective lateral stiffness, K_e, and a yield load, P_y as shown in Figure 3.11. The effective lateral stiffness is chosen as the secant stiffness calculated at 60% of yield load. From the approximated bilinear relationship between the top displacement and the applied lateral load, the yield displacement (Δ_y) can be defined as the top displacement at approximately 2.5 inches.

---

[3] It is note here that the convergence difficulties were also observed even if a force-controlled loading strategy was adopted during the computations.

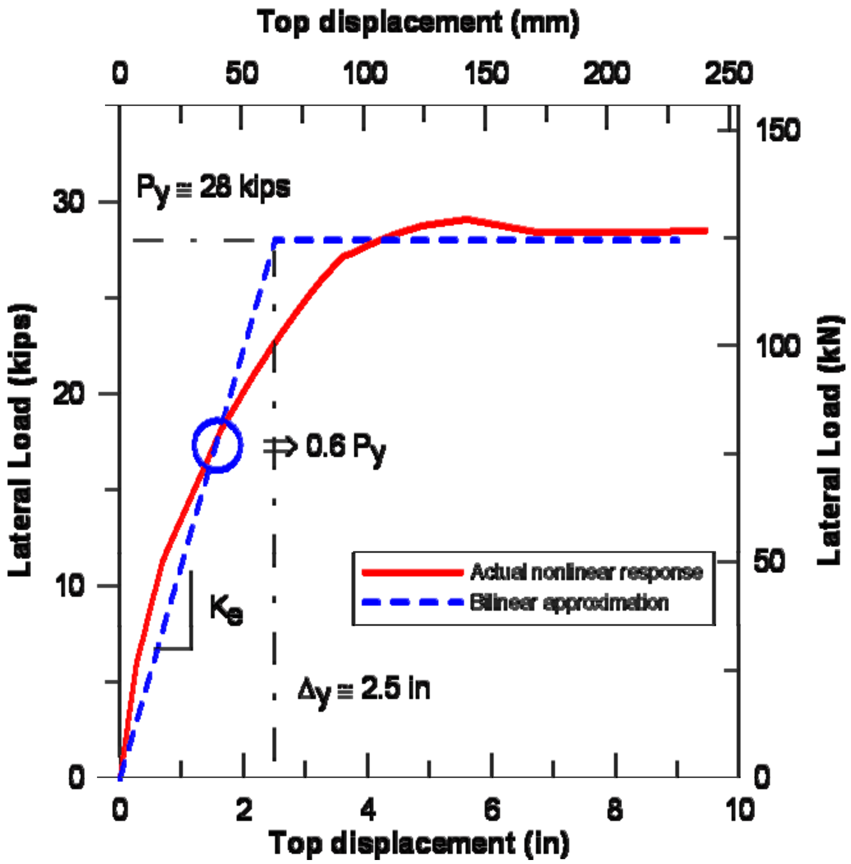

Figure 3.11. Top displacement vs. the applied lateral load for the flagpole shaft (FEM model).

The slope or curvature profiles of the shaft can be obtained from the displacements. The deflection profiles are obtained by compiling the lateral displacement values at the central node of the shaft along its depth. The slope and curvature profiles can be obtained by single and double differentiation of the deflection profiles, i.e.

$$s(z) = \frac{d}{dz} y(z) \quad \text{and} \quad \phi(z) = \frac{d}{dz} s(z) = \frac{d^2}{dz^2} y(z) \tag{3.1}$$

where $y(z)$, $s(z)$, and $\phi(z)$ denote the lateral deflection, slope, and curvature profiles, respectively. Alternatively, the curvature distribution along the shaft can be obtained by dividing the strain by the distance of each successive finite element node. This alternative method produces nearly the same results as those obtained by differentiation. Figure 3.12 displays the variation of the maximum curvature of the shaft with respect to its top displacement. The curvature at the yield displacement (Δ_y) can be defined as yield curvature (ϕ_y) and it is approximately 0.0002/in. As it can be seen from Figure 3.12, the maximum curvature increases drastically when the top deflection reaches 6 inches, far exceeding the yield displacement.

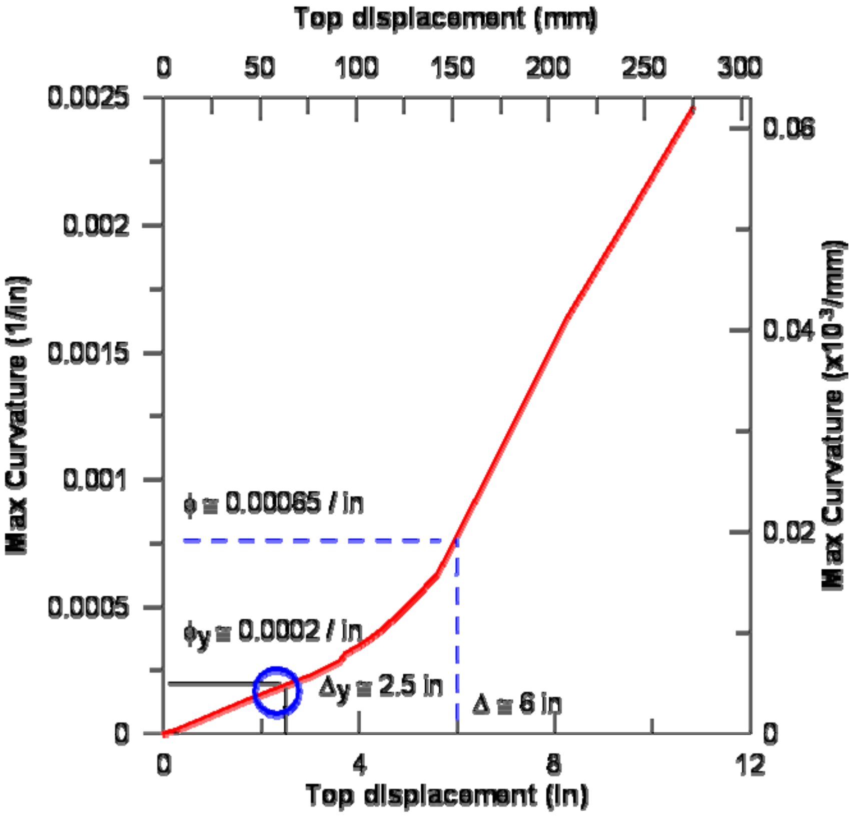

Figure 3.12. Maximum curvature vs. top displacement for the flagpole shaft (FEM model).

The deflection, slope, and curvature profiles are displayed in Figure 3.13. The displacement profiles indicate that the top deflection begins to increase drastically when it exceeds the yield displacement, which is marked on the Figure 3.13 with a dotted line. The deflection at the ground is about 0.5 inches when the top deflection of the shaft reaches 8 inches. The curvature profiles indicate that the location of the maximum curvature point migrates downward as the top displacement increases and a plastic hinge forms at 1ft below the ground line (the yield curvature is also marked with a dotted line in Figure 3.13).

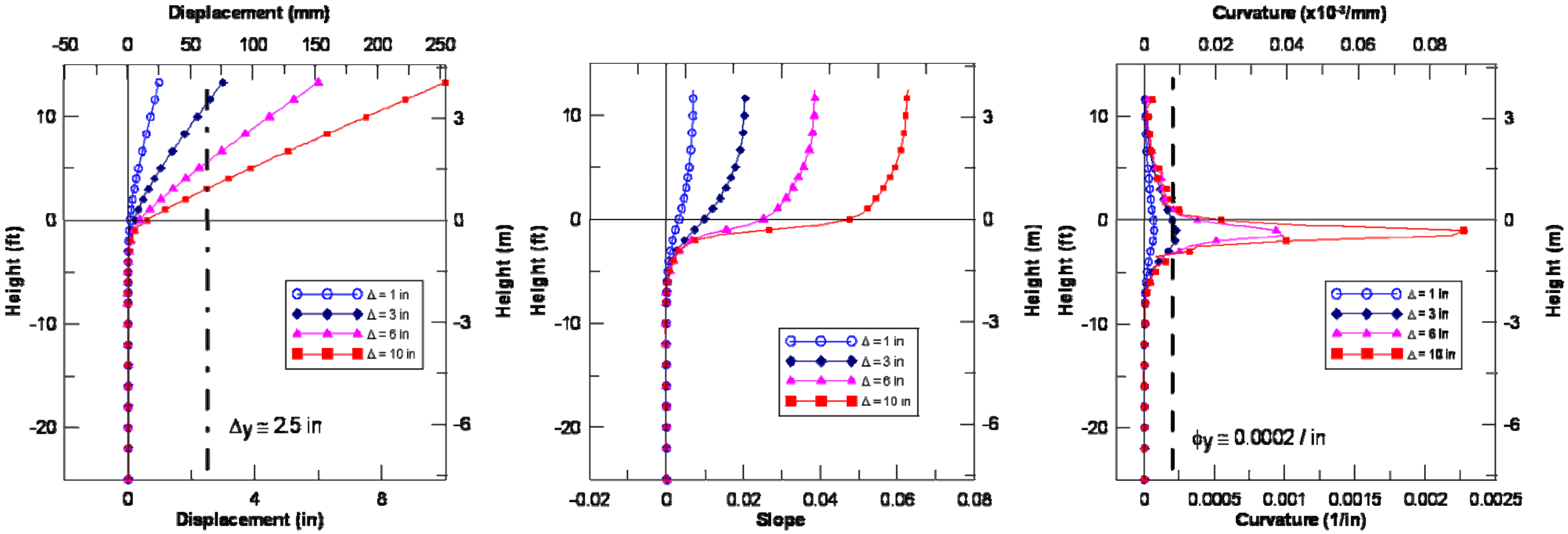

Figure 3.13. Displacement, slope and curvature profiles for the flagpole shaft (FEM).

The other response quantities of interest are the moment, shear, and soil reaction profiles. In a traditional (basic Winkler-type) model, which assumes that the shaft is elastic, the moment and curvature are related to each other through a constant bending rigidity (*EI*) along the depth; i.e., $M(z) = EI\phi(z) = EI\, d^2y(z)/dz^2$. Under the same assumption, the shear and the soil reaction distributions can be computed by single and double differentiations of the moment, and hence, by third and fourth differentiations of the lateral deflections, respectively. To wit,

$$V(z) = \frac{d}{dz}M(z) = EI\frac{d^3}{dz^3}y(z) \text{ and } p(z) = \frac{d}{dz}V(z) = EI\frac{d^4}{dz^4}y(z) \tag{3.2}$$

where *M*(*z*)*, V*(*z*)*,* and *p*(*z*) denote the moment, shear, and soil reaction profiles. Therefore, the shaft deflection profile is the only data that is required to derive all the results in the traditional approach.

For an inelastic shaft, the process is different: The moment at any depth along the length of the shaft can be obtained by integrating (summing, in a discrete model) all of the resultant forces multiplied by their respective moment arms. The moment profile generated thus, can be used to generate, in turn, the shear and soil reaction profiles as,

$$V(z) = \frac{d}{dz}M(z) \text{ and } p(z) = \frac{d}{dz}V(z) = \frac{d^2}{dz^2}M(z) \tag{3.3}$$

Therefore, the resisting forces (moment, shear, soil reaction) can be obtained via direct equilibrium, independent of the inelastic material response and the deformations. These resisting forces (i.e., moment) combined with their respective strain resultants (i.e., curvature) form the nonlinear constitutive relationships for the inelastic beam.

The moment-curvature relationship, obtained using the procedure described above, at 1ft below the ground where maximum moment along the shaft occurs is displayed in Figure 3.14. Figure 3.14 also displays the moment-curvature relationships from other programs such as Biax and OpenSees for validation purpose. We compare our models with commercial codes for flagpole shaft to make sure that the models (FEM (ABAQUS) and FRAMELAB) are yielding reasonable results with respect to more established procedures. The moment-curvature relationships from Biax and OpenSees are obtained simply by loading a cantilever column model at its tip, and by determining the moment and the curvature at its fixed end. The moment-curvature relationship produced via ABAQUS appears to be very similar to those by Biax and OpenSees, but displays more degradation of the moment capacity after yielding. The yielding moment and yielding curvature can be obtained by the same approach used for defining the yield displacement earlier in Figure 3.11 (i.e., by taking the effective stiffness as secant stiffness at a moment equal to 60% of the yield moment). The yield moment M_y, and the yield curvature obtained thus, are approximately 4500 kips-in and 0.0002/in, respectively, as indicated in Figure 3.14. Note that this yield curvature is nearly identical to that in Figure 3.12.

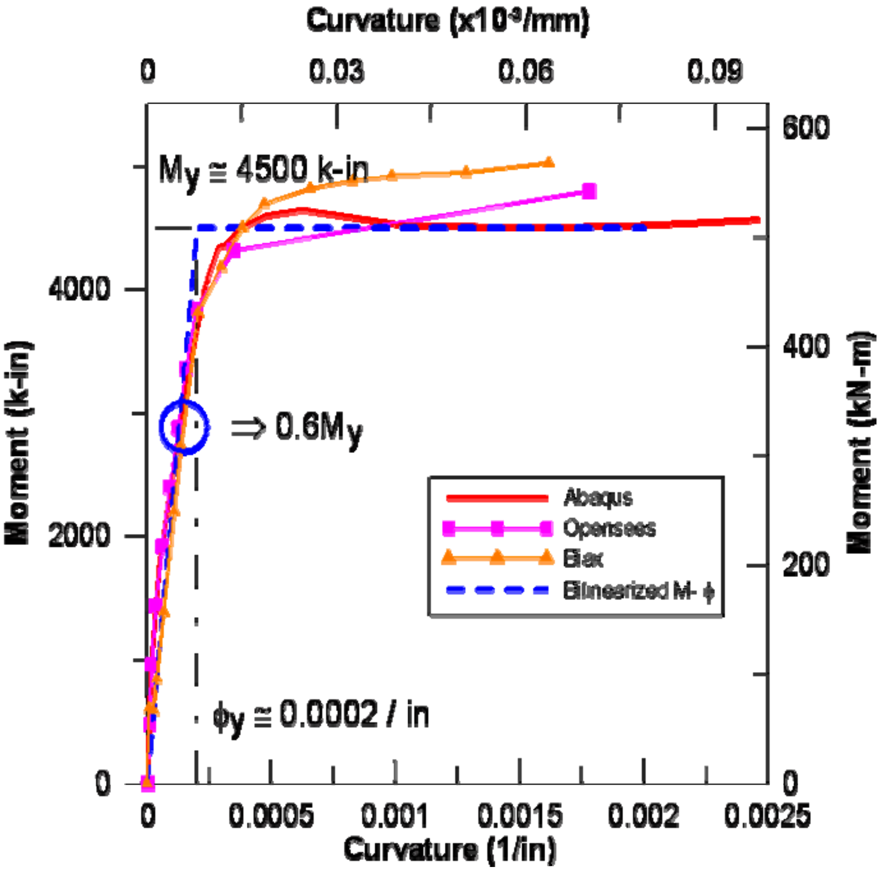

Figure 3.14. Moment-curvature relationship comparisons for the flagpole shaft.

The profiles for moment, shear, and soil reaction, as well as the *p-y* curves at various depths are displayed in Figure 3.15. The moment profiles indicate that the maximum moment on the shaft occurs at the ground level when the shaft behaves elastically; and the location of the maximum moment migrates downward as the shaft starts responding inelastically. The maximum moment occurs at 1 ft below the ground level as the top displacement reaches nearly 4 inches. The inflection point forms at about 10 ft below the ground (the yield moment value is shown with a dotted line).

The shear-force profiles are obtained via single differentiation of the moment profiles, as mentioned earlier (shown in top-right graph in Figure 3.15). The shear capacity of the section is determined by the sum of the shear strength associated with the transverse reinforcement (hoops) and the concrete. According to the ATC-32 (1996) recommendation, the shear strengths of the circular hoops and concrete are determined as:

$$\begin{aligned} V_S &= \frac{\pi}{2}\frac{A_{sp} f_{yh}\ D'}{s} = \frac{\pi}{2}\frac{0.44 \times 72 \times (24-4)}{4} = 249 \text{ kips} \\ V_c &= 2\sqrt{f_c^{'}}\ A_e = 2\sqrt{4000}\left(\pi \times 12^2\right) = 57 \text{ kips} \end{aligned} \tag{3.4}$$

where D' is the diameter of the hoop reinforcement measured to the hoop centerline, s is the vertical hoops spacing and A_{sp} is the cross-sectional area of the hoop, and A_e is the effective shear area of the shaft. The total shear capacity, therefore, is about 306 kips, mainly resisted by the shear reinforcement, and thus, the shaft appears to have a sufficient shear resistance.

The profiles for the lateral soil reaction (*p*) are displayed in (the bottom-left graph of) Figure 3.15. The direction of soil reaction is changing through the depth, at approximately 5 ft and 20 ft below the ground.

The combined response, load transfer (*p-y*) curves are obtained by combining the soil reaction profiles—*p*(*z*) in Figure 3.15—and the deflection profiles—*y*(*z*) in Figure 3.13—at each depth. The *p-y* curves at selected depths (i.e., -0.5 ft, -1 ft, -2 ft, and -3 ft from the ground level) are shown in (the bottom-right graph of) Figure 3.15. As expected, the larger soil resistance increases with depth.

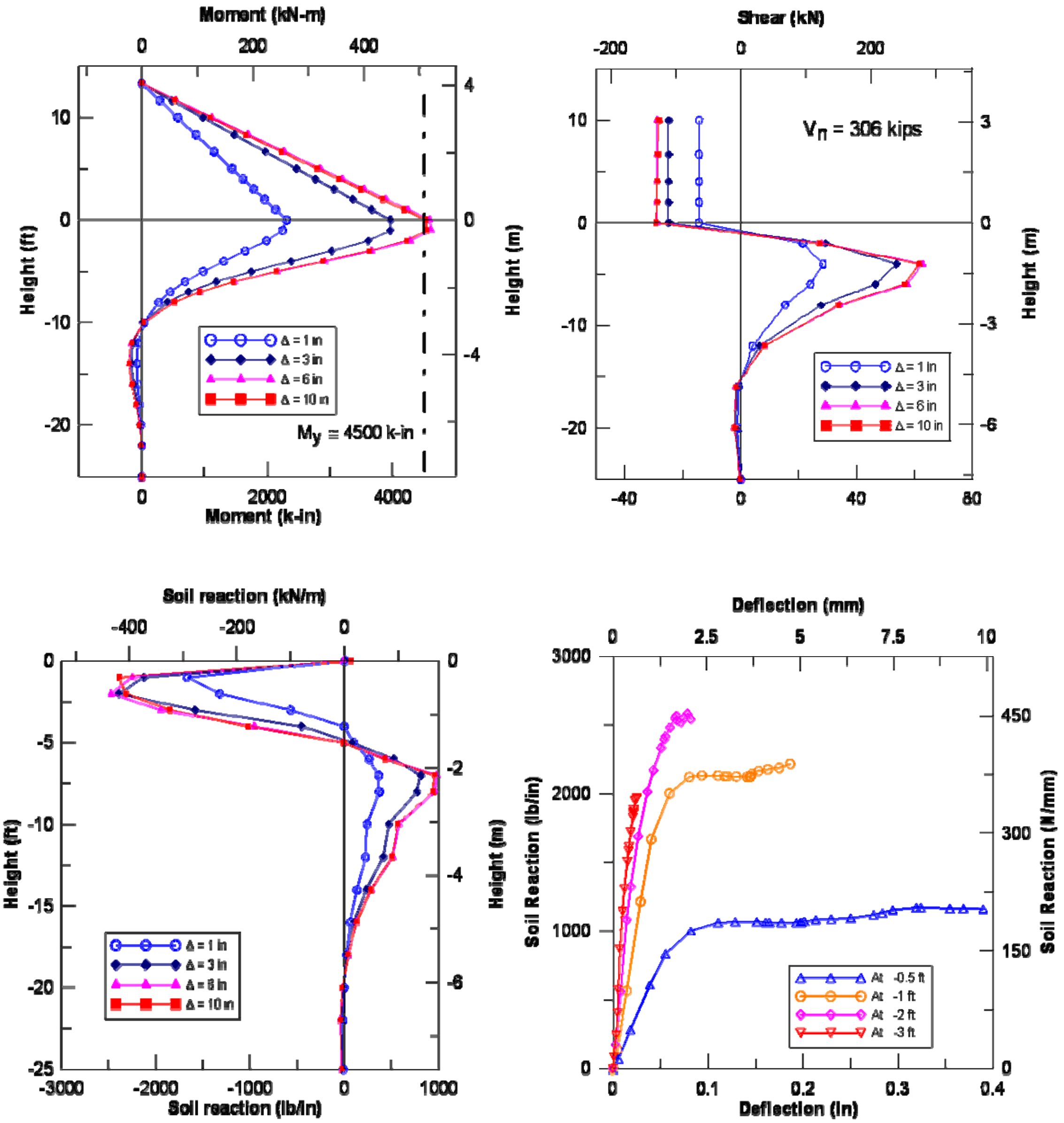

Figure 3.15. Profiles of moment, shear-force, and soil reaction, and the p-y curves at various depths of the flagpole shaft (FEM).

Flagpole Shaft Simulation Results with the p-y Approach

The analysis results via the *p-y* approach, using the standard API and the "*experimental*" *p-y* envelope (backbone) curves, are presented side-by-side in Figures 3.16 through 3.25. These figures present the same response quantities obtained via the three-dimensional finite element simulations (i.e., Figures 3.11 through 3.15) in the same order. The responses obtained with the *experimental* envelope curves are generally stiffer than those obtained with the API *p-y* curves.

Flagpole Shaft Simulation Results with the Strain Wedge Model

The analysis results with the strain wedge model are also presented in the same order as with the previous models, in Figures 3.26 through 3.28. The main difference between the strain wedge model and the other approaches are the specific *p-y* curves used. The *p-y* curves deduced from the SWM indicate that the maximum soil reaction (*p*) tends to decrease with soil depth as shown in Figure 3.28.

An Overview of Simulation Results for the Flagpole Shaft

The results obtained using the three-dimensional finite element simulation using ABAQUS (Figures 3.11-15), the *p-y* approach (Figures 3.16-25), and strain wedge model (Figure 3.26-28) display similar responses. The top lateral displacements versus force obtained with the three different approaches indicate that the FEM model (ABAQUS) displays stiffer soil response than the *p-y* model using the API *p-y* curves (FrameLab) or the strain wedge model (SWM) as displayed in Figure 3.29. However, the responses of the *p-y* model using experimental *p-y* curves are very close to the FEM results, especially prior to yielding. Generally, the finite element model predicts a stiffer soil response than both the *p-y* model and the strain wedge model. This observation is more clearly made when the lateral soil reaction versus the lateral displacement curves (i.e. the *p-y* curves) at various depths are inspected (Figure 3.30). In other words, the API *p-y* curves, the experimental *p-y* curves, and the *p-y* curves deduced from the strain wedge model are softer than those predicted by FEM model in general, for the soil profile and the shaft geometry investigated here. It is noteworthy that the *p-y* curves from SWM resemble those deduced from ABAQUS at shallower depths and become closer to the FrameLab (standard API or experimental) curves as the depth increases. Although the global responses do not differ by much as predicted by any of the three models, it is possible that these differences would be larger at higher values of the top displacement.

The general observations from the flagpole shaft simulations are as follows:

- The yielding top displacement of the shaft is expected at about 2.5 inches (ABAQUS), 3.0 ~ 3.75 inches (FrameLab, w/ experimental or standard API *p-y* curves), or 4.5 inches (SWM). Note that these yield displacements are based on the previously described bilinear approximation and the actual behavior predicted by the three models are highly nonlinear as displayed in Figure 3.59. The corresponding yield load is about 28 kips (ABAQUS), 29 ~ 31 kips (FrameLab, w/ experimental or standard API *p-y* curves) or 27 kips (SWM). The expected yielding moment of the shaft is about 4500 kips-in (ABAQUS and SWM) or 4800 kips-in (FrameLab) and the corresponding yielding curvature is about 0.0002/in (ABAQUS), 0.00017/in (FrameLab), or 0.00025/in (SWM).
- Maximum shaft moment is expected to occur at ground line in the beginning stage but will be move downward as the load or top displacement increased. The plastic hinge is anticipated at about 1ft ~ 2 ft below the ground and other inflection point is expected at 10 ft (ABAQUS), 12 ft ~ 15 ft (SWM), or 10 ~ 15 ft (FrameLab, w/ experimental or standard API *p-y* curves) below the ground line.
- Top displacement of the shaft is anticipated to increase drastically when the top displacement reaches about 6 inches (ABAQUS), 5.5 ~ 7 inches (FrameLab, w/ experimental or standard API *p-y* curves), or 4 inches (SWM).
- Shaft deflection at the ground is anticipated to about 0.5 ~ 1 inch when the top displacement reaches about 9 ~10 inches.
- The direction of soil reaction is expected to reverse around 5 ft and 20 ft below the ground line.
- The experimental *p-y* curves lie between those deduced from FEM and the standard API curves except at depths shallower than 3 ft. where the experimental *p-y* curves were assumed constant up to the ground level.

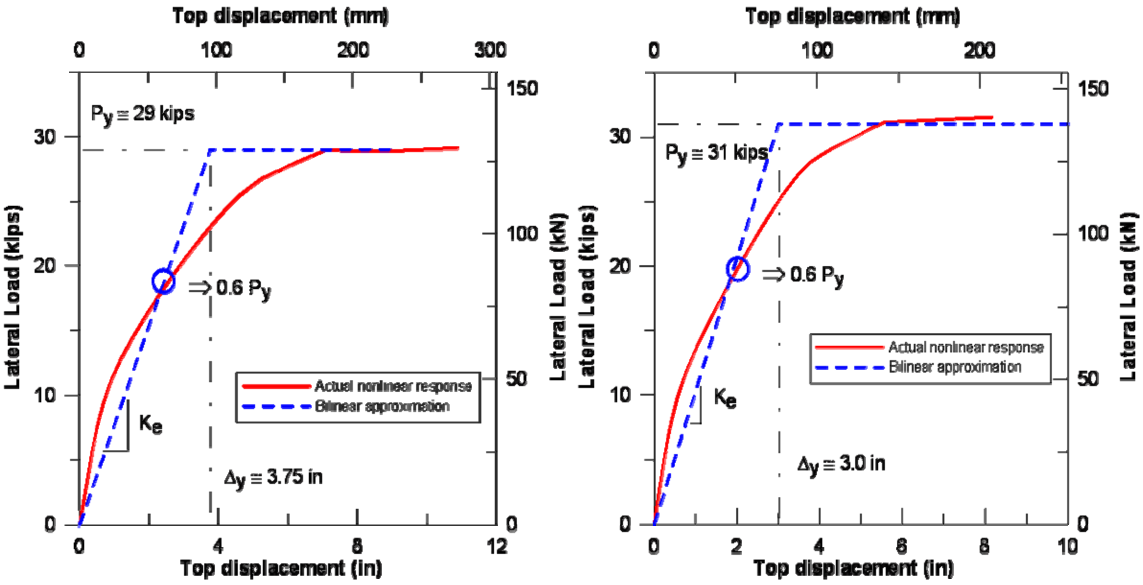

Figure 3.16. Top displacement versus the applied lateral load for the flagpole shaft using conventional API (left) and experimental p-y curves (right).

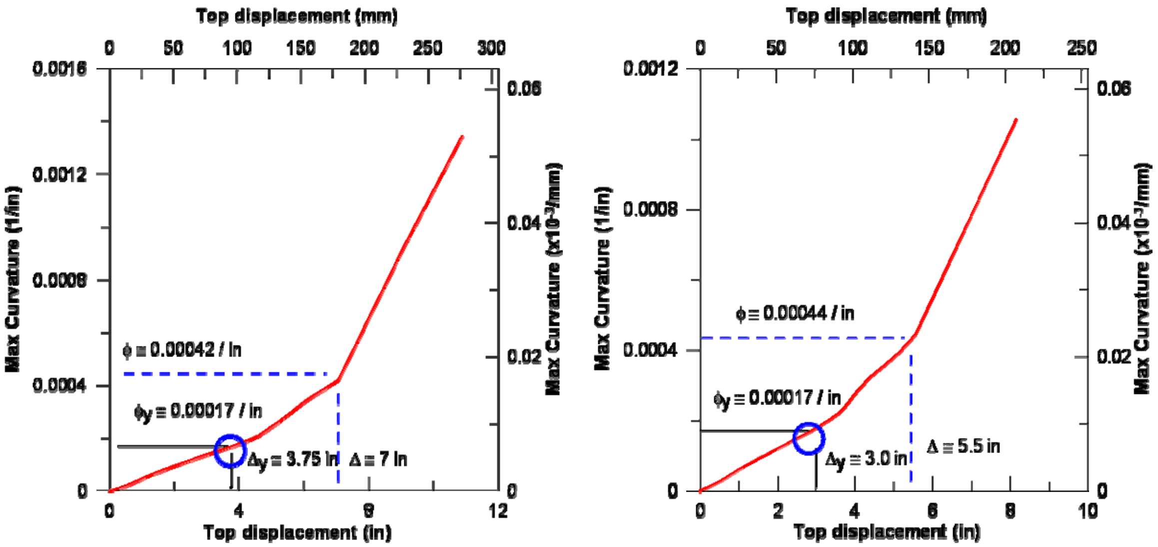

Figure 3.17. Maximum curvature versus the top displacement for the flagpole shaft using conventional API (left) and experimental p-y curves (right).

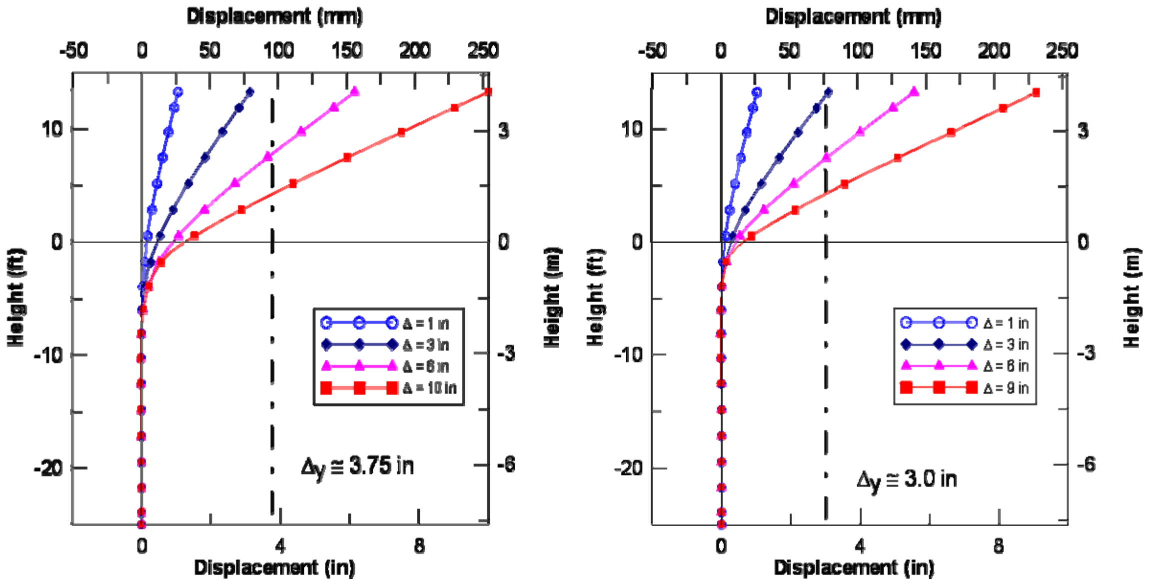

Figure 3.18. Displacement profiles for the flagpole shaft using conventional API (left) and experimental p-y curves (right).

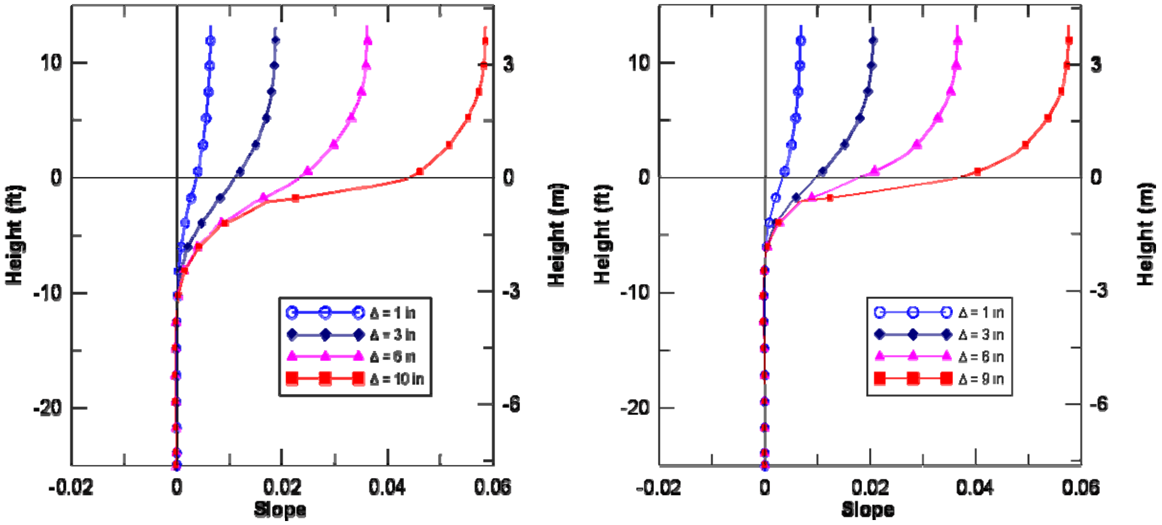

Figure 3.19. Slope profiles for the flagpole shaft using conventional API (left) and experimental p-y curves (right).

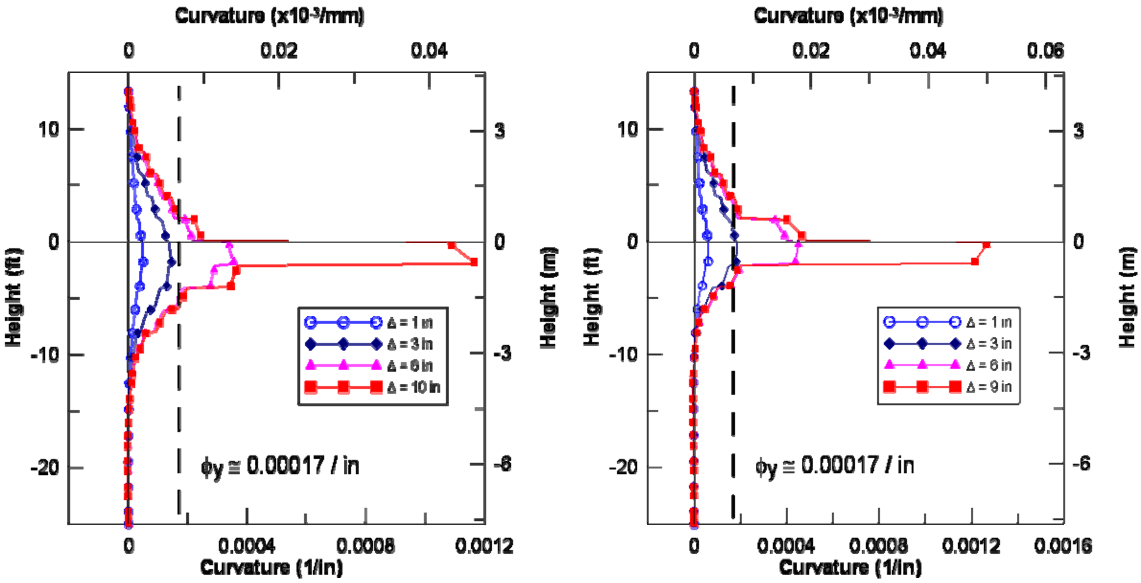

Figure 3.20. Curvature profiles for the flagpole shaft using conventional API (left) and experimental p-y curves (right).

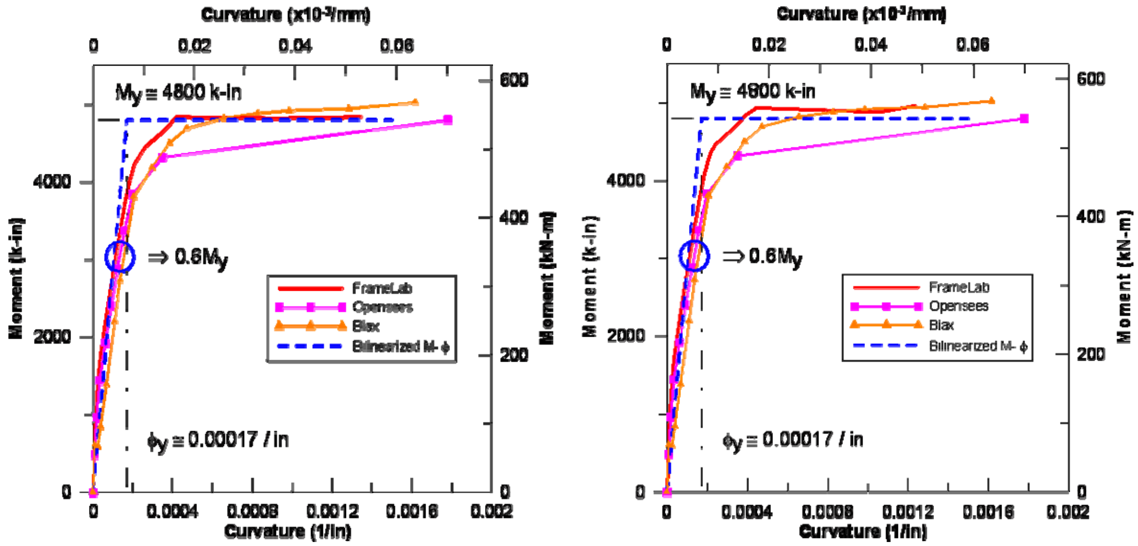

Figure 3.21. Moment-curvature relationship comparisons for the flagpole shaft using conventional API (left) and experimental p-y curves (right).

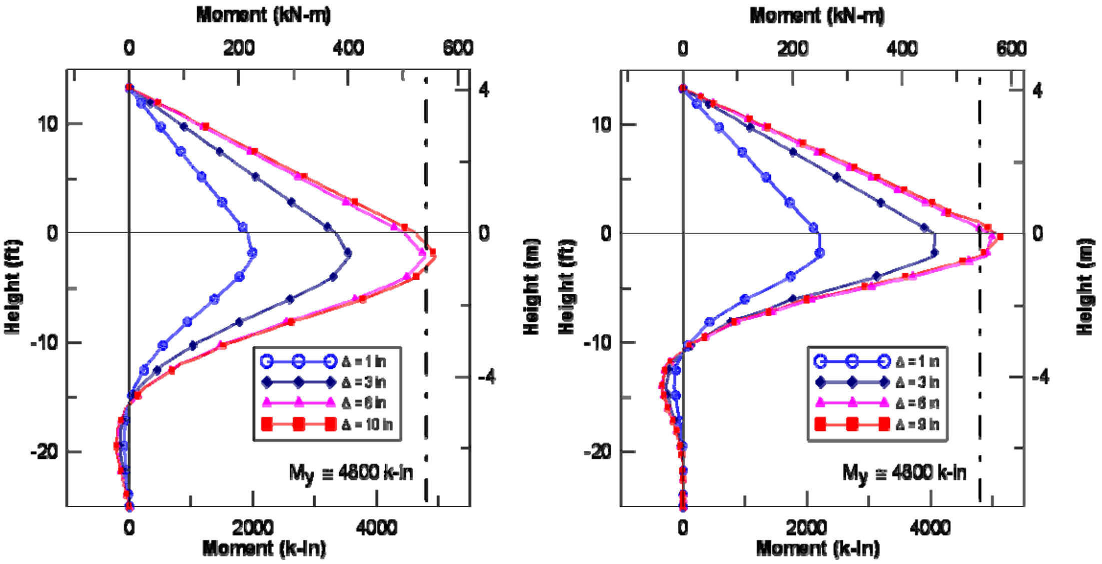

Figure 3.22. Moment profiles for the flagpole shaft using conventional API (left) and experimental p-y curves (right).

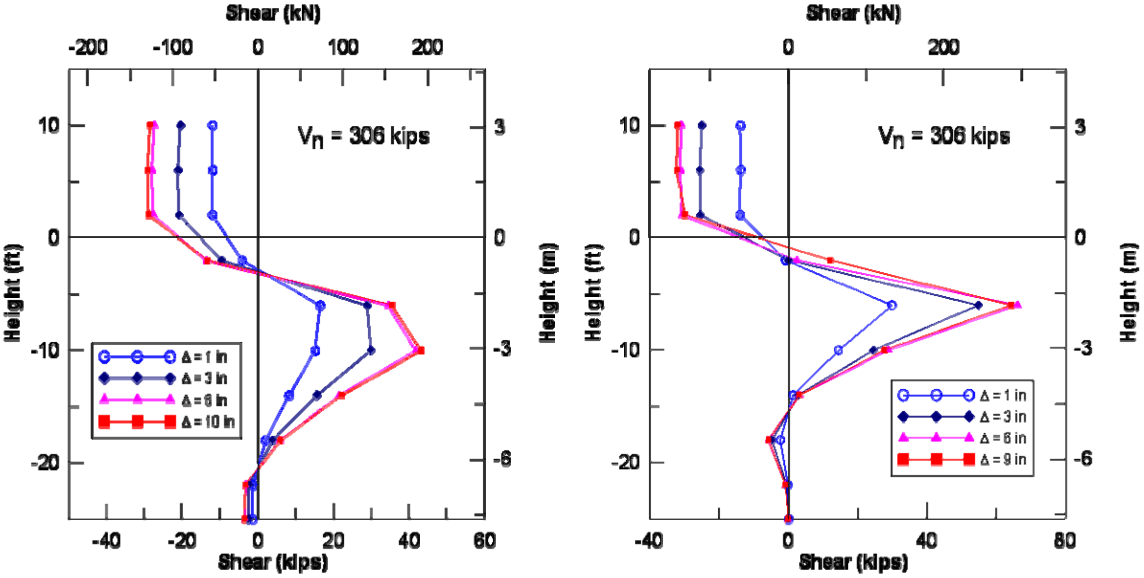

Figure 3.23. Shear force profiles for the flagpole shaft using conventional API (left) and experimental p-y curves (right).

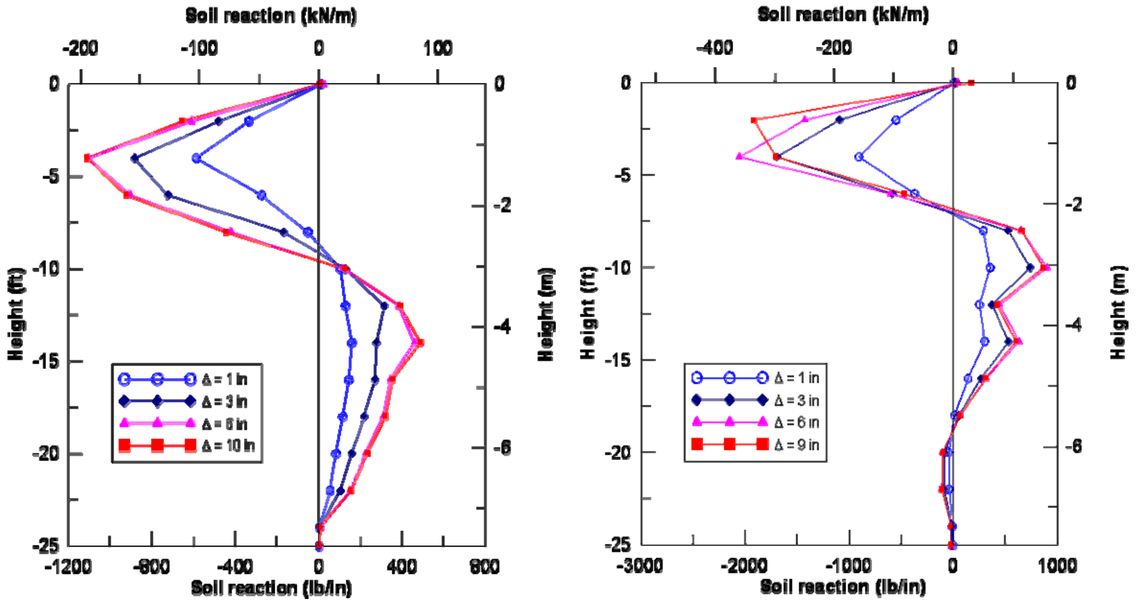

Figure 3.24. Soil reaction profiles for the flagpole shaft using conventional API (left) and experimental p-y curves (right).

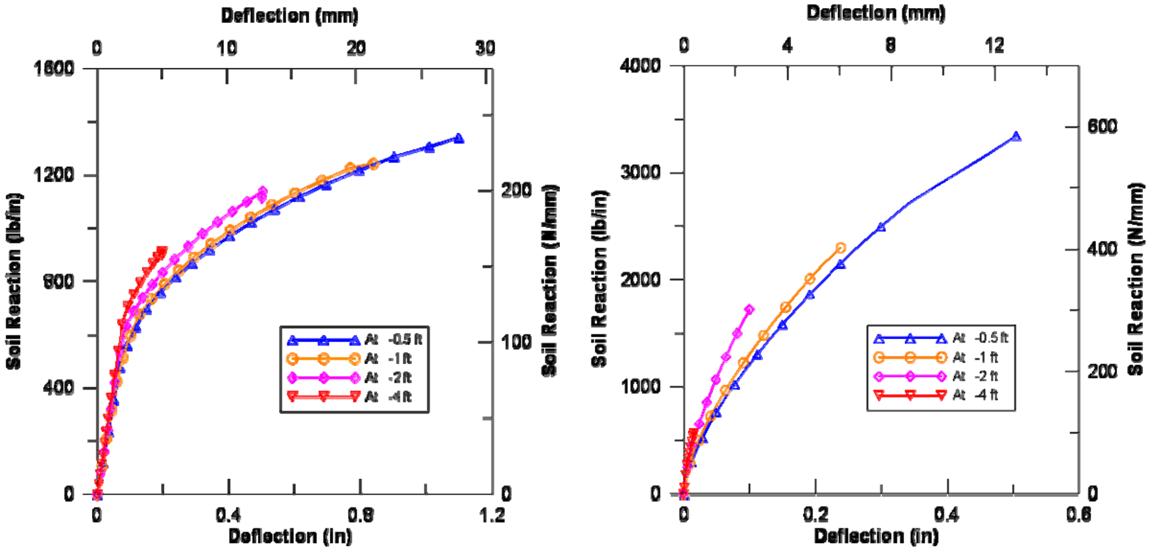

Figure 3.25. The p-y curves at various depths of the flagpole shaft: Conventional API (left); experimental p-y curves (right).

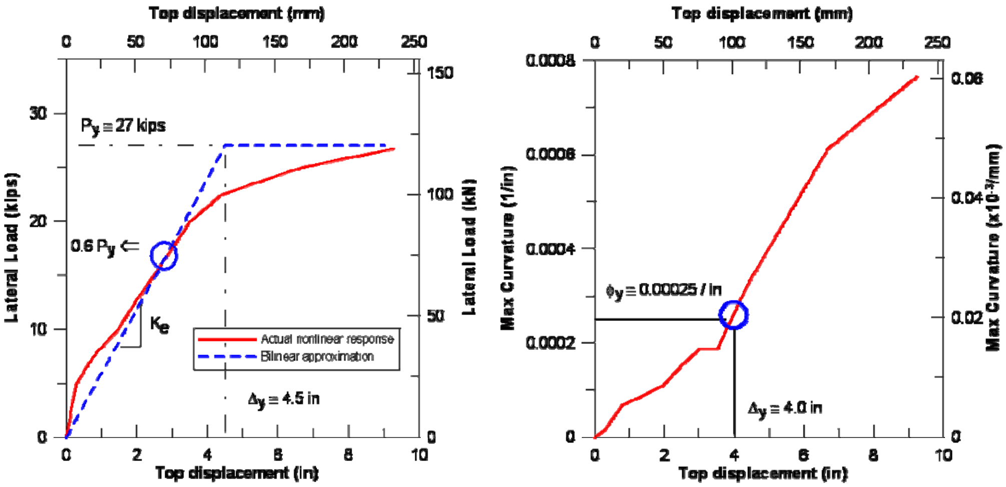

Figure 3.26. Top displacement versus the applied lateral load, and maximum curvature versus the top displacement for the flagpole shaft (SWM).

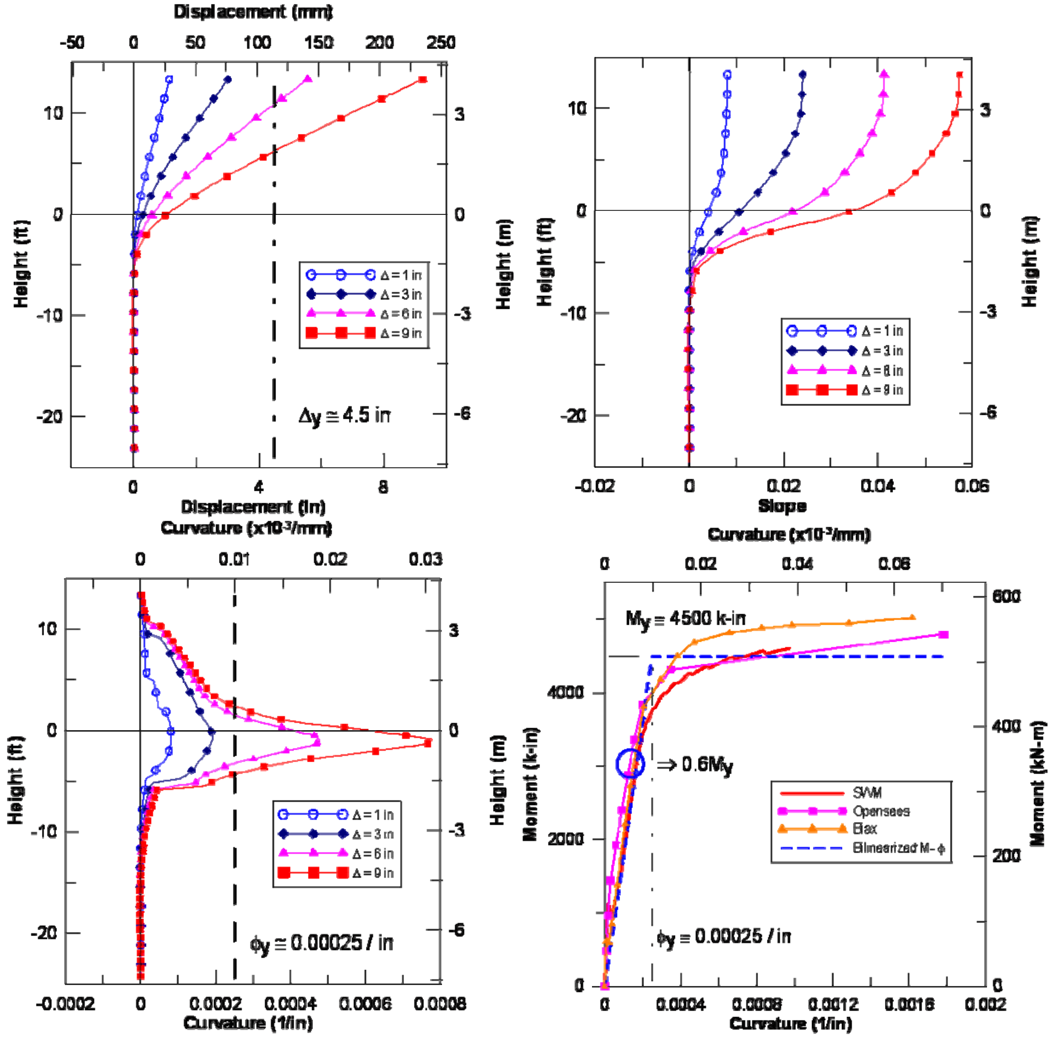

Figure 3.27. Displacement, slope, and curvature profiles, and moment-curvature relationship comparisons for the flagpole shaft (SWM).

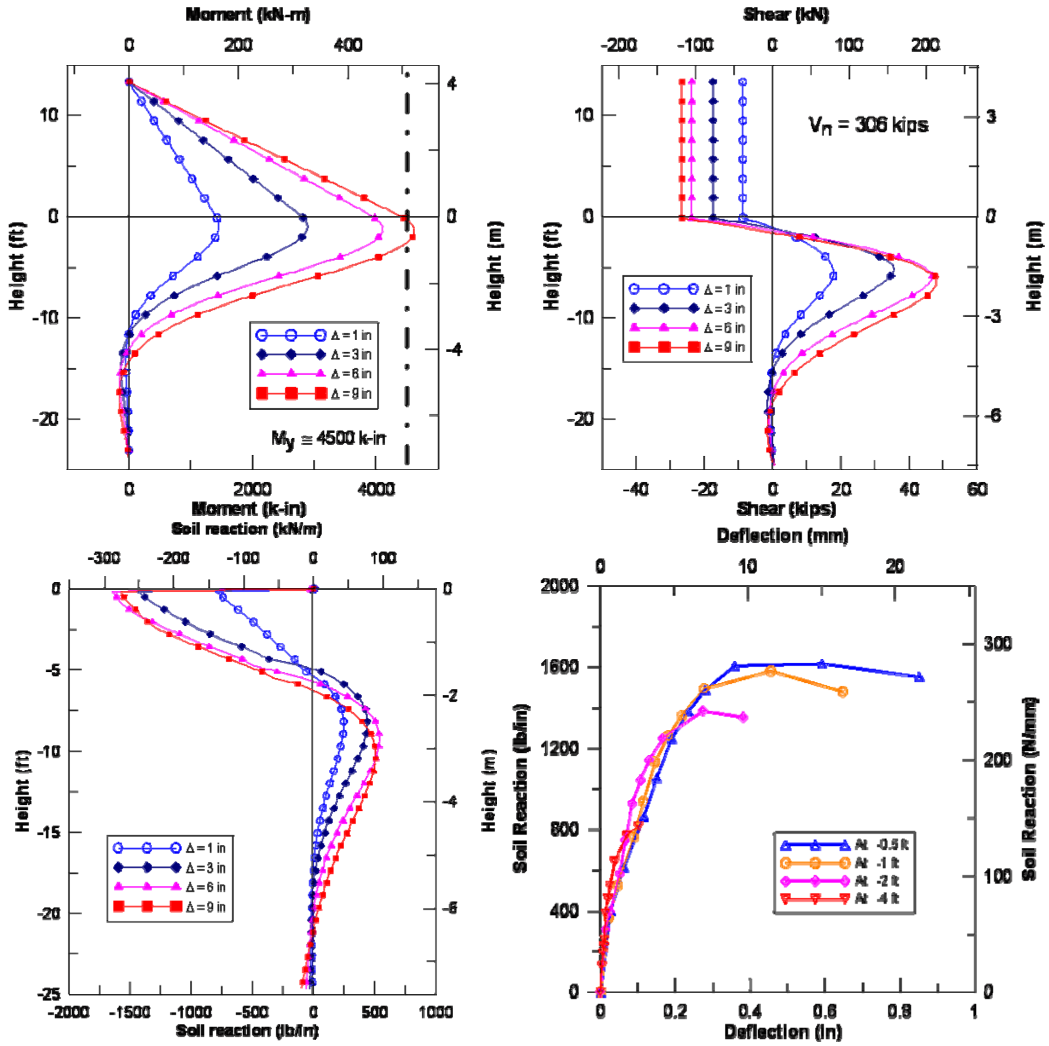

Figure 3.28. Profiles of moment, shear force, and soil reaction, and the p-y curves at various depths for the flagpole shaft (SWM).

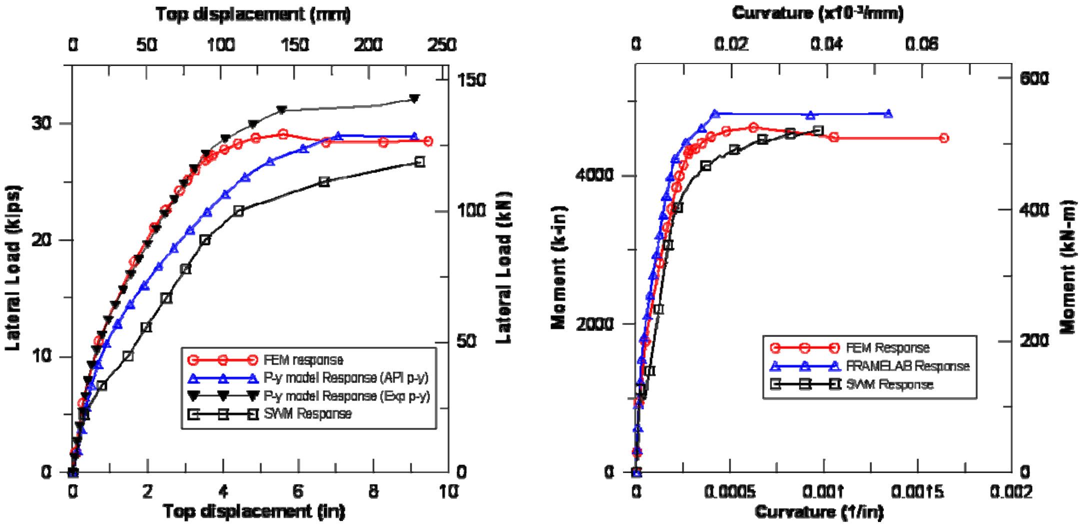

Figure 3.29. Load-displacement, and moment-curvature responses of the flagpole shaft, as computed via FEM, API/Experimental p-y and SWM approaches.

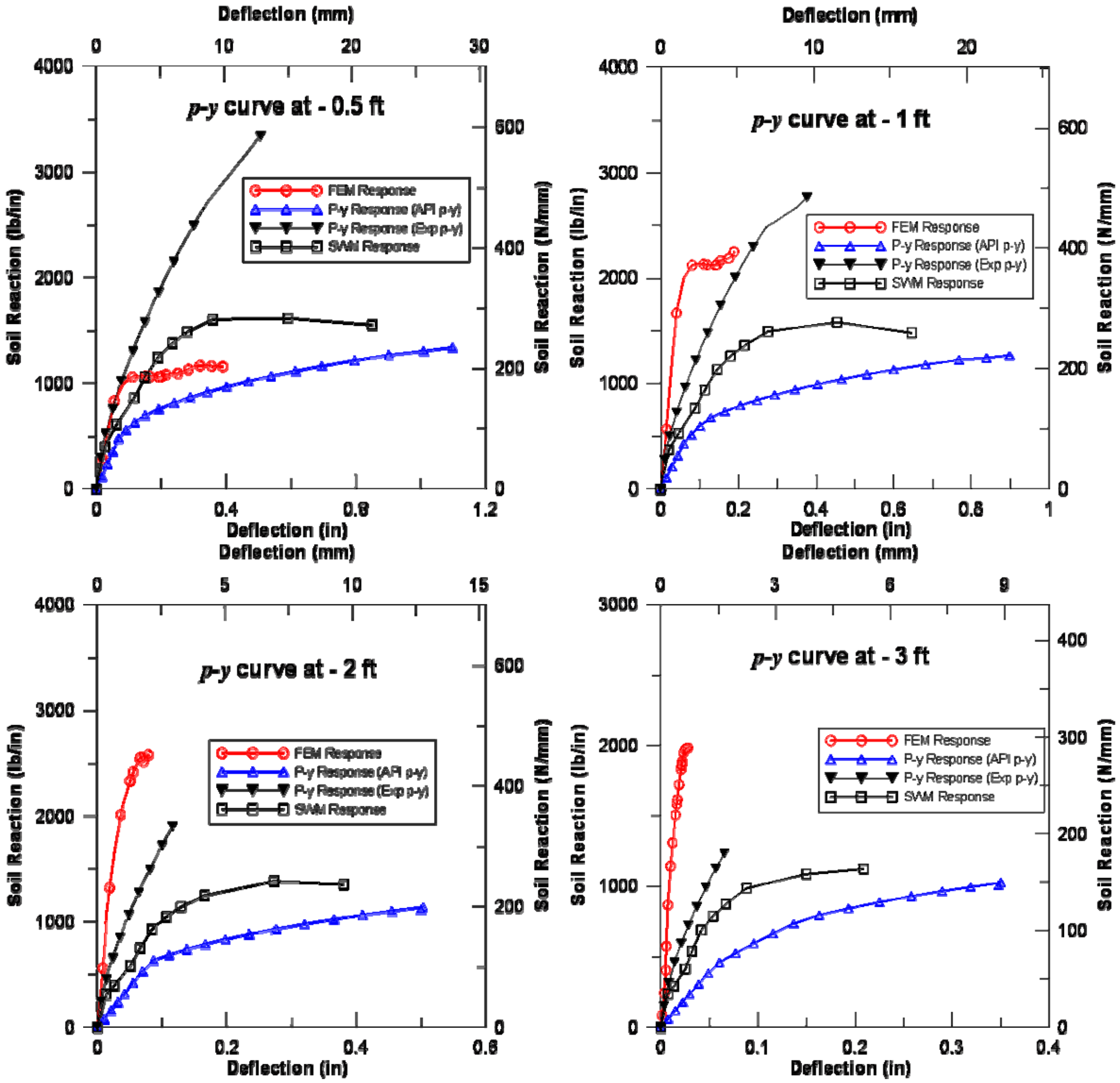

Figure 3.30. Comparison of the p-y curves for the flagpole shaft at various depths as computed/used in FEM, API/Experimental p-y and SWM simulations.

3.6.2 Fixed-Head Shaft

Load-Displacement Responses for the Fixed-head Shaft

The load-displacement results obtained using the three-dimensional finite element, macroelement (*p-y*), and strain wedge methods are displayed together in Figure 3.31. Two different types of boundary conditions are considered at the shaft top in the finite element model: In case 1, the shaft-top is fixed for rotation and axial displacement, and in case 2, the shaft-top is free to move axially while the rotation is fixed at zero. As previously mentioned, case 2 is a more realistic model of the field test set-up. The differences between these two sets of results are due to the effects of axial forces (or their lack thereof) on the nonlinearity of reinforced concrete. The top lateral displacements versus lateral force obtained from the three different approaches indicate that the FEM model with upper limit value of soil Young's modulus and *p-y* model with experimental *p-y* curves display much stiffer load-displacement response than the FEM model with lower limit value of soil Young's modulus, *p-y* model using API *p-y* curves, and the strain wedge model. Especially, the responses of the FEM model using lower limit of Young's modulus for soil and the response by strain wedge model display very soft responses in the initial range where the top displacement is less than 0.25 in.

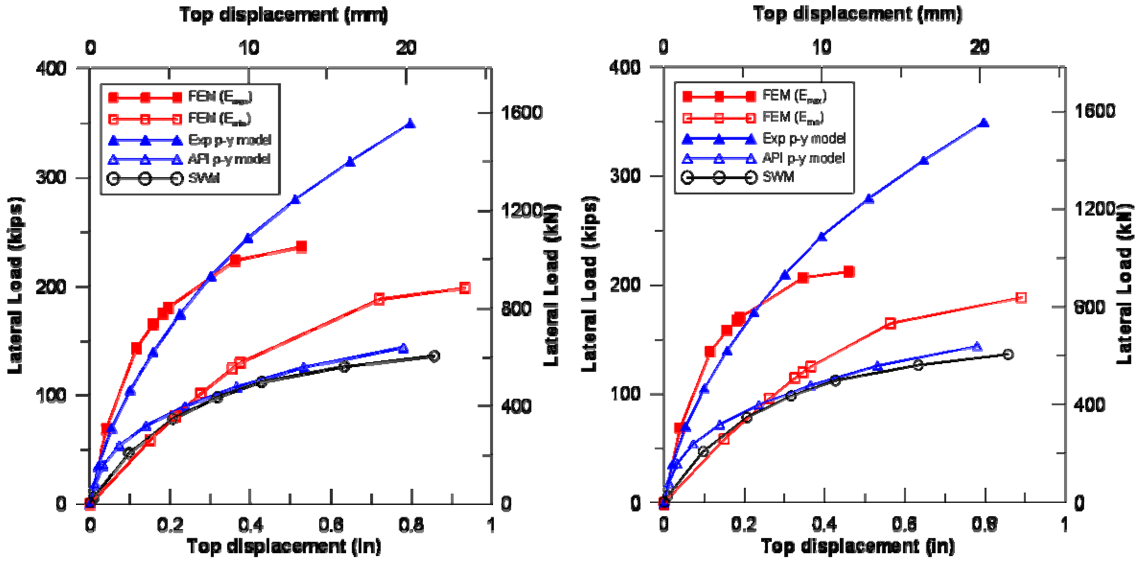

Figure 3.31. Top displacement versus the applied load for the fixed-head shaft: Axially fixed (left), and axially free (right) shaft responses.

Moment-Curvature Responses for the Fixed-head Shaft

The moment-curvature responses of the fixed-head shaft obtained through various modeling approaches are illustrated in Figure 3.32. Again, the differences between the two sets of three-dimensional FEM results are due to the effects of axial forces (or their lack thereof) on the nonlinearity of reinforced concrete. The effects of the axial force on the moment-curvature response are illustrated in Figure 3.33 through the pushover analysis of a freestanding column. The section and material properties of this column are taken to be identical to those of the 2ft-diameter fixed-head shaft. It can be observed that the column with constrained axial displacement (Figure 3.33a) displays a larger moment capacity than the column without this constraint (i.e., the cantilever in Figure 3.33b). The comparisons of moment-curvature responses for these two different boundary conditions are displayed in Figure 3.33c.

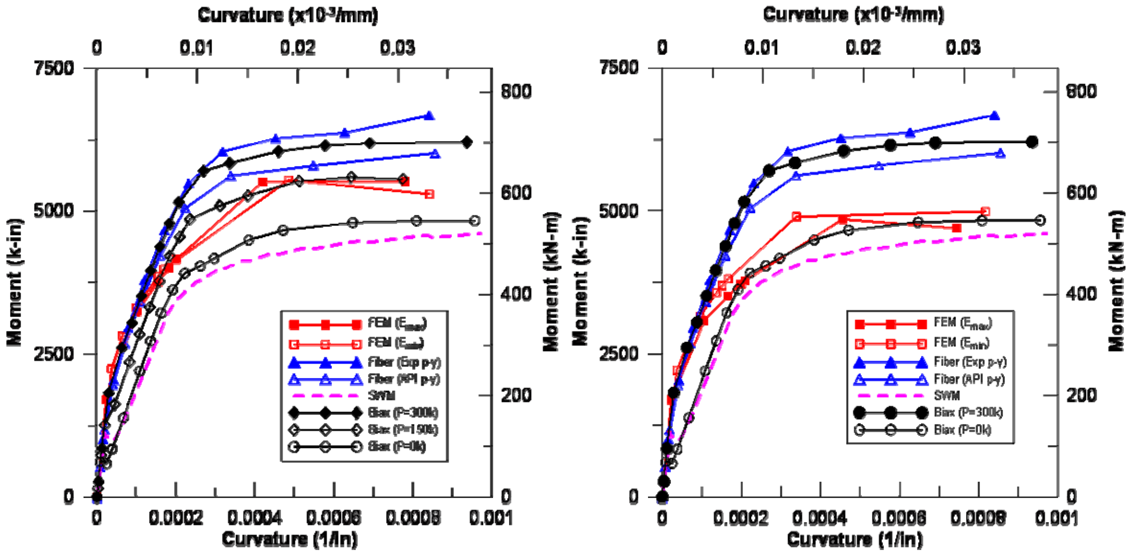

Figure 3.32. Moment-curvature response of the fixed-head shaft: Axially fixed (left), and axially free (right) shaft responses.

The difference in the moment capacity in FEM models in Figure 3.32 is also due to the axial constraint conditions at the shaft top. Since the shaft bottom is not constrained in the finite element model, the moment-curvature relationship from the finite element model produces yields smaller capacities than those from the *p-y* model. The strain wedge model predicts the lowest moment capacity for the shaft, and this implies that the shaft used in the SWM program is free to displace axially.

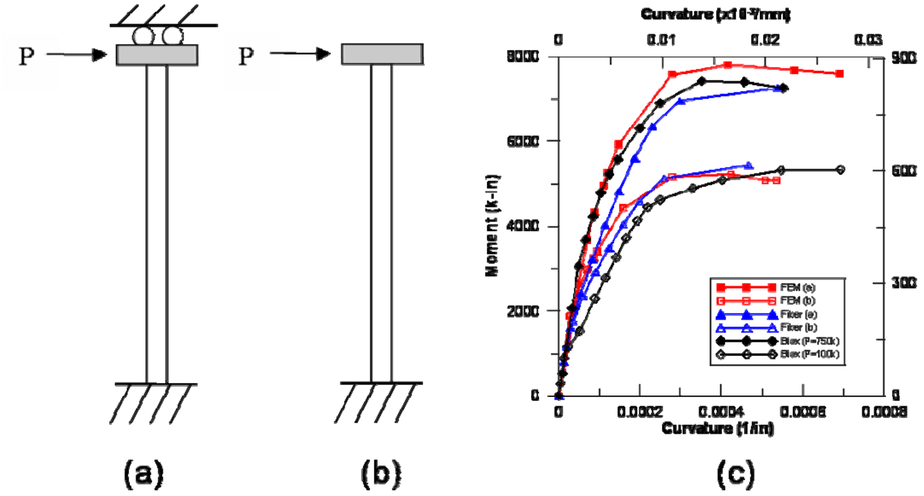

Figure 3.33. Moment-curvature response (c) of an axially fixed (a), and free (b) shafts.

Lateral Displacement and Moment Profiles for the Fixed-Head Shaft

The lateral displacement profiles along the length of the *axially free* shaft (i.e., case 2) are displayed in Figure 3.34. The displacement profiles, predicted by each modeling approach, are provided when the shaft top has reached 0.6 in. displacement. Because the finite element model with the upper bound of Young's modulus for the soil, and the macroelement (FrameLab) model with the experimental *p-y* curves are stiffer, the displacement profiles for these two models display inflection points at a shallower depth (approximately at 10 ft below the ground line). The other three models (i.e., FEM with soft soil, FrameLab with API *p-y*, and SWM) display softer responses with inflection points occurring at around 15 ft from the ground level.

The moment profiles along the shaft are also provided in Figure 3.34. Again, the FEM model with the stiff soil and macroelement model using the experimental *p-y* curves present the similar responses and are stiffer than the other models (i.e., the maximum moments occur at a shallow depth of about 6 ft. from the ground line). The other three models (i.e., FEM using soft soil, macroelement model using API *p-y* curves, and SWM) predict the maximum moment occurring at a deeper location (i.e., 8 ft to 10 ft from the ground line).

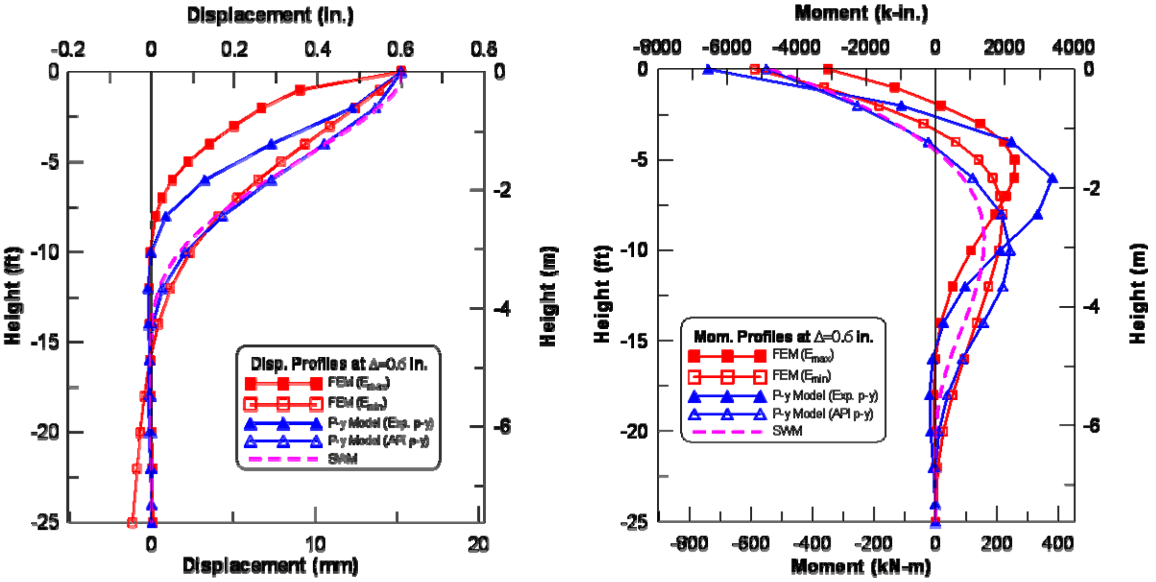

Figure 3.34. Lateral displacement and moment profiles for the fixed-head shaft, as computed via FEM, API/Experimental p-y and SWM approaches.

The p-y Curves of the Fixed-head Shaft

Lateral soil resistance-deflection relationships for the soil are presented by so called *p-y* curves; and the curves used for (or deduced from) each model at selected depths are shown in Figure

3.35. The *p-y* curves from the FEM model with the higher value of Young's modulus for soil produces the stiffest lateral soil response, followed by the experimental *p-y* curves. The initial stiffnesses (slope) of the *p-y* curves deduced from the SWM and the FEM (with soft soil) models are the lowest, as might be expected.

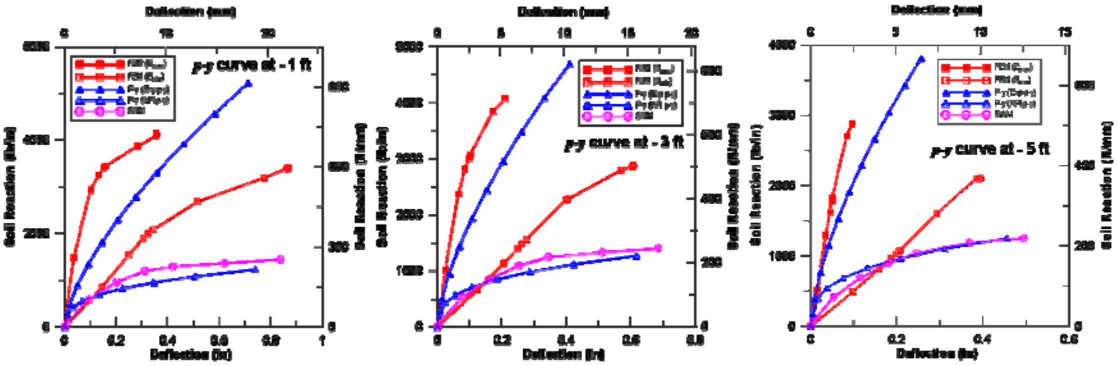

Figure 3.35. The p-y curves for the fixed-head shaft at various depths.

3.6.3 The 9-Pile Group

Load-Displacement Relationships for the Pile Group

The global load-displacement results obtained through FEM, the *p-y* approach, and SWM are displayed in Figure 3.36. Two extreme values ($E_{\max}$, $E_{\min}$) are considered for Young's modulus of the soil in the finite element model. The load-displacement response curves obtained from the *p-y* model using API *p-y* curves bracketed by curves obtained via FEM with lower and upper bound of soil Young's modulus, *when the p-multiplier for each pile is assumed to be unity.* When the recommended *p*-multipliers from Rollins *et al.* (2006) are used (see, §3.4.2), the API *p-y* model's load-displacement curve is reduced below that of the finite element model with $E_{\min}$, as shown Figure 3.36.

The strain wedge model fails to produce a result due to a "short pile behavior" error when the 1% reinforcement ratio is used—as designed for the current test specimen. The reinforcement ratios of all piles were then incrementally increased until they reached 1.8% for each pile, when numerical stability/convergence in SWM computations were attained. The SWM load-displacement curve shown in Figure 3.36 is obtained thus. Despite the increased reinforcement ratio, the load-displacement response obtained via SWM is the softest of all of the simulation results.

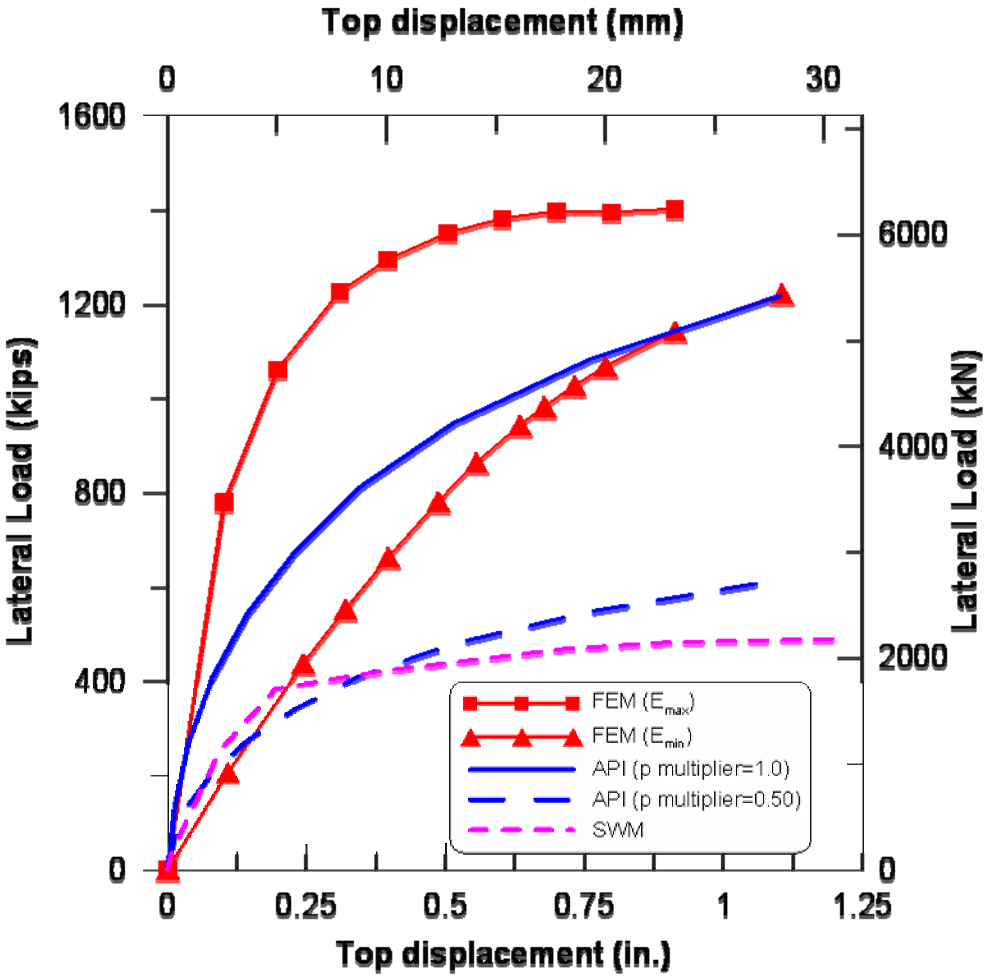

Figure 3.36. The overall load-displacement curves for the 9-pile group obtained via all simulation models.

Figure 3.37 displays the predicted load-displacement curves for several individual piles (i.e., piles 4, 5, 6, and 9). These results are obtained via FEM, API *p-y* model, and SWM. Load-displacement response curves for solitary (single) piles (obtained via FEM) are also shown in this Figure 3.as a reference. The solitary pile load-displacement response is stiffer than the response of individual piles in the group—implying pile-to-pile interactions within the group.

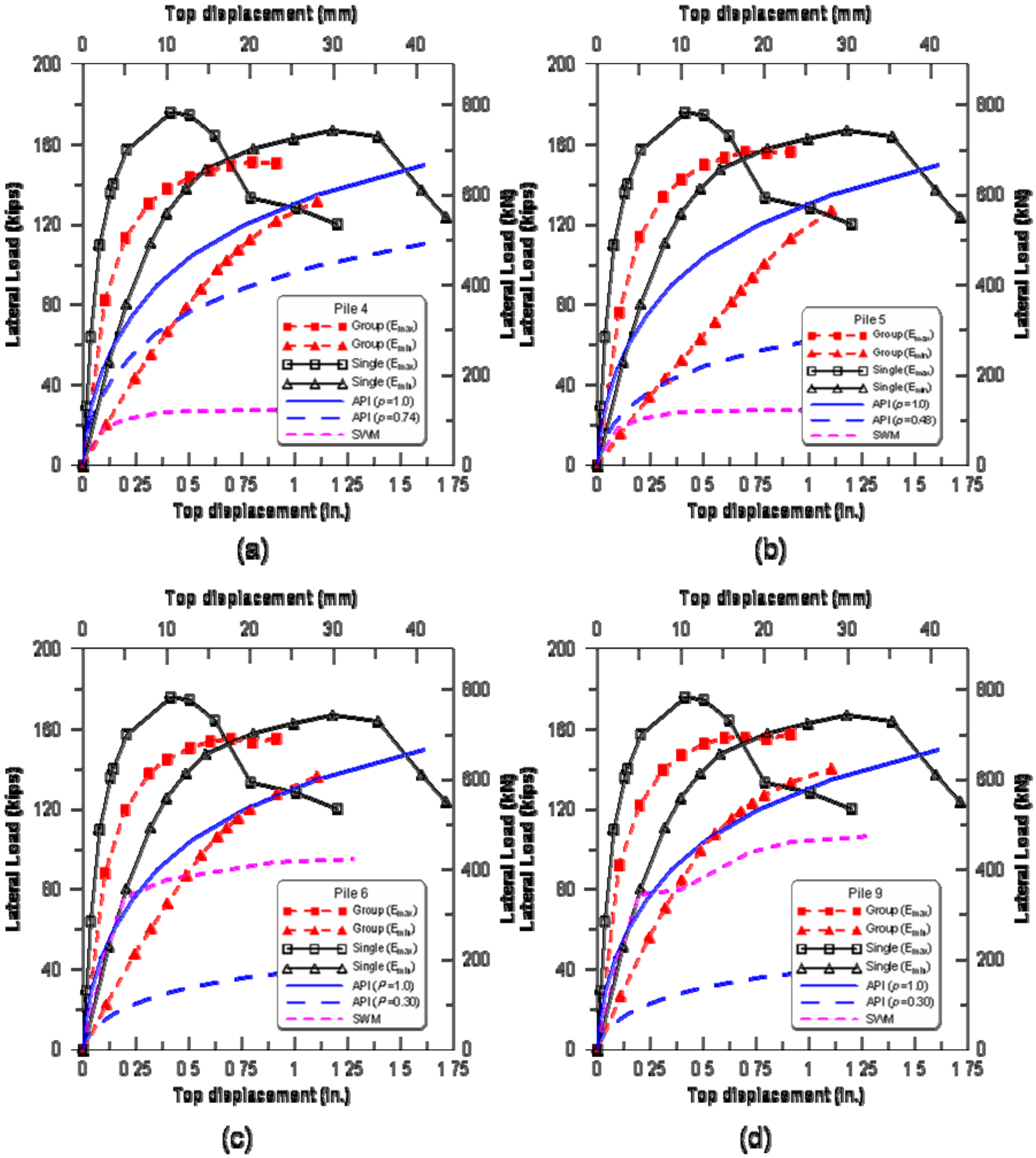

Figure 3.37. The load-displacement curves for piles (a) 4, (b) 5, (c) 6, and (d) 9.

The load-displacement responses of the same piles (as obtained via FEM) are shown together in a single graph in Figure 3.38. The reaction forces from each pile vary with their location and with the soil modulus. The middle piles (i.e., piles 2, 5, and 8) produce the smallest resisting forces, while the rear piles (i.e., piles 3, 6, and 9) produce the largest. The inside piles (i.e., piles 4, 5, and 6) produce resisting forces that are smaller than those by outside piles (i.e., piles 1, 2, 3, 7, 8, and 9). This observation may be attributed to the, so-called, “shadow effect” observed in pile groups.

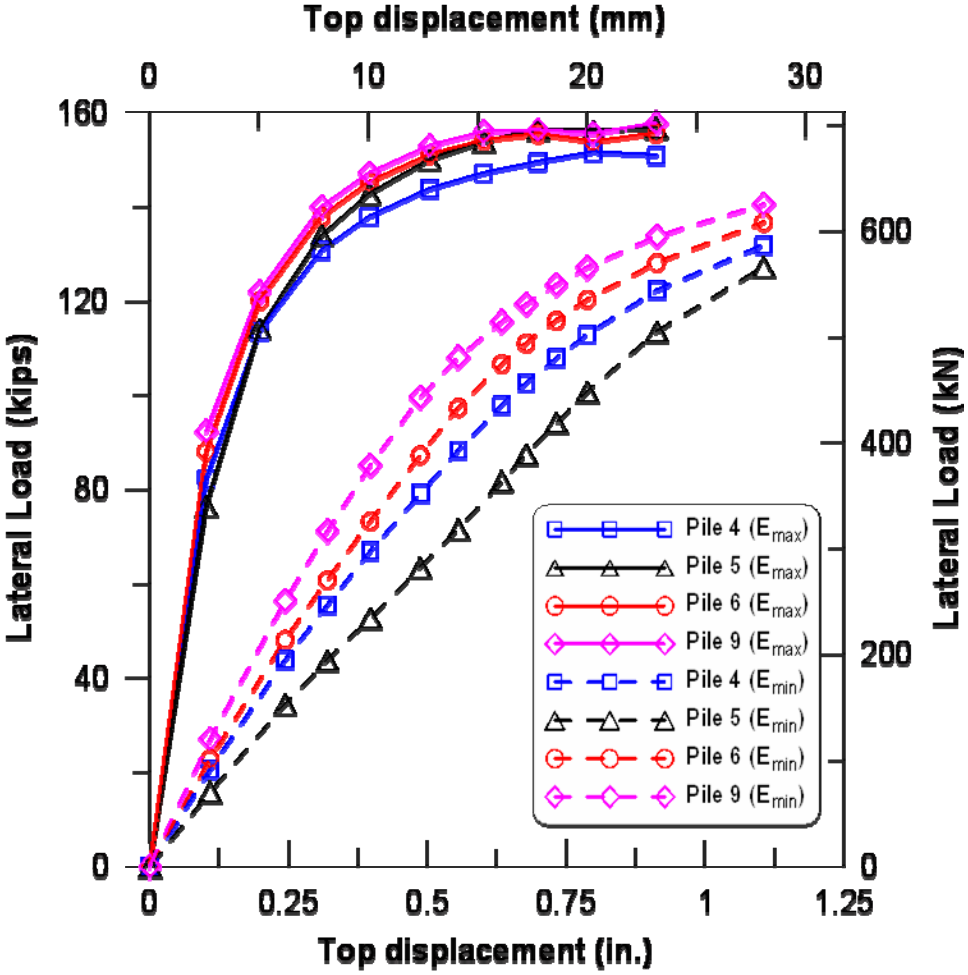

Figure 3.38. The load-displacement curves for piles (a) 4, (b) 5, (c) 6, and (d) 9 of the 9-pile group.

Moment-Curvature Relationships for the Pile Group

The moment-curvature relationship at a given cross-section (depth) can be computed from the nodal data from the three-dimensional finite element model. To wit, the moment at each cross-section can be calculated by integrating the product of nodal tractions and their respective distances from the centroid. The curvature information can be obtained by dividing the difference of nodal strains of two diametrical nodes by the distance between them. The moment-curvature relationships for each shaft, computed thus, are provided in Figure 3.39. The moment-curvature relationships for all of the piles of the FEM are similar, and display smaller capacities than that obtained from the fiber model. Among the moment-curvature relationships obtained from the finite element model, some degradations in moment capacities are observed in the piles located rear side (i.e., piles 6 and 9) as compared to the front or center piles (i.e., pile 4 and 5). These variations are due to axial loads introduced to the pile as a result of the pile-head constraint applied by the pile cap. The average yield moment and yield curvature are M_y = 3,500 k-in. (≈ 400 kN-m) and ϕ_y = 0.0002/in. (≈ 0.008/m) through a bilinear approximation.

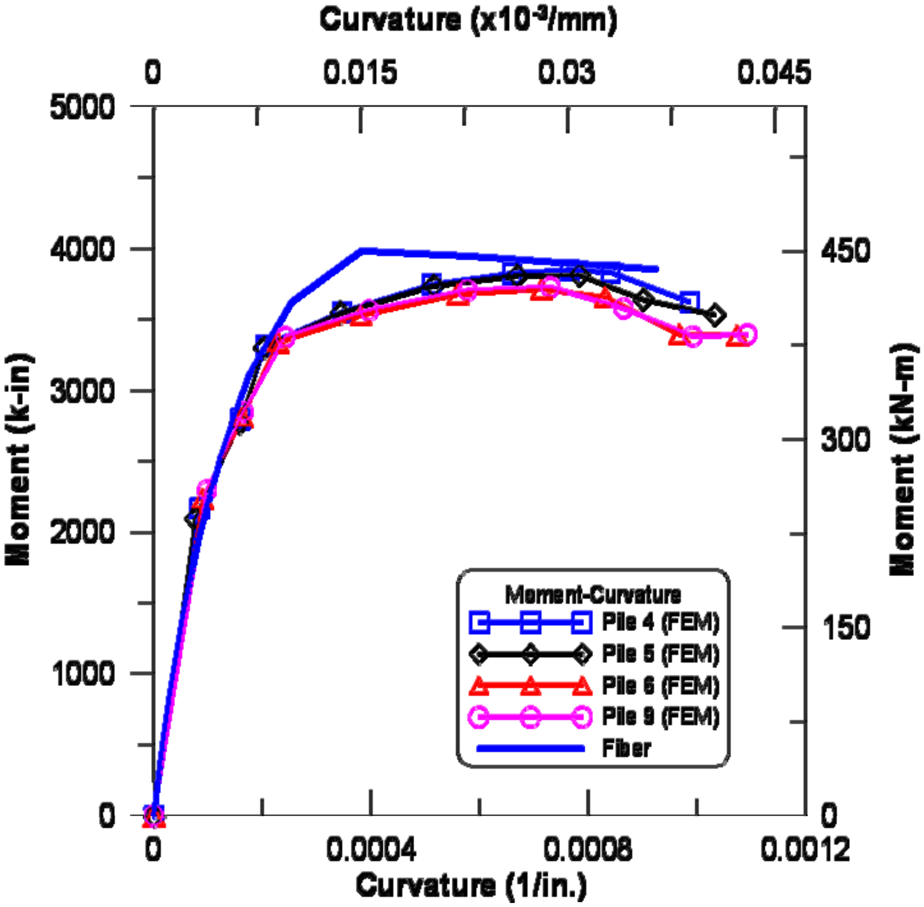

Figure 3.39. The moment-curvature relationships of representative piles of the 9-pile group.

Response Profiles for the Pile Group

The kinematic response profiles (such as deflection and curvature profiles) and the force response profiles (such as moment and soil reaction) are investigated here. In the finite element model, deflection profiles are obtained by connecting the lateral displacement values at the central node of the piles along its depth. The curvature profiles can be obtained either by double differentiation of the deflection profiles, or by directly computing curvature values at each section using nodal strains. The latter method is used in here. The reaction profiles can be derived by double differentiation of the moment profiles, or by integrating the cross-sectional tractions (the product of the tributary width and the contact pressure at each node are summed). The latter method is used to obtain the reaction profiles here. All of these response profiles are displayed in Figures 3.40-55 for piles 4, 5, 6, and 9. These piles are representative of the 9-pile group and are chosen from the front, middle, and rear (center and side) rows (see, Figure 3.1).

The displacement profiles are shown in Figures 3.40-43. Again, only representative profiles are provided for each pile (i.e., when the top displacement of the piles is 0.4 in. or 0.8 in.). The profiles include responses with the upper, and lower bound of the soil moduli. To provide a reference, the response profiles of a single pile (obtained via FEM, *p-y* model with API curves, and SWM) are also shown in these figures. The displacement profiles indicate that the lateral deflections of the group pile are softer than the deflections of the single pile, as expected. The deflection increases drastically around 12 ft of depth for each pile in the group, while the solitary (single) pile deflects drastically at 8 ft depth when the upper bound of soil modulus is used. The group pile response reaches an extreme (often dubbed as "short-pile behavior") when the lower bound of soil modulus is used. Discarding this extreme response as unrealistic for the test specimen, the displacement profiles of the API *p-y* model with API curves can be treated as a lower bound response. SWM fails to converge at larger displacement levels despite the increased reinforcement ratio used for the piles.

Representative curvature profiles for the same piles are displayed in Figures 3.44-47. The maximum curvatures are observed at the pile head as expected, because the heads are constrained. The inflection point (zero-curvature) is located around 2-4 ft depth from the ground level; and the maximum positive curvatures are observed around 5-10 ft depth. The depth of the inflection points and maximum curvatures depend on the model used. The response of the single pile with the upper bound soil modulus displays the stiffest response, while the *p-y* model with the API curves and SWM (which is nearly identical to API) display the softest responses.

Representative moment profiles for the same piles are displayed in Figures 3.48-51. These have similar patterns to the curvature profiles, as expected. Specifically, the locations of maximum moment (negative or positive) or the inflection points (zero-moment) are (nearly) identical. The moment profiles are more flexible for the group piles than for the single pile. The same is true when the lower bound of soil modulus is used. The moment profiles from the *p-y* and the strain wedge models are displayed for comparison; and they are softer than those obtained from the finite element model in general.

Representative soil reaction profiles are shown in Figures 3.52-55. The reaction profiles display the very different patterns depending on the numerical model and the chosen soil properties (for example, note the differences in these figures between the finite element and the *p-y* model results, and those between the finite element models with different soil moduli).

The p-y Curves of the Pile Group

Lateral soil-resistance versus deflection relationships (i.e., the *p-y* curves) obtained from various finite element models, and from the API *p-y* model are presented in Figures 3.56-60. The *p-y* curves obtained from the single-pile finite element model is stiffer than those obtained from the group-pile finite element model. When the upper bound value of the soil modulus is used, the *p-y* curves of the single-pile finite element model are stiffer than those of the group pile finite element model, as well as the API *p-y* curves. However, the *p-y* curves of both the single-pile and the group-pile finite element models are softer than the API *p-y* curves, if the lower bound value of the soil modulus is used. In the 9-pile group, the rear piles (e.g., piles 6 or 9) have the stiffer *p-y* curves than the front (e.g., pile 4) or the middle pile (e.g., pile 5).

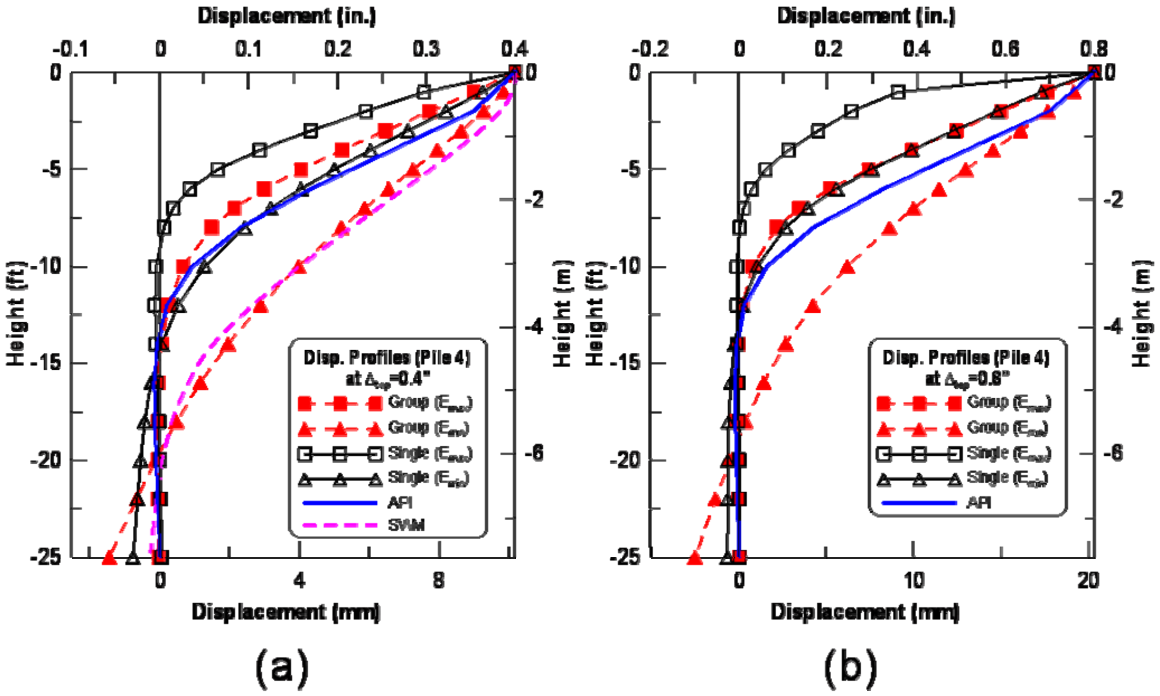

Figure 3.40. The displacement profile of pile 4 at (a) 0.4 in, and (b) 0.8 in top displacement.

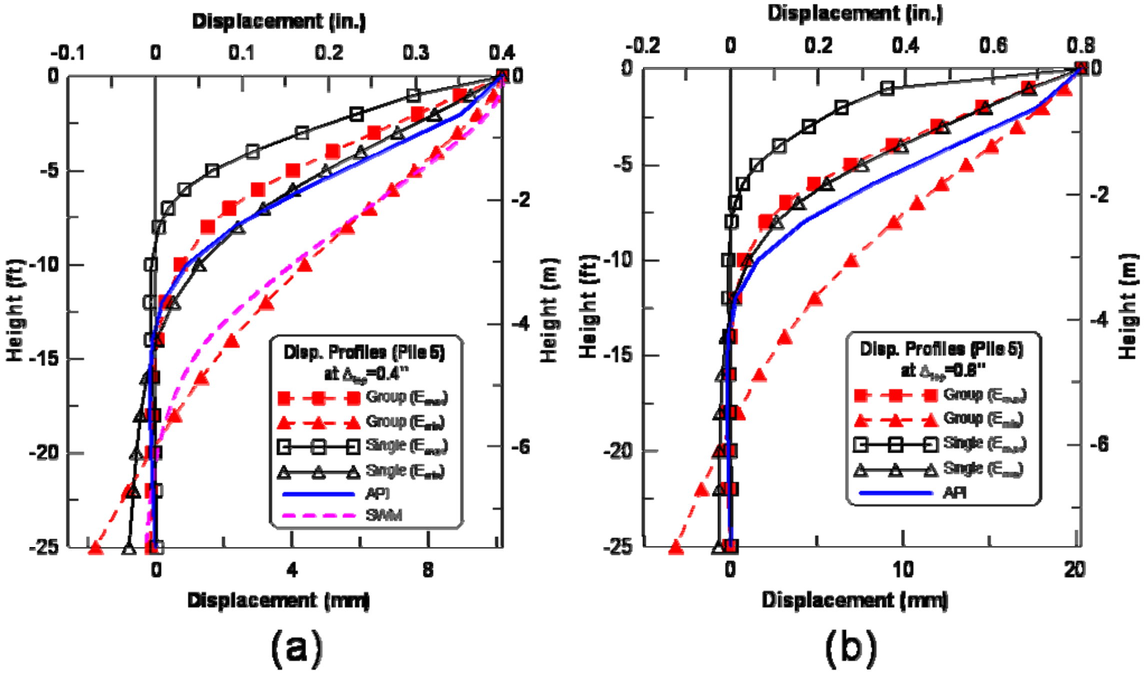

Figure 3.41. The displacement profile of pile 5 at (a) 0.4 in, and (b) 0.8 in top displacement.

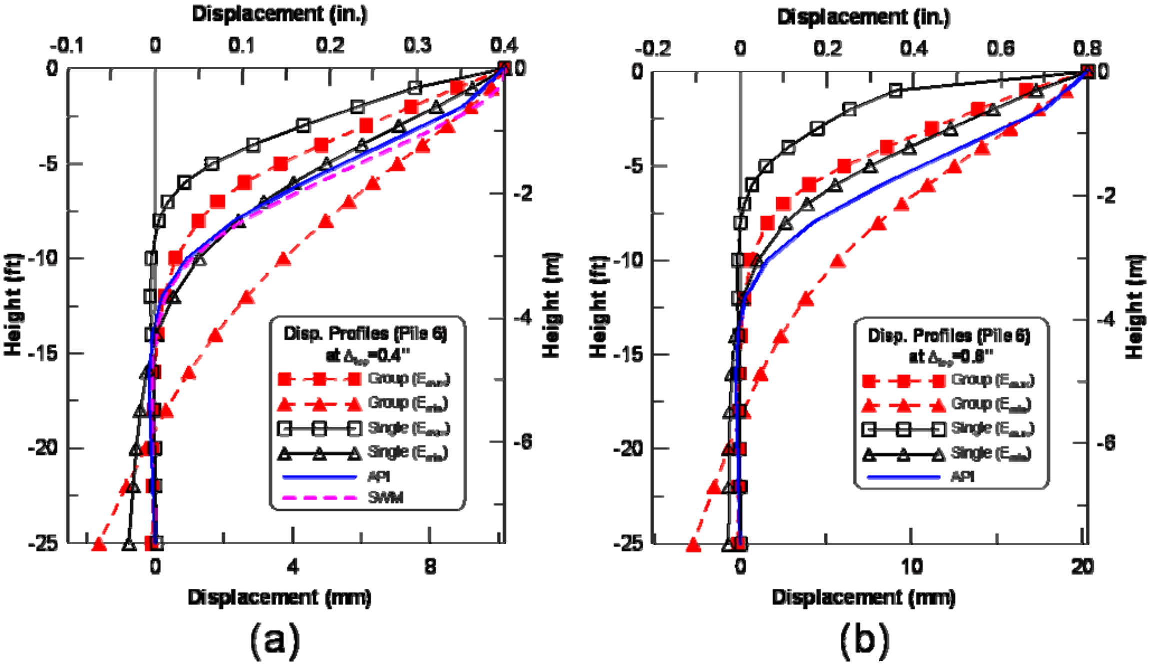

Figure 3.42. The displacement profile of pile 6 at (a) 0.4 in, and (b) 0.8 in top displacement.

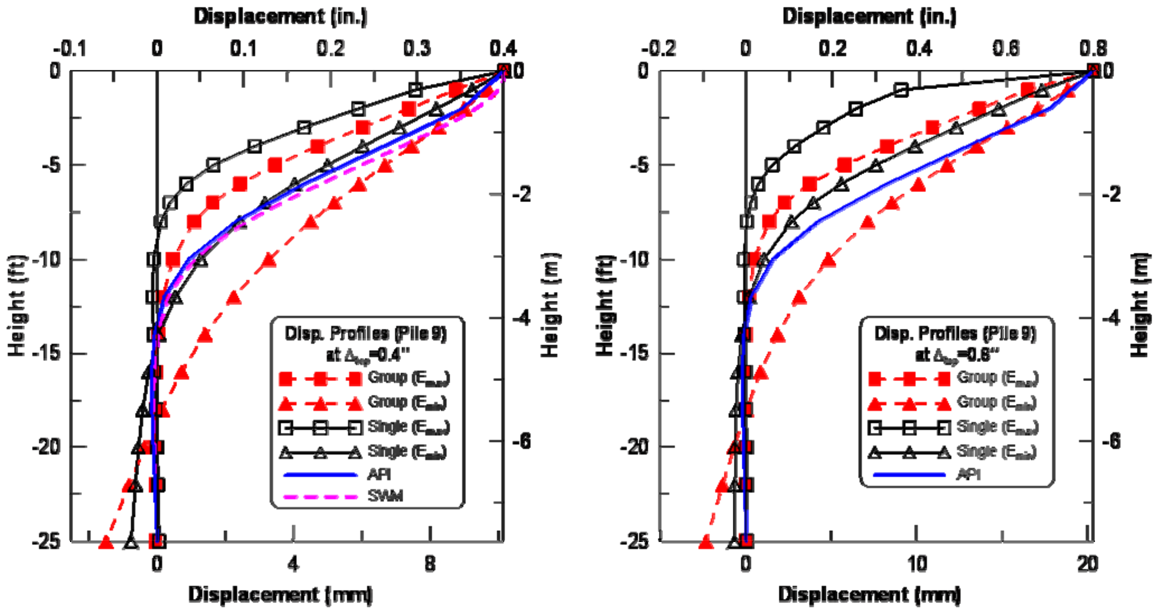

(a) (b)

Figure 3.43. The displacement profile of pile 9 at (a) 0.4 in, and (b) 0.8 in top displacement.

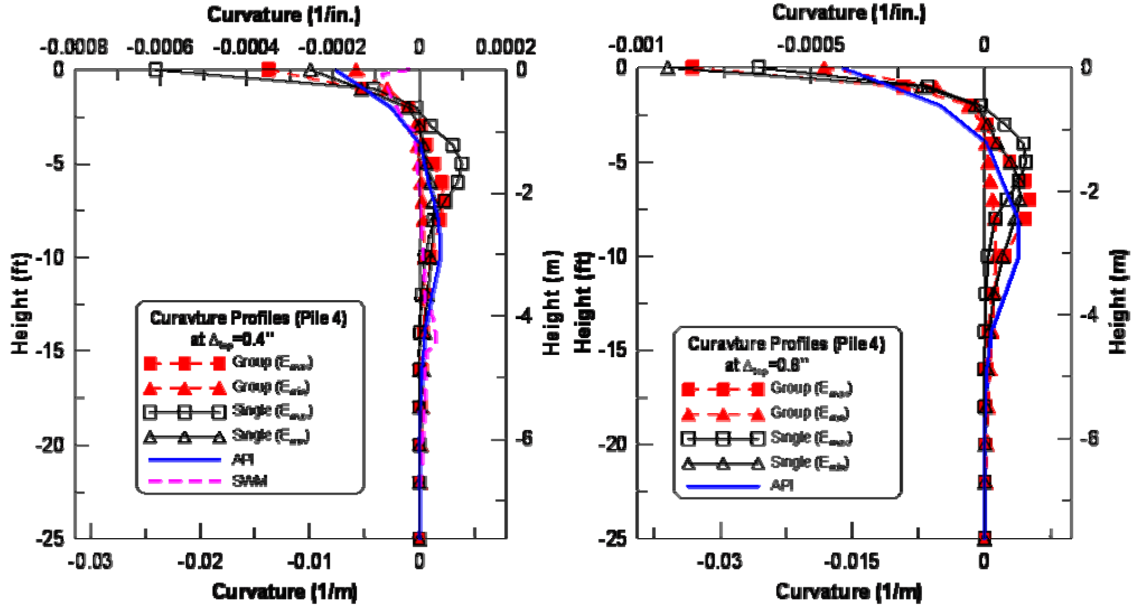

(a) (b)

Figure 3.44. The curvature profile of pile 4 at (a) 0.4 in, and (b) 0.8 in top displacement.

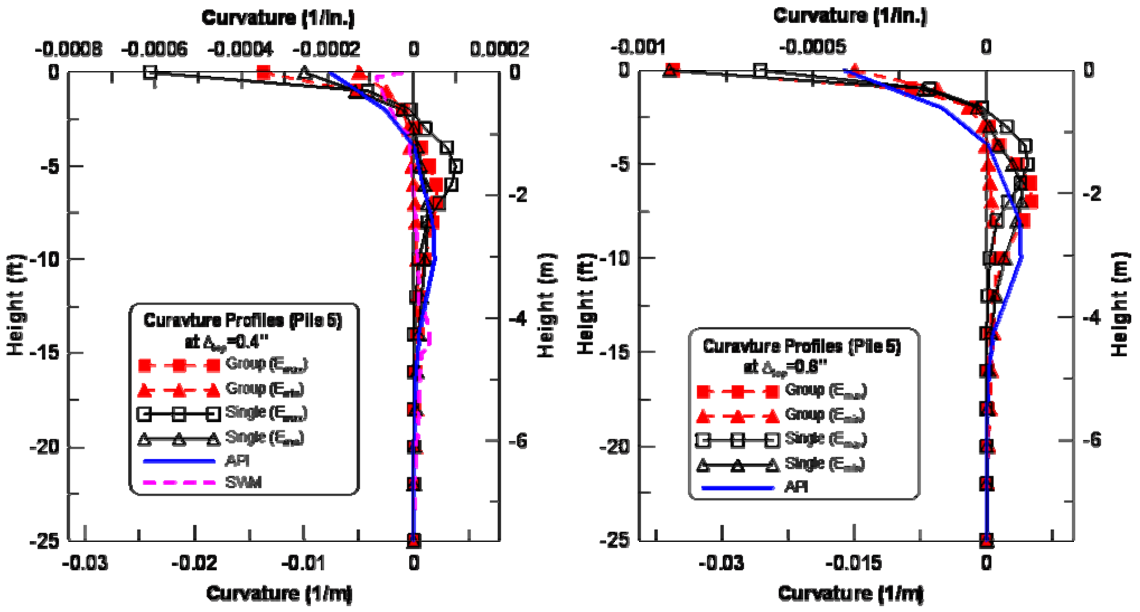

(a) (b)

Figure 3.45. The curvature profile of pile 5 at (a) 0.4 in, and (b) 0.8 in top displacement.

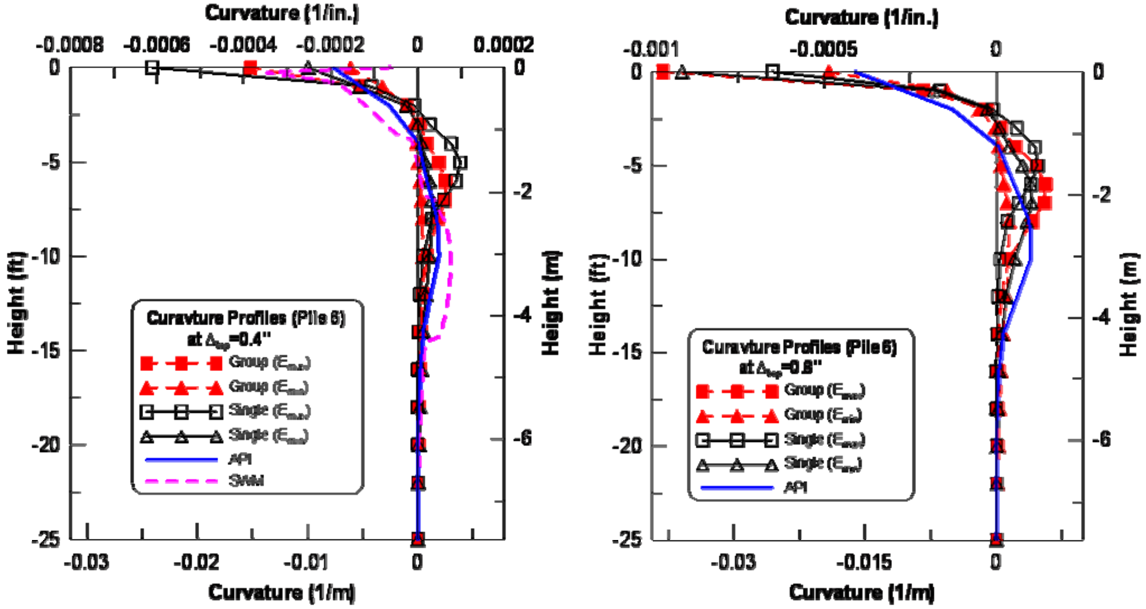

(a) (b)

Figure 3.46. The curvature profile of pile 6 at (a) 0.4 in, and (b) 0.8 in top displacement.

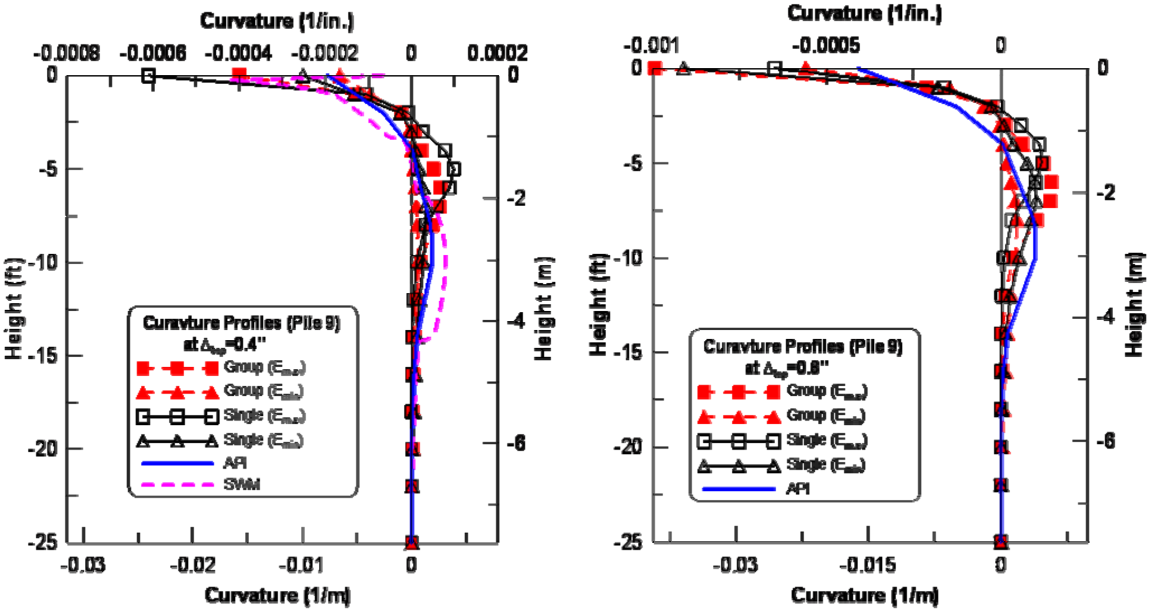

(a) (b)

Figure 3.47. The curvature profile of pile 9 at (a) 0.4 in, and (b) 0.8 in top displacement.

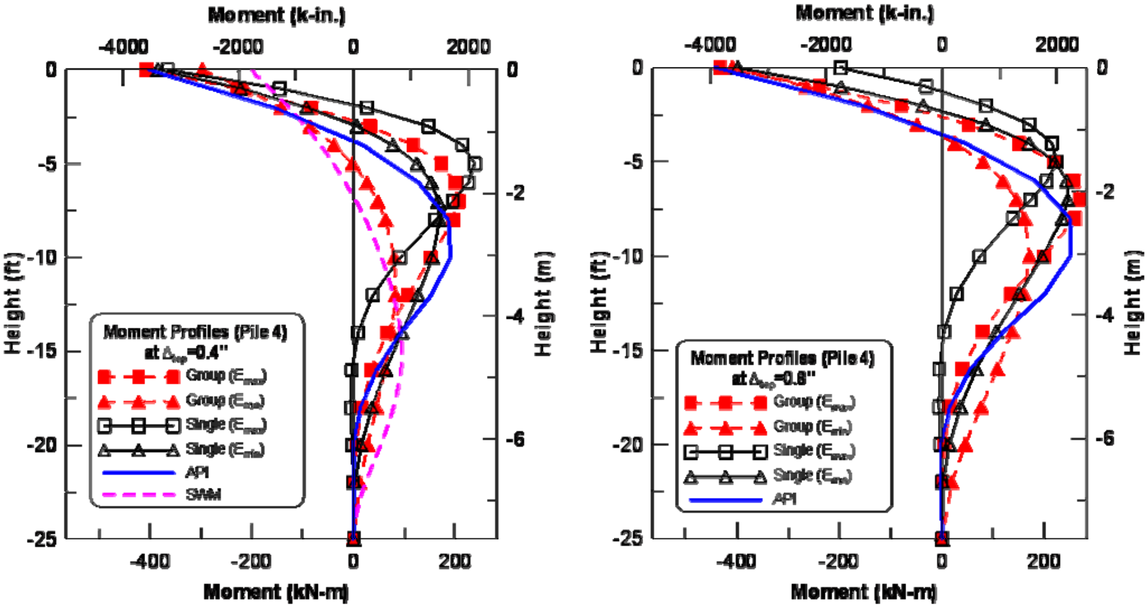

(a) (b)

Figure 3.48. The moment profile of pile 4 at (a) 0.4 in, and (b) 0.8 in top displacement.

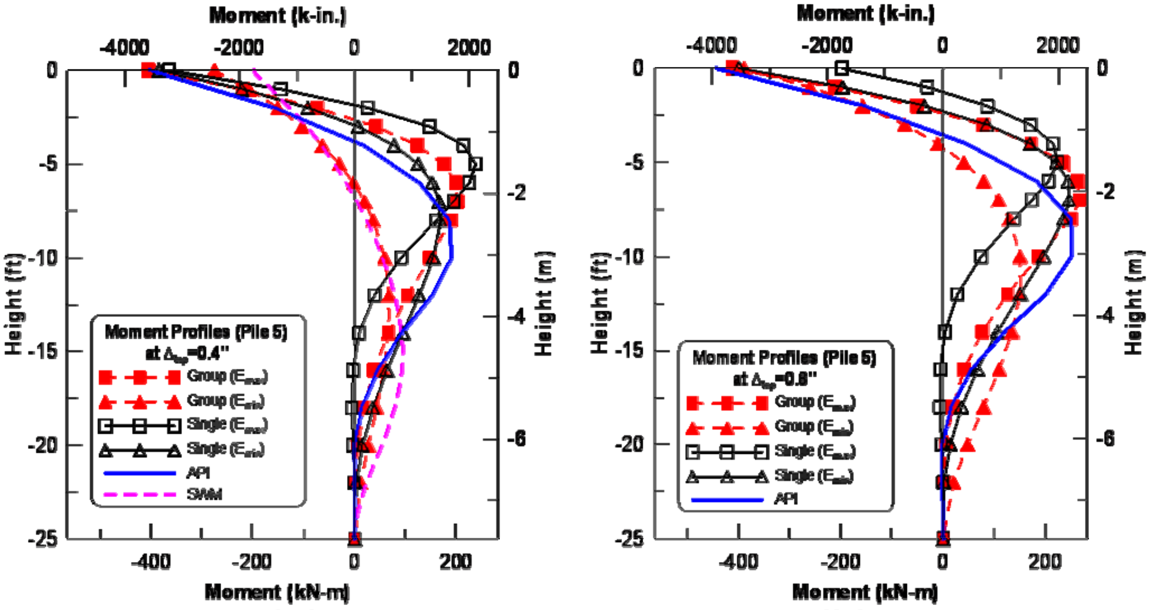

(a) (b)

Figure 3.49. The moment profile of pile 5 at (a) 0.4 in, and (b) 0.8 in top displacement.

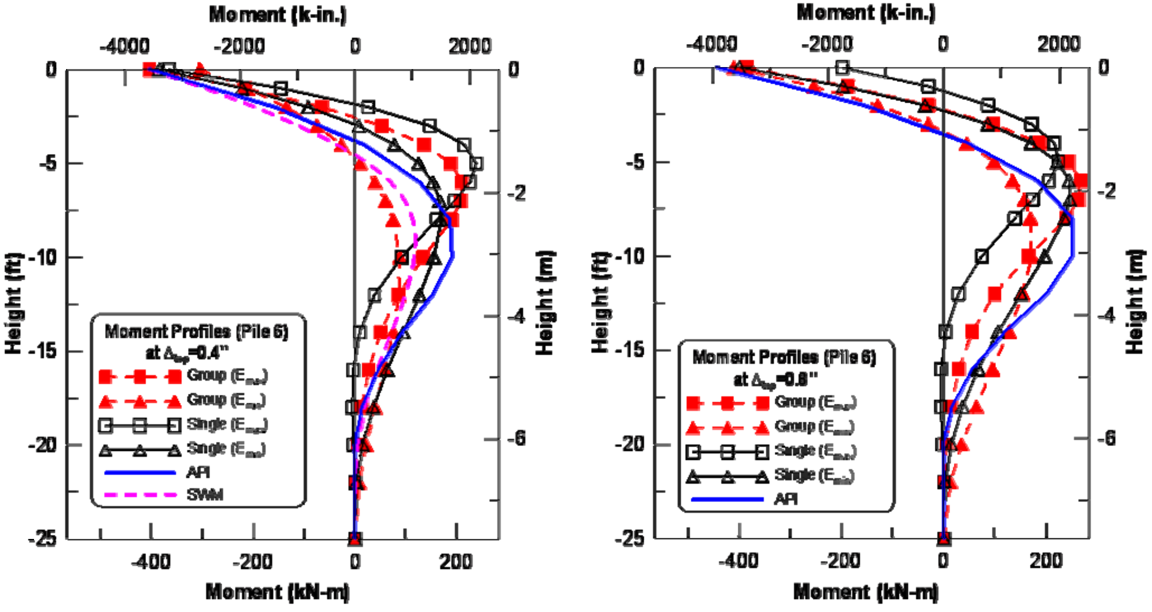

(a) (b)

Figure 3.50. The moment profile of pile 6 at (a) 0.4 in, and (b) 0.8 in top displacement.

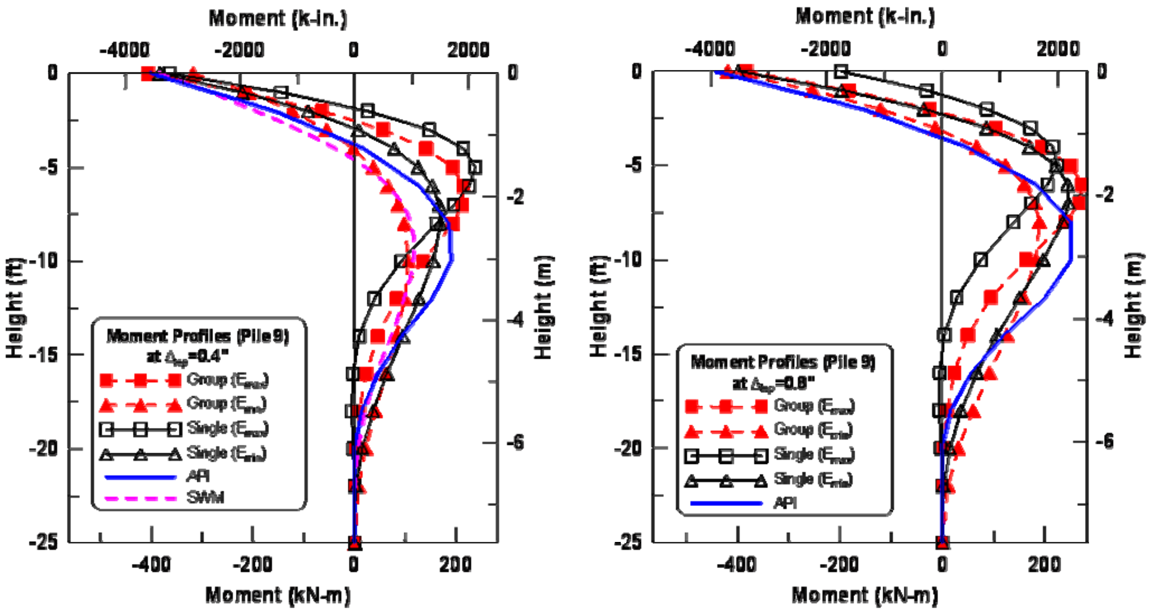

(a) (b)

Figure 3.51. The moment profile of pile 9 at (a) 0.4 in, and (b) 0.8 in top displacement.

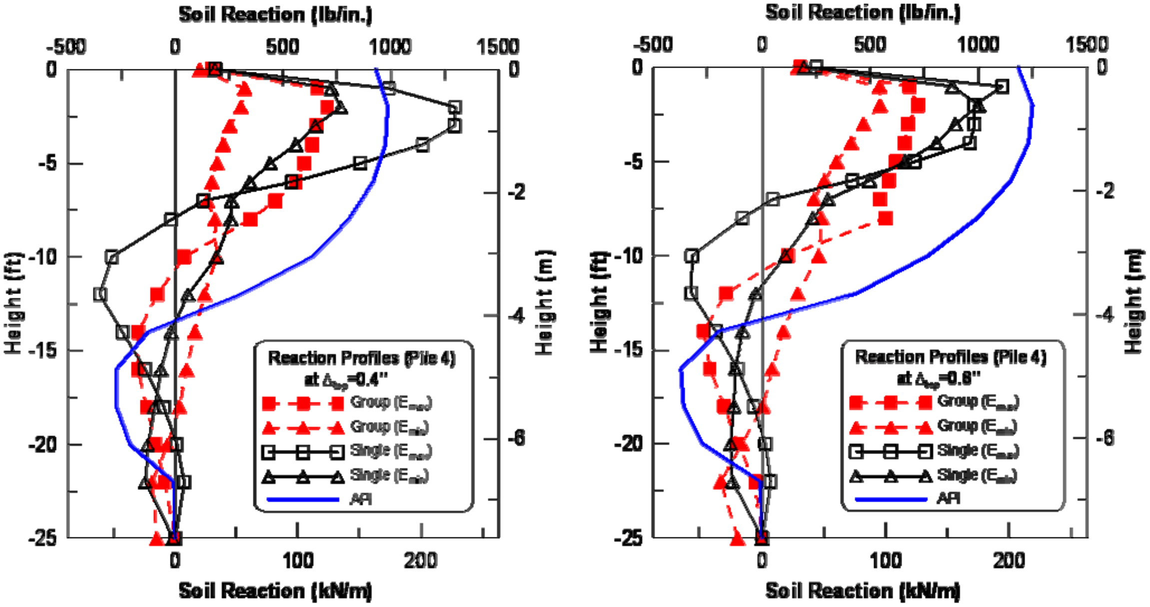

(a) (b)

Figure 3.52. The soil reaction profile of pile 4 at (a) 0.4 in, and (b) 0.8 in top displacement.

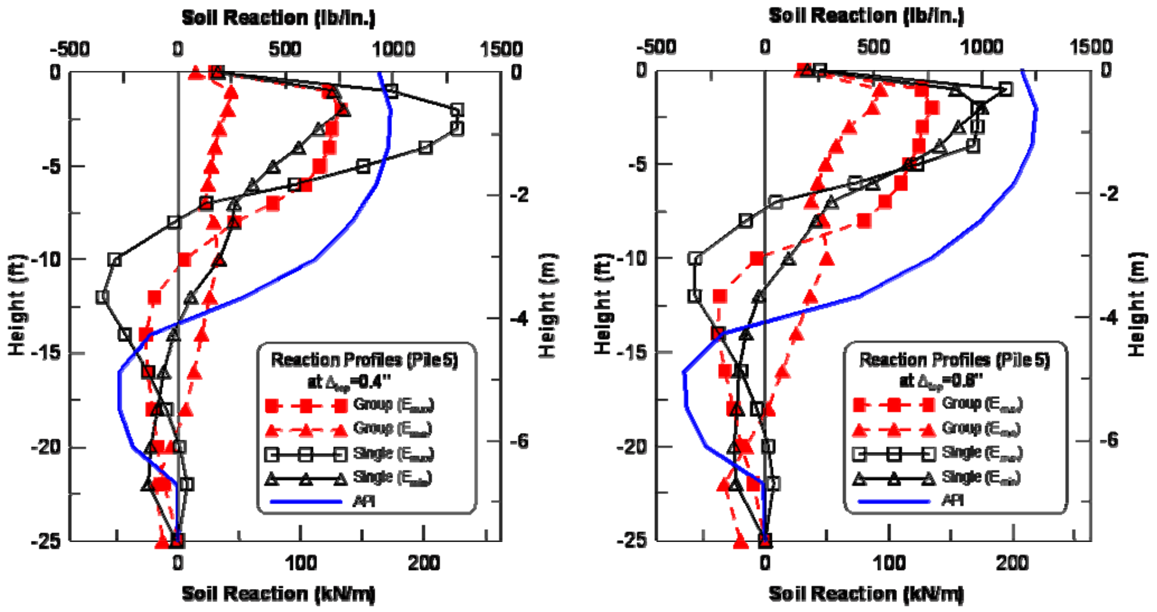

(a) (b)

Figure 3.53. The soil reaction profile of pile 5 at (a) 0.4 in, and (b) 0.8 in top displacement.

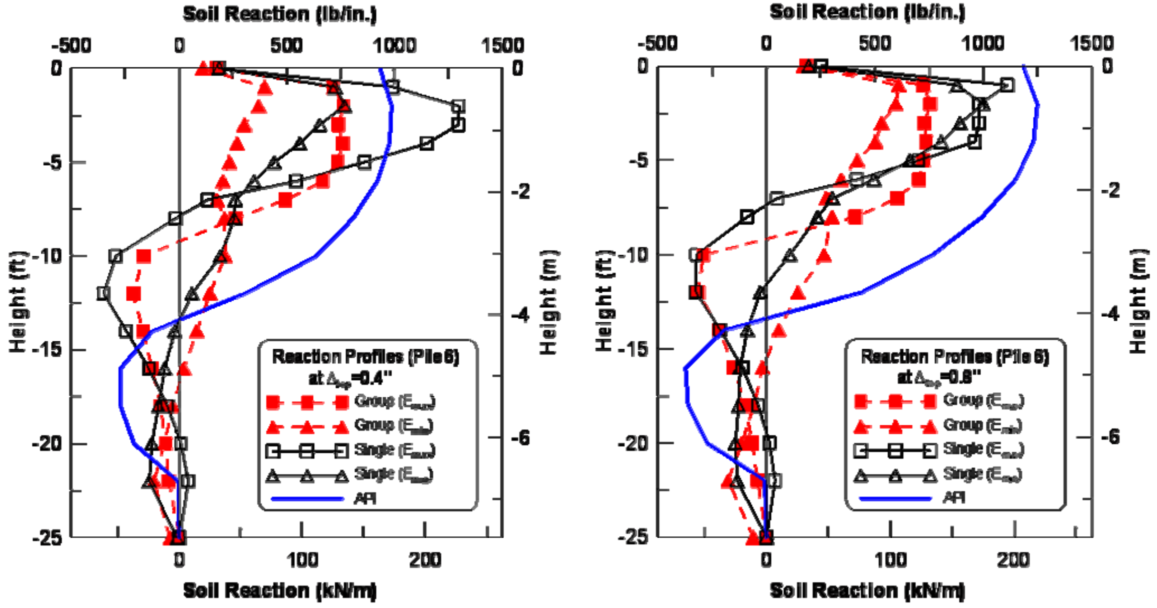

(a) (b)

Figure 3.54. The soil reaction profile of pile 6 at (a) 0.4 in, and (b) 0.8 in top displacement.

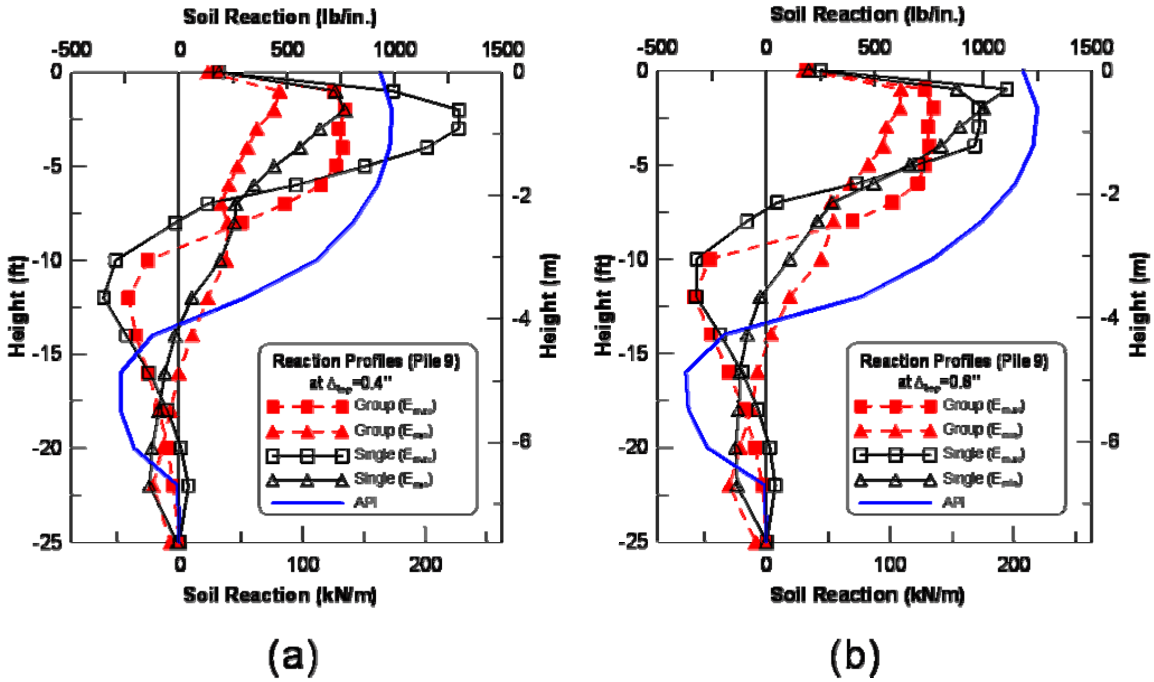

Figure 3.55. The soil reaction profile of pile 9 at (a) 0.4 in, and (b) 0.8 in top displacement.

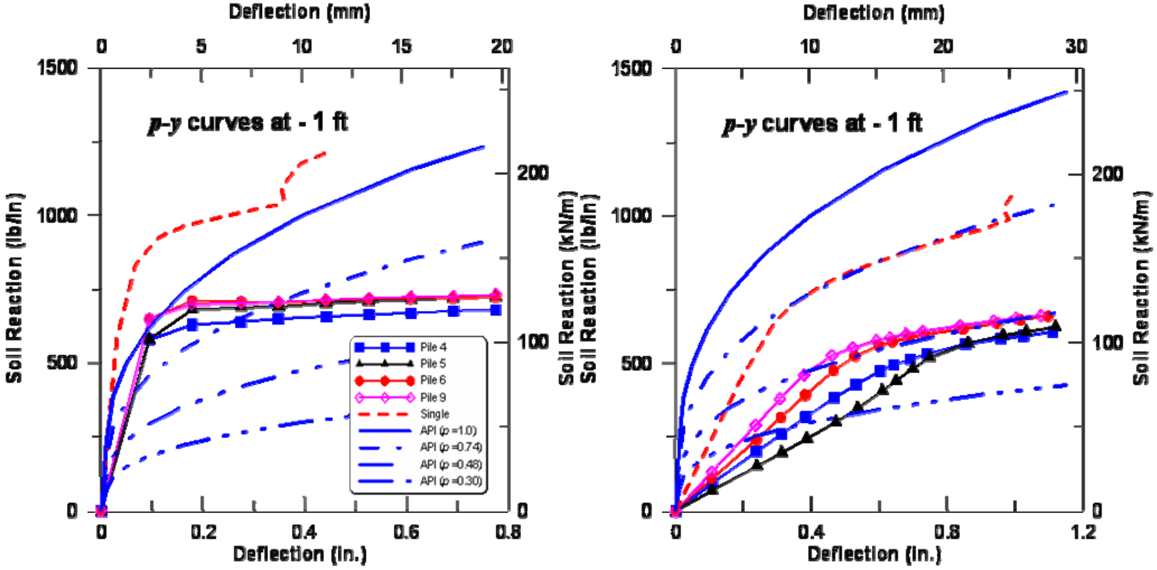

Figure 3.56. The p-y curves at 1 ft depth obtained for upper (left) and lower (right) bounds of the soil modulus.

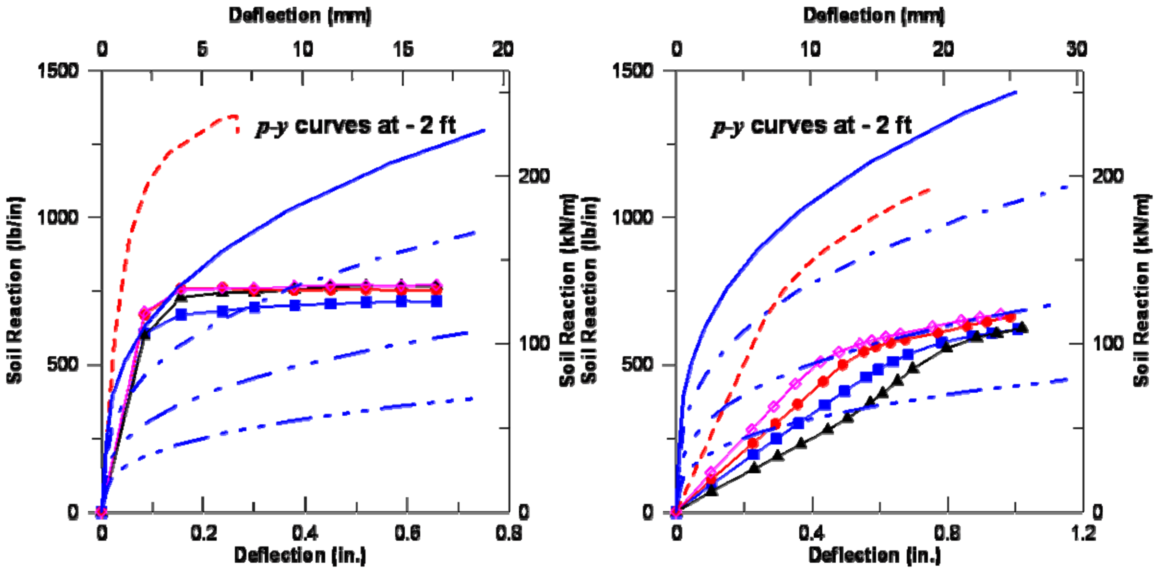

Figure 3.57. The p-y curves at 2 ft depth obtained for upper (left) and lower (right) bounds of the soil modulus.

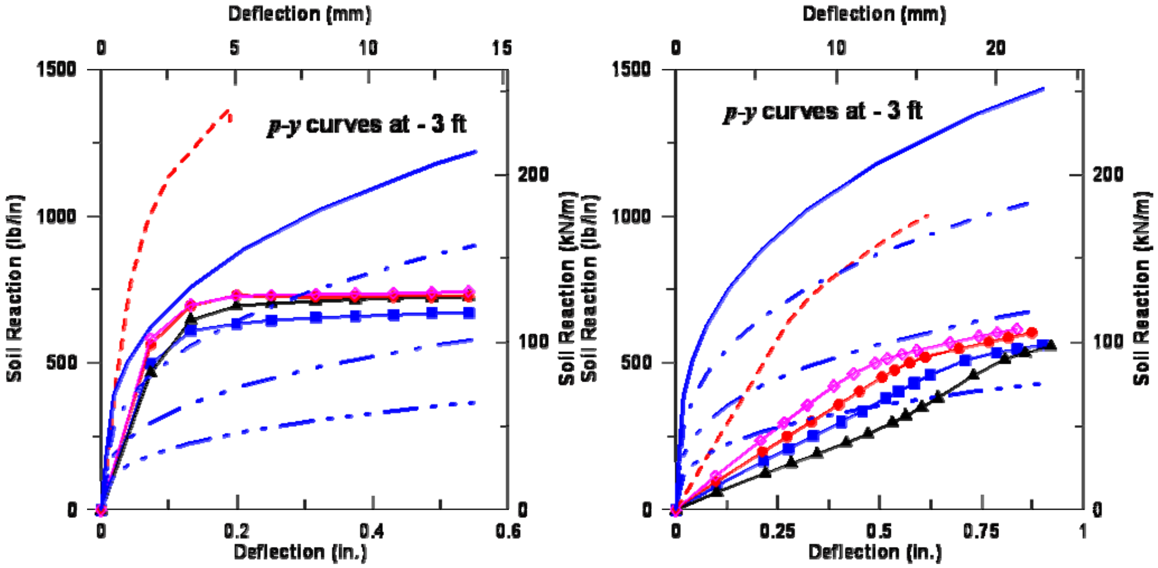

Figure 3.58. The p-y curves at 3 ft depth obtained for upper (left) and lower (right) bounds of the soil modulus.

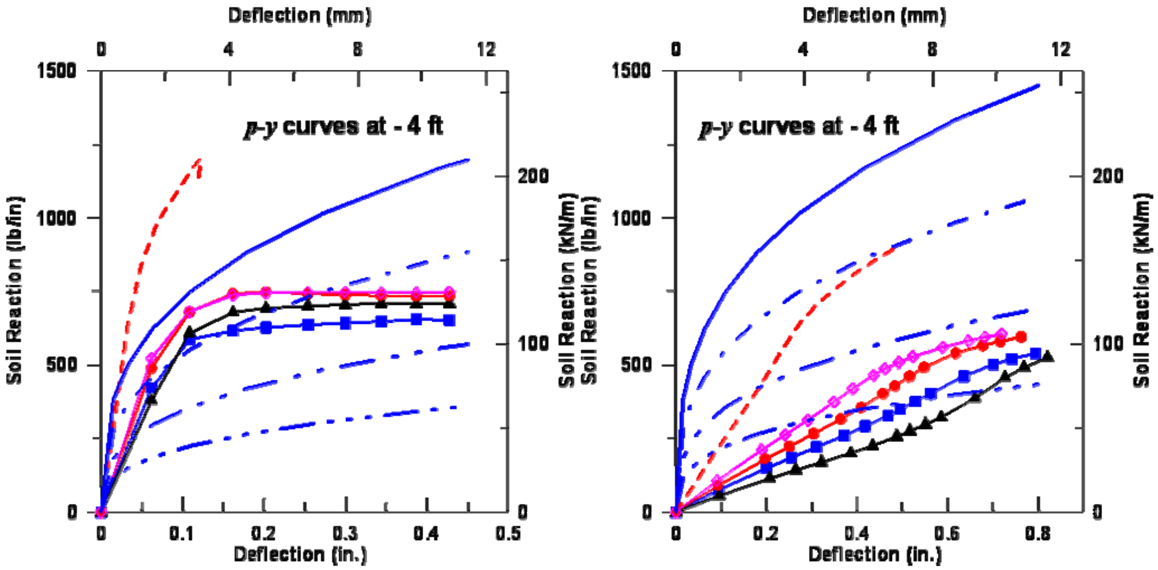

Figure 3.59. The p-y curves at 4 ft depth obtained for upper (left) and lower (right) bounds of the soil modulus.

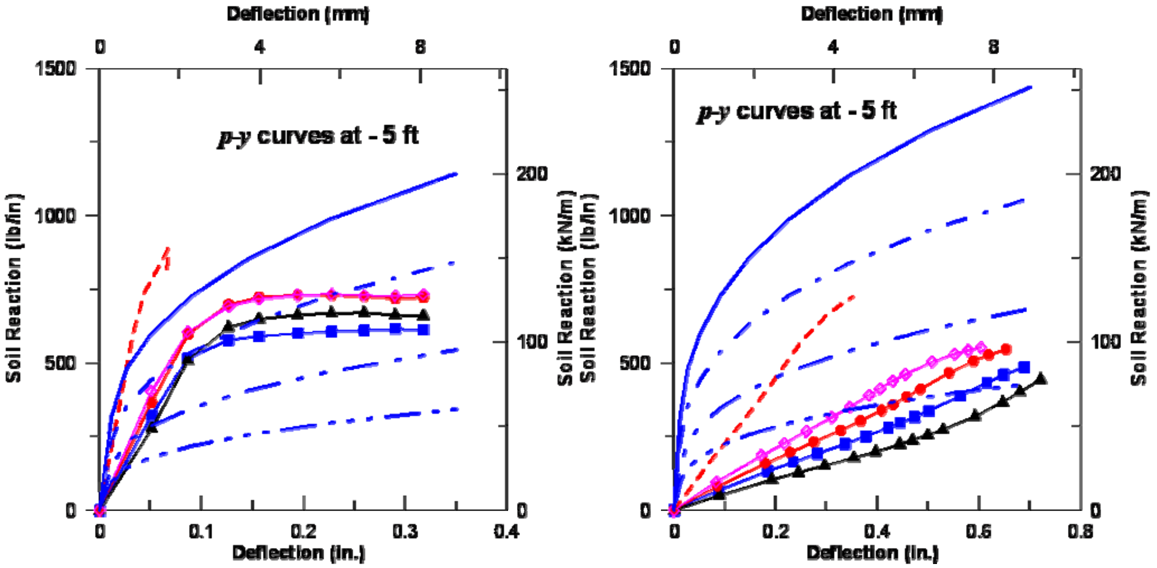

Figure 3.60. The p-y curves at 5 ft depth obtained for upper (left) and lower (right) bounds of the soil modulus.

4 TEST RESULTS

Test results and observations for the 2 foot diameter flagpole and fixed-head tests are summarized in the following subsections.

4.1 2ft Flagpole Results

Construction of the 2 ft flagpole specimen began in October, 2004, was delayed for several months by heavy rains, and was finally completed in April, 2005. Testing began April 21, 2005, and was completed April 27, 2005.

(a) (b)

Figure 4.1. (a) Head deflection and (b) soil gapping at -16” of head displacement.

(a) (b)

Figure 4.2. (a) Spalling of cover concrete below the ground surface and above the center of the plastic hinge; (b) outmost rebar fracture points at 3.5 feet below the ground surface.

Figure 4.1a shows the deflected shape of the specimen at a head displacement of -16 inches and Figure 4.1b shows the ground surface deformation of the shaft and soil gapping at a displacement of -16 inches. At this level of displacement, the primary component of lateral displacement is due to inelastic rotation at the so-called plastic hinge; therefore, the above hinge (ground) portion of the specimen is effectively rotating as a rigid body (i.e., elastic deformations are dwarfed by inelastic deformations). Soil gapping was observed during the test but the horizontal extent of the gaps was difficult to quantify due to soil sloughing into gap spaces and concrete cracking and spalling near the surface. Attempts were made to measure the vertical extend of gaps formed but the gap width is highly uncertain due to the rough surface of the shaft below the ground line. A plastic hinge in the shaft was observed to form at between 1.5 and 2 shaft diameters (3 to 4 feet) from the ground surface, as noted during the post-test excavation which indicated spalling below the ground surface (See Figure 4.2a) and bar fractures at 3.5 feet from the ground surface (See Figure 4.2b). As well, measured curvatures, discussed later (Figure 4.29) reveal yielding within this region.

4.1.1 Load vs. Deflection

Backbone load vs. deflection curves are shown in Figure 4.1. Also shown for reference purposes are the results of pre-test blind predictions reported in Rha, et al. (2005) using a p-y curve approach, finite element methods (denoted FEM in figure), and a strain wedge model (denoted SWM). The predicted “yield” displacement was from 2 to 4 inches, depending on the model and parameters used. The maximum load observed in the south loading direction was 24.0 kips at 8 inches of displacement, whereas the maximum load observed in the north direction was 24.5 kips at 12 inches of displacement.

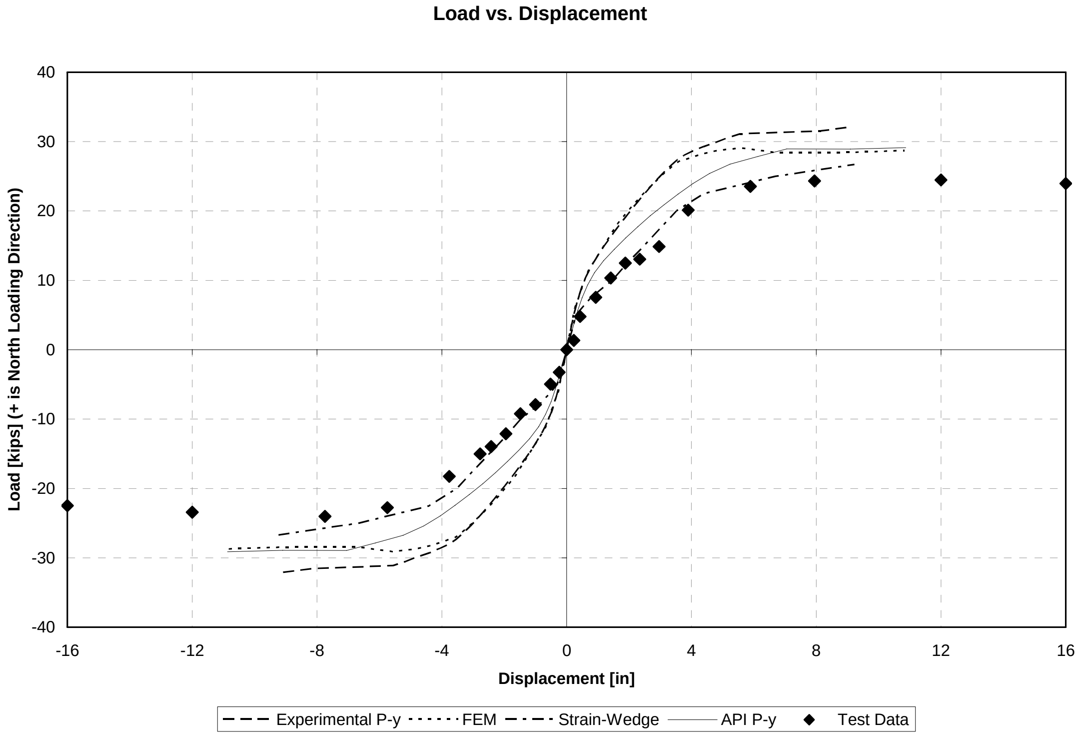

Figure 4.3. Head load vs. displacement predictions and data

The measured cyclic response of the shaft is shown in Figure 4.4. For peak displacement levels of 6 inches and below, there was a consistent 15% to 17% drop in load capacity from the maximum absolute displacement of the first to maximum absolute displacement of the third cycle, which is fairly common in cyclic testing with multiple cycles to the same displacement level. For displacement levels higher than 6 inches, the strength loss was greater, with as much as a 60% drop for the 16 inch displacement level.

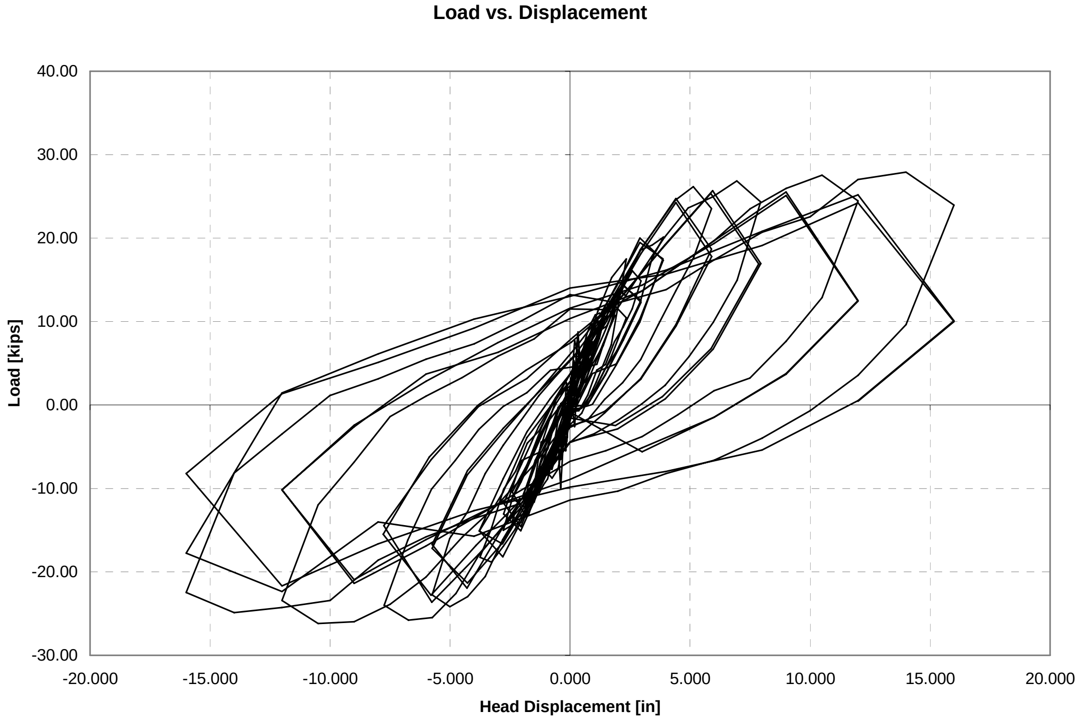

Figure 4.4. Cyclic response of the shaft to the 12 inch displacement level.

4.1.2 Representative Sensor Response Histories

(a) Strain Gauges

Figure 4.5 shows response histories at the 1.0 inch displacement level of strain gauges affixed to longitudinal reinforcing bars farthest from the center of the shaft cross-section at zero depth. The strain gauges, which were located directly opposite each other on the shaft cross section, recorded maximum tensile values of 0.00127 for the North sensor and 0.00142 for the South sensor. These values, which are slightly larger than half of the predicted reinforcing bar yield strain, are consistent with expectations, as the 1.0 inch displacement level is pre-yield (recall from Section 4.1.1 that the yield deflection is from 2 to 4 inches).

Figure 4.6 shows the same sensors at the +/- 6 inch displacement level and shows a typical strain gauge response as the sensor begins to fail. Note that the sensor values become unrealistic as the sensor breaks, even though the sensor appears to provide readings that are realistic at later points in the history. Once the gauge begins to fail, however, the readings are discarded from that point on.

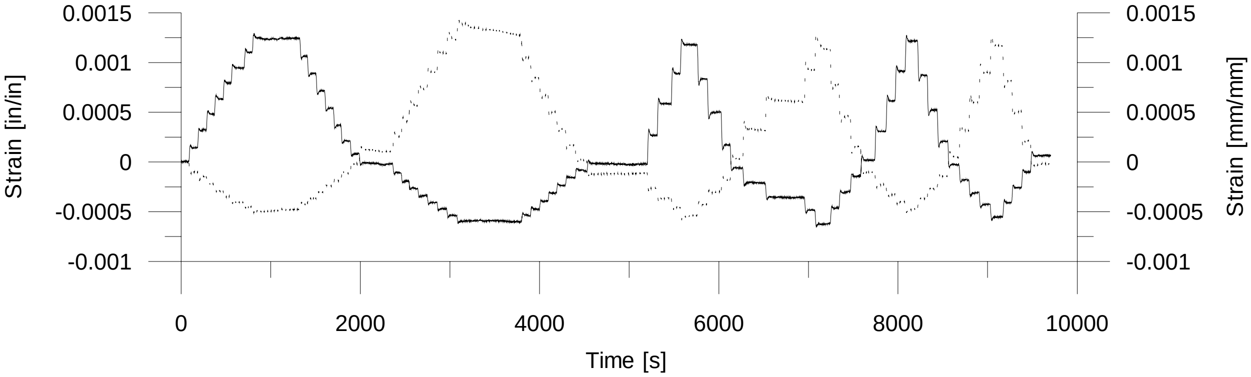

Figure 4.5. Strain gauge histories on opposite bars at the ground surface during the 1.0 inch displacement level. Solid line is the North sensor, dotted line is South sensor.

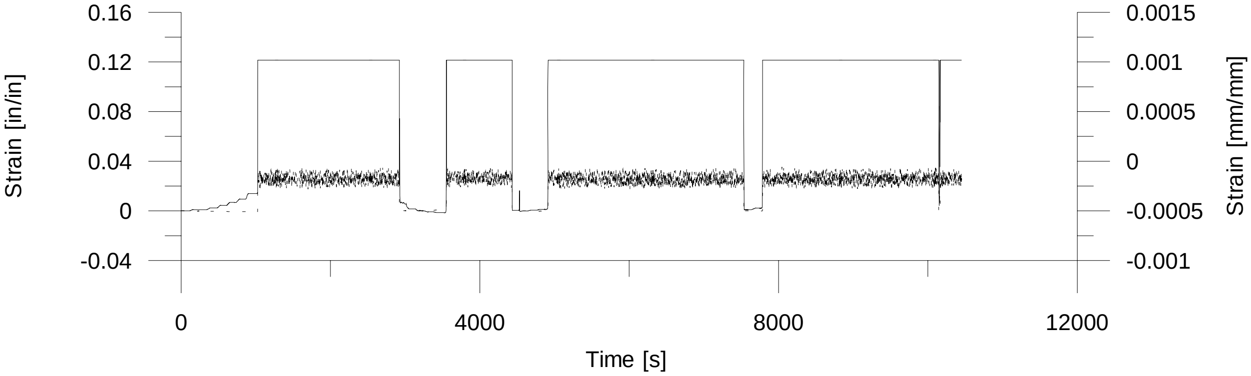

Figure 4.6. Strain gauge histories on opposite bars at the ground surface during the 6.0 inch displacement level. Solid line is the North sensor, dotted line is South sensor.

(b) Inclinometers

Figure 4.7 and Figure 4.8 show the ground surface inclinometer response histories for the +/-1 inch and +/-6 inch displacement levels, respectively. The maximum rotations at the +/-1 inch and +/-6 inch head displacement levels were +/-0.005 and +/-0.047 radians, respectively. The rotations experienced by the shaft at the ground surface, the largest for all inclinometers, were well within the sensor limits; therefore, the inclinometers were undamaged during the test and produced reasonable data over the entire range of displacement levels applied during the test.

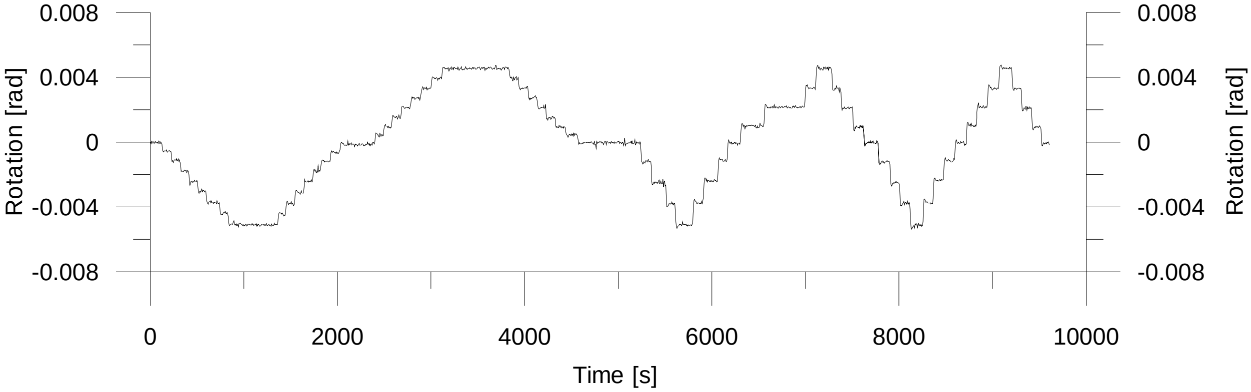

Figure 4.7. Inclinometer history at the ground surface during the 1.0 inch displacement level.

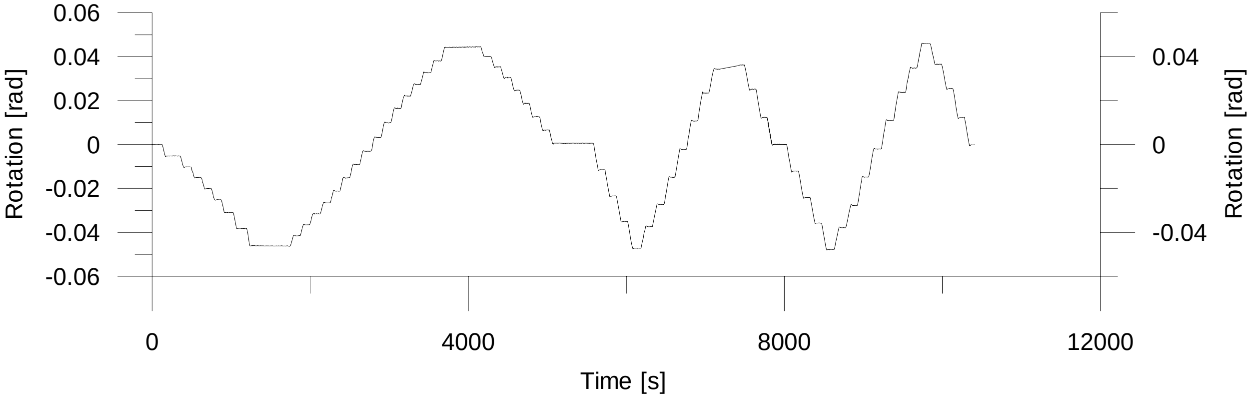

Figure 4.8. Inclinometer history at the ground surface during the 6.0 inch displacement level.

(c) LVDTs

The LVDT data for the 2ft flagpole test were of generally poor quality due to a design flaw in the exterior housing of the sensors. Because the housing was plastic and did not bond well with the adhesive to the stainless steel LVDT housings, most of the LVDT bodies were able to move freely inside the housing. This caused an offset in the sensor reading when the sensor went into compression. Histories from a sensor pair that did not have this problem are shown in Figure 4.9 and Figure 4.10. A representative LVDT history that shows the compression offset is shown in Figure 4.11. Where this offset occurred, the LVDT data are considered unreliable. Also, because the housing was plastic, the diagonal LVDTs, which were exposed to the most differential force during the concrete placement, did not produce meaningful results. The design of the LVDT housings was improved for the fixed-head test.

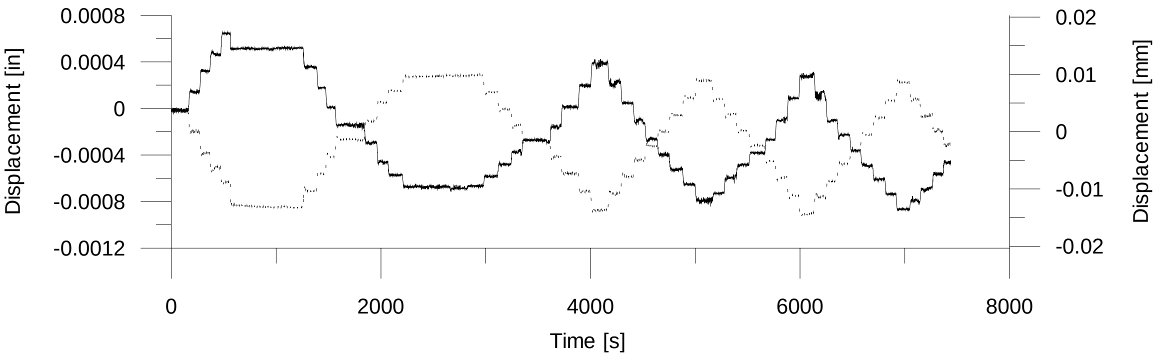

Figure 4.9. LVDT history at 51 inches below ground surface during the 1.0 inch displacement level

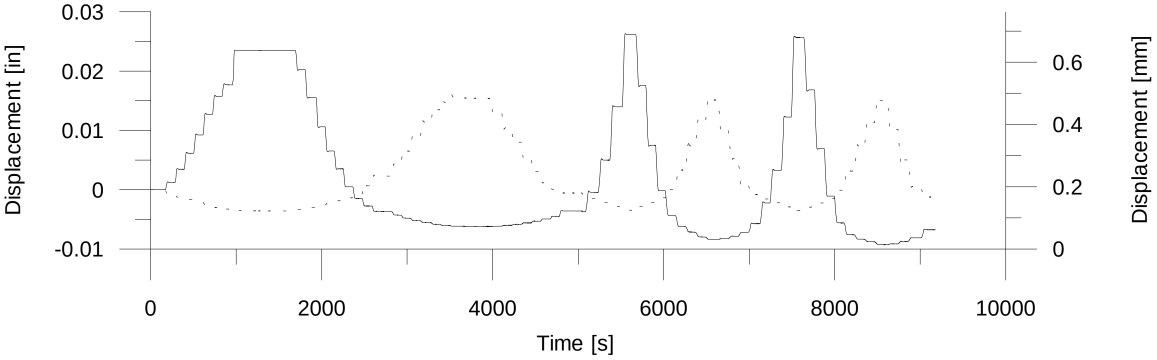

Figure 4.10. LVDT history at 51 inches below ground surface during the 6.0 inch displacement level

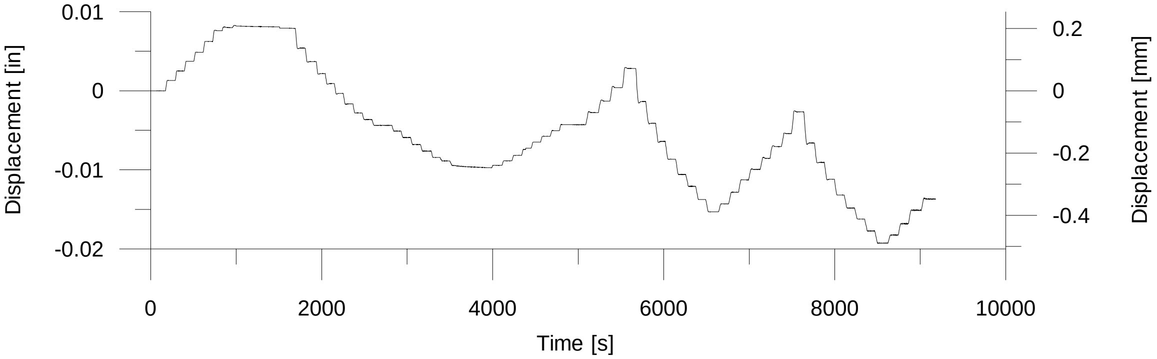

Figure 4.11. LVDT history at 15 inches below ground surface during the 6.0 inch displacement level

(d) Fiber-optic sensors

Figure 4.12 and Figure 4.13 show the fiber-optic response histories 3 inches above the ground line at the +/-1 inch and +/-6 inch displacement levels, respectively. The maximum wavelength changes at +/-1 inch of head displacement were -0.3 nm and 1.2 nm, respectively, while the maximum wavelength changes at +/-6 inch of head displacement were -0.6 nm and 2.4 nm, respectively. Both sets of results appear to provide reliable data.

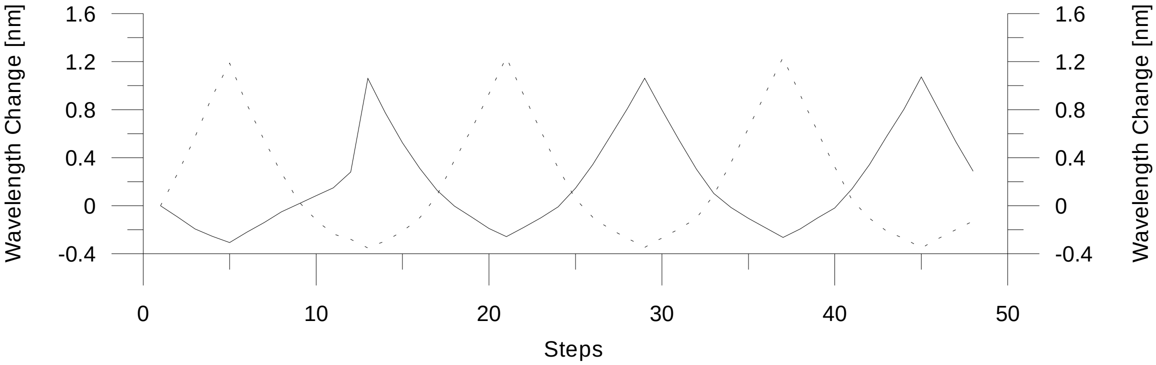

Figure 4.12. FO history at 3 inches above ground surface during the 1.0 inch displacement level

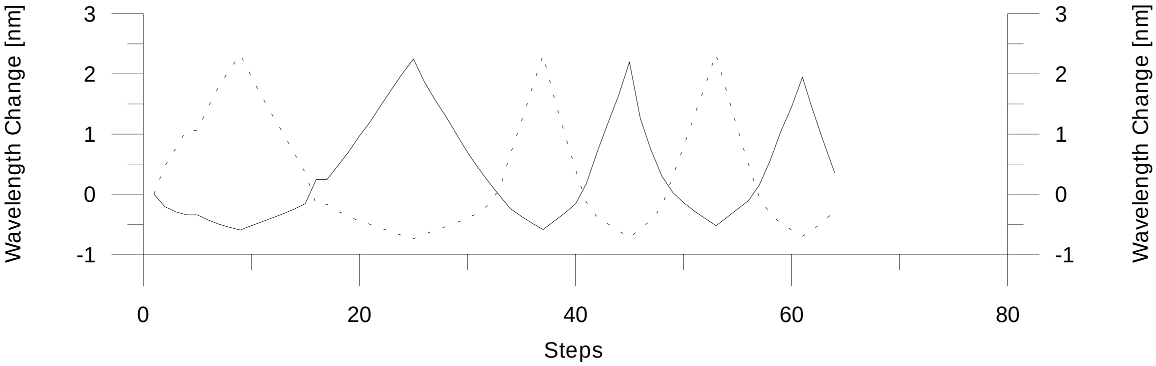

Figure 4.13. FO history at 3 inches above ground surface during the 6.0 inch displacement level

4.1.3 Curvature Profiles

Curvature values calculated for the below-ground portion of the shaft are shown in Figure 4.14. Sensor depths and head displacements are noted on the plots.

Curvature Profiles for +/-0.25" Head Displacement

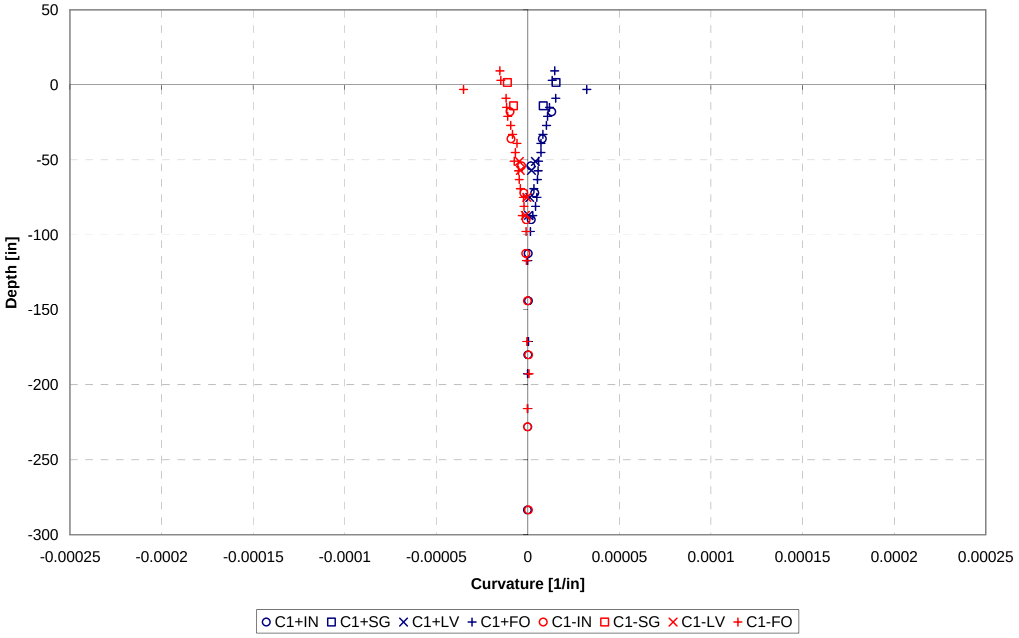

Curvature Profiles for +/-0.5" Head Displacement

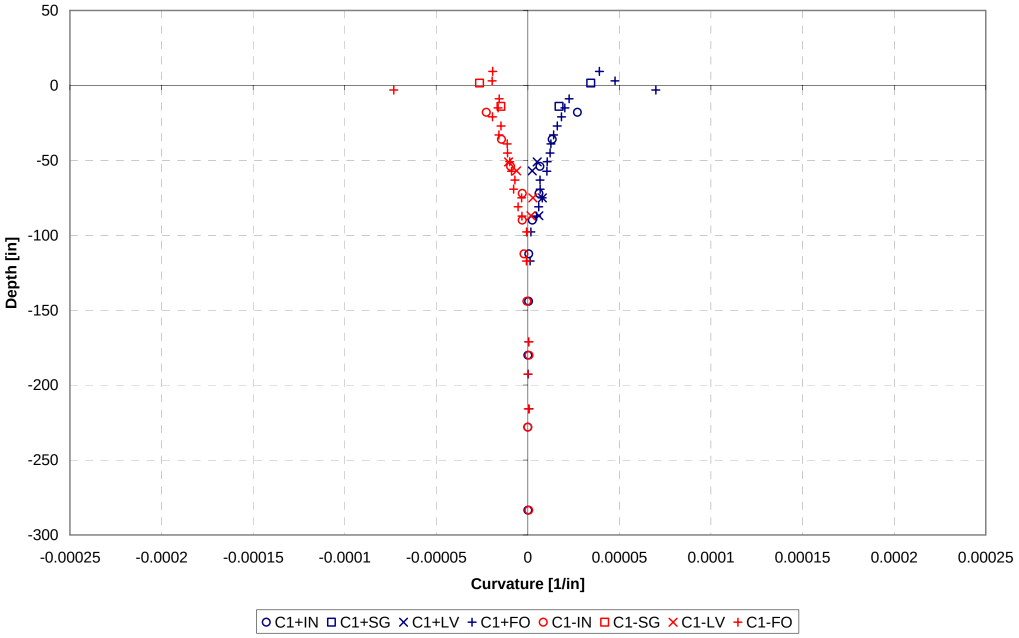

Figure 4.14. Curvature profiles from the 0.25 inch through the 8.0 inch displacement levels, respectively. "+" or "-" prefixes indicate curvature values for positive or negative displacement cycles. IN is for inclinometer, SG is for strain gauge, LV is for LVDT, and FO is for fiber-optic derived curvatures.

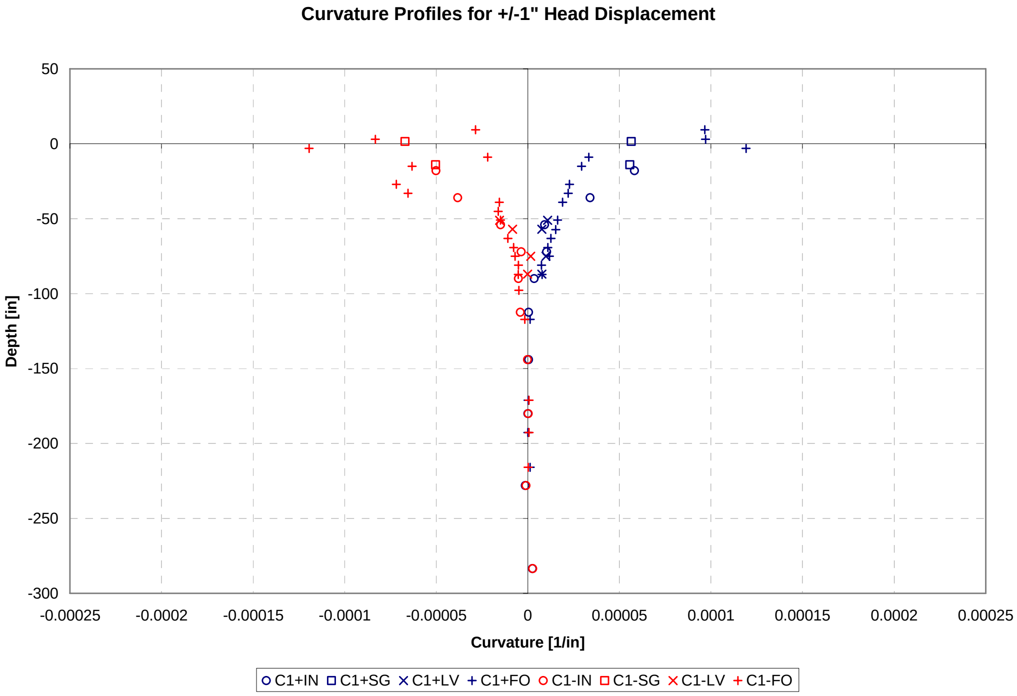

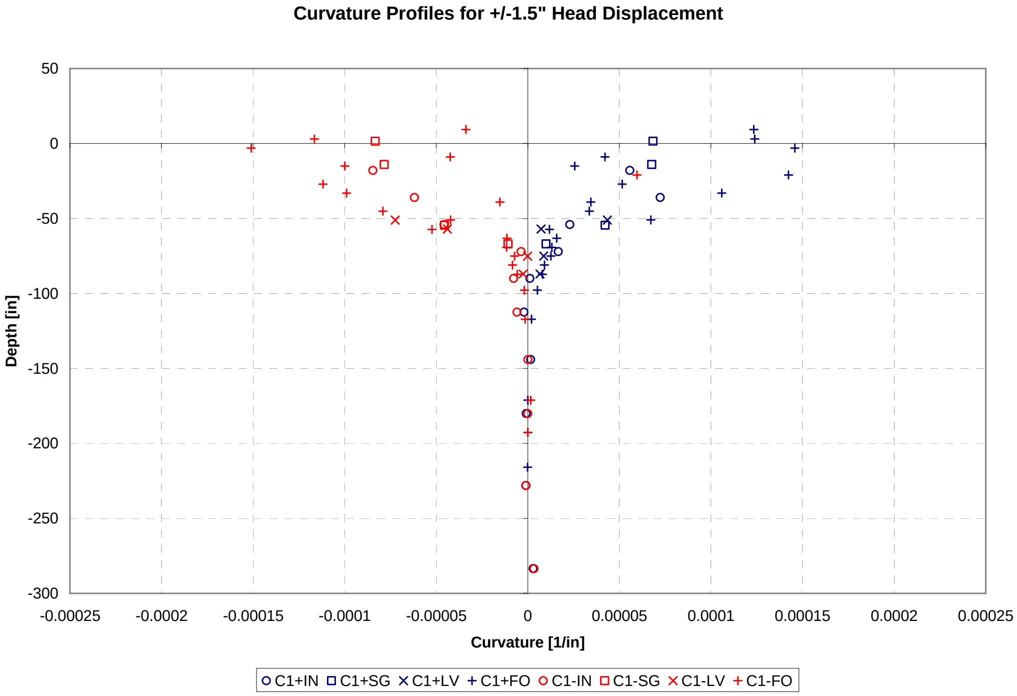

Figure 4.14 (continued). Curvature profiles from the 0.25 inch through the 8.0 inch displacement levels, respectively. "+" or "-" prefixes indicate curvature values for positive or negative displacement cycles. IN is for inclinometer, SG is for strain gauge, LV is for LVDT, and FO is for fiber-optic derived curvatures.

Curvature Profiles for +/-2" Head Displacement

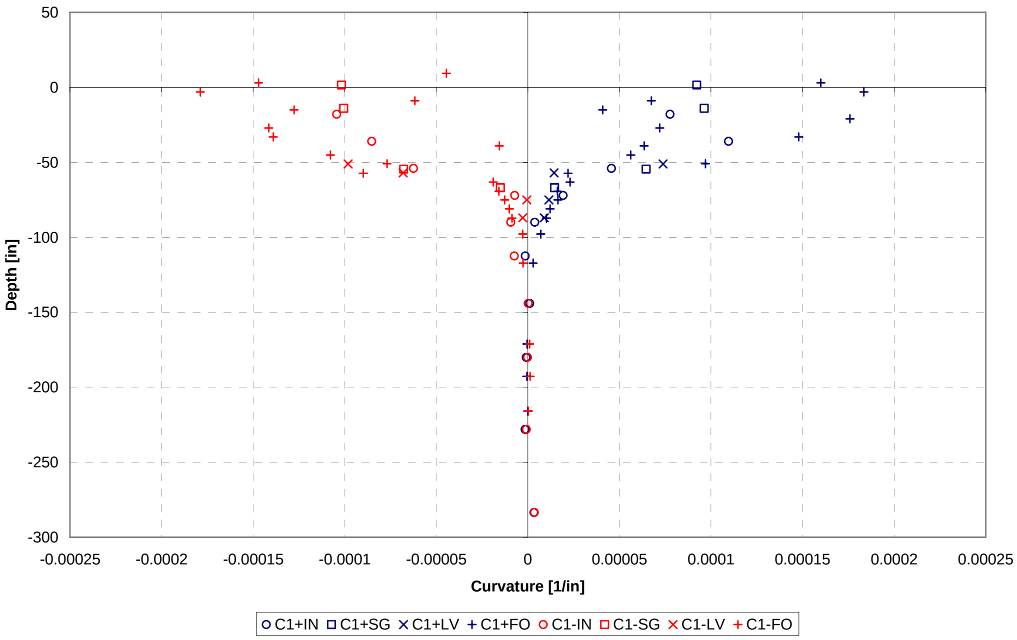

Curvature Profiles for +/-2.5" Head Displacement

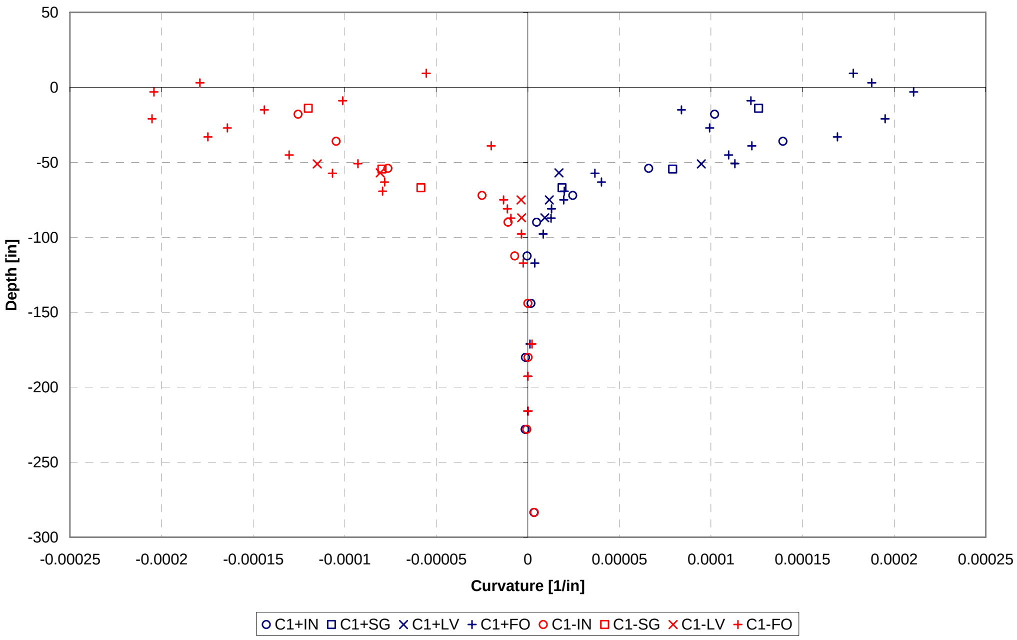

Figure 4.14 (continued). Curvature profiles from the 0.25 inch through the 8.0 inch displacement levels, respectively. "+" or "-" prefixes indicate curvature values for positive or negative displacement cycles. IN is for inclinometer, SG is for strain gauge, LV is for LVDT, and FO is for fiber-optic derived curvatures.

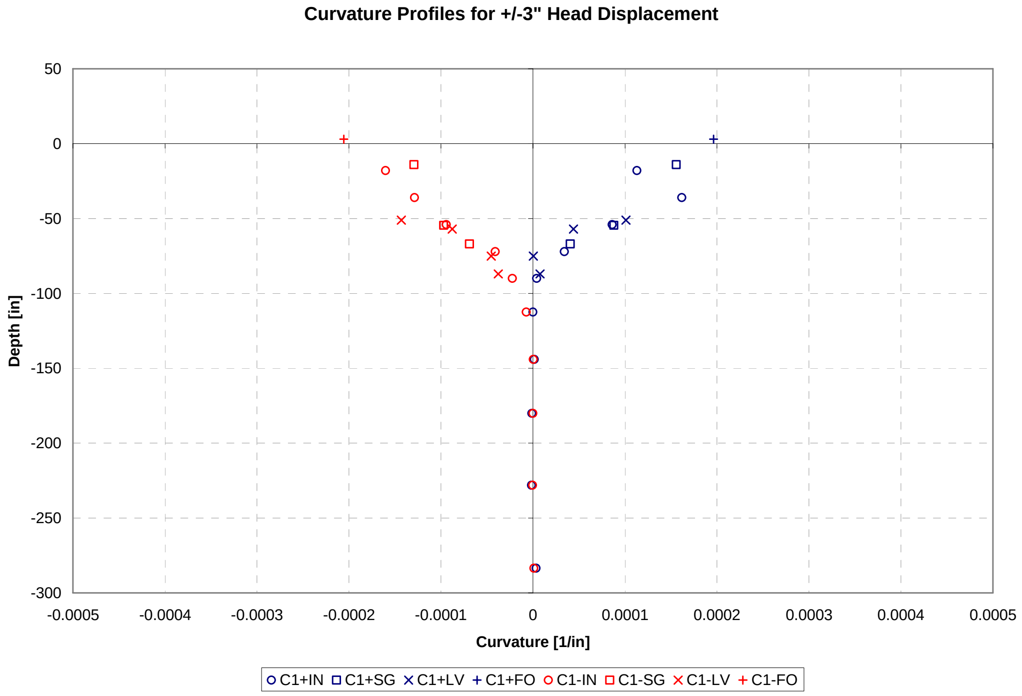

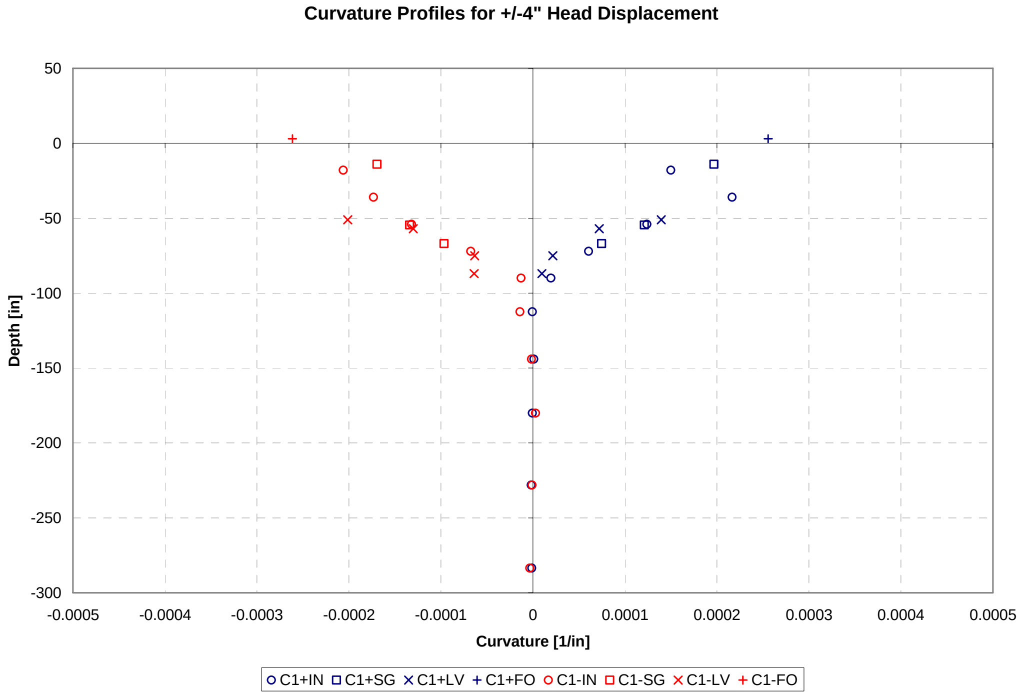

Figure 4.14 (continued). Curvature profiles from the 0.25 inch through the 8.0 inch displacement levels, respectively. "+" or "-" prefixes indicate curvature values for positive or negative displacement cycles. IN is for inclinometer, SG is for strain gauge, LV is for LVDT, and FO is for fiber-optic derived curvatures.

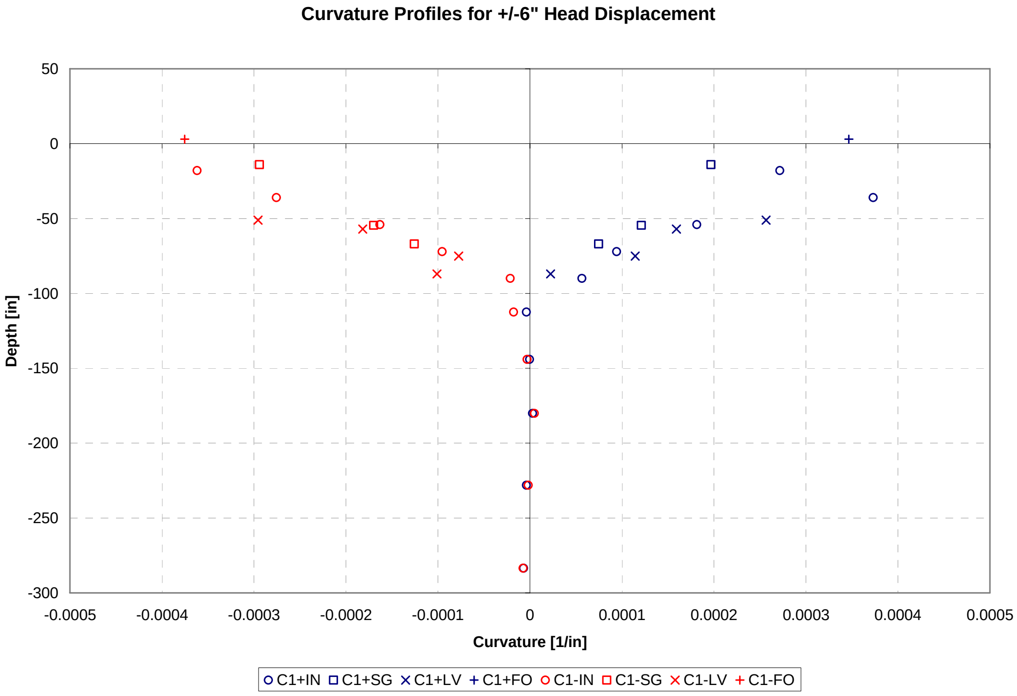

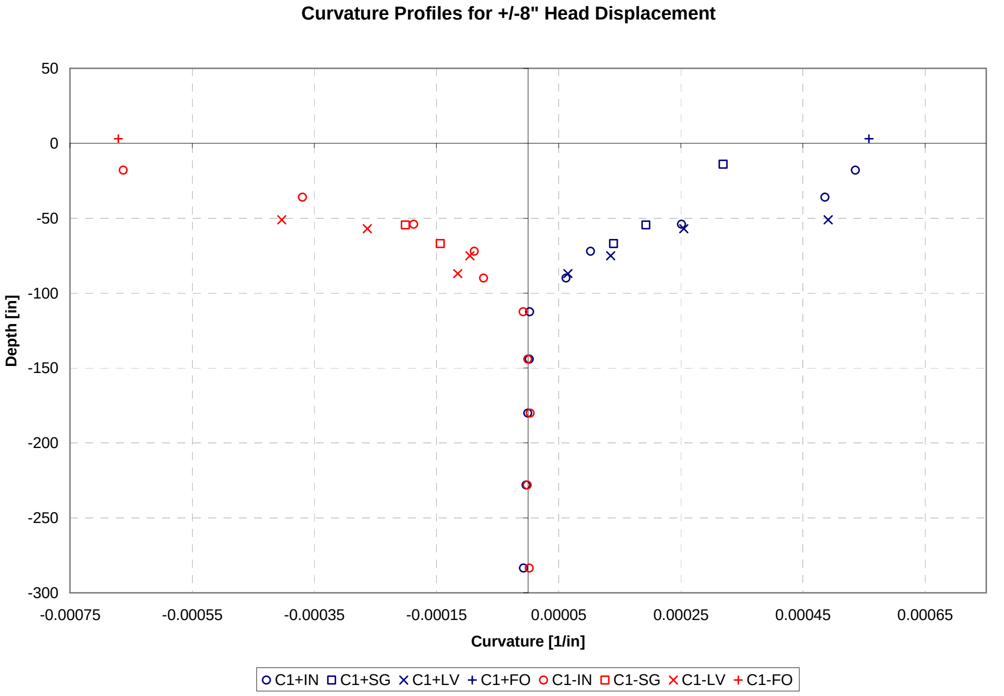

Figure 4.14 (continued). profiles from the 0.25 inch through the 8.0 inch displacement levels, respectively. "+" or "-" prefixes indicate curvature values for positive or negative displacement cycles. IN is for inclinometer, SG is for strain gauge, LV is for LVDT, and FO is for fiber-optic derived curvatures.

Curvatures are calculated from pairs of FBG, strain gauge, and LVDT sensors. The curvature at each depth is calculated as the difference in strain measured by the sensors divided by the horizontal sensor spacing. The largest curvature values for all sensor types were recorded within the yielding region (plastic hinge region) that formed at approximately 3 to 4 ft (1.5 to 2 shaft diameters) below ground surface. In general, the four sensor types gave consistent curvature values outside the high curvature region just below the ground surface. Where curvatures were high, there was significant scatter within data from the same sensor type, as well as between data from different sensor types. The fiber-optic data generally gave higher curvature readings than the strain gauge, inclinometer, and LVDT data in this region (up to 68% higher at the 2.5 inch displacement level).

4.1.4 Experimental Moment-Curvature Relationship

The experimental moment-curvature relationships derived from test data, as well as predicted relationships, are shown in Figure 4.15. The predicted relationships were produced by using fiber element models with concrete tension (Fiber T/S) and without concrete tension (Fiber No T/S), concrete models inherent to the Abacus (FEM) and Strain-Wedge (SWM) software packages, and by the BIAX software package for the p-y analyses (Rha, et al., 2005).

Experimental moment-curvature relationships were produced by correlating known moments at the ground surface with curvature measurements derived from sensors at the ground surface. The experimental data show a shaft response that is less stiff and lower capacity than that of the analytical models; however, this “experimental” relationship has only been measured at one location.

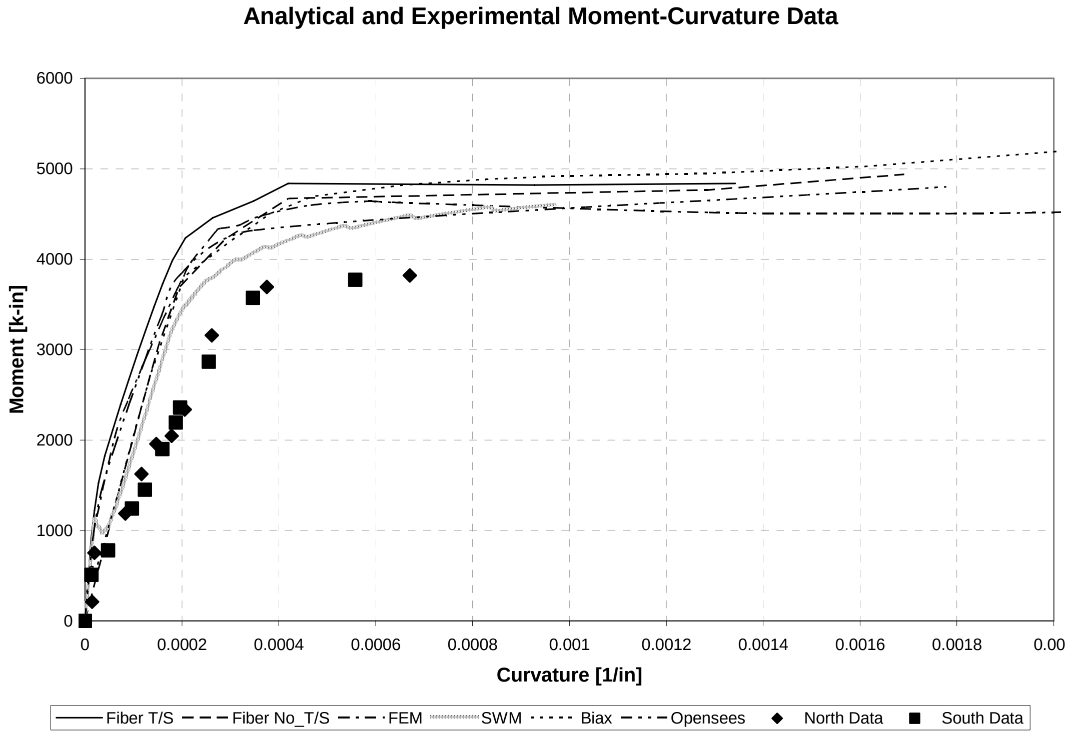

Figure 4.15. Experimental and predicted moment-curvature relationships

4.2 2ft Fixed-Head Results

Construction of the 2 ft flagpole specimen began in September, 2005 and was completed in November, 2005. Testing began on December 7, 2005 and was completed on December 12, 2005.

Figure 4.16. Heave and ground deformations observed at 4 inches of head displacement.

Figure 4.17. Soil cracking observed from above at 4 inches of head displacement.

Significant heave and soil cracking was observed at head displacements greater than 1.5 inches (See Figure 4.16 and Figure 4.17). Also, bar fractures were observed at the cap-shaft interface near the ground surface (See Figure 4.18), but no fracturing was observed where a second peak moment was observed approximately 5 to 7 feet below the ground surface (e.g., see Fig. 4.29). Small diameter foam cylinders placed vertically 24 and 36 inches from the shaft did not experience a brittle failure.

Figure 4.18. Investigation of longitudinal bars at the cap-shaft interface.

4.2.1 Load vs. Deflection

The measured backbone load vs. deflection curves are shown in Figure 4.19. As before, also shown for reference purposes are the results of various pre-test analyses discussed in Chapter 3. The maximum load observed in the south loading direction was 273 kips at 3 inches of head displacement, whereas the maximum load observed in the north direction was 272 kips at 2 inches head displacement. It is notable that the variation in predicted results for the 2 ft fixed-head test is much wider than predictions for the 2 ft flagpole. This is due to a larger influence of soil behavior on the fixed-head configuration response compared with the flagpole response. The analytical models differ principally in their modeling of soil behavior, which is manifest in the variation of predicted system response in Figure 4.19.

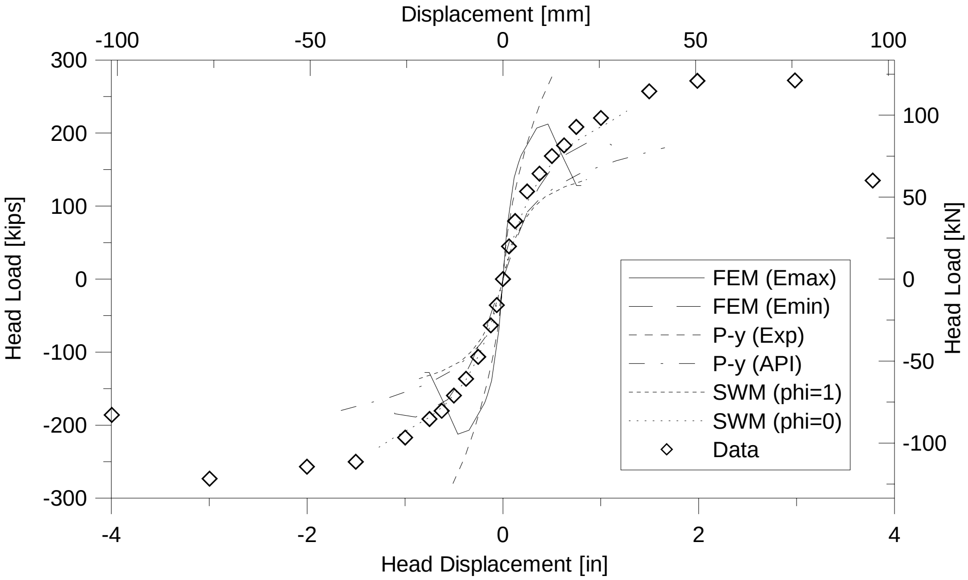

Figure 4.19. Experimental and predicted head load vs. displacement data

The measured cyclic response of the shaft is shown in Figure 4.20. The drop in load capacity from the maximum displacement in the first cycle to the third cycle increased with displacement level. The drop in load capacity at the first cycle (0.0625 inches) was 7%, while the capacity drop near the predicted "yield" displacement (0.5 inches) was 11%. As noted for the flagpole test, this inter-cycle drop in strength is common for tests with repeated cycles to the same peak displacement level. At the three largest displacement levels of 2, 3 and 4 inches, the drop in the peak lateral load was 17%, 31%, and 56%, though at the 4 inch displacement level the first cycle load capacity was significantly reduced indicating that the shaft was severely damaged at that point (permanent strength loss).

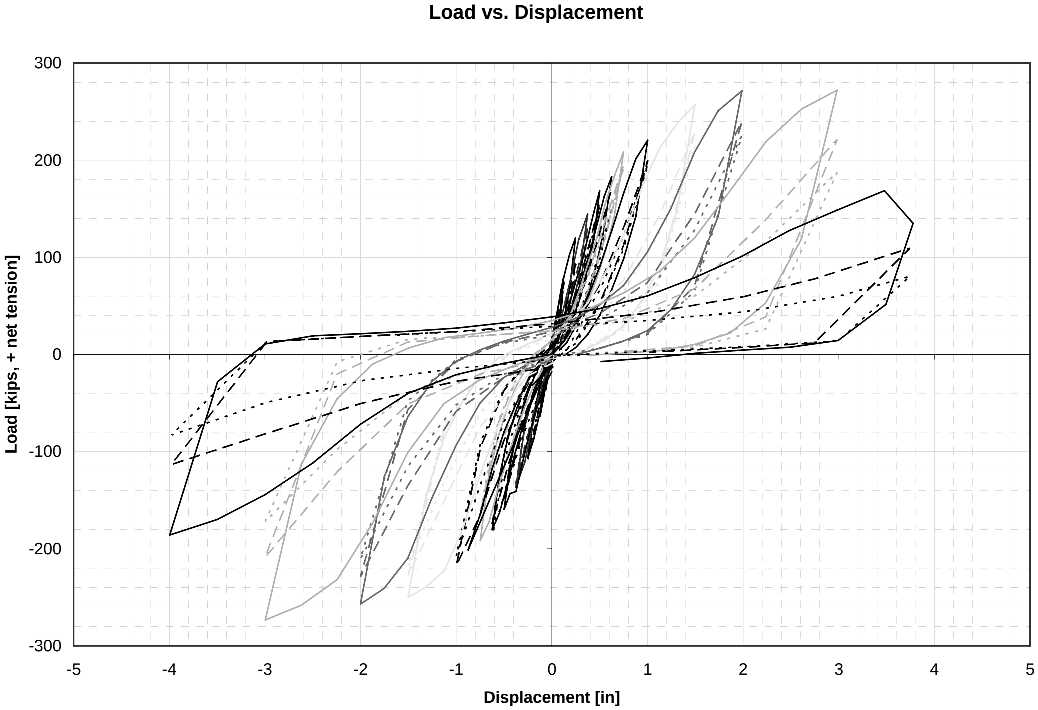

Figure 4.20. Cyclic response of the shaft

4.2.2 Representative Sensor Response Histories

(a) Strain Gauges

Figure 4.21 shows the response histories of embedded strain gauges at the ground surface on longitudinal reinforcing bars farthest from the center of the shaft cross-section. Strain gauge readings, which were directly opposite each other, recorded maximum tensile values of 0.0020 for the South sensor and 0.0021 for the North sensor. These values, which are near the predicted reinforcing bar yield strain, correspond to a head displacement of +/- 0.375 inches as compared to the predicted yield head displacement of +/- 0.45 inches. The second half of the second cycle includes an extra peak that occurred when the control system displaced the specimen by an extra step. This extra peak was not used for inter-cycle comparisons for this displacement level. The processed data indicate that reliable and consistent results were obtained with the strain gauges.

Figure 4.22 shows the same sensors at the +/- 1.5 inch displacement level where sensor failure is observed. Note the permanent strain offsets after each cycle due to tensile yielding of the reinforcing bars. Strain gauge failures produced erroneous data values similar to results shown in Figure 4.6.

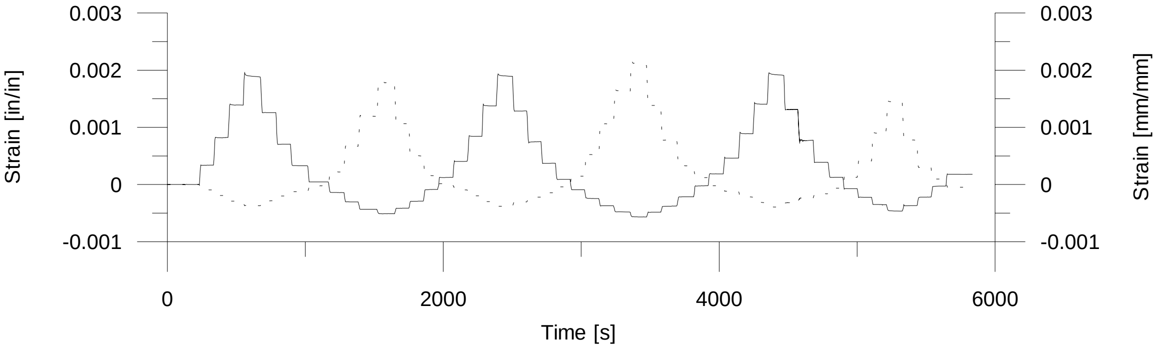

Figure 4.21. Strain gauge histories on opposite bars at the ground surface during the 0.375 inch displacement level. Solid line is the South sensor, dotted line is North sensor.

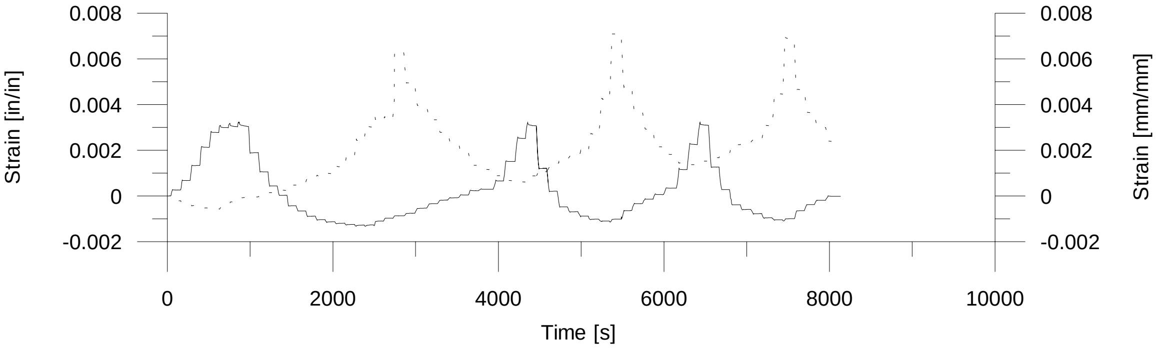

Figure 4.22. Strain gauge histories on opposite bars at the ground surface during the 1.5 inch displacement level. Solid line is the South sensor, dotted line is North sensor.

(b) Inclinometers

Figure 4.23 and Figure 4.24 show the inclinometer response histories for a depth of -19 inches at the +/-0.375 inch and +/-1.5 inch displacement levels, respectively. The maximum rotations at +/-0.375 inches of head displacement were -0.0043 and +0.0048 radians, and +/-0.02 radians for +/-1.5 inches of head displacement. The cause of the extra peak in the second half of the second cycle in the 0.375 inch displacement level is described in part (a). The rotations experienced by the shaft at the ground surface, the largest for all inclinometers, were well within the range of the sensors. Inclinometers were undamaged during the test and produced reasonable data over the entire range of displacement levels applied during the test. Inclinometer 5, at a depth of -41 inches, did not work properly for the fixed head test; therefore, data from this sensor were not included in the data reduction.

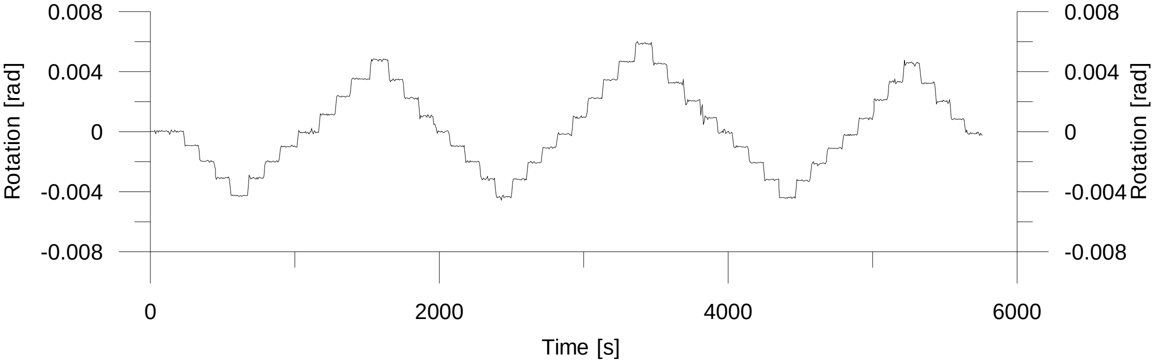

Figure 4.23. Inclinometer history at a depth of -19 inches during the 0.375 inch displacement level.

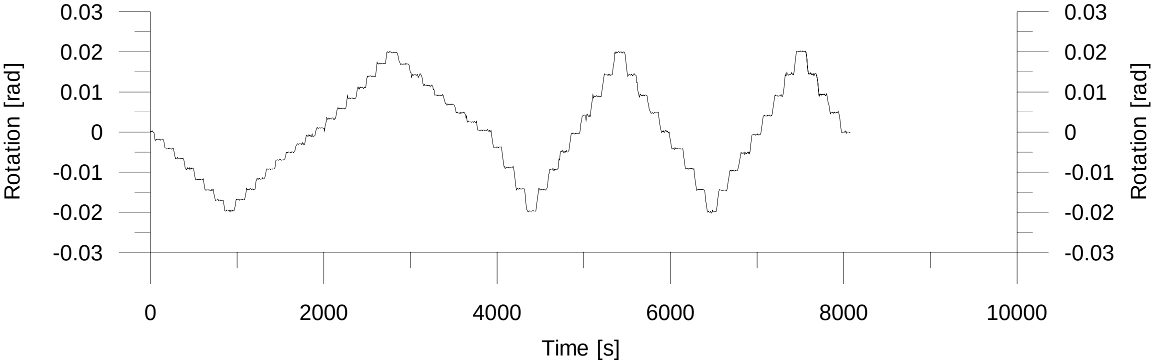

Figure 4.24. Inclinometer history at a depth of -19 inches during the 1.5 inch displacement level.

(c) LVDTs

Figure 4.25 and Figure 4.26 show the LVDT response histories for a depth of -6 inches at the +/-0.375 inch and +/-1.5 inch displacement levels, respectively. The maximum displacements at +/-0.375 inches of head displacement were -0.0035 inches and +0.0071 inches, and -0.01 inches and +0.068 inches for +/-1.5 inches of head displacement. The cause of the extra peak in the second half of the second cycle in the 0.375 inch displacement level is described in part (a).

LVDT data were generally offset relative to positive and negative halves of each cycle as shown in Figure 4.26, likely because of axial growth of the pile due to cracking. Although results for the North sensor appear more reliable, as the relation displays distinctive load steps, curvature values generated from the pair of LVDT sensors tend to match well with strain gauge derived curvature values as shown in Chapter 5.

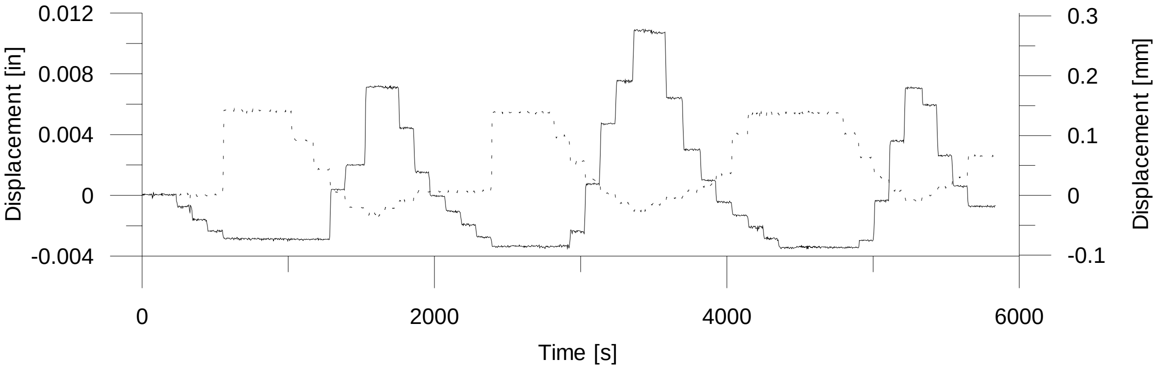

Figure 4.25. LVDT histories at a depth of -6 inches during the 0.375 inch displacement level. Solid line is North LVDT, dotted line is South LVDT.

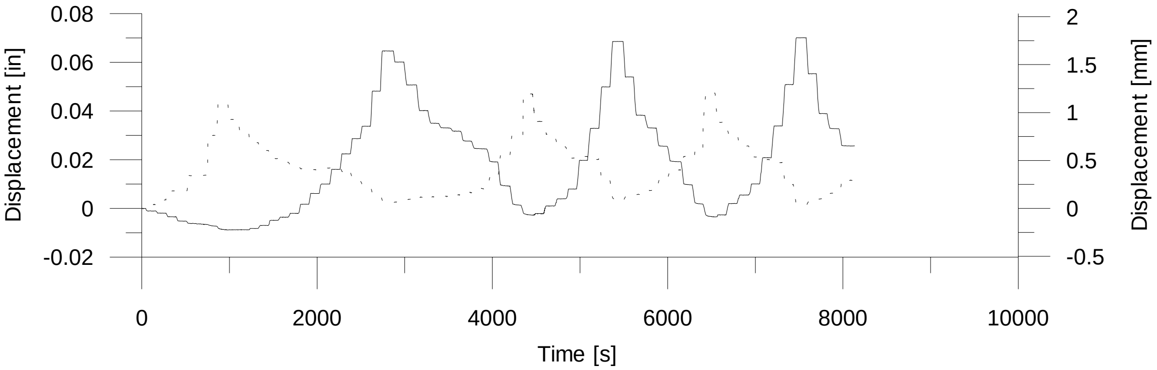

Figure 4.26. LVDT histories at a depth of -6 inches during the 1.5 inch displacement level. Solid line is North LVDT, dotted line is South LVDT.

(d) Fiber-optics

Figure 4.27 and Figure 4.28 show the fiber-optic response histories for a depth of -17 inches at the +/-0.375 inch and +/-1.5 inch displacement levels, respectively. The maximum wavelength changes at +/-0.375 inches of head displacement were -0.17 nm and 0.9 nm. The fluctuations in sensor readings shown in Figure 4.21 are due to failure of the fiber-optic sensors. The fiber-optics sensors tended to become unreliable after the +/-0.375 inch displacement level.

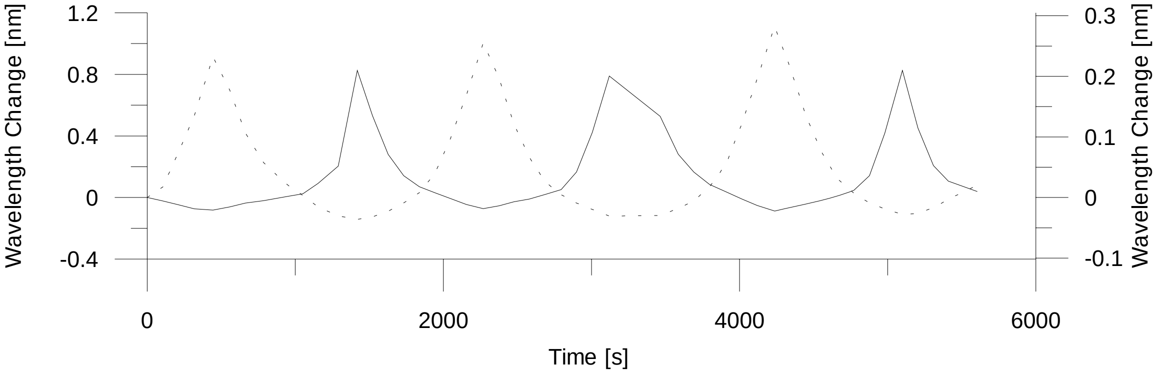

Figure 4.27. Fiber-optic sensor histories at a depth of -17 inches during the 0.375 inch displacement level. Solid line is North fiber-optic sensor, dotted line is South fiber-optic sensor.

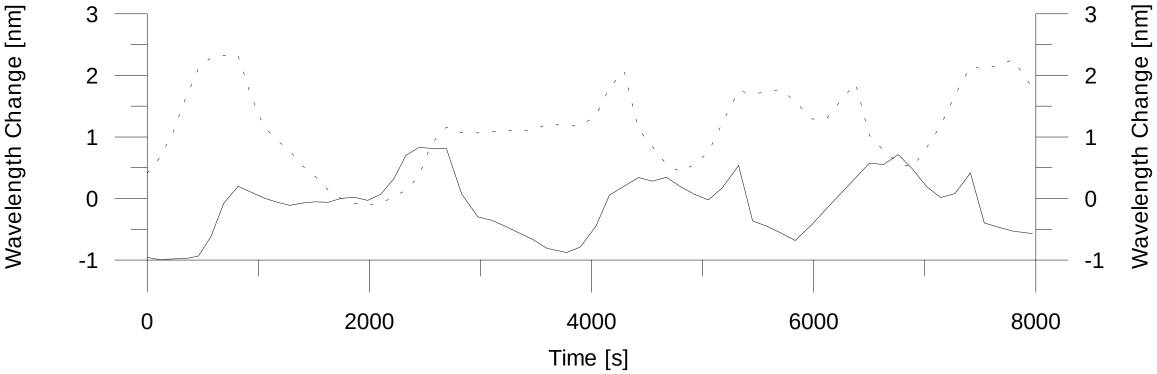

Figure 4.28. Fiber-optic sensor histories at a depth of -17 inches during the 1.5 inch displacement level. Solid line is North fiber-optic sensor, dotted line is South fiber-optic sensor.

4.2.3 Curvature Profiles at Displacement Levels

Curvature values calculated from each sensor type from the 0.0625 inch through the 2 inch displacement level are shown in Figure 4.29. Head displacements are noted on the plots. The maximum curvature values recorded were located at the plastic hinge that formed just below the cap at the ground surface elevation and at a second plastic hinge that formed at a depth of approximately 4 to 8 ft (2 to 4 shaft diameters below ground line). Relatively large curvature values (~ twice the yield curvature) were observed at depths 2 to 3 times greater than that of the 2 ft flagpole test. Strain gauge and LVDT data were generally more reliable than the fiber-optic data at shallow depths. This is most likely due to the fragile nature of the fiber-optic sensors and their sensitivity to damage or misalignment during installation.

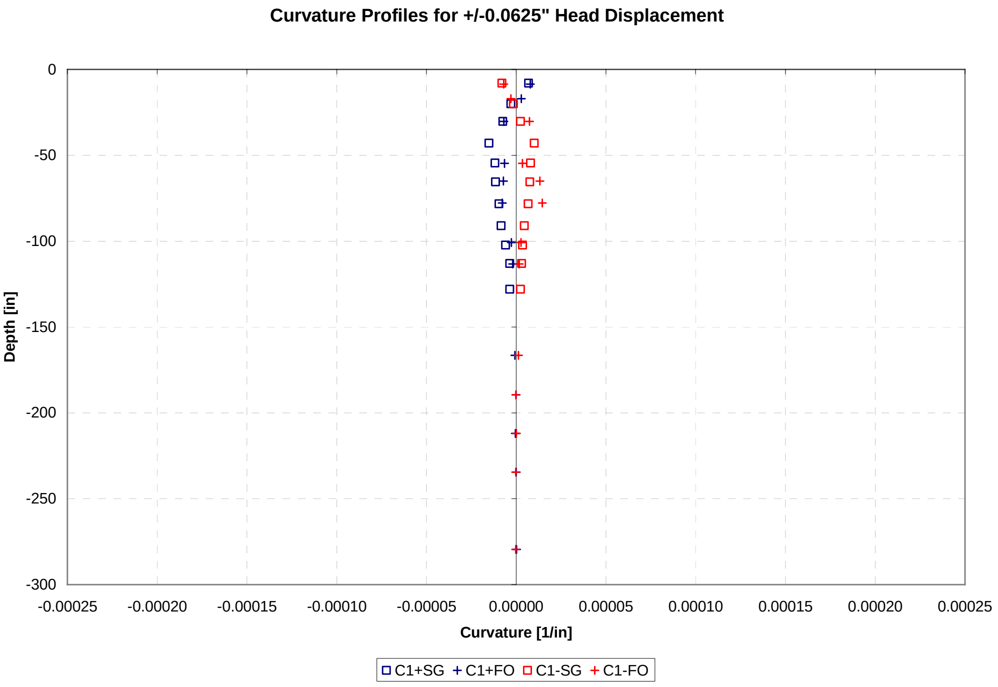

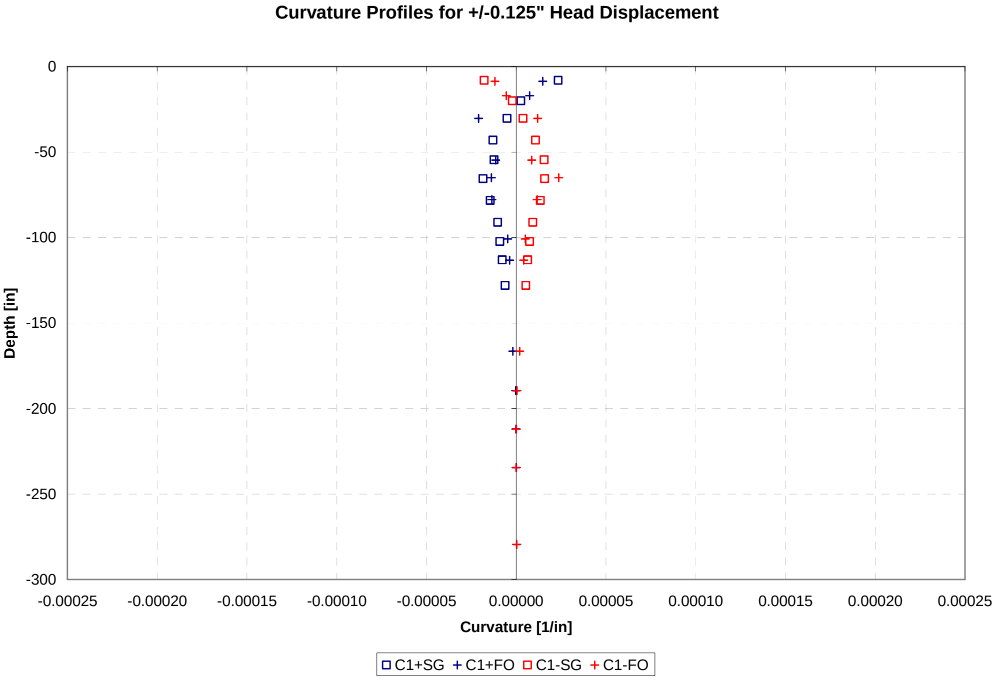

Figure 4.29. Curvature profiles from the 0.0625 inch through the 2.0 inch displacement levels, respectively. "+" or "-" prefixes indicate curvature values for positive or negative displacement cycles. SG is for strain gauge, LV is for LVDT, and FO is for fiber-optic derived curvatures.

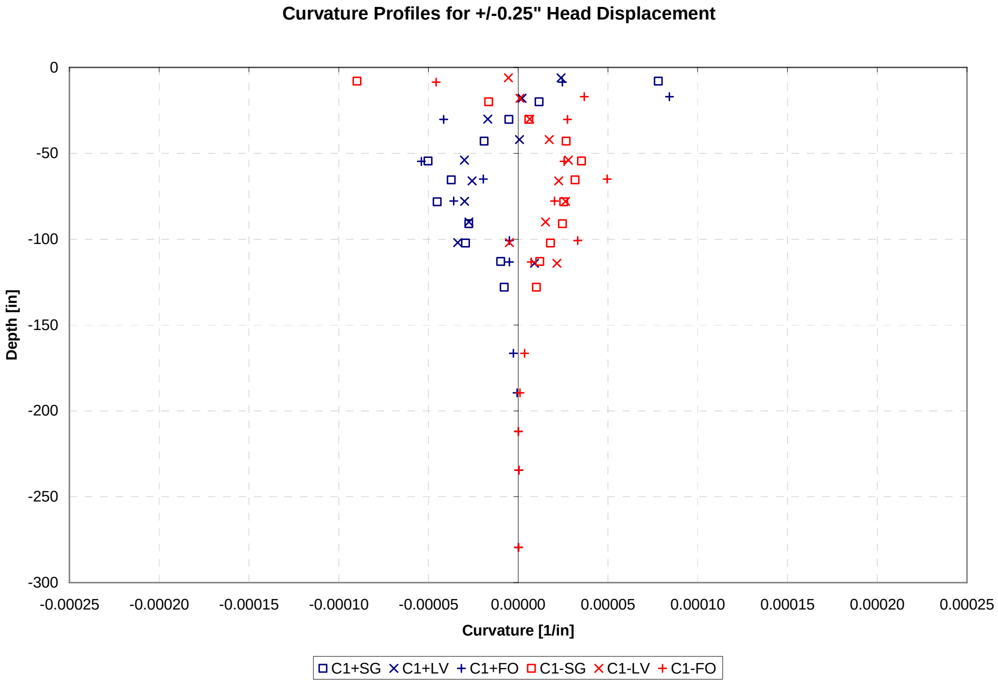

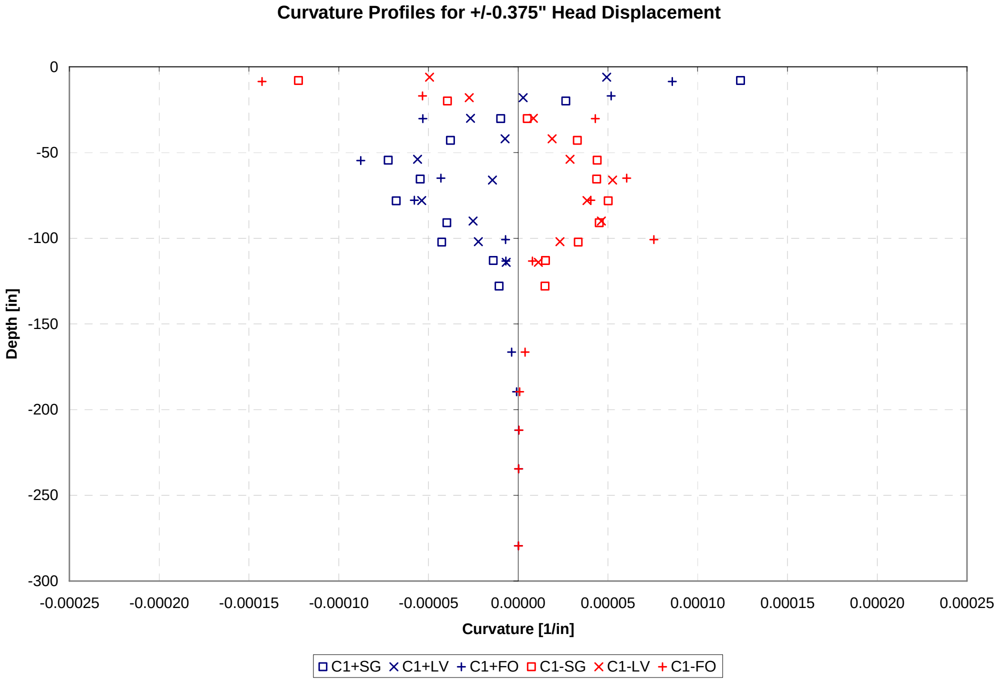

Figure 4.29 (continued). Curvature profiles from the 0.0625 inch through the 2.0 inch displacement levels, respectively. "+" or "-" prefixes indicate curvature values for positive or negative displacement cycles. SG is for strain gauge, LV is for LVDT, and FO is for fiber-optic derived curvatures.

Curvature Profiles for +/-0.5" Head Displacement

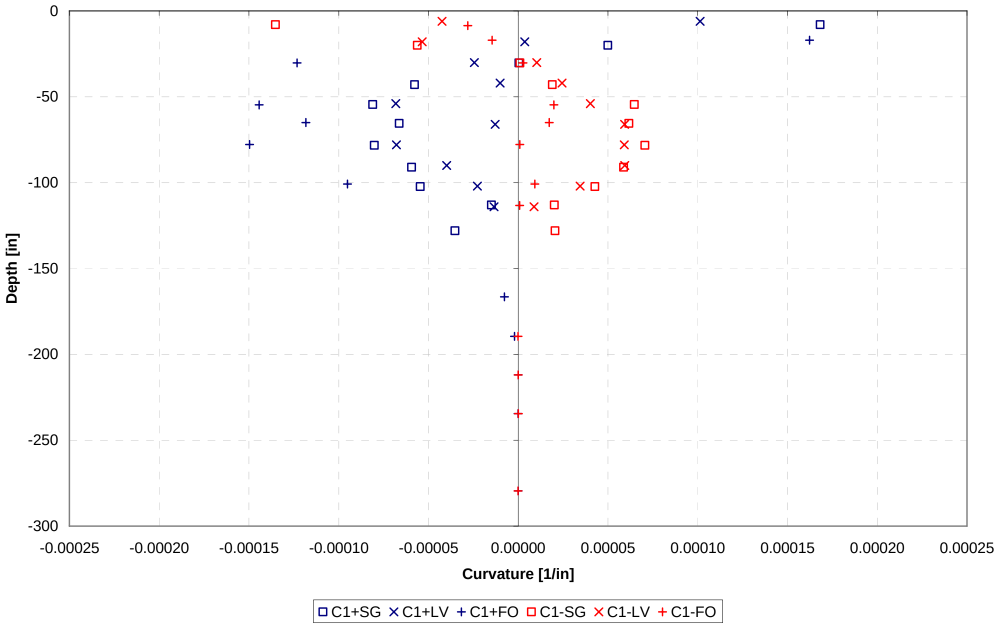

Curvature Profiles for +/-0.625" Head Displacement

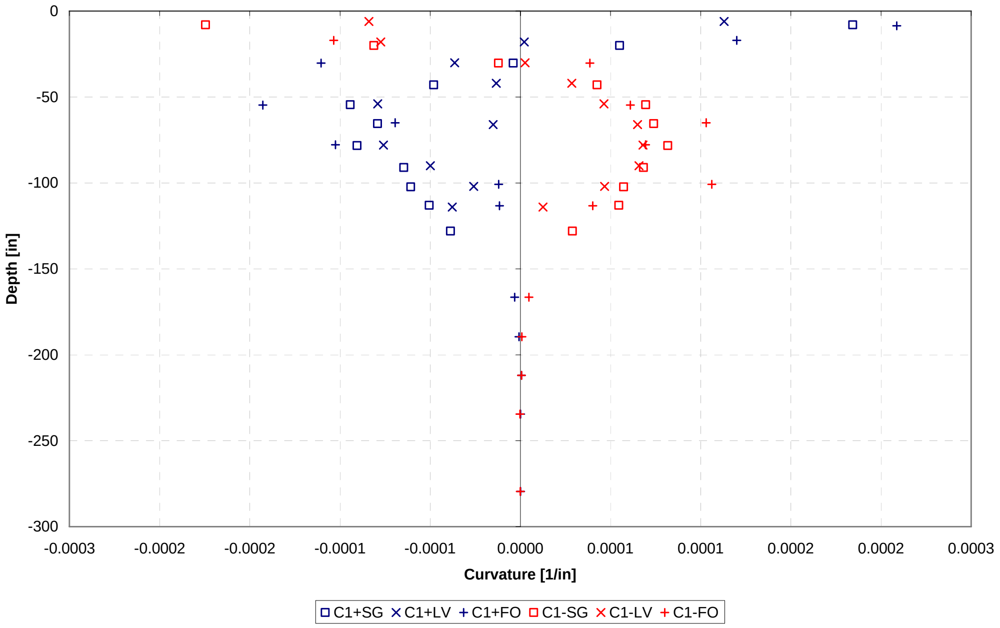

Figure 4.29 (continued). Curvature profiles from the 0.0625 inch through the 2.0 inch displacement levels, respectively. "+" or "-" prefixes indicate curvature values for positive or negative displacement cycles. SG is for strain gauge, LV is for LVDT, and FO is for fiber-optic derived curvatures.

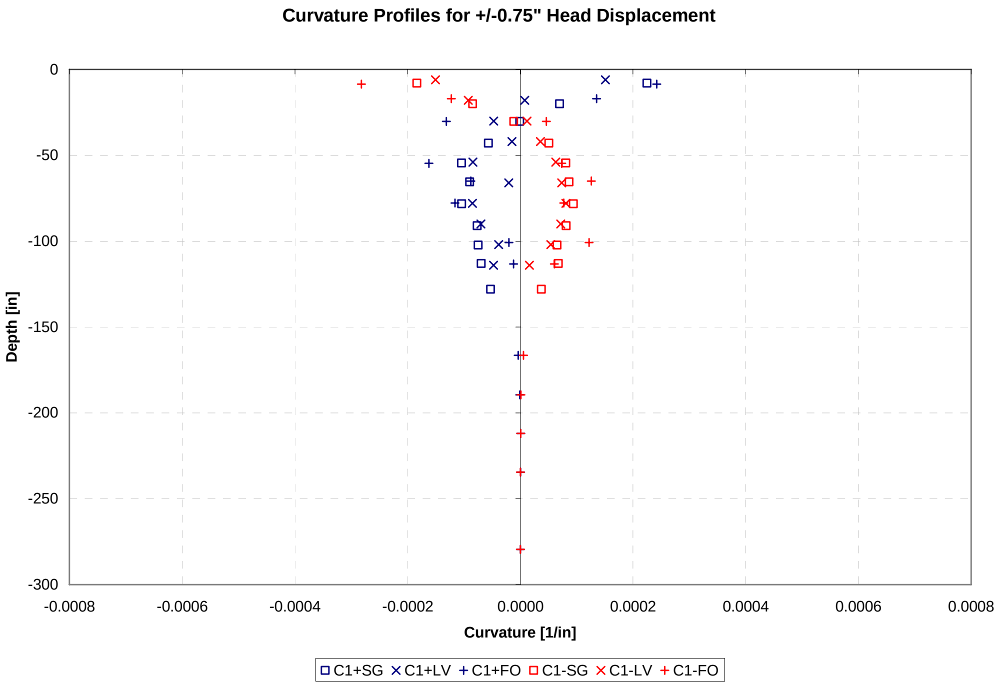

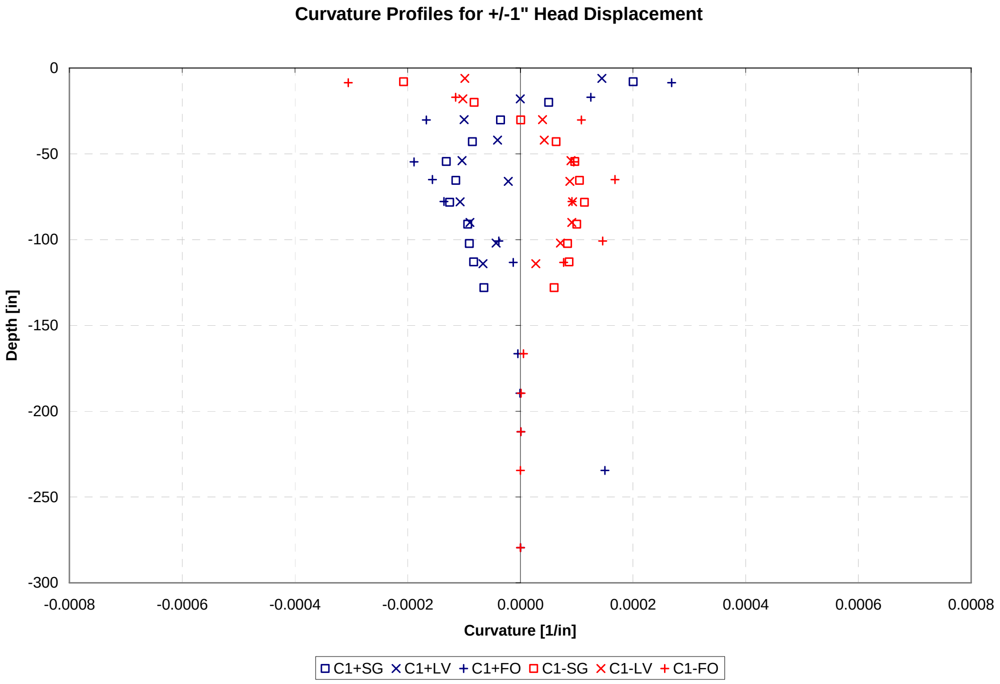

Figure 4.29 (continued). Curvature profiles from the 0.0625 inch through the 2.0 inch displacement levels, respectively. "+" or "-" prefixes indicate curvature values for positive or negative displacement cycles. SG is for strain gauge, LV is for LVDT, and FO is for fiber-optic derived curvatures.

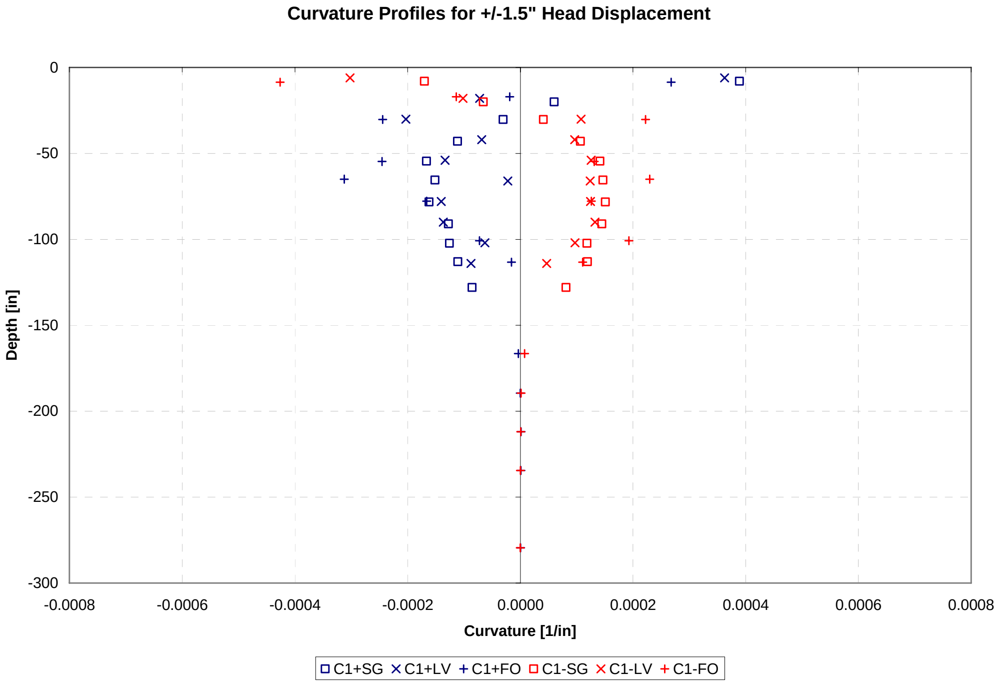

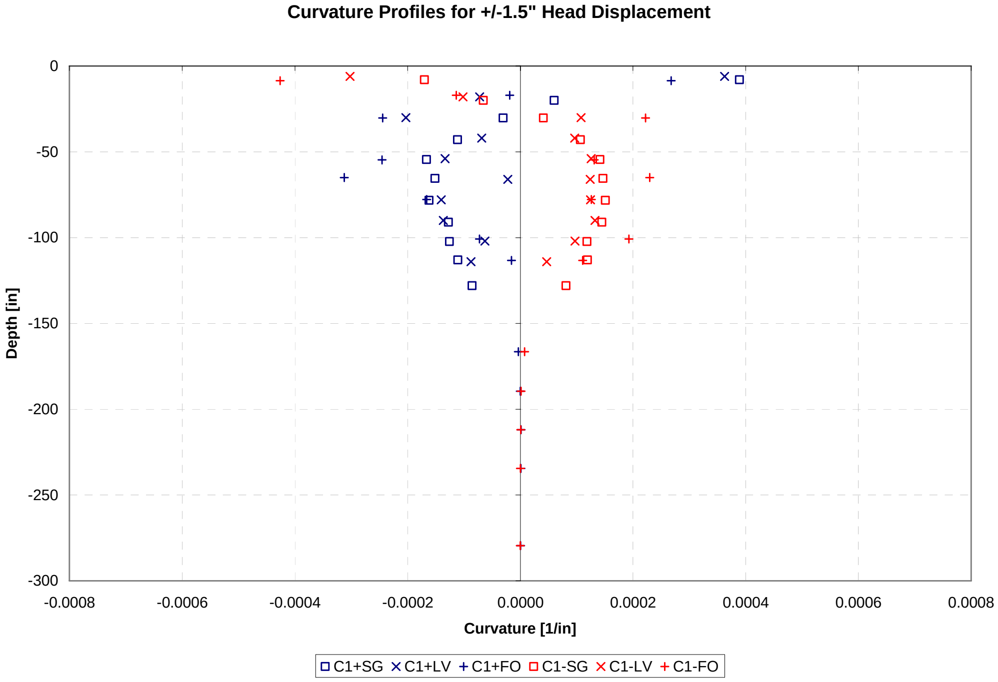

Figure 4.29 (continued). Curvature profiles from the 0.0625 inch through the 2.0 inch displacement levels, respectively. “+” or “-” prefixes indicate curvature values for positive or negative displacement cycles. SG is for strain gauge, LV is for LVDT, and FO is for fiber-optic derived curvatures.

4.2.4 Experimental Moment-Curvature Relationship

Predicted moment-curvature relationships, produced with the same software packages used for the 2ft flagpole test, are shown in Figure 4.30.

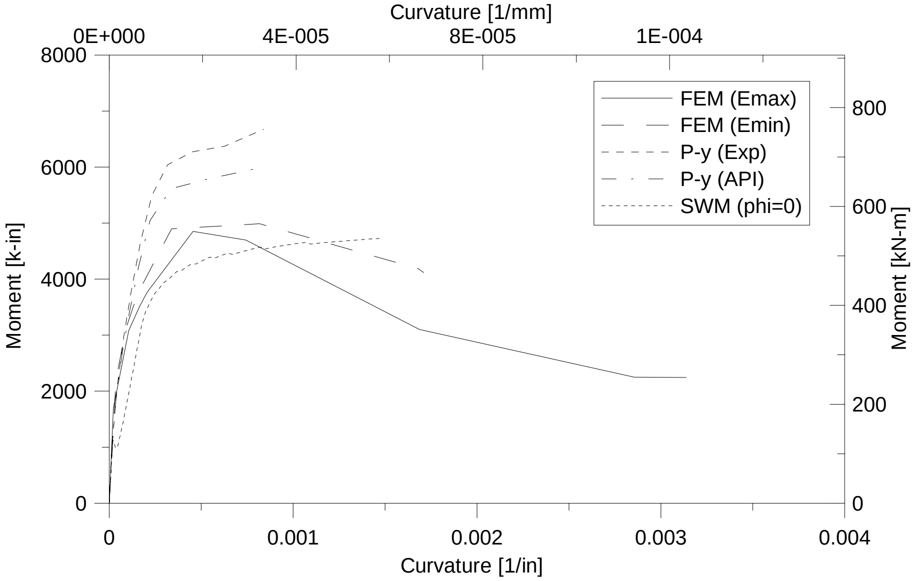

Figure 4.30. Predicted moment-curvature relationships

Generating moment-curvature relationships from the test data is complicated by the difficulty in evaluating curvatures at the interface between the cap and shaft. Measuring curvatures near the top of the shaft is difficult due to the small sensor gauge length required given the steep curvature gradient at this location. Also, reinforcement slip and extension (Alsiwat and Saatcioglu, 1992) at the cap-shaft interface reduces the stiffness of the overall load – displacement relation and also influences curvature measurements at the shaft-cap interface. Because of these difficulties, curvature values at the ground surface were extrapolated from curvature values obtained at depth and verified with expected curvatures from predicted results. The moment-curvature relationship used to analyze the shaft response is discussed in Section 5.3.4.

4.3 Nine Shaft Group Results

4.3.1 Load vs. Deflection

Measured data for all displacement cycles were investigated to assess data reliability as noted in Section 2.4.2. Data collected near the peak displacement levels for the 0.25 in., 0.35 in., and some cycles for 0.5 inch displacement levels, were typically excluded due to a problem with test control. A complete load deflection curve, excluding unreliable data, is depicted in Figure 4.31.

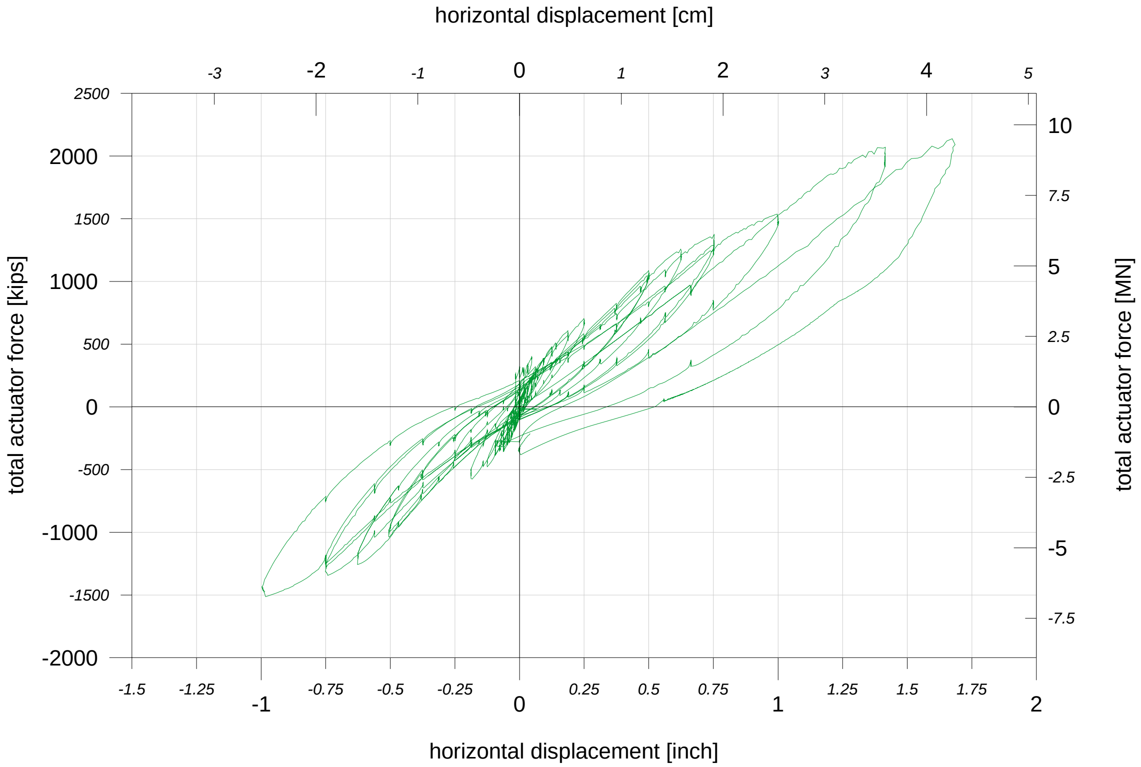

Figure 4.31 Load displacement relationship for 9-pile group test

The envelope or backbone relation for the results shown in Figure 4.31, is presented in Figure 4.32. The relation for negative loads stops at a maximum cap displacement of one inch because the load capacity of the actuators for this direction (actuator pull) was reached.

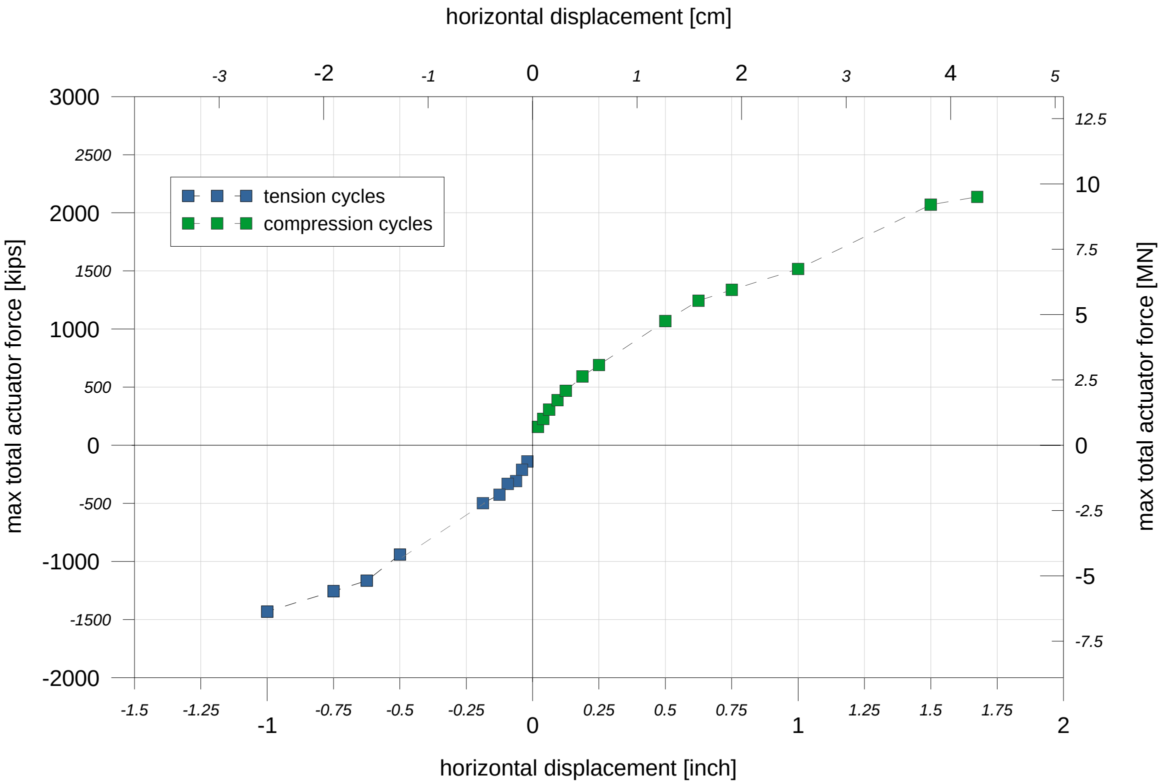

Figure 4.32. Backbone relation for 9-pile group test

4.3.2 Rotation versus cap horizontal deflection

The rotation of the pile cap under lateral displacement was assessed using the three LVDTs installed along the top surface of the pile cap (Figure 4.33). The layout of the three sensors enables the rotation and vertical displacement due to axial pile growth at the pile cap center to be calculated. Pile growth occurs due to concrete cracking and reinforcement yielding in the 2ft diameter piles. It is noted that the relationship shown in Figure 4.34 is effectively linear and provides boundary conditions required to enable accurate future analytical studies (since the load capacity of the test system could not enforce zero cap rotation, which is often assumed in analytical studies). The impact of the known rotation of the cap on the load versus displacement response of the test specimen will be studied analytically.

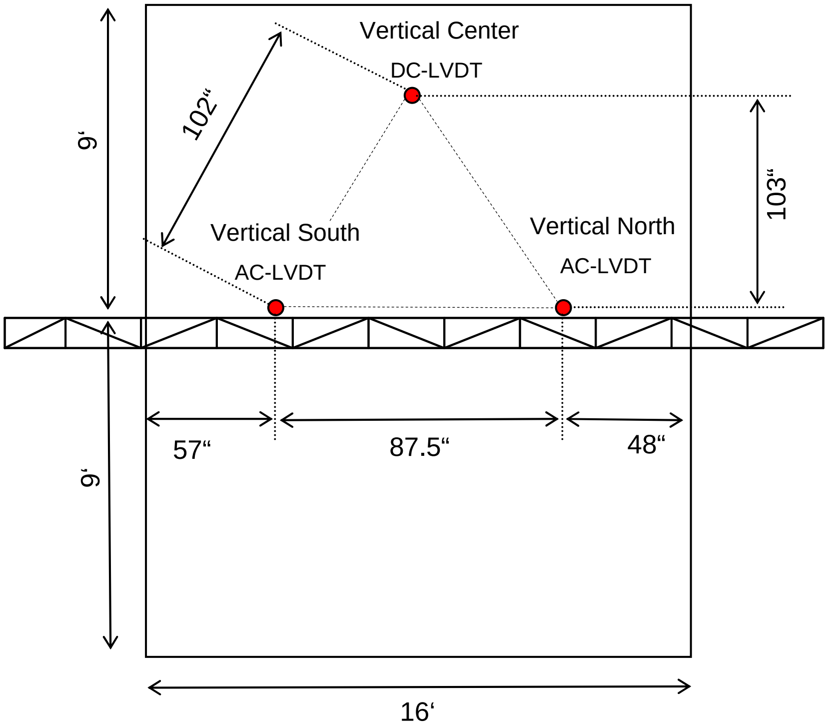

Figure 4.33. LVDT sensors used to assess cap rotation

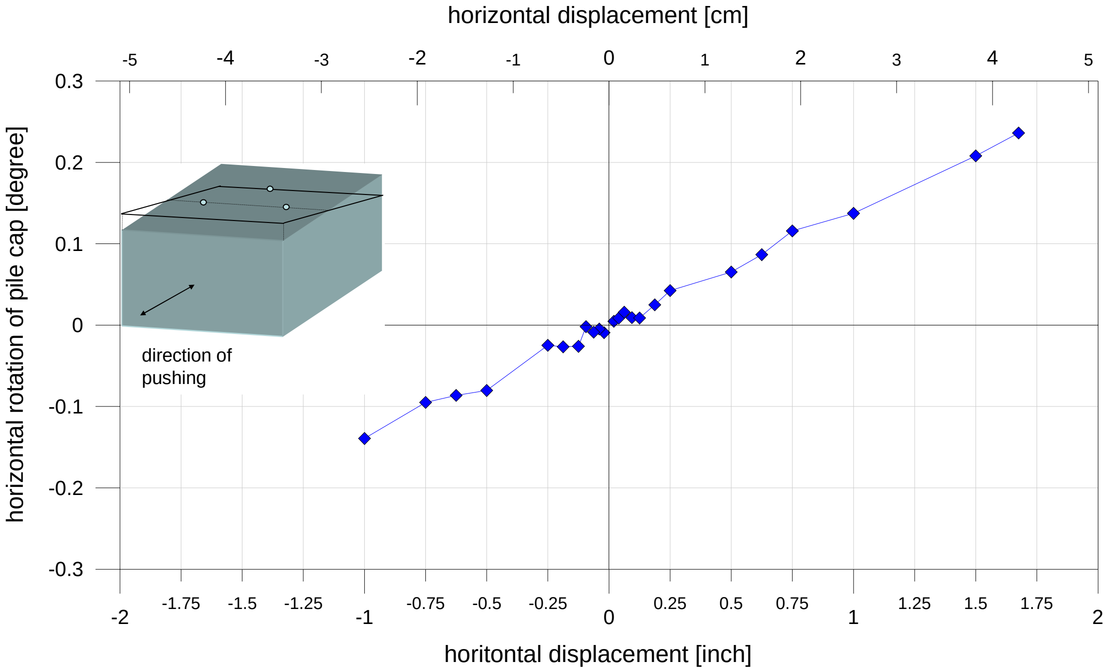

Figure 4.34. Lateral cap displacement versus cap rotation

4.3.3. Large Displacement Loading

A “final push” was performed after completion of the cyclic testing to determine the ultimate capacity of the 9 pile group. In order to obtain the necessary load capacity, three additional actuators were installed between the pile cap and the reaction block as shown in Figure 4.35 to supplement the existing four actuator system. The test proceeded by first applying load up to the capacity of the original four actuators under load control, which was then held constant under load control, followed by the application of additional lateral load using the 3 supplemental actuators. Manual control was used for the three supplemental actuators (servo control would have taken too long to setup) and explains the irregularity in the load displacement curve in Figure 4.36. It is noted that this final push was performed after a residual cap displacement of 0.2-0.3 inches occurred. A maximum capacity of about 2300 kips was reached at a displacement level of 2.5 inches.

Figure 4.35. Installation of 3 supplemental actuators

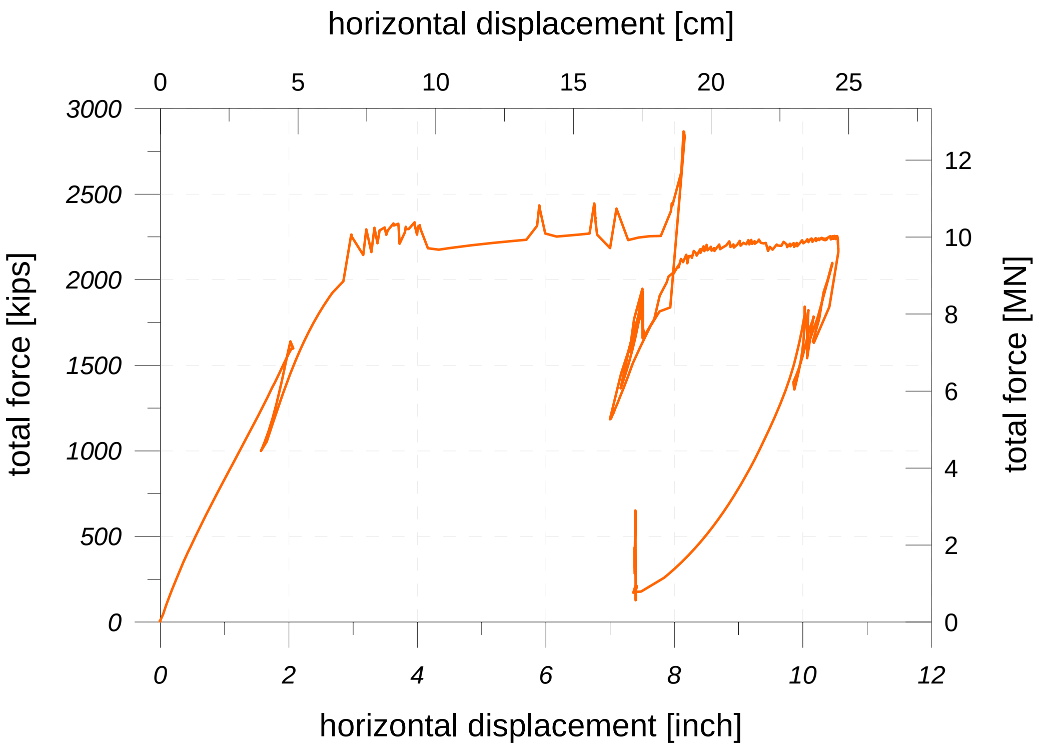

Figure 4.36. Load Displacement curve of final push

4.3.4. Displacement of Reaction Block

The displacement of the reaction block (shown in Figure 2.8 and Figure 2.10) was measured using a string potentiometer installed at the geometric center of the reaction block and the center of the abutment back wall facing the reaction block. Figure 4.37 describes the measured load-deflection relationship. It can be seen that an almost linear relationship between the horizontal reaction block movement and the horizontal cap displacement was observed. Data do not include the measurements of the 'Final Push'.

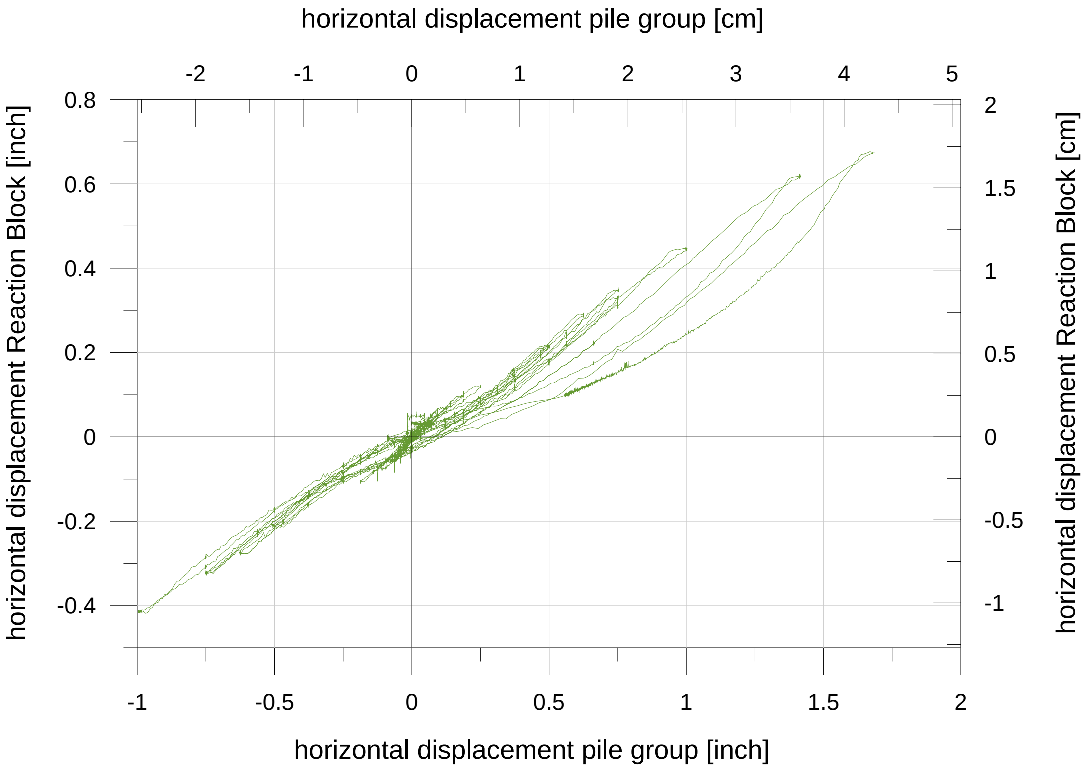

Figure 4.37. Horizontal displacement of Reaction Block versus horizontal displacement of 9 pile group

4.3.5 Representative Sensor Response Histories

(a) Strain Gauges

In order to evaluate the quality of the measured data, response histories for each sensor pair necessary to create curvature profiles along the pile depth were investigated at several displacement levels. Strain gauge locations and nomenclature are noted in Figure 4.38, where sensor numbers for each of the three instrumented piles is determined by adding 100, 200, or 300. Based on the measured responses shown in Figure 4.39, many of the gauges appear to provide reliable results. For cases where sensors did not work, sensor data substation will be explored to obtain curvature profiles (see section (d).

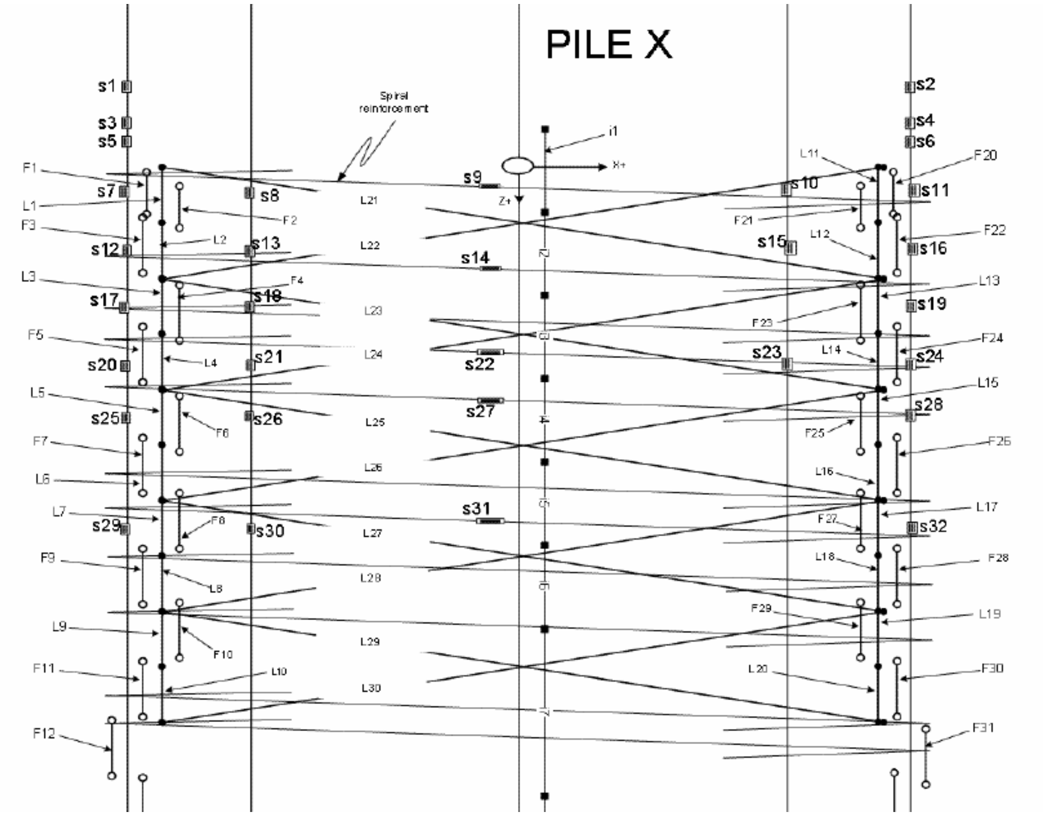

Figure 4.38. Sensor layout for each instrumented pile for the 9-pile group test

Representative response histories are provided for Pile 1 in Figure 4.39. It is noted that the readings have not been corrected to eliminate the initial sensor offset. In Figure 4.39(a), results are shown for a cap displacement level of 0.0625 inches. Results obtained for some gauges, SG 107, 111, and 112, appear reasonable; however, results for other gauges are clearly unreliable (e.g., SG 116). Strain gauge data have been processed and found to be usable in pile 1 and 2. For pile 3 some strain gauges did not provide any readings throughout the whole test, hence creating challenges for future analyses. Curvature profiles for some displacement levels might be able to be determined, however, as noted, in some cases where reliable data were not obtained, data substitution may be needed to construct curvature profiles.

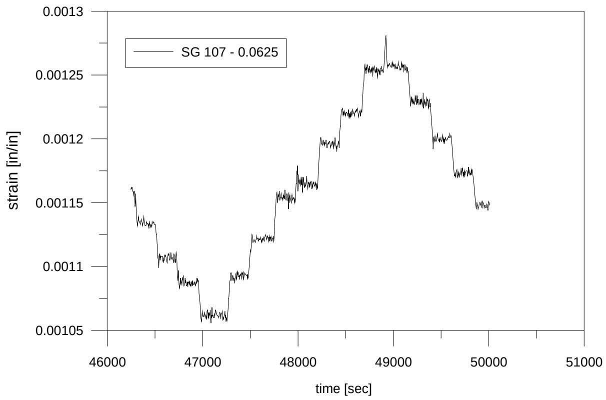

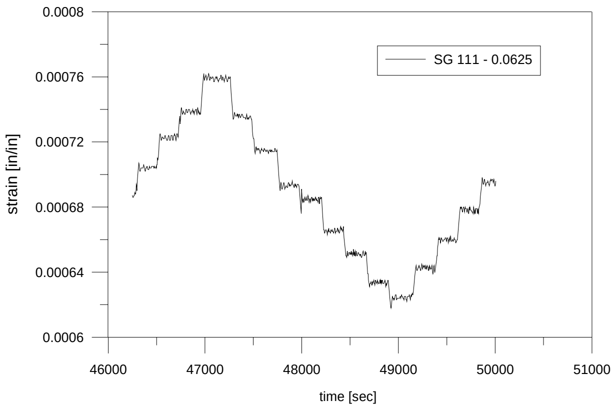

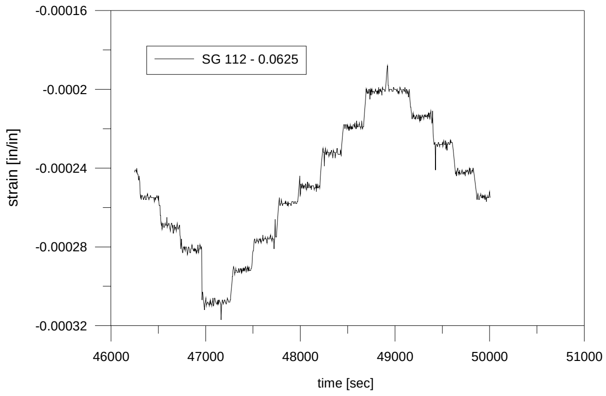

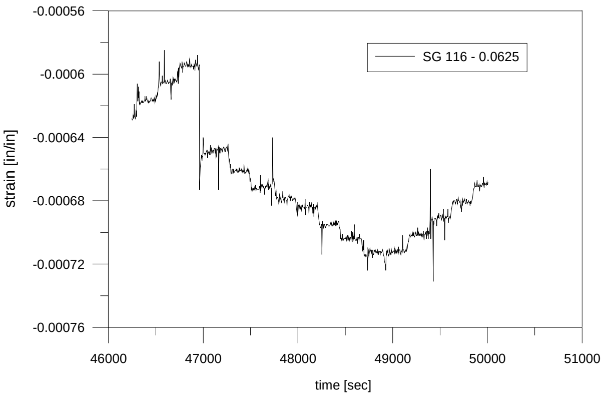

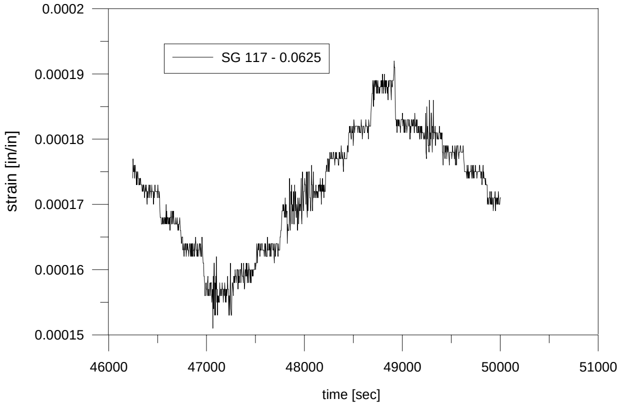

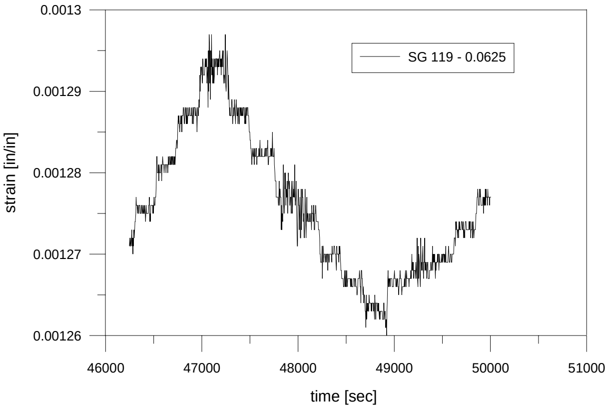

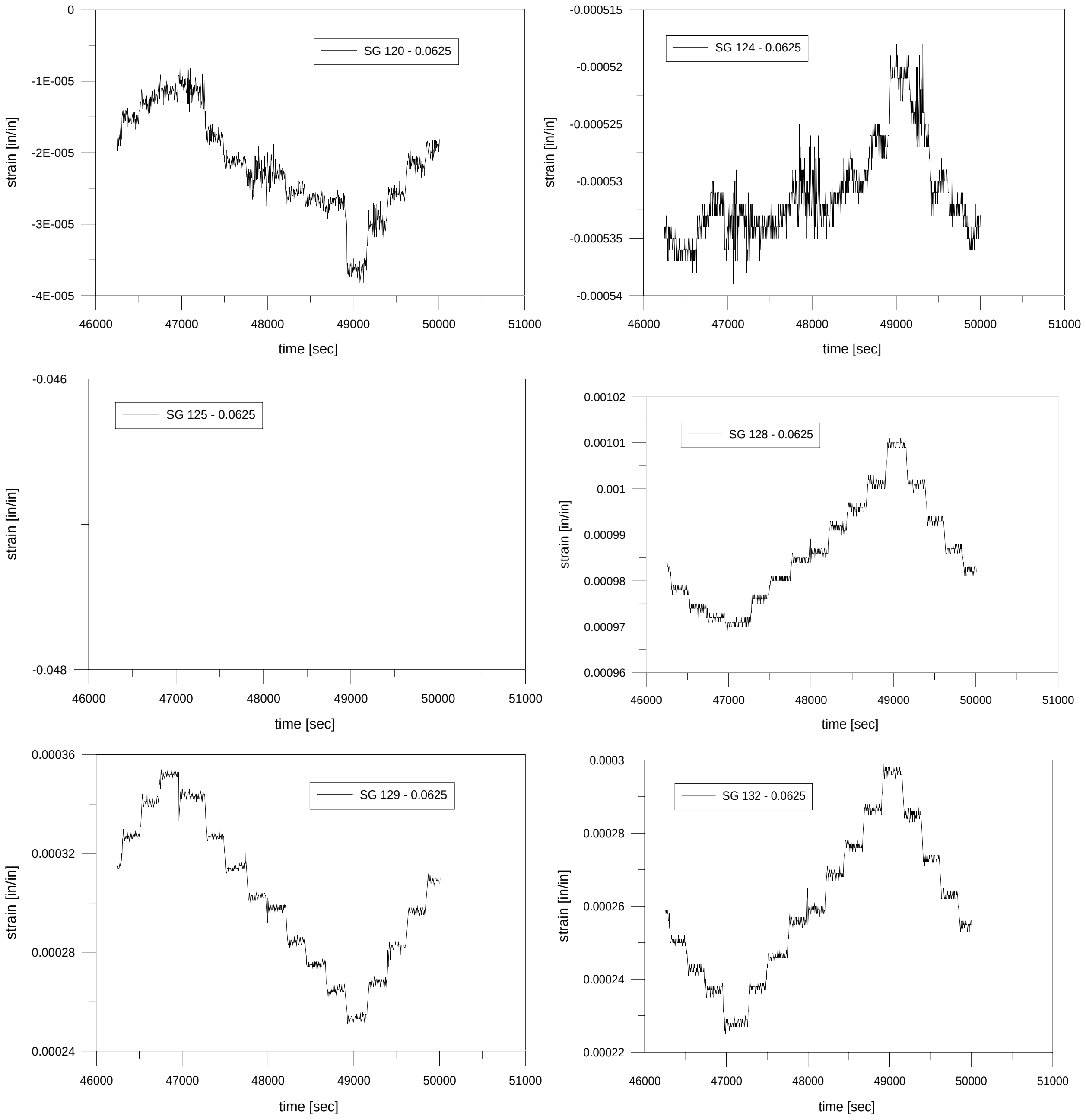

Figure 4.39(a) Pile 1 – 0.0625 inch Cap displacement

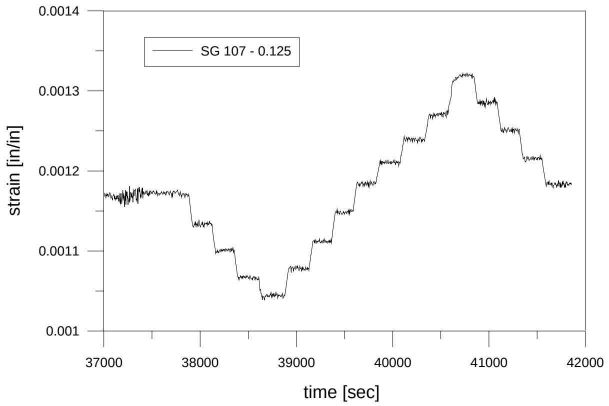
SG 107 - 0.125
strain [in/in]
time [sec]
0.0014
0.0013
0.0012
0.0011
0.001
37000
38000
39000
40000
41000
42000

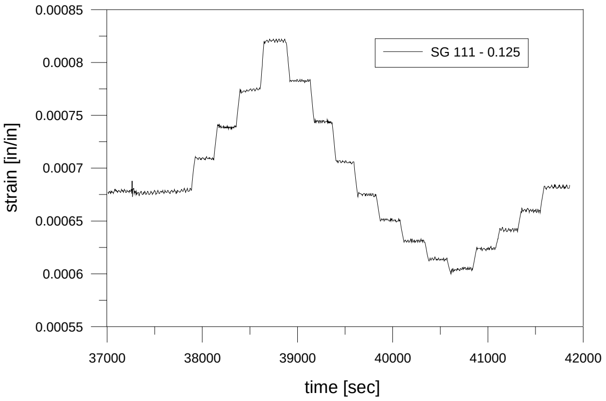
SG 111 - 0.125
strain [in/in]
time [sec]
0.00085
0.0008
0.00075
0.0007
0.00065
0.0006
0.00055
37000
38000
39000
40000
41000
42000

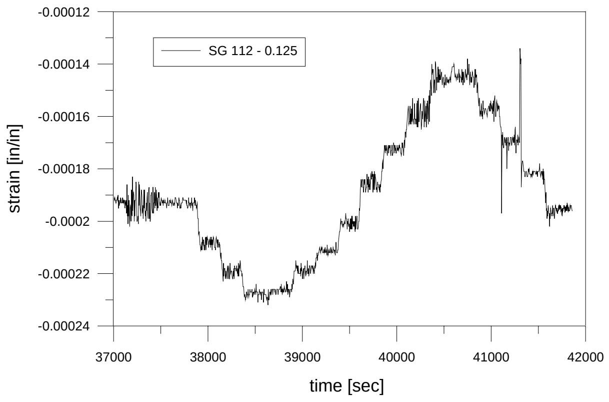
SG 112 - 0.125
strain [in/in]
time [sec]
-0.00012
-0.00014
-0.00016
-0.00018
-0.0002
-0.00022
-0.00024
37000
38000
39000
40000
41000
42000

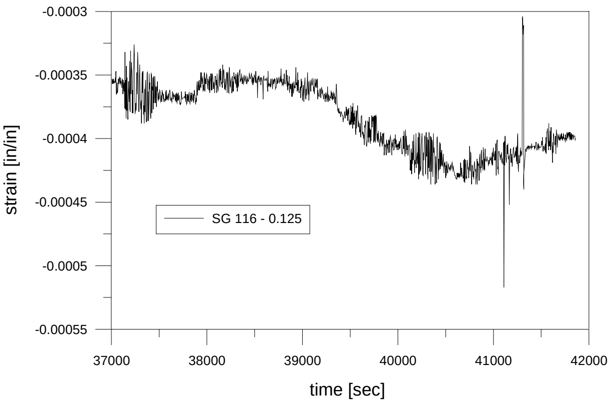
SG 116 - 0.125
strain [in/in]
time [sec]
-0.0003
-0.00035
-0.0004
-0.00045
-0.0005
-0.00055
37000
38000
39000
40000
41000
42000

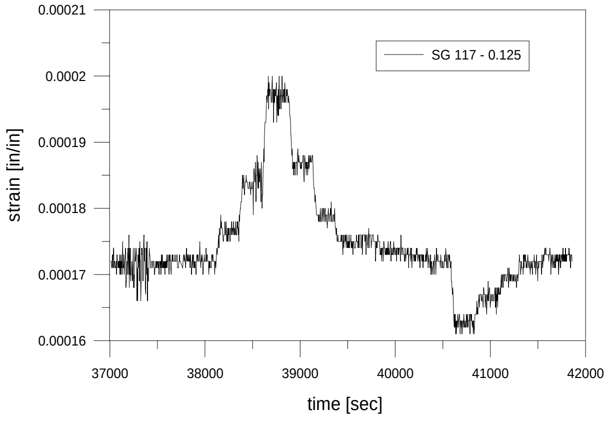
SG 117 - 0.125
strain [in/in]
time [sec]
0.00021
0.0002
0.00019
0.00018
0.00017
0.00016
37000
38000
39000
40000
41000
42000

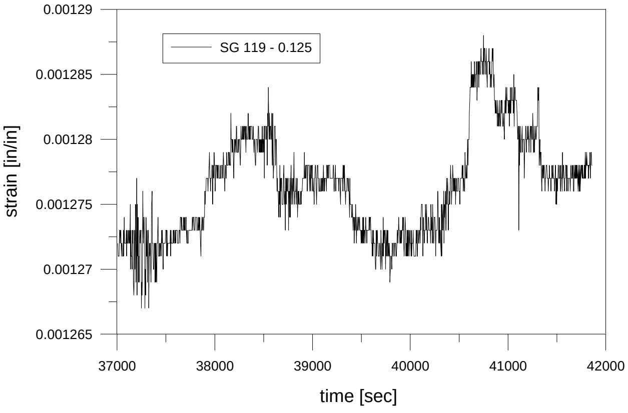
SG 119 - 0.125
strain [in/in]
time [sec]
0.00129
0.001285
0.00128
0.001275
0.00127
0.001265
37000
38000
39000
40000
41000
42000

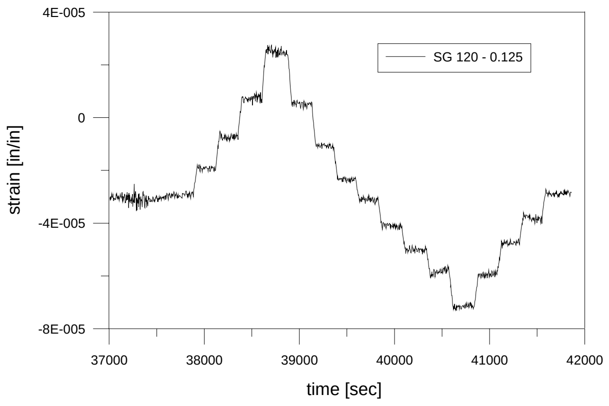
SG 120 - 0.125
strain [in/in]
time [sec]
4E-005
0
-4E-005
-8E-005
37000
38000
39000
40000
41000
42000

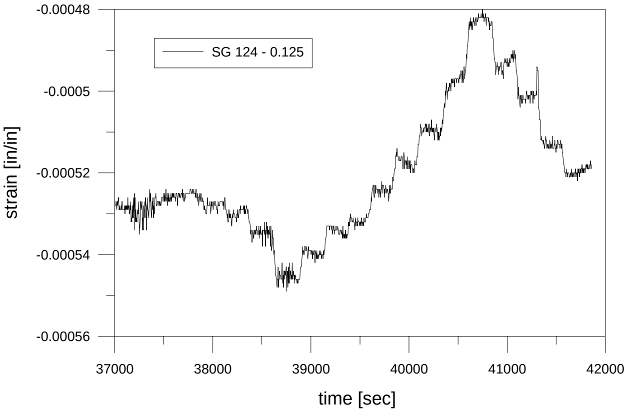
SG 124 - 0.125
strain [in/in]
time [sec]
-0.00048
-0.0005
-0.00052
-0.00054
-0.00056
37000
38000
39000
40000
41000
42000

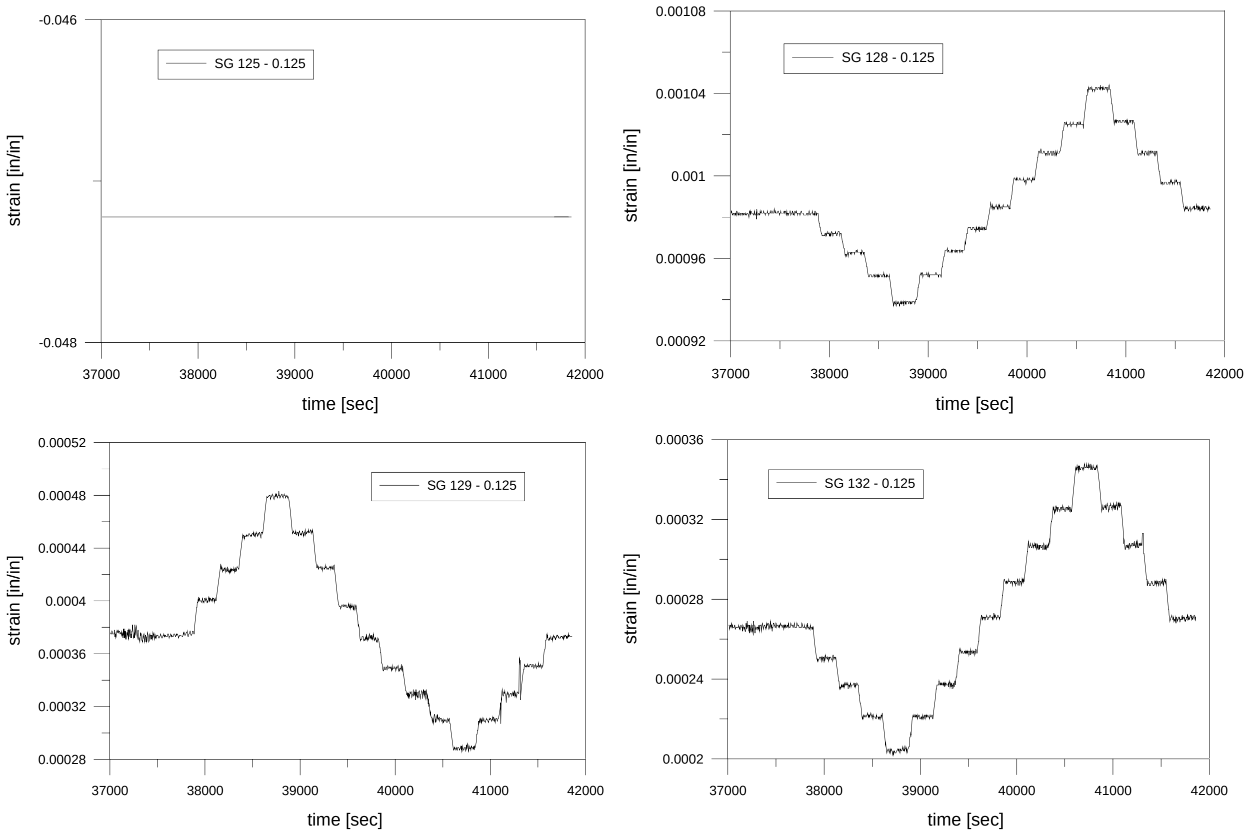

Figure 4.39(b) Pile 1 – 0.125 inch Cap displacement

(b) LVDT's

Several example LVDT sensor histories are depicted in Figure 4.40. Displacement readings are obtained for levels of 0.25 inch and higher; readings were within the noise range at lower applied displacements.

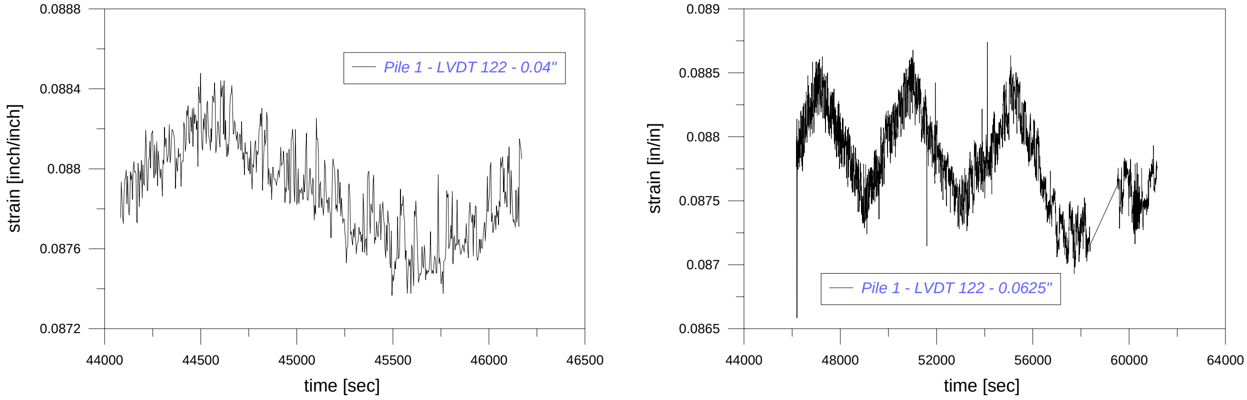

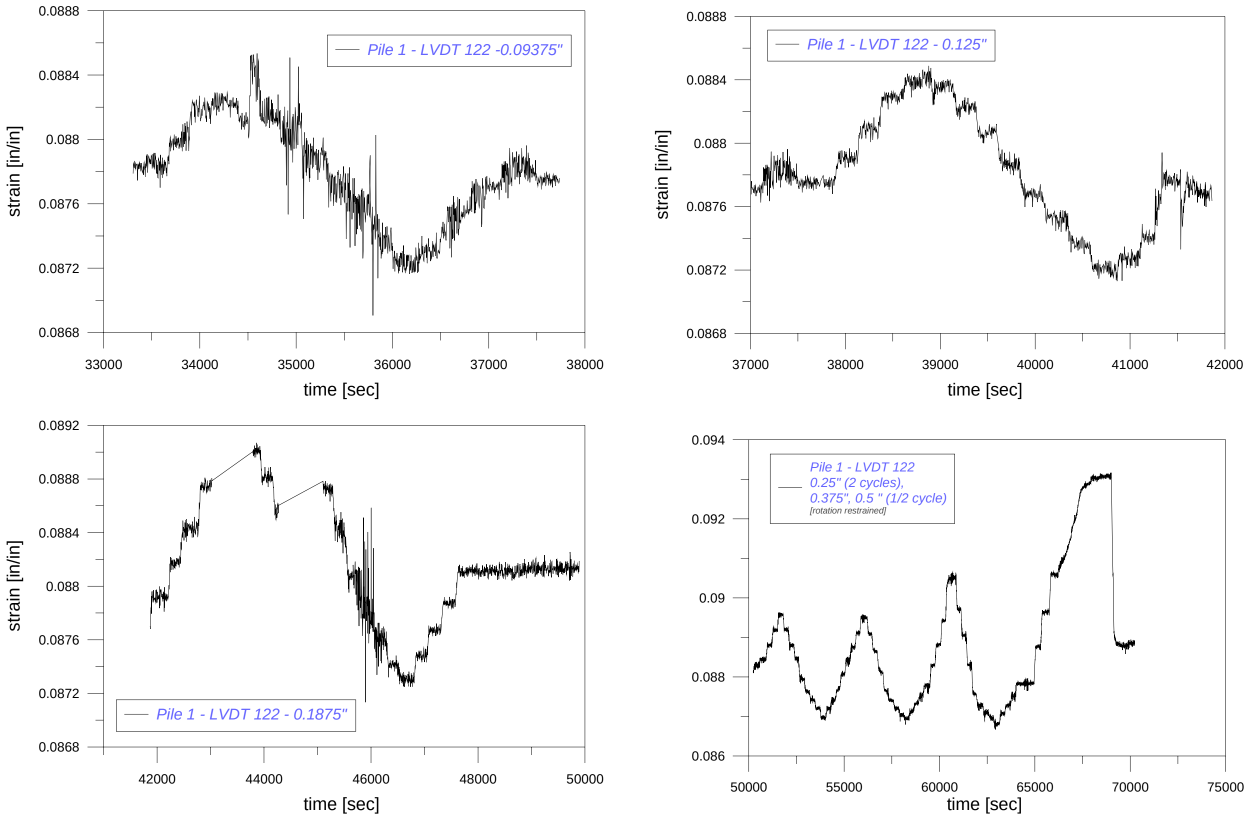

Figure 4.40. Increase of sensor accuracy with increasing cap displacement for LVDT 122, displacement levels 0.04 inch to 0.5 inch

However, after processing all LVDT data it appears that even if good readings were obtained for some displacement levels, generally the data were sufficiently inconsistent that reliable curvature profiles could not be obtained. Currently LVDT data are investigated with respect to data substitution and possible verification of strain gauge readings.

(c) Fiber Optic Sensors

Fiber Optic Sensor (FOS) data were recorded using a data acquisition setup independent of that for other sensors. Before processing FOS data, the data collected must be decoded and formatted to obtain compatible time histories. This process is currently in progress.

(d) Proposed data substitution

Since a large number of sensors were used within the pile from ground line to a depth of 10 ft below ground line, sensor redundancy can be used to provide the data needed to determine pile curvature. For example, in Figure 4.41, the curvature profile at a given depth is obtained by combining strain gauge, LVDT, and FOS data. Once the process of data substitution is complete, curvature profiles will be generated to enable the definition of p-y curves.

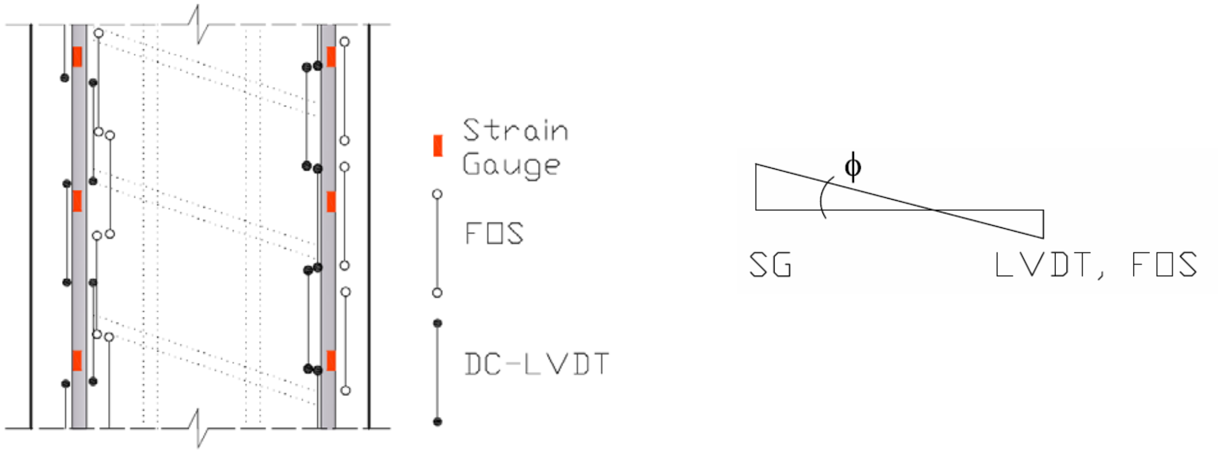

Figure 4.41. Redundancy of Sensors along the vertical rebar

The symmetry of the pile cross section also allows for data substitution for missing sensor readings using results from alternate sensors. For example, for the symmetrically placed strain gauges shown in Figure 4.42, if no reliable readings were obtained from SG 1, the missing data can be replaced using the readings of the opposite cycle for sensor SG 2.

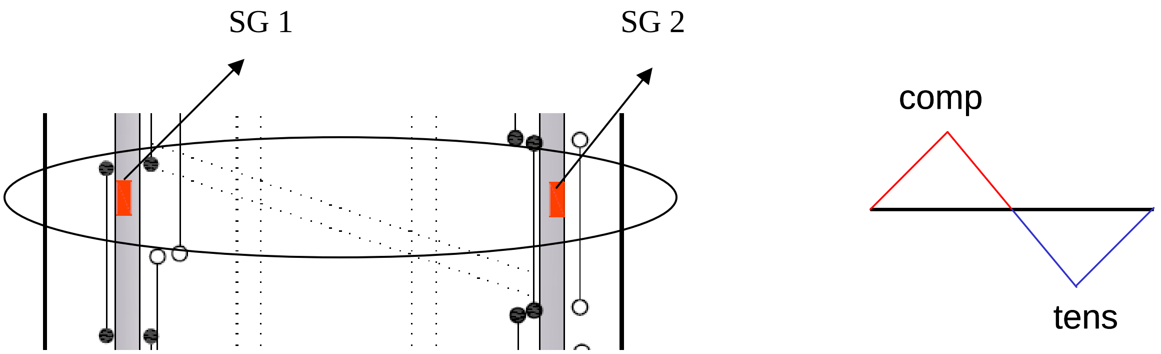

Figure 4.42. Proposed data substitution using geometric symmetry of sensors

5 DATA INTERPRETATION

5.1 Curvature and Moment Profile Fitting Techniques

A key element in procedures to extract *p-y* curves from experimental data is fitting a smooth curve through measured curvature and moment profiles. A well-behaved curve representing the depth variation of moment is necessary to obtain reliable soil reaction (*p*) profiles. This process is challenging due to the sensitivity of the double-differentiation process that generates *p*-profiles from moment profiles. This section describes four methods found in the literature for fitting curvature and moment data, two based on the weighted residuals method (Wilson, 1998 and Janoyan et al., 2001), one based on a combination of cubic B-spline fitting and weighted residuals (Coutinho, 2006), and one based on Fourier series fitting (Lin and Liao, 2006).

Wilson (1998) adapted the weighted residuals method, described by Cook et al. (1989), as one solution to the pile data fitting problem. This method treats known data points as nodes in a finite element model of the curvature or moment profile of the shaft. Between these nodes, an approximation function that describes the profile, with a residual error, is found. Generally, the approximation function is based on piecewise linear basis functions (See Figure 5.1), and so must be reapplied after the second differentiation to avoid singularities at the nodal points.

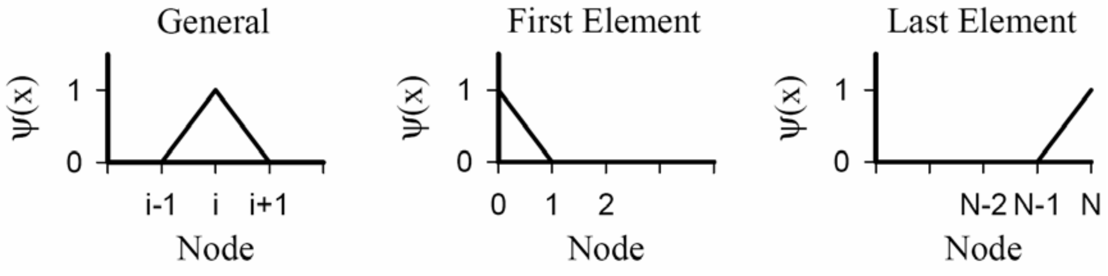

Figure 5.1. Basis functions for the finite element approximation of a shaft moment profile (Wilson, 1998).

Janoyan et al. (2001) extended the weighted residuals method for use with data containing inherent variability. In the data set used by Janoyan et al., multiple values of curvature, and thus moment, at various depths along the profile were obtained. To accommodate this data redundancy, all possible realizations of this profile were computed for the data. Weight was given to realizations that best fit the aggregate data in the sense that they match (within a specified margin of error) the ground-level shear and moment, and from these realizations a mean profile was obtained (See Figure 5.2). At 12 different depths in the shaft, three values of curvature (representing three types of sensor) were measured. This equated to over 500,000 possible curvature profiles. For practical purposes, only a limited number of possibilities were considered, but even with this scaled-down set of curves, the data analysis task was very computationally intensive.

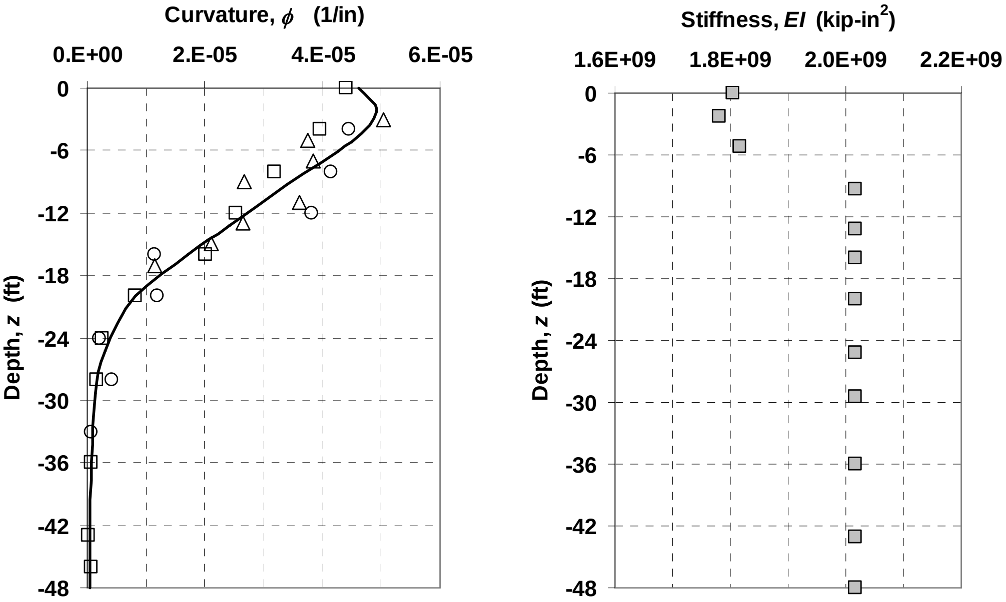

Figure 5.2. Curvature fit using weighted residuals and having inherent data variability, with shaft stiffness profile (Janoyan, et al., 2001).

Coutinho (2006) approached the problem by integrating a piecewise B-spline curvature fit to obtain a deflection profile (for more information on B-splines, see Section 5.2.2), and solved a Volterra integral for an assumed functional form for the soil reaction profile. The Volterra integral to be solved, as shown in Coutinho (2006), has the form

$$H(e+z)-M(z)=\int_0^z p(\xi)(z-\xi)d\xi \tag{5.1}$$

where *H* is the applied force on the pile, *e* is the height of the applied force, *M(z)* is the moment at depth *z*, and *p(ξ)* is the soil reaction per unit length at depth *ξ* as shown in Figure 5.3. This integral equation can be solved "weakly" by the use of a series expansion. An example of the fitting process is shown in Figure 5.4.

Because the spline fitting process employs a least-squares regression to minimize residuals, the data points for the profile can be minimized using a single cumulative residual. The nodal points and spline polynomial order were determined through trial and error.

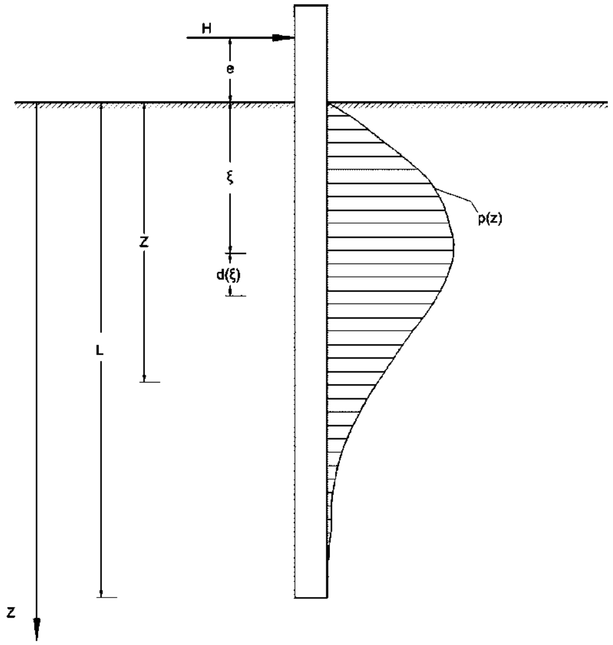

Figure 5.3. Relationship between applied force and soil reactions (Coutinho, 2006).

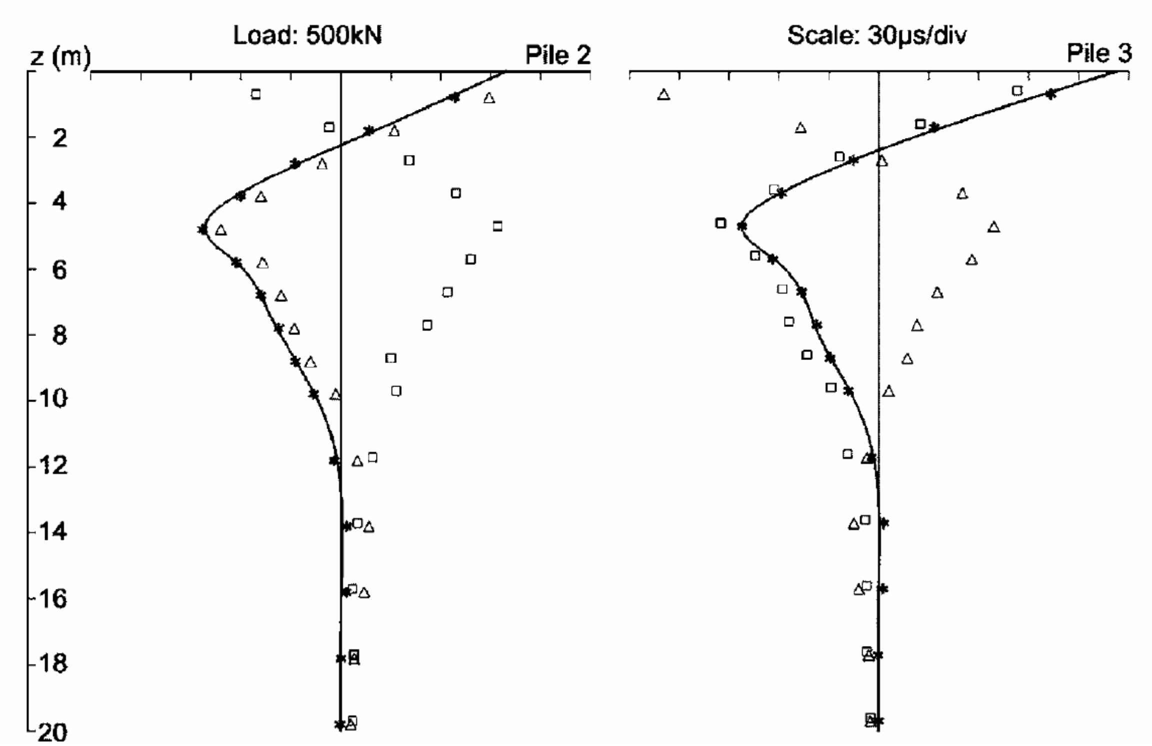

Figure 5.4. B-splines fitted to curvature strains for two capped piles (Coutinho, 2006)

In 2006, Lin and Liao approached the data fitting problem with the use of a Fourier series. Lin and Liao used inclinometer data to experimentally determine the displacement profile of the shaft. Each displacement data point was then combined with a cosine term to arrive at a Fourier series with a number of terms equal to the number of data points. However, differentiation of this series can lead to ill-conditioned functions for moment, shear and soil reaction. This problem is circumvented by using a Cesaro sum technique to choose term(s) in the Fourier series that will guarantee convergence. An example of the differentiation results from their paper is shown in Figure 5.5. This technique appears promising for processing the test data from the present study, but was discovered too late in the analysis process to be considered among the other techniques mentioned. However, it is recommended in Chapter 6 that this procedure be investigated with respect to the data generated from the tests described in Chapters 3 and 4.

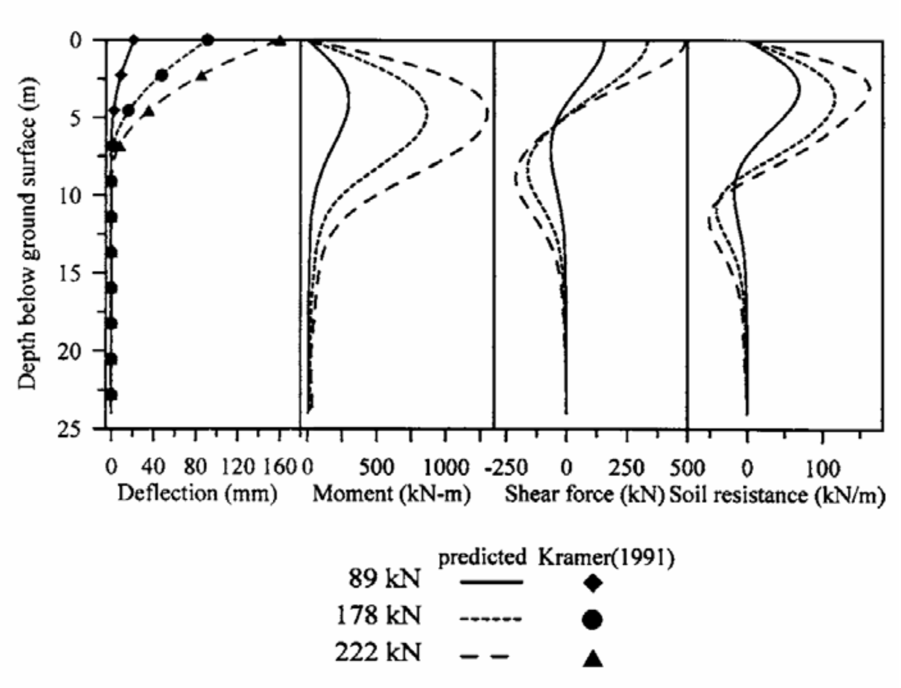

Figure 5.5. Deflected pile shape compared with Kramer (1991) data; moment, shear and soil reaction plots (Lin and Liao, 2006).

5.2 Piece-Wise Polynomial LS Fit with Boundary Conditions

5.2.1 Methodology

In order to find a more computationally efficient and less mathematically complex method of processing curvature data, a procedure employing piecewise polynomial data fitting was developed. This method uses curvature data, as well as known boundary conditions above ground and at the tip of the shaft, to formulate a least-squares fit for the curvature and moment profiles. A piecewise polynomial with two sections was initially investigated as described in the following sections. This method has advantages over those described in Section 5.1 because it accounts for data scatter, is less computationally intensive than the multiple fits required by Janoyan, et al. (2001) and the solution of an integral equation required by Coutinho (2006).

5.2.2 Piecewise Polynomial Fitting Using B-Splines

Representing a piecewise polynomial function as a linear combination of basis or *B*-splines provides an efficient framework for analyzing spline fits through curvature data. As described in Lowther and Shene (2003), to generate a composite spline from a set of B-splines, a knot sequence [u_0, u_1, … u_m], which must be in non-decreasing order, and spline degree (p), must be specified. The component B-splines ($N_{i,p}$) are generated recursively starting with the i-th degree zero B-spline:

$$N_{i,0}(u) = \begin{cases} 1 & \text{if } u \in [u_i, u_{i+1}) \\ 0 & \text{otherwise} \end{cases}. \tag{5.2}$$

The i-th B-spline of degree p is then:

$$N_{i,p}(u) = \frac{u - u_i}{u_{i+p} - u_i} N_{i,p-1}(u) + \frac{u_{i+p+1} - u}{u_{i+p+1} - u_{i+1}} N_{i+1,p-1}(u)\,. \tag{5.3}$$

The composite spline is then defined as:

$$C(u) = \sum_{i=0}^{n} N_{i,p}(u) P_i\,, \tag{5.4}$$

where m+1 is the number of knots, $n = m+p+1$, and P_i are the B-spline coefficients.

The coefficients P_i are determined by solving a system of equations generated from least-squares criteria, as described in Coutinho (2006). The system equations are given by:

$$\frac{\partial}{\partial P_i} \sum_{j=1}^{q} \left[C(u_j) - \phi(u_j) \right]^2 w(u_j) = 0, \text{ for } i = 0..n\,, \tag{5.5}$$

where q is the number of curvature data points, $\phi(u_j)$ is the curvature data point at depth u_j, and $w(u_j)$ is the weight assigned to the data point at u_j.

5.2.3 Application to Virtual Data Set with Added Noise and Sparseness

In order to gauge the performance of the piece-wise polynomial method, a virtual data set was created by modeling a shaft-soil system with defined p-y curves. The system was displaced and calculated curvature values at various depths were tabulated to form "virtual" curvature profiles. The robustness of the regression method was gauged by its ability to reproduce known p-y curves from this virtual data set. In order to assess the effect of data variability and sparseness on the method, artificial random noise and data point exclusion were applied to the virtual data. Randomness was added to the virtual data by multiplying the data values by random scatter with a coefficient of variation of 10%. Sparseness was added by removing 9 out of every ten data points. The results of this study are presented in

Figure 5.6 and indicate that the method could reliably generate p-y curves from sparse and scattered, though well defined, data sets.

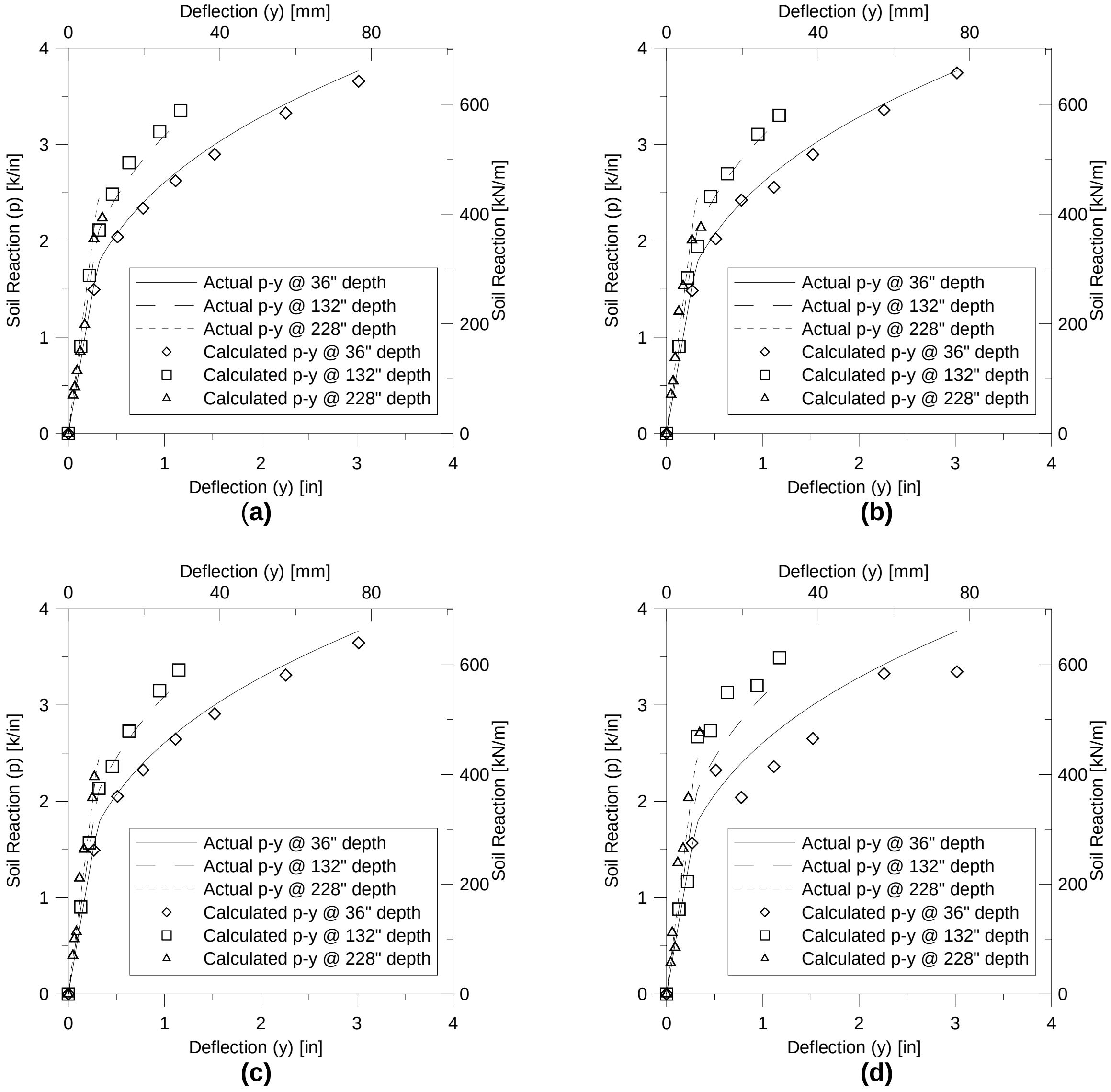

(a) **(b)**

(c) **(d)**

Figure 5.6. Actual and generated p-y curves using virtual data set for (a) no scatter, 100% of data; (b) no scatter, 10% of data; (c) COV = 5%, 100% of data; (d) COV = 5%, 10% of data

The results presented in

Figure 5.6 provide us with confidence that the general method of generating p-y curves described in Section 5.2.1 can provide reasonable estimates of p-y curves. Additional details regarding the implementation of this approach to the data from the present experimental program are given in the following sections.

5.3 Analysis of Curvature Data from 2ft Diameter Tests

Results in this section are based on analysis of data from the 2ft fixed-head test, but apply equally to the 2ft flagpole data set.

5.3.1 MATLAB B-Spline Implementation

Data fitting using B-spline formulations and least-squares approximation has been implemented in the MATLAB 6.5 Spline Toolbox. The robust spline structure and function suite programmed in the Spline Toolbox allows very efficient generation and manipulation of B-splines, as well as seamless operations, such as addition, multiplication, differentiation, and integration, to be performed on splines.

To construct a B-spline composite function using least-squares criteria, the Spline Toolbox function `spap2` is invoked, with the form:

```
spline1 = spap2(knots,order,x,y,w)
```

where `spline1` is the constructed spline in B form, `knots` is an array of knot locations, `order` is the polynomial order, `x` is an array of the data locations, `y` is an array of the data values, and `w` is an array of the weights at the data sites.

Other Spline Toolbox functions used in the curvature analysis were `fnder`, which computes the derivative of a composite spline over its defined domain, `fnint`, which computes the indefinite integral of a composite spline over its defined domain without an integration constant, and `fnplt`, which shows a graphical representation of the spline.

5.3.2 Curvature Fitting Procedure

The first step in the curvature fitting procedure for a specific shaft head displacement is to analyze the curvature data along the shaft profile. Any data points that are determined to be erroneous due to sensor malfunction or failure are given a weight of zero, which excludes them from the analysis. Typically, the point at which a sensor becomes unreliable can be readily determined by observing the response history of that sensor, as described in Chapter 4. Each curvature value in the data set, however, is typically a product of two sensor readings, which means that if one sensor in the pair fails, the curvature data based on that pair may be useless. Figure 4.6 shows the response history of a sensor that failed before testing was completed.

Once the data points deemed unreliable have been excluded, the remaining data points are each given an equal weight of 1. Since there were no obvious indications that one type of sensor systematically outperformed others, curvature data points were not weighted differently based on instrumentation type.

For the curvature data fitting, a boundary condition of zero curvature and zero change in curvature at the bottom tip of the shaft was enforced. This boundary condition was based on the observation, as shown in Figure 4.11 and Figure 4.22, that the strains measured by fiber-optic sensors and rotations measured by inclinometers did not change significantly from the pile head at its null position to the pile head at its maximum displacement. To enforce the boundary condition at the shaft tip, artificial data points at -300 inches to -304 inches, each with a curvature value of zero and a weight of 1000, were added the curvature data. This ensured that the curvature spline approximation would have a smooth transition to zero curvature at the bottom of the shaft. The curvature fit for the 0.375 inch displacement level during the fixed-head test is shown in Figure 5.7. Results for all displacement levels are shown in Figure 5.15.

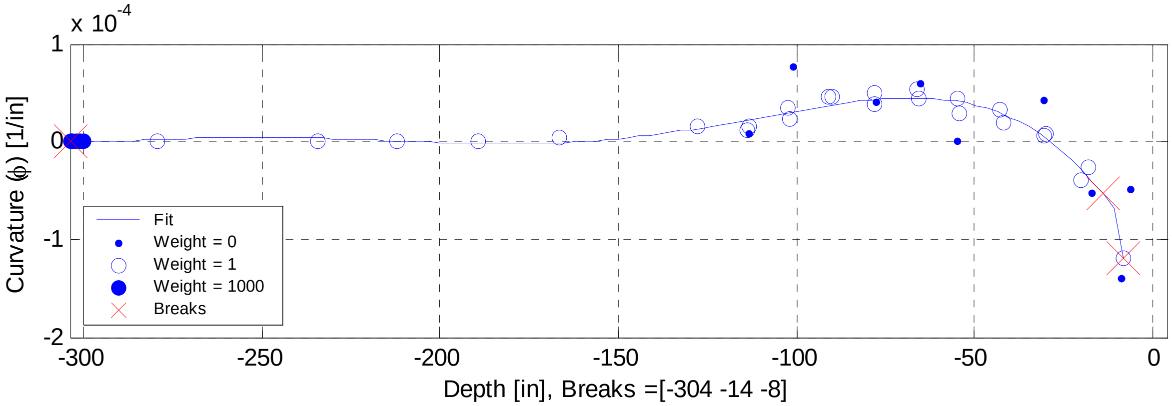

Figure 5.7. Polynomial fit through 0.375” head displacement level curvature data

The spline fit of the curvature data is sensitive to the location and number of knots, and the polynomial degree chosen for the regression. Regressions with high-degree polynomials having more than one interior knot tended to locally oscillate around the curvature points, while low-degree polynomials tended to degrade unacceptably when differentiated. Typically splines of degree 5 to 7, with one interior knot, achieved a balance between desired smoothing and acceptable differentiation performance. (A more detailed discussion of the differentiation process is presented in Section 5.4.) For the regressions shown, a polynomial degree 7 was used.

In order to choose the optimum location of the interior knot, splines were evaluated with different interior knot locations spaced at one inch intervals. At each interior knot location a least-squares composite error term was calculated from profiles of fit residuals. After evaluating the composite error term for multiple locations, the knot was set at the location with the smallest error value. An example of the composite error distribution as a function of interior knot location can be found in Figure 5.8.

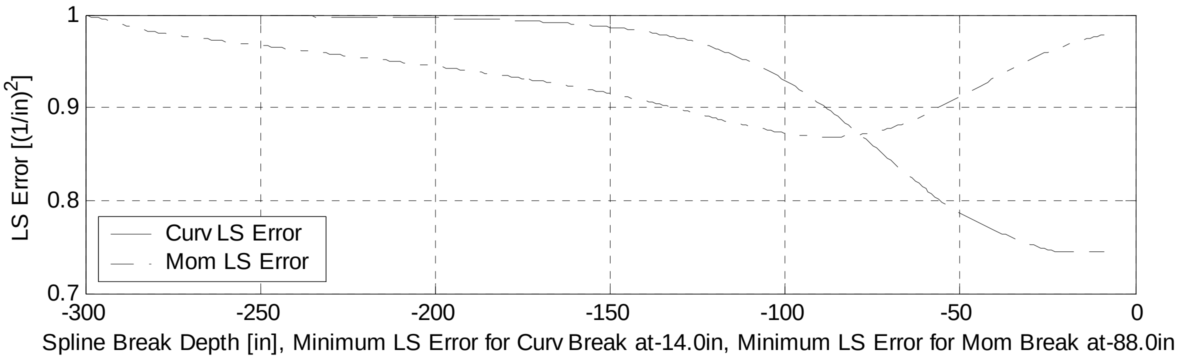

Figure 5.8. Curvature and moment least-squares errors as a function of interior knot depth at the 0.375 inch head displacement level

5.3.3 Moment Fitting Process

In addition to the fitted curvature profiles, moment profiles must be fitted in order to achieve well-behaved soil reaction profiles from the differentiation process. Curvature data points can be translated into moment data by the use of a moment-curvature relationship. Depending on the specimen configuration, the moment-curvature relationship can either be determined experimentally or analytically. As explained in Sections 4.1.4 and 4.2.4, an experimental moment-curvature relationship is readily available for the 2ft flagpole test, whereas an experimentally calibrated analytical relationship was used for the 2ft fixed-head test.

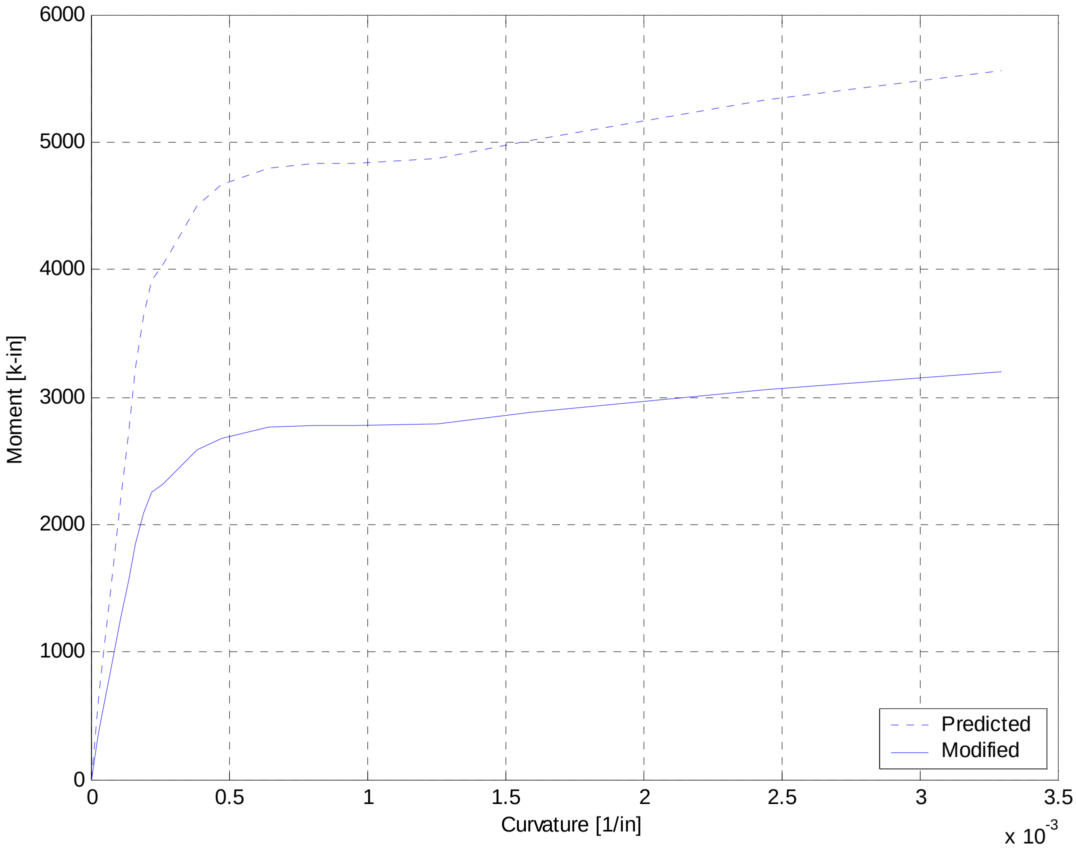

Figure 5.9. Predicted and modified moment-curvature relationships

The moment-curvature relationship used in the analysis of the 2ft fixed-head test data, as well as the predicted relationship, is shown in Figure 5.9 (See Rha, et al., 2005, for details on the predicted capacity). Because the ultimate moment capacity of the shaft was significantly less than predicted, the predicted relationship was scaled by the measured ultimate moment capacity of the shaft. This modified relationship allowed the moment fit to better match measured boundary conditions at the ground surface. A possible cause of the decreased moment capacity is the influence of shear, as discussed in Section 5.6.

Once curvature data are transformed into moment data using the moment-curvature relationship, the data are fit using a similar procedure to the one described in Section 5.3.3. Boundary conditions at the bottom tip of the shaft are identical, but additional artificial points are added at the top of the shaft to enforce measured moments and shears at the ground line. The moment and shear at the ground surface can be calculated using the measured forces and geometry of the actuators at the surface. Free-body diagrams of the flagpole and fixed-head systems are shown in Figure 5.10. Artificial data points are added at elevations of 0 inches and +1 inches (i.e., one inch above the ground surface). The value of the moment point at 0 inches is equal to the measured ground surface moment, while the value of the point at +1 inches is the measured ground surface shear multiplied by the distance between the two points, and added to the ground surface moment. Each point is given a weight of 1000, which ensures that the moment and shear profiles will match the measured surface values. The moment fit for the 0.375 inch displacement level during the fixed-head test is shown in Figure 5.11. (Results for all displacement levels are shown in Figure 5.17.)

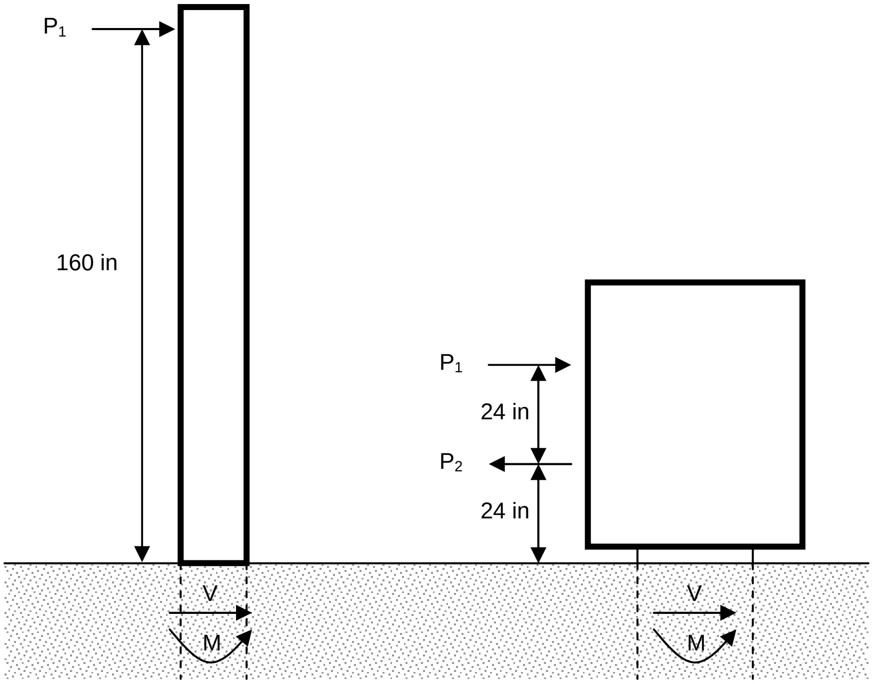

Figure 5.10. Free-body diagram of the flagpole and fixed-head specimens above ground.

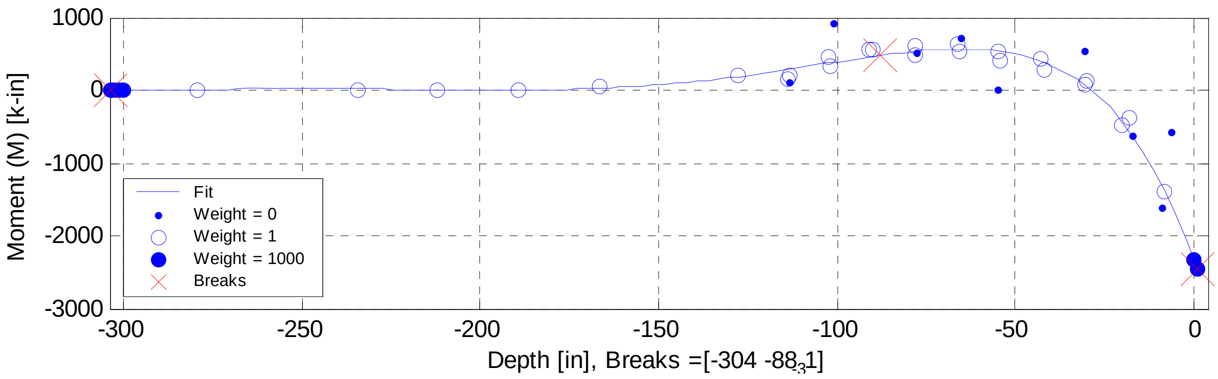

Figure 5.11. Polynomial fit through 0.375" head displacement level moment data

5.4 Generated Deflection and Soil Reaction Profiles

The standard approach to obtaining soil reaction (*p*) and deflection (*y*) profiles is to doubly differentiate the moment profile and doubly integrate the curvature profile. This process is schematically shown in Figure 5.12. When integrating from curvature to rotation, zero rotation at the bottom tip of the shaft is used as the integration constant. When integrating from rotation to deflection, zero deflection at the bottom tip of the shaft is used as the integration constant. The shear profile, which is generated by differentiating the moment profile, should provide the correct value of shear at the ground surface since this boundary condition was included in the fitting procedure for the moment profile. Results from the analysis are shown in Figure 5.15.

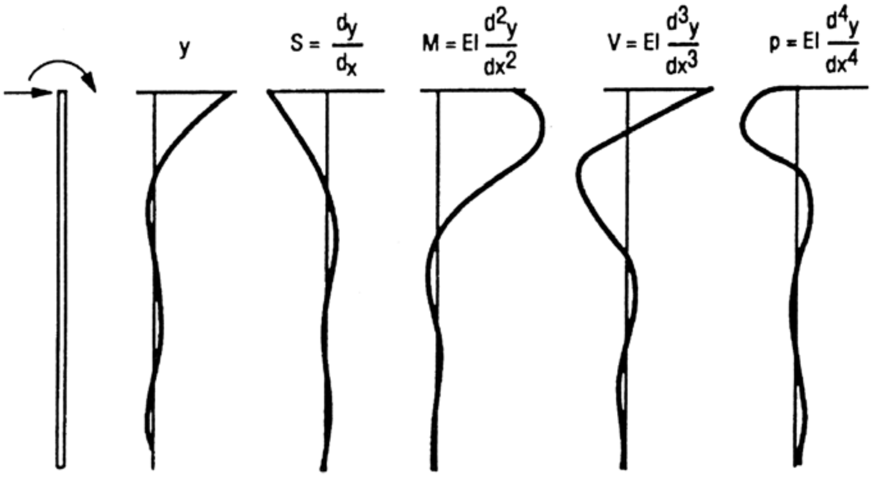

Figure 5.12. Schematic of p and y profile generation procedure (Reese and Van Impe, 2001)

The deflection and soil reaction profiles generated for the flagpole and fixed-head tests seem to match the data well. Especially noteworthy is the excellent agreement of the fitted rotation profiles with rotation measurements from inclinometers. For the flagpole test the rotation profiles follow the inclinometer data well at every displacement level. The rotation measurements for the fixed-head test tend to depart from the fitted profiles at depths above -50 inches (See Figures 5.15-5.21). This is possibly due to the influence of shear deformations in the fixed-head test as described in Section 5.6. The influence of shear deformations also likely explains smaller than measured deflections at the ground surface. The fact that the rotation measurements better match the rotation profiles in the flagpole test, where significantly less shear demand was observed, reinforces this point.

It is important to note the poor match between measured moment boundary conditions and moment data for the 0.0625 inch displacement level during the fixed-head test, shown in Figure 5.13. This is most likely due to the simple scaling used to modify the moment-curvature relationship as described in Section 5.3.4.

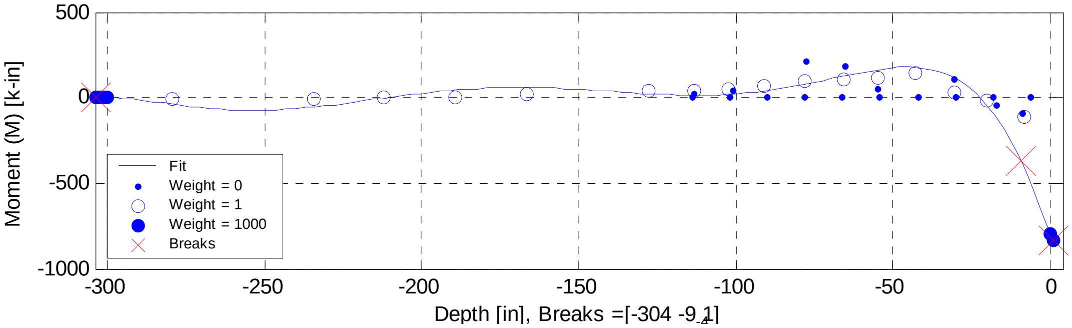

Figure 5.13. Polynomial fit through 0.0625” head displacement level moment data

5.5 Assembly of P-Y Curves

Once *p* and *y* profiles have been obtained, *p-y* relationships can be readily assembled at various depths along the shaft. *P-y* curves at depth will not be defined over as large a displacement range as *p-y* curves at the surface due to the small displacements of the shaft at depth.

A *p-y* curve for a given soil depth is assembled by evaluating the deflection and soil reaction at that depth for various head displacement levels. Each deflection and soil reaction ordinate at the given depth forms a point on the *p-y* curve. When repeated over a range of depths, this process gives a suite of *p-y* curves for the specific soil and shaft conditions.

5.5.1 P-y Curves from Fixed-head Test

Figure 5.14a shows generated fixed-head backbone *p-y* curves to a depth of -120 inches. Also shown on the graph, for reference, are curves for two depths as predicted by the modified API curves described in Section 2.2. The experimental curves in Figure 5.14a are generated using data from the peak of the first-cycle at the corresponding displacement level (using only data for head displacement levels ≤ 1.5 inches). Figure 5.14b shows *p-y* curves generated from intermediate points (i.e., within-cycle displacements less than the peak) during the first cycle of the 1.5 inch displacement level, along with the same API reference curves shown in Figure 5.14a.

One obvious characteristic of the *p-y* curves presented is the counter-intuitive observation that the stiffness of the *p-y* curves decreases with depth. However, these curves do not take into consideration deformations in the shaft due to shear. Shear deformations were significant to a depth of about -50 inches, which means that the inclusion of shear effects will reduce the stiffness of shallow curves, while having little effect on deeper curves.

Also of note is the difference between the backbone and intra-cycle p-y curves shown in Figure 5.14. The intra-cycle *p-y* curves are, as expected, less stiff than the backbone curves. This is due to the closing of soil gaps formed by previous cycles at lower displacement levels. Also, as expected, the intra-cycle curves approach the backbone curves at displacements larger than at previous displacement levels. This is due to the soil being deformed at those displacements for the first time.

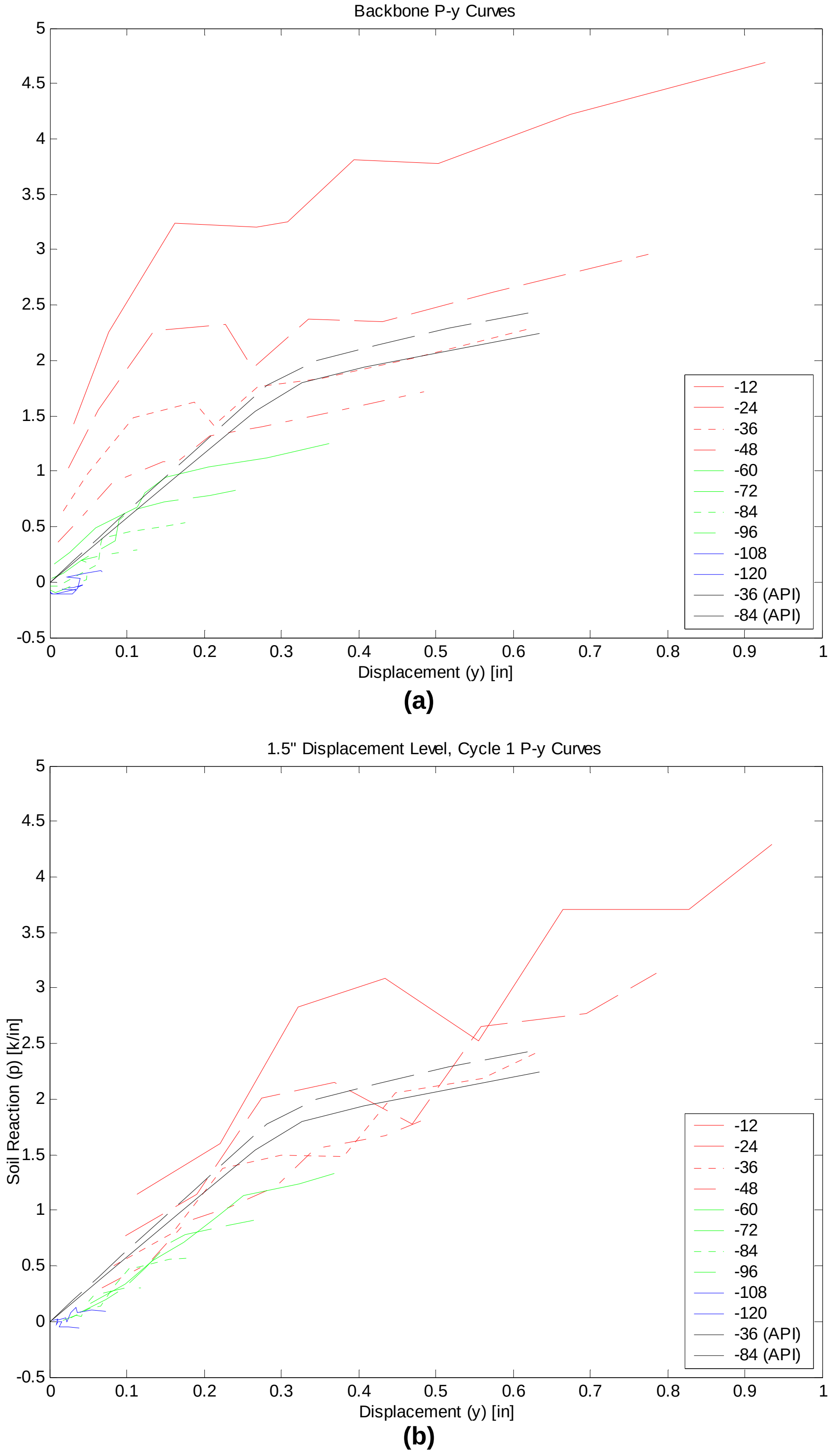

(a)

(b)

Figure 5.14. Fixed-head (a) backbone p-y curves and (b) intra-cycle p-y curves

Referring back to the backbone p-y curves in Figure 5.14a, a working hypothesis for the apparent softening of the deep curves at large displacements is that following yielding of the shaft (which occurs at relatively shallow depth), the moment and shear at the plastic hinge is essentially fixed for all subsequent displacement levels. Hence, the lower part of the shaft is simply cycled back and forth with a constant applied shear load and moment. Much of these displacements may well occur within gaps opened during previous cycles. Moreover, the repeated cycling may produce a cyclic degradation effect. The combined effects of gapping, cyclic soil degradation, and shear deformations likely are responsible for the flattening of the p-y curves at these large depths. These phenomena should be investigated further in subsequent research.

The fitting, integration and differentiation process for the 2ft fixed-head data set are summarized in Figure 5.15.

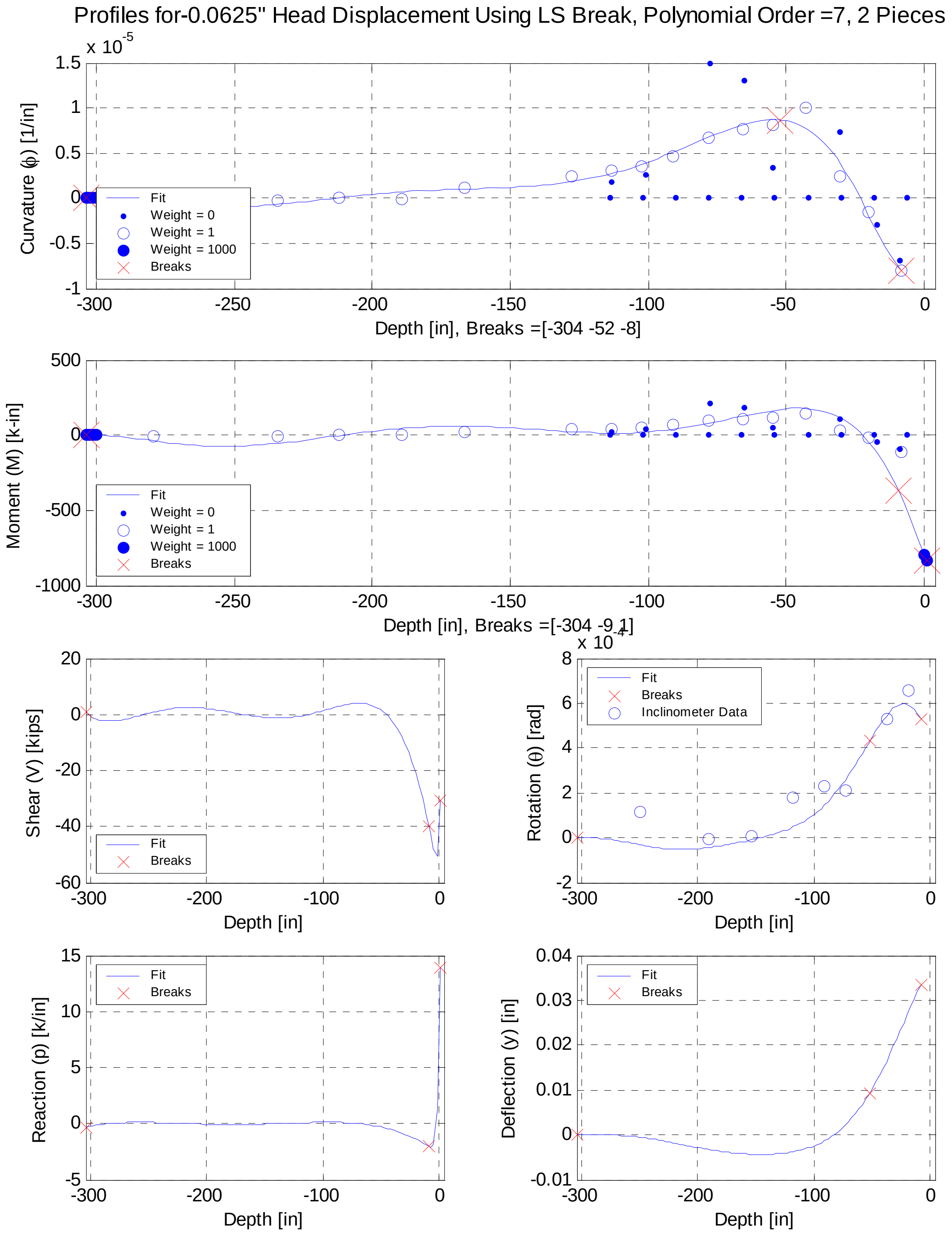

Figure 5.15. Curvature and moment B-spline fits; differentiation and integration of fits to soil reaction (*p*) and shaft deflection (*y*).

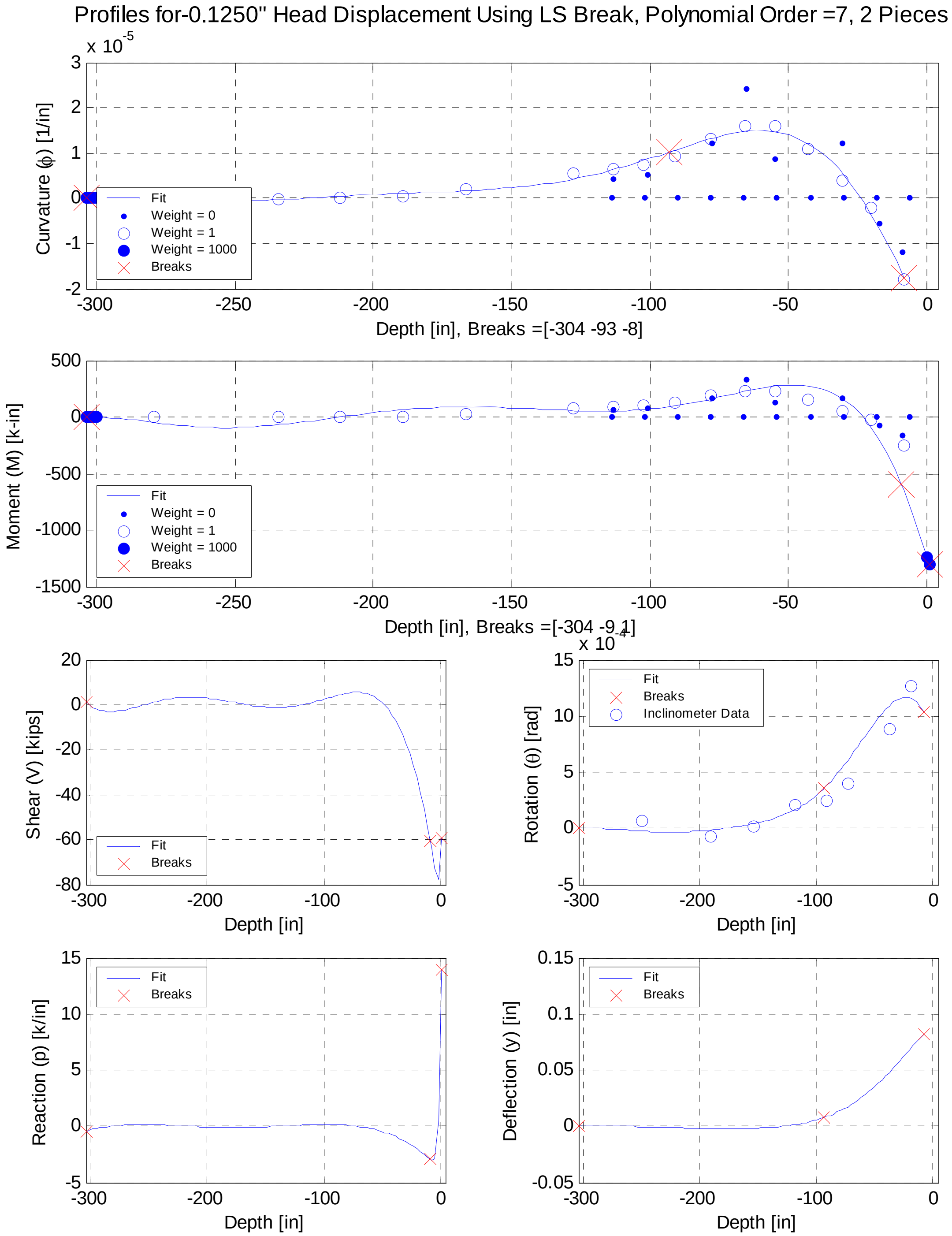

Figure 5.15 (continued). Curvature and moment B-spline fits; differentiation and integration of fits to soil reaction (*p*) and shaft deflection (*y*).

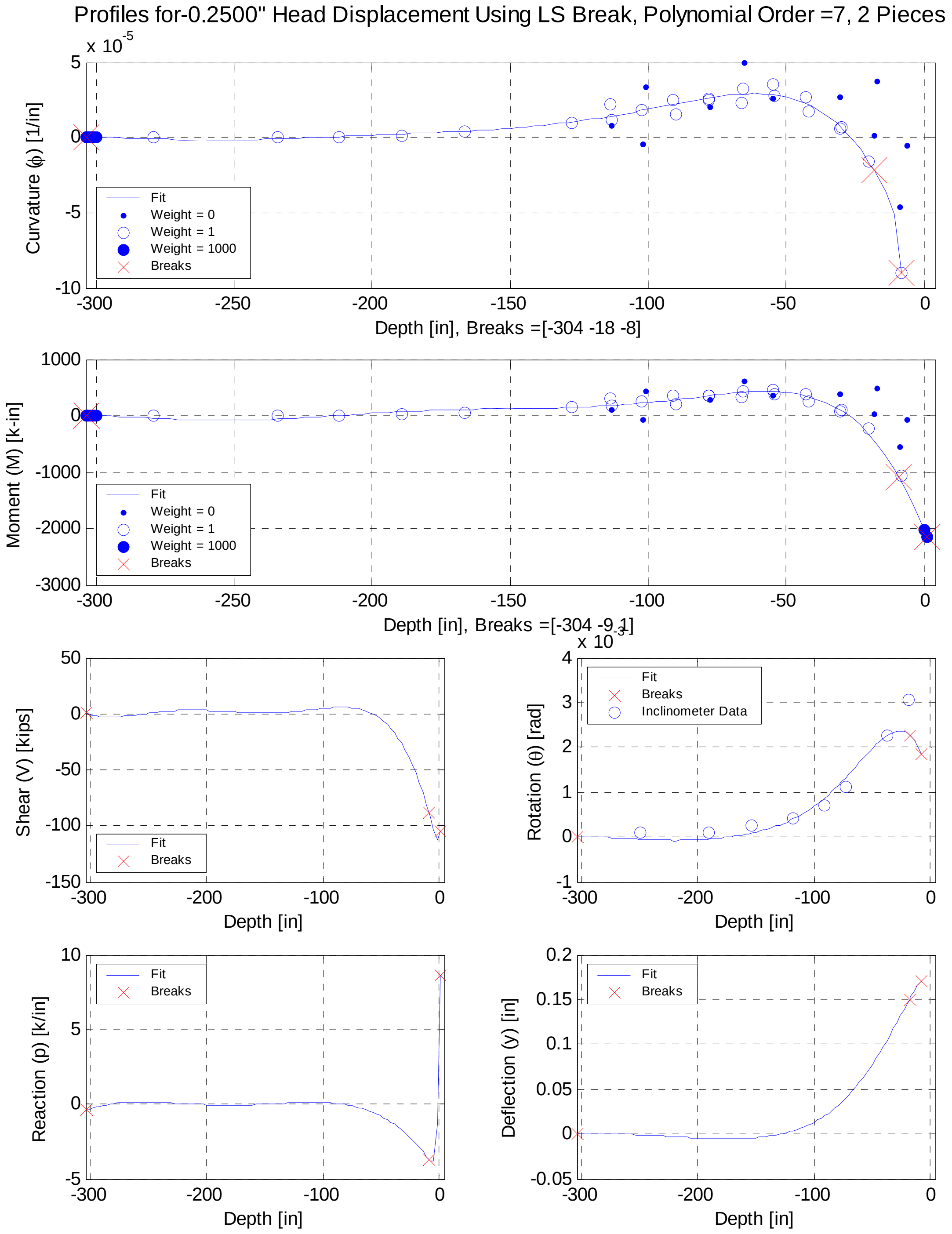

Figure 5.15 (continued). Curvature and moment B-spline fits; differentiation and integration of fits to soil reaction (*p*) and shaft deflection (*y*).

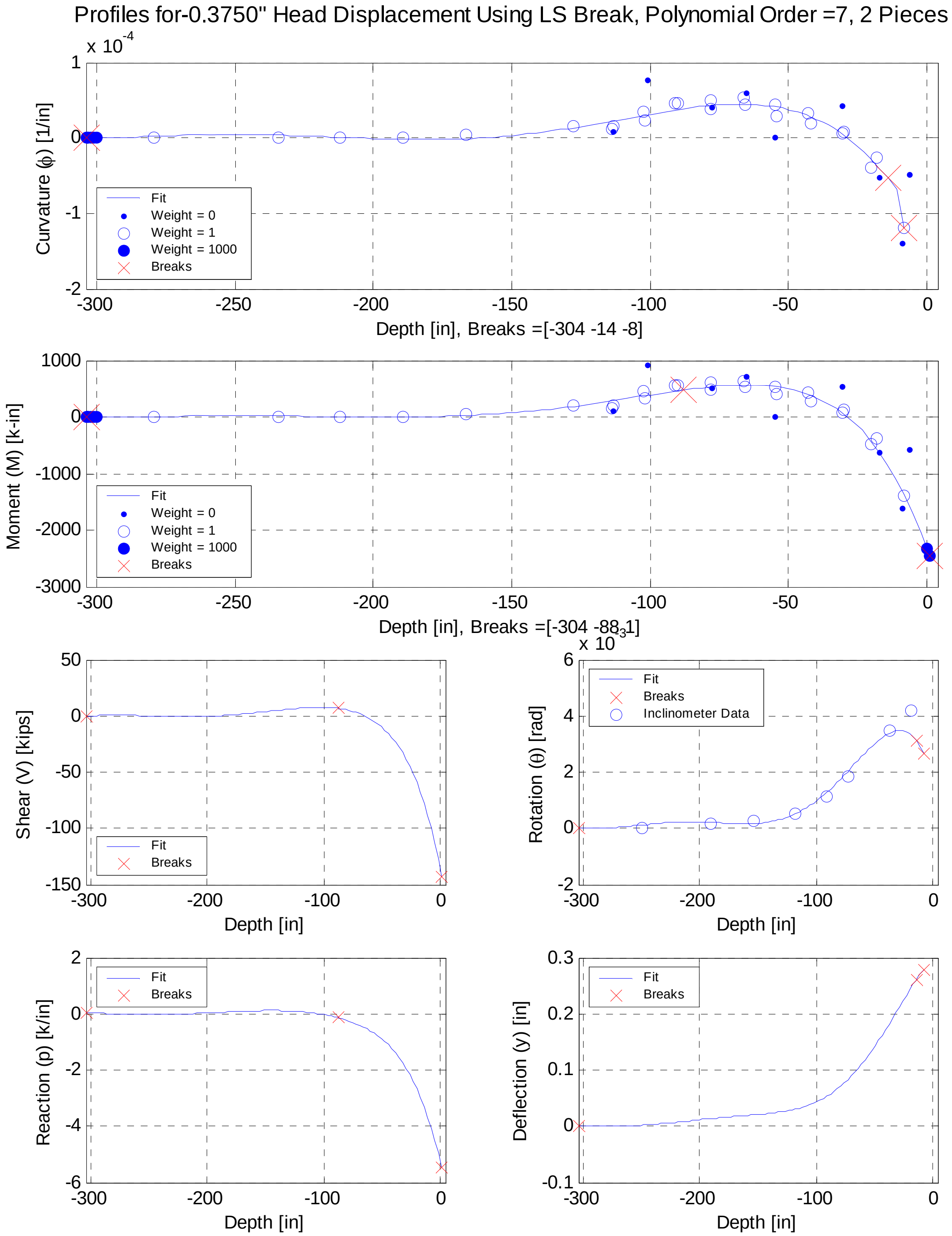

Figure 5.15 (continued). Curvature and moment B-spline fits; differentiation and integration of fits to soil reaction (*p*) and shaft deflection (*y*).

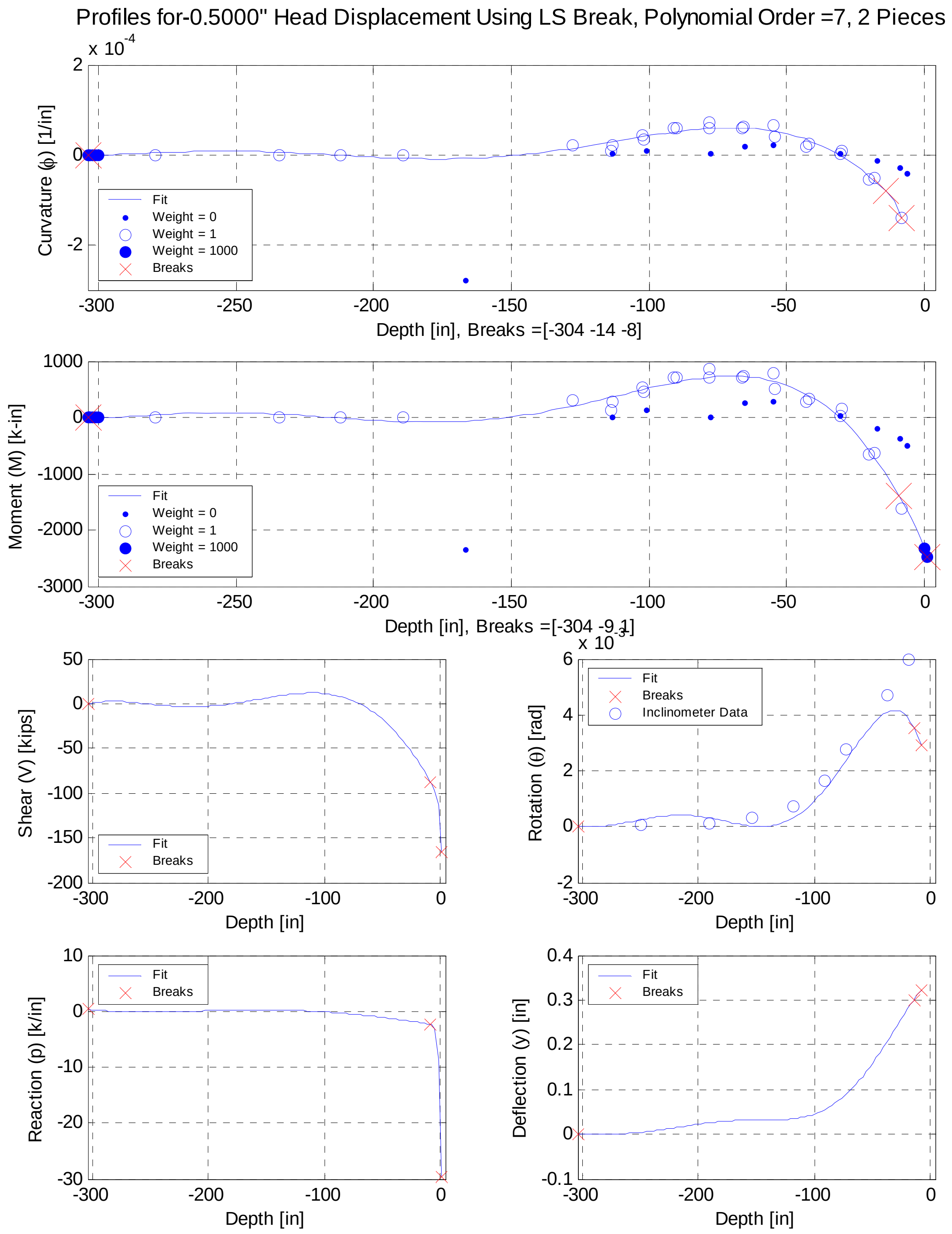

Figure 5.15 (continued). Curvature and moment B-spline fits; differentiation and integration of fits to soil reaction (*p*) and shaft deflection (*y*).

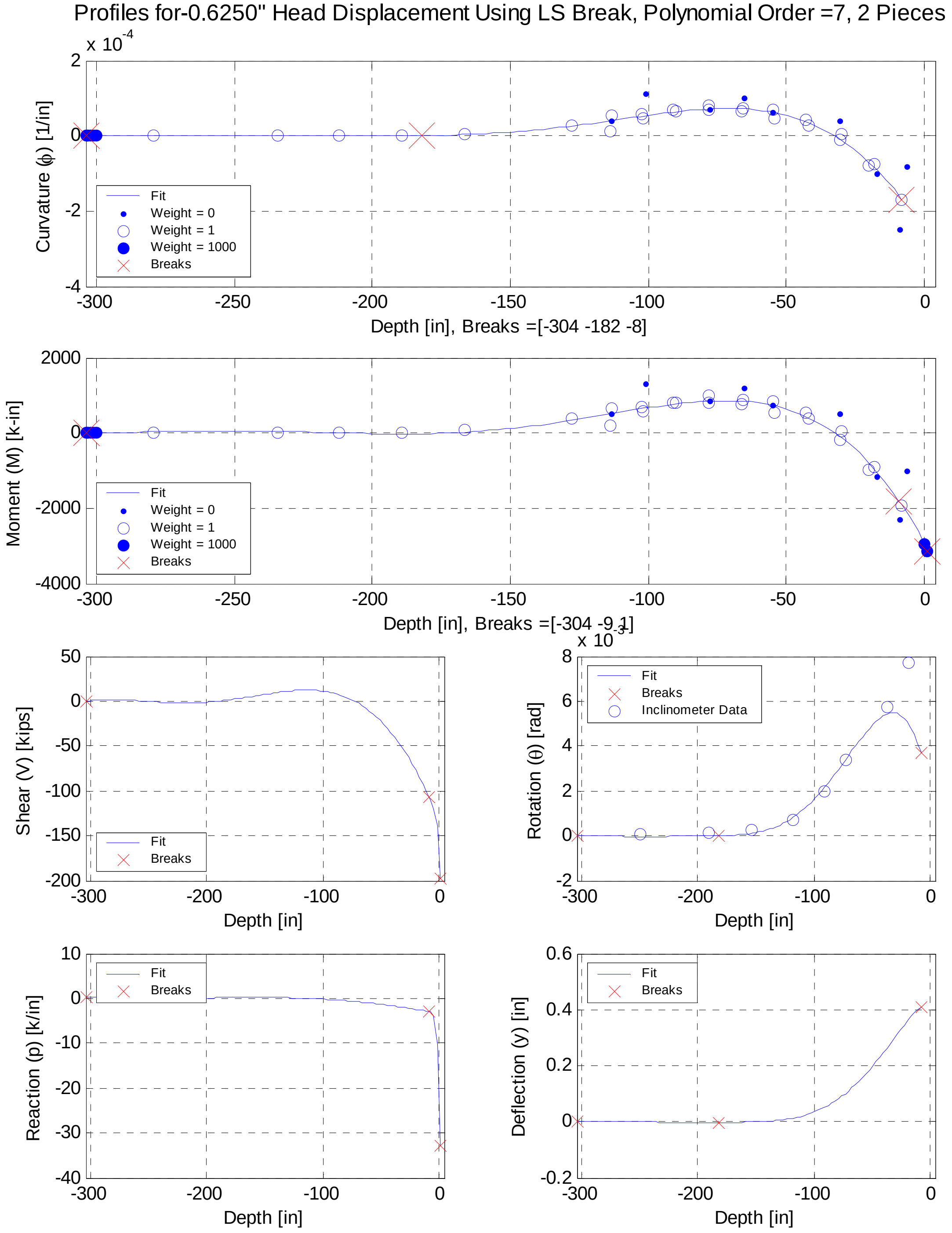

Figure 5.15. (continued). Curvature and moment B-spline fits; differentiation and integration of fits to soil reaction (*p*) and shaft deflection (*y*).

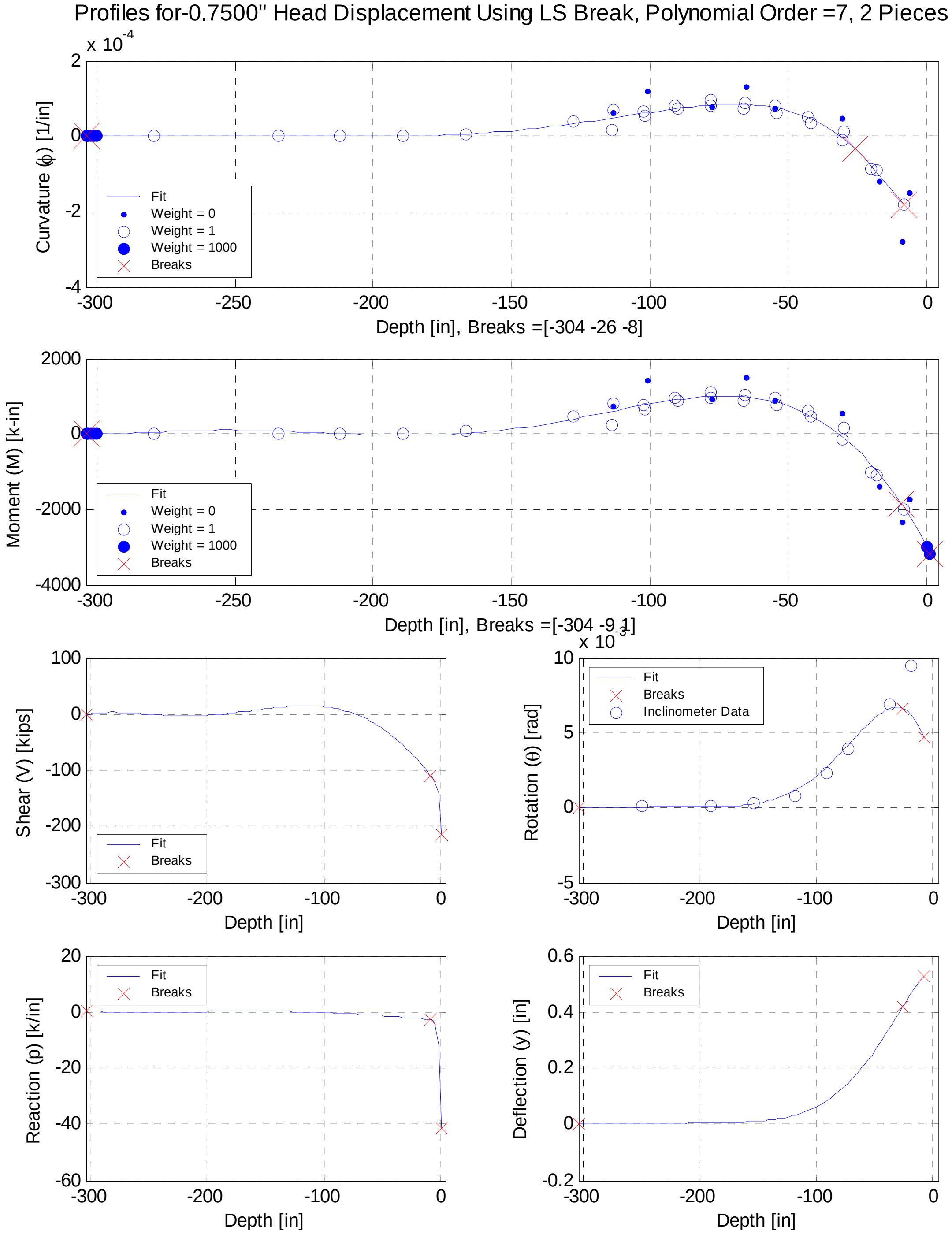

Figure 5.15 (continued). Curvature and moment B-spline fits; differentiation and integration of fits to soil reaction (*p*) and shaft deflection (*y*).

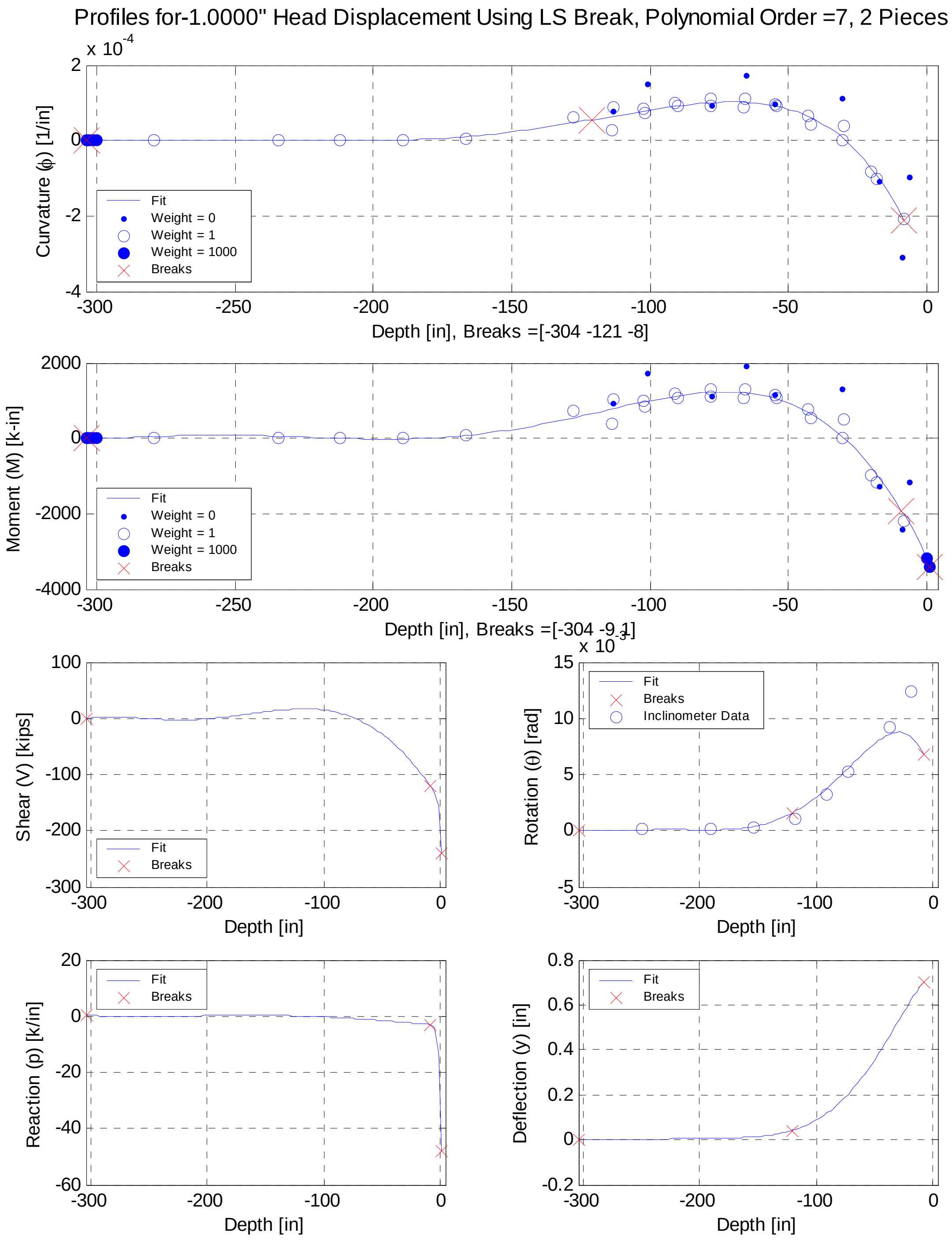

Figure 5.15 (continued). Curvature and moment B-spline fits; differentiation and integration of fits to soil reaction (*p*) and shaft deflection (*y*).

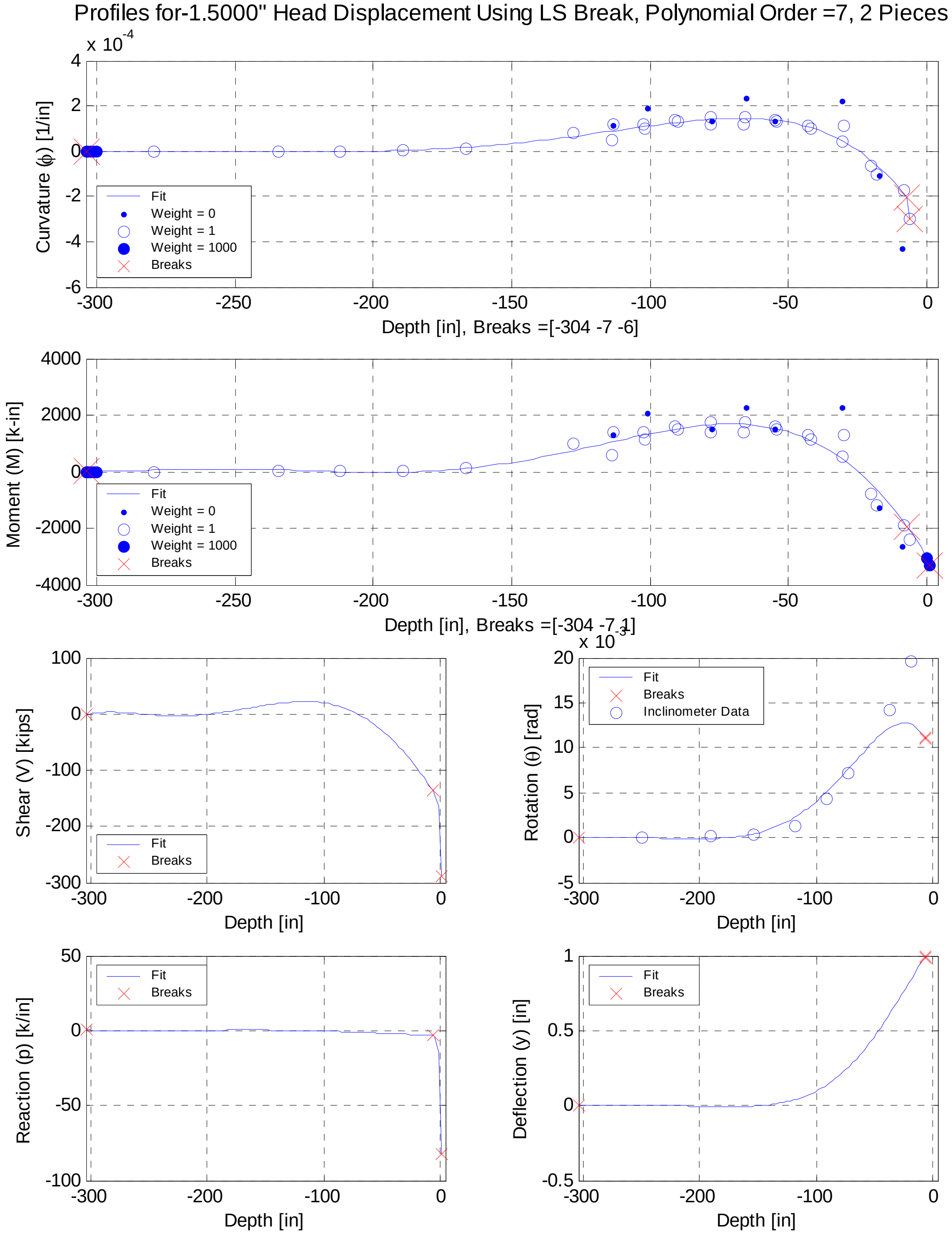

Figure 5.15 (continued). Curvature and moment B-spline fits; differentiation and integration of fits to soil reaction (*p*) and shaft deflection (*y*).

5.5.2 *P-y* Curves from Flagpole Test

The backbone *p-y* curves from the flagpole test at depths of 12, 24 and 36 inches are shown in Figure 5.11. *P-y* curves could only be generated at these depths because only shallow soil (above the plastic hinge center at depths of 2-4 ft) was mobilized. The *p-y* curve at 12 inches is significantly scattered due to its proximity to the boundary condition at the ground surface. As the fitting process simultaneously minimizes error residuals and matches boundary conditions, the second derivative of the moment fit can be poorly behaved. The *p-y* curves at the two depths below have less scatter and are practically identical up to a displacement of 0.3 inch. The 24 inch deep curve extends to larger load and displacement levels, but does not appear to reach a plateau that would be indicative of ultimate capacity. Hence, neither curve is significantly nonlinear. Note also that both curves are stiffer than would be predicted by the API recommendations.

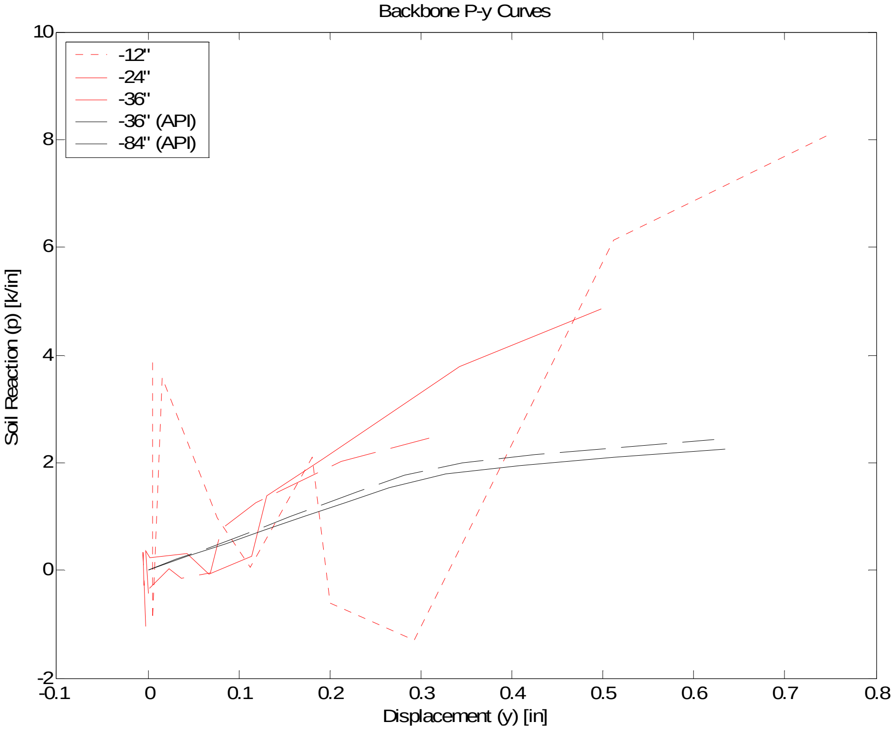

Figure 5.16. Flagpole backbone *p-y* curves

The fitting, integration and differentiation process for the 2ft fixed-head data set are summarized in Figure 5.17. Due to the high-order polynomials used, some unrealistic values are generated for the soil reaction profiles at depths near the tip of the shaft. Since this area was not used to generate *p-y* curves, the values were ignored.

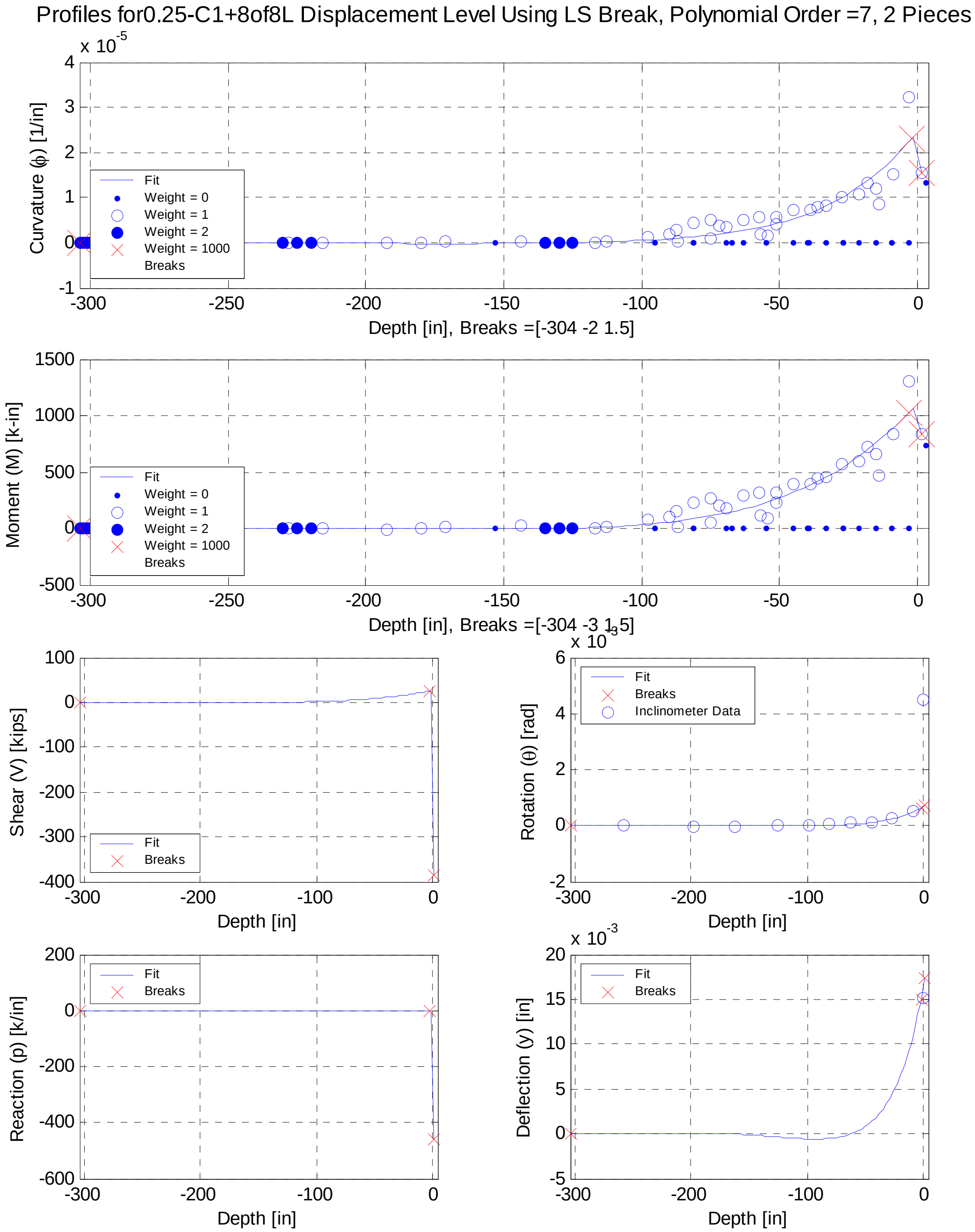

Figure 5.17. Curvature and moment B-spline fits; differentiation and integration of fits to soil reaction (p) and shaft deflection (y).

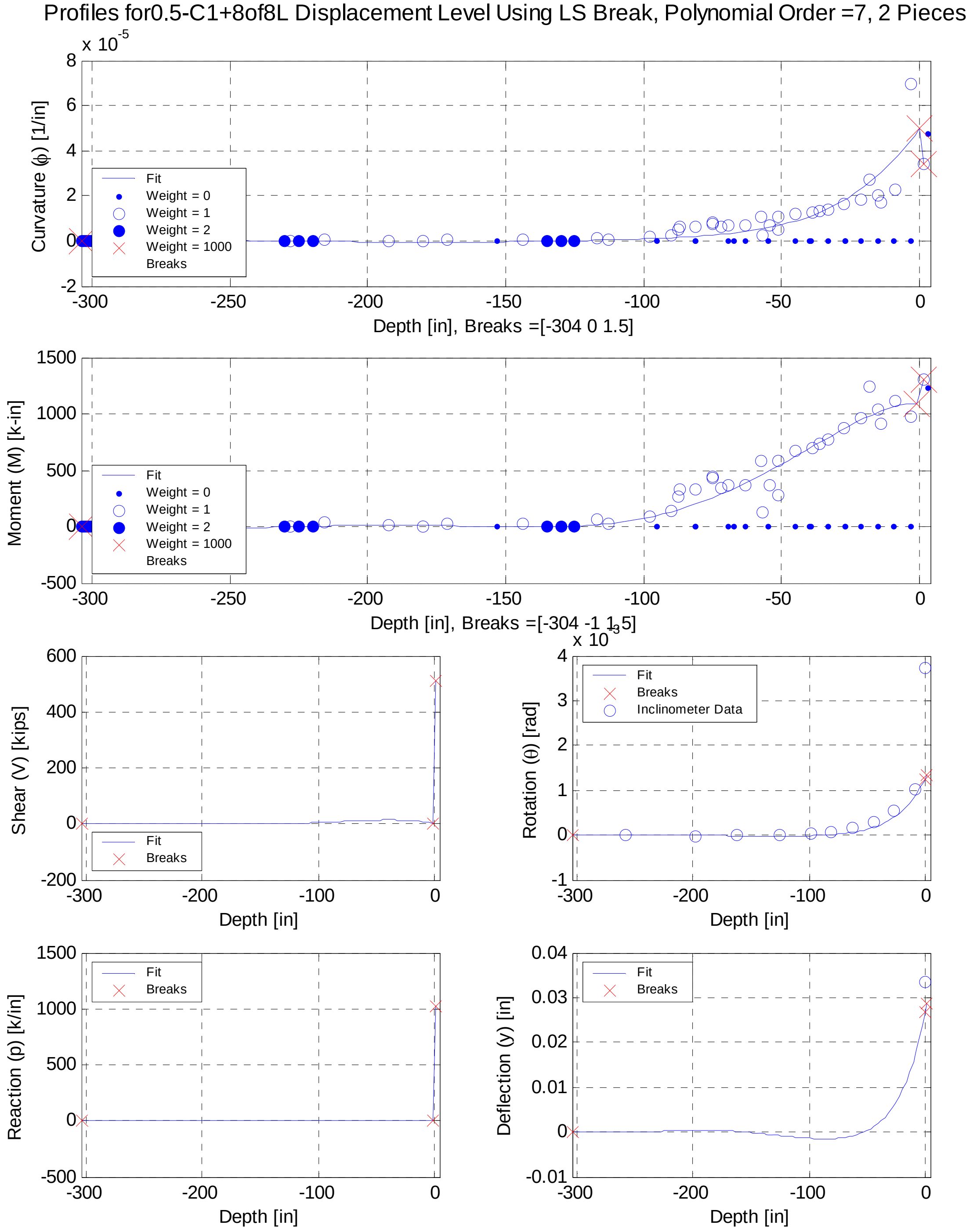

Figure 5.17 (continued). Curvature and moment B-spline fits; differentiation and integration of fits to soil reaction (*p*) and shaft deflection (*y*).

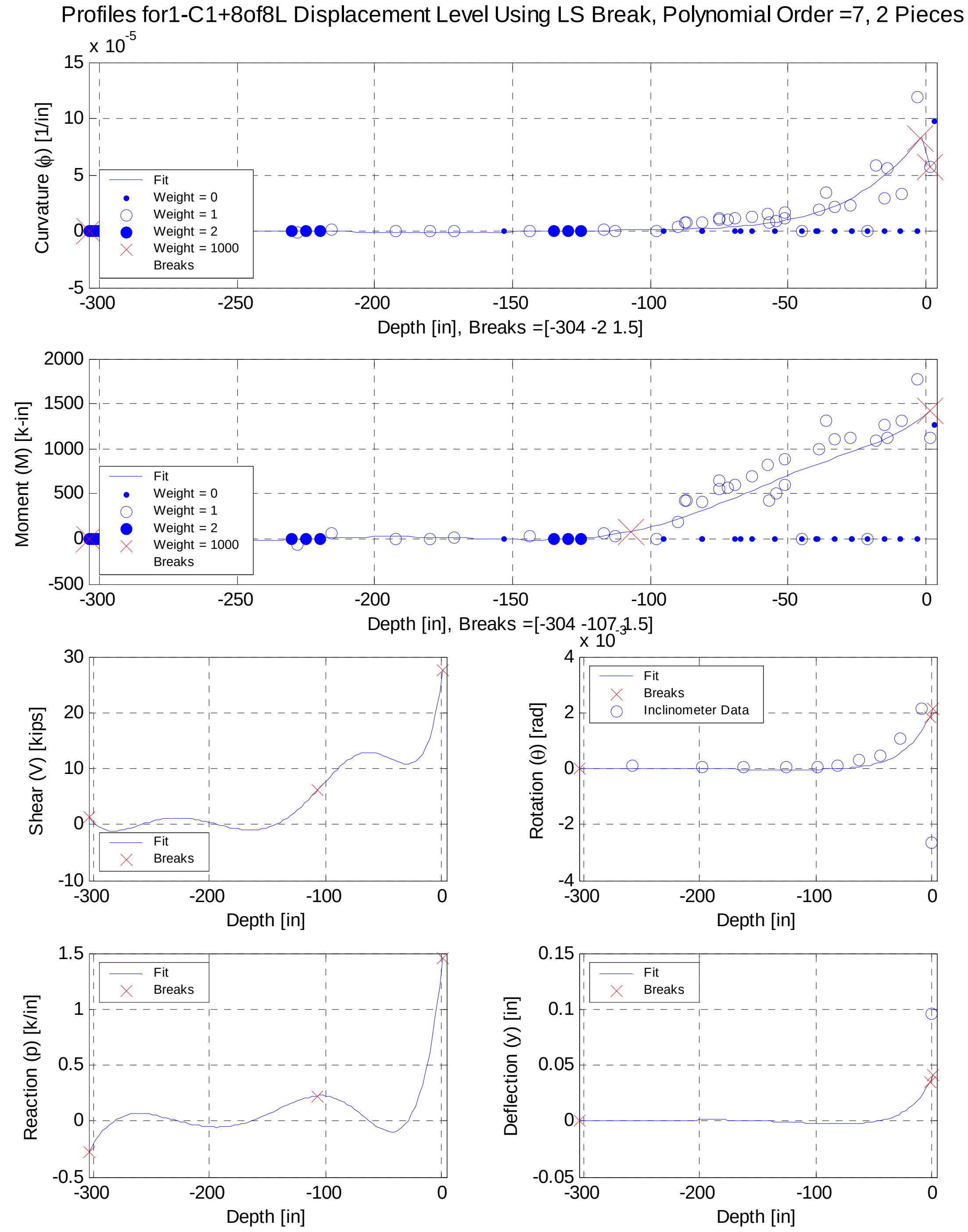

Figure 5.17 (continued). Curvature and moment B-spline fits; differentiation and integration of fits to soil reaction (*p*) and shaft deflection (*y*).

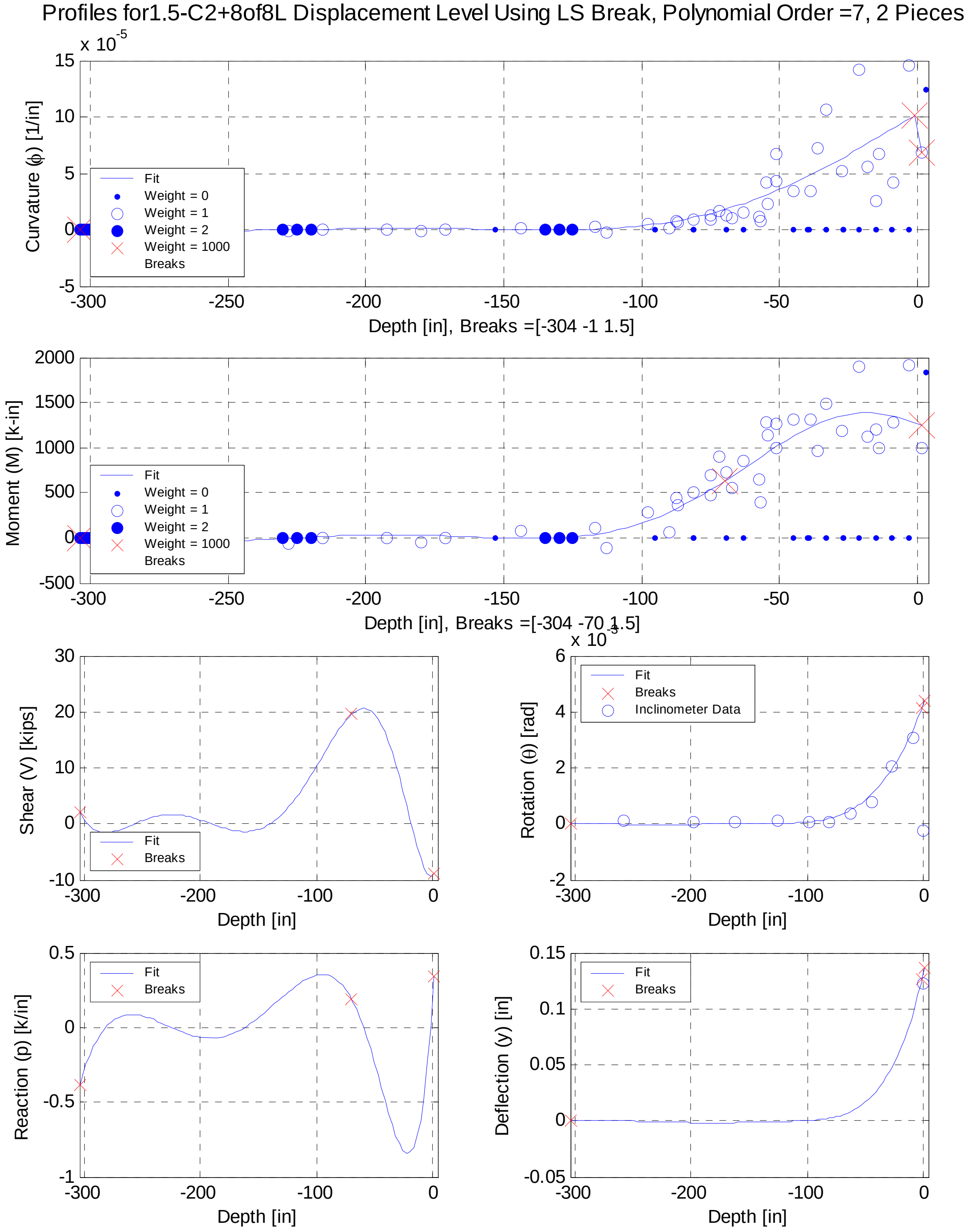

Figure 5.17 (continued). Curvature and moment B-spline fits; differentiation and integration of fits to soil reaction (*p*) and shaft deflection (*y*).

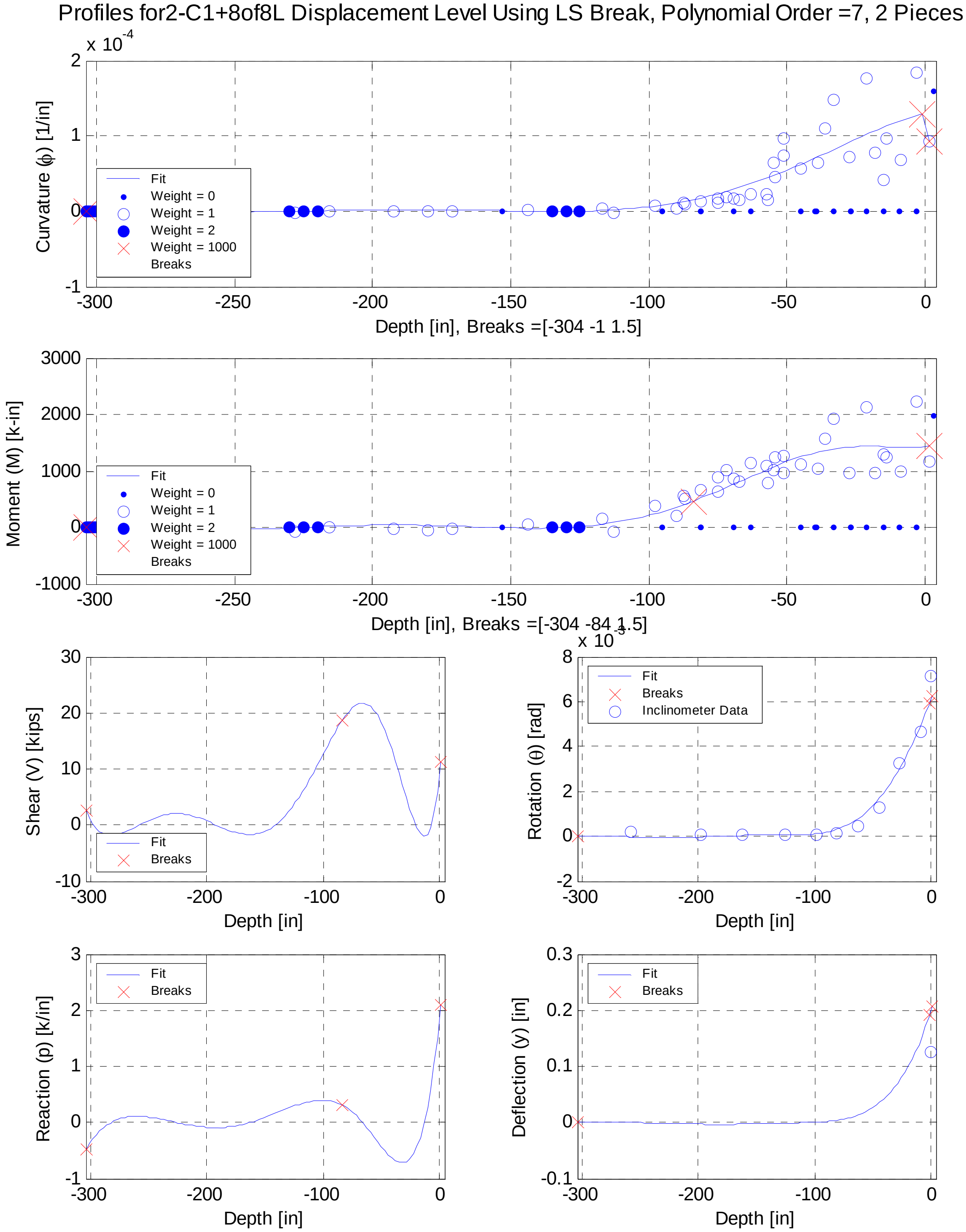

Figure 5.17 (continued). Curvature and moment B-spline fits; differentiation and integration of fits to soil reaction (*p*) and shaft deflection (*y*).

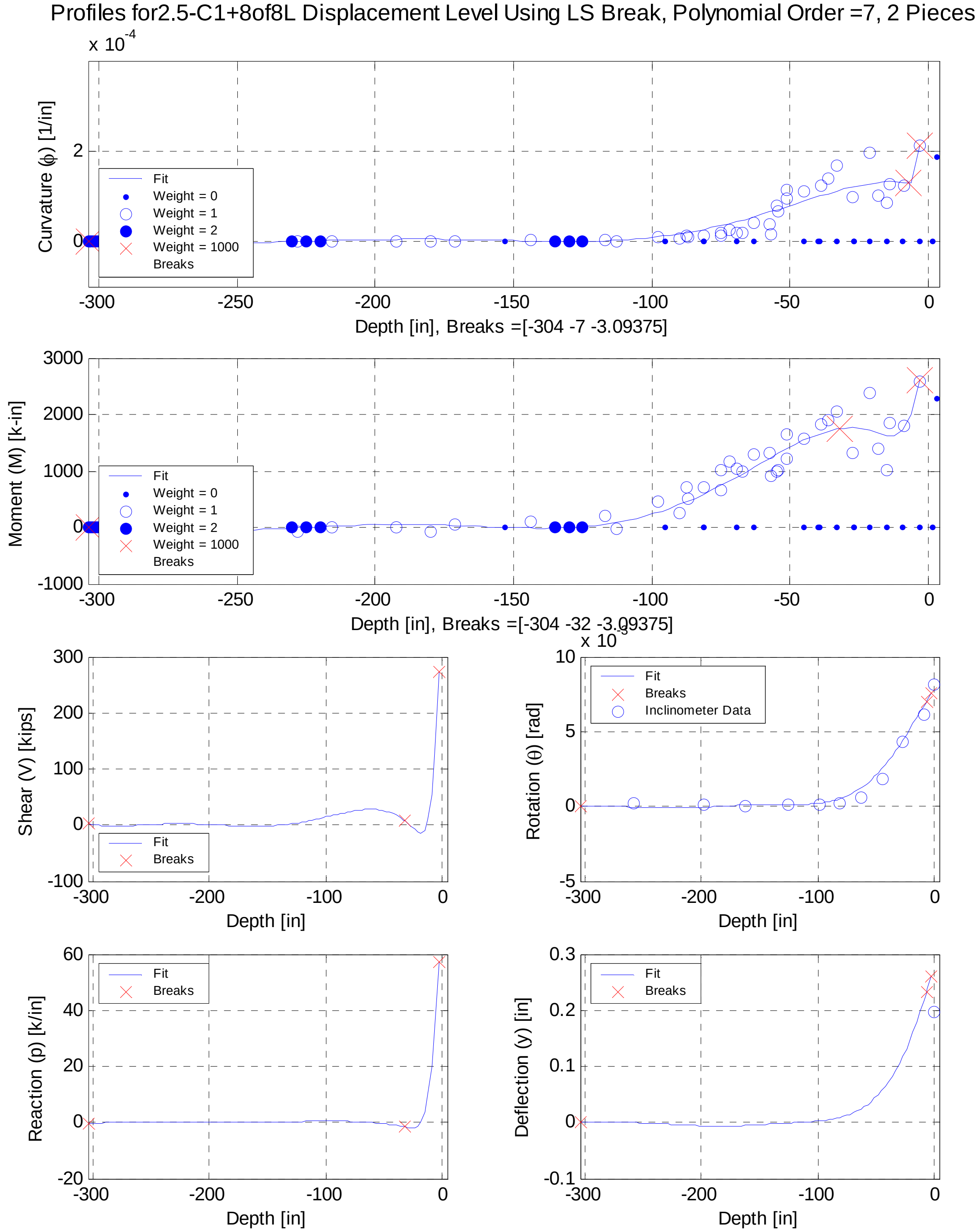

Figure 5.17 (continued). Curvature and moment B-spline fits; differentiation and integration of fits to soil reaction (*p*) and shaft deflection (*y*).

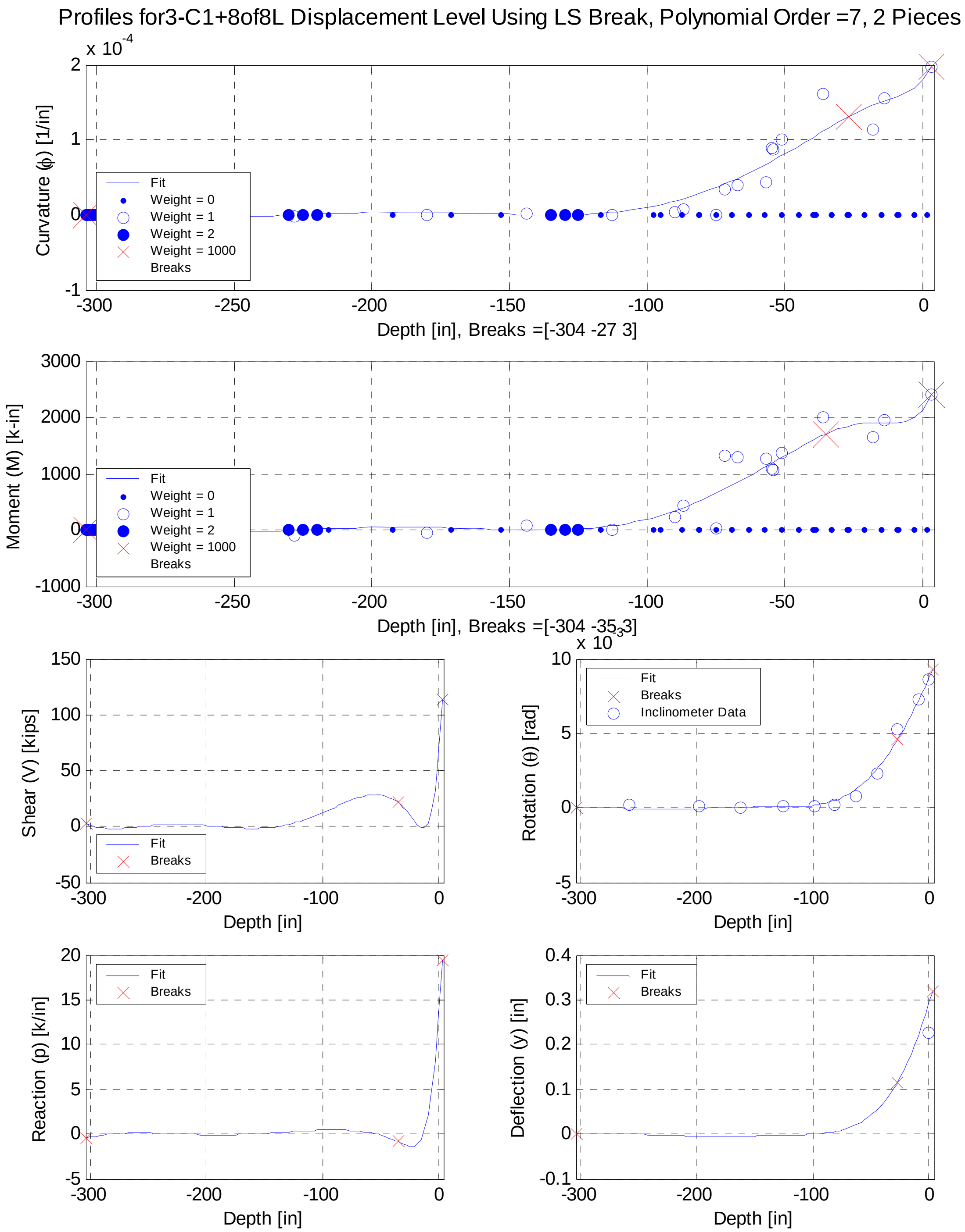

Figure 5.17 (continued). Curvature and moment B-spline fits; differentiation and integration of fits to soil reaction (*p*) and shaft deflection (*y*).

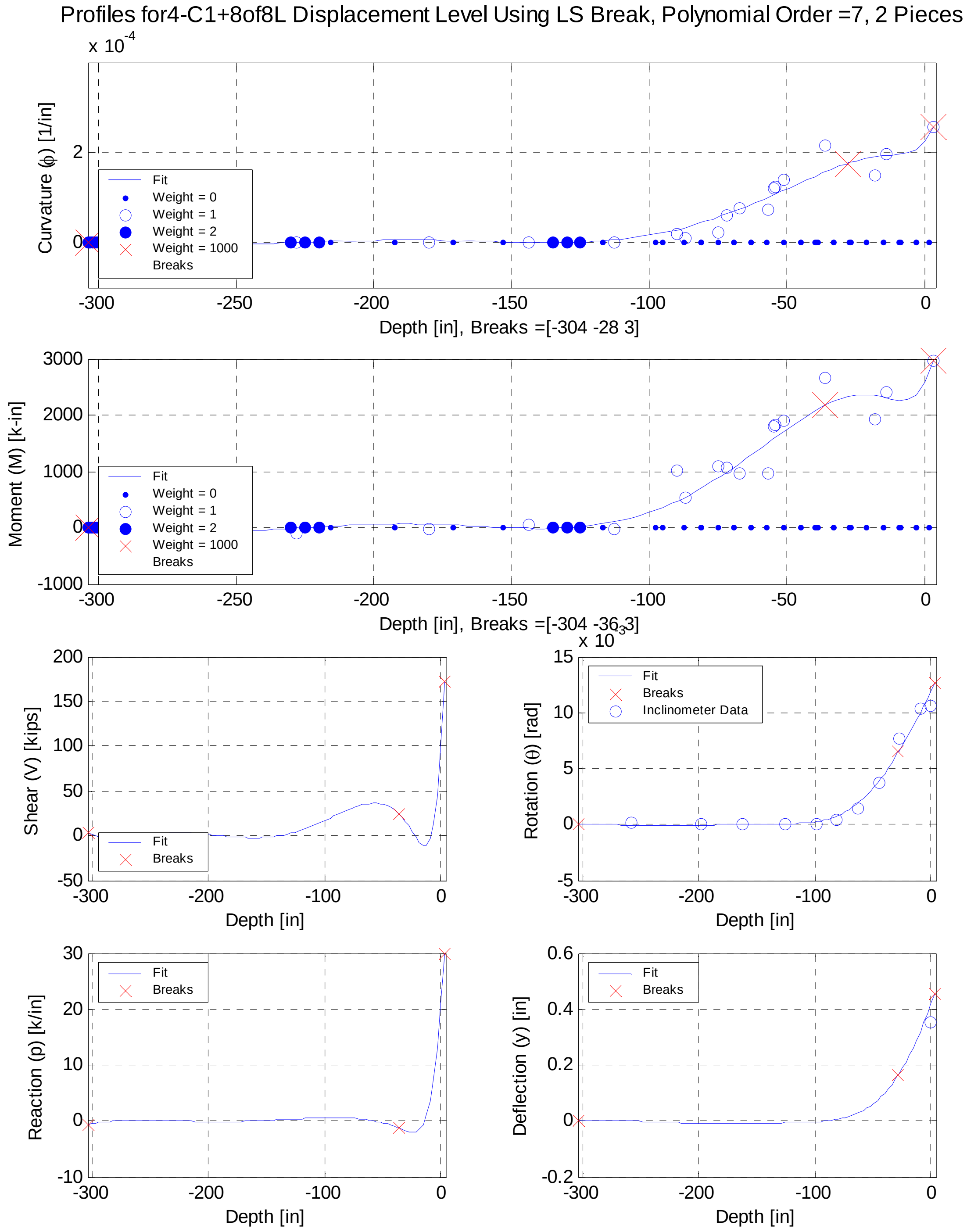

Figure 5.17 (continued). Curvature and moment B-spline fits; differentiation and integration of fits to soil reaction (*p*) and shaft deflection (*y*).

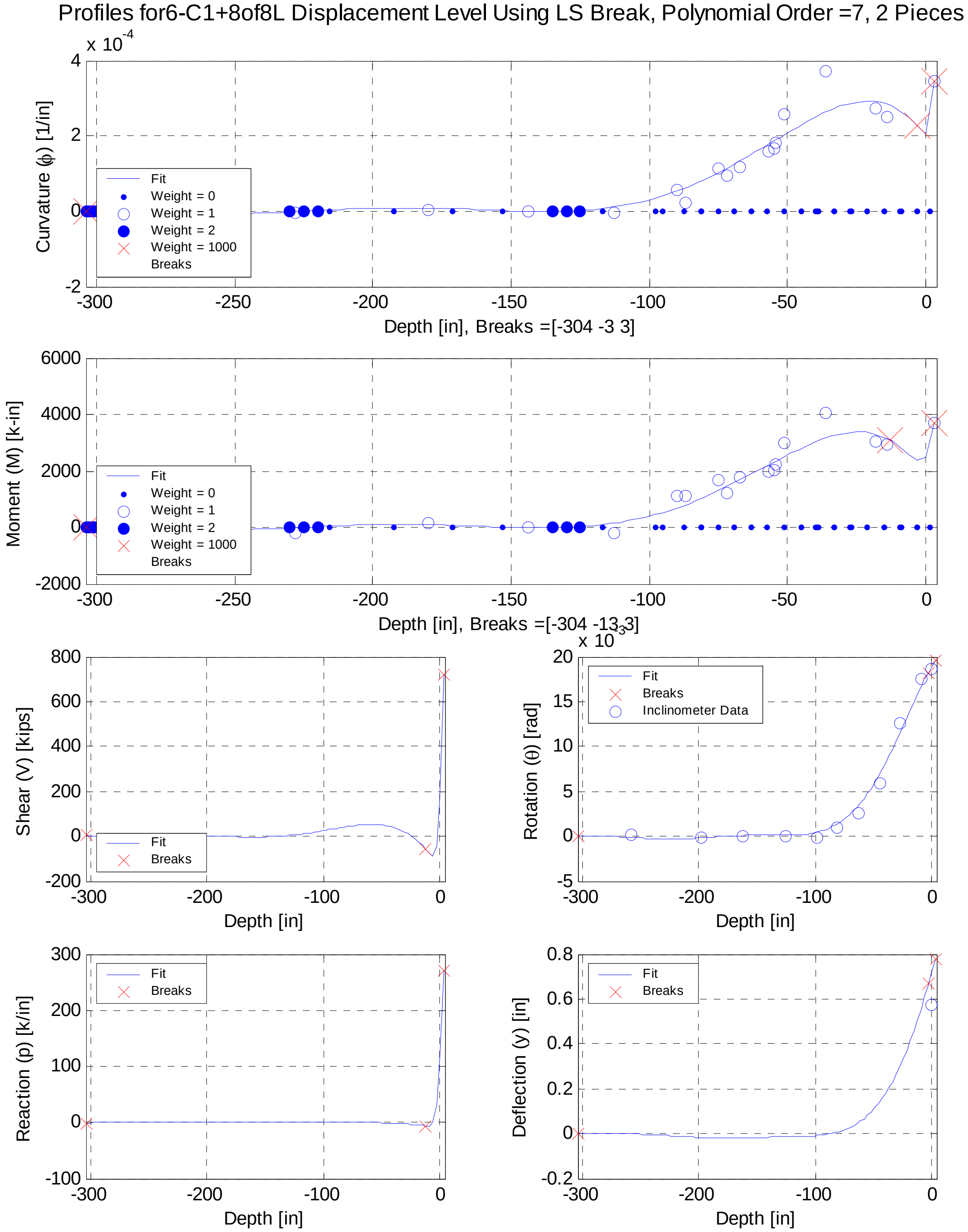

Figure 5.17 (continued). Curvature and moment B-spline fits; differentiation and integration of fits to soil reaction (*p*) and shaft deflection (*y*).

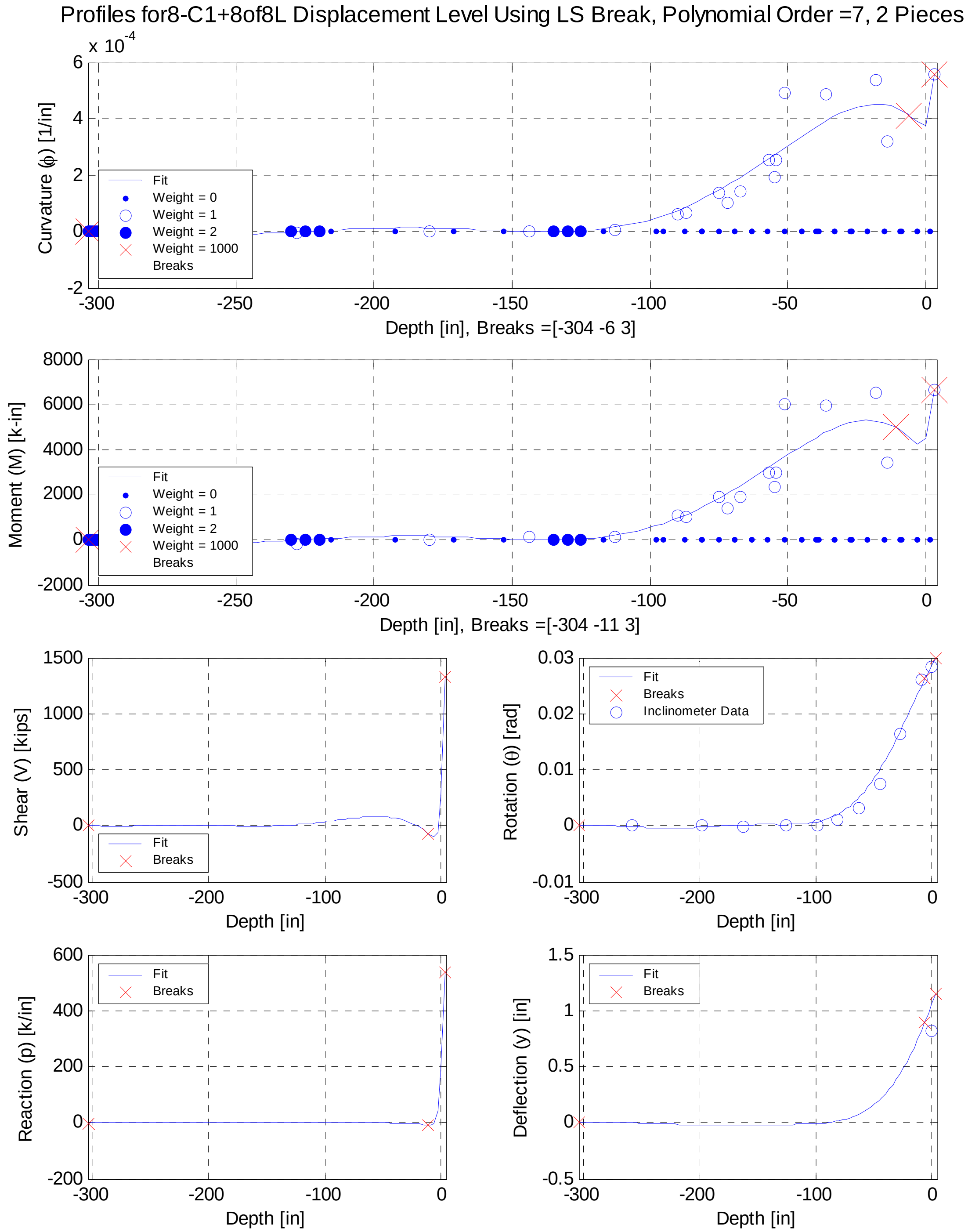

Figure 5.17 (continued). Curvature and moment B-spline fits; differentiation and integration of fits to soil reaction (*p*) and shaft deflection (*y*).

5.5.3 Comparison of Flagpole and Fixed-head P-y Curves

A comparison of the *p-y* curves generated from the flagpole and fixed head tests reveals that both curves are stiffer than the API curves, as shown in Figure 5.18. The stiffness of the fixed-head curves is slightly higher than that for the flagpole test, although these differences may not be statistically significant. The most notable difference between the curves is a relatively linear behavior in the flagpole case and a relatively nonlinear behavior for fixed-head. The soil capacity seems to have been reached in the fixed-head case but not in the flagpole case at the depths for which *p*-*y* curves were generated (soil failure did occur at depths above the plastic hinge, which was at 3.5 ft depth). It is interesting that this capacity (from fixed-head) is less than the ordinate of the flagpole *p*-*y* at large displacement. However, it is not yet clear whether this difference is statistically significant. A factor that may contribute to lower apparent capacity in the fixed-head case is decreased moment capacity due to flexure-shear interaction (see Section 5.6).

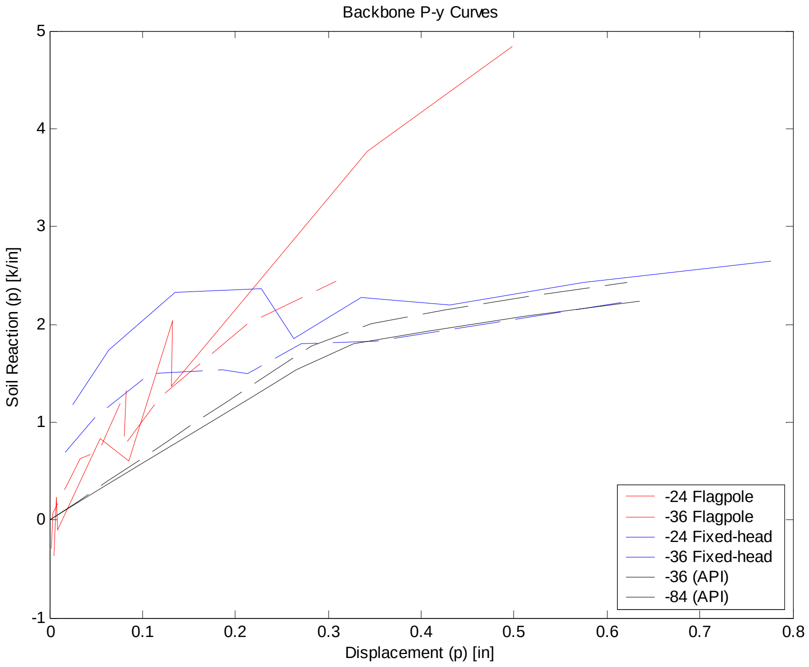

Figure 5.18. Flagpole, fixed-head and modified API backbone p-y curves

5.6 Analysis of Shear Deformation Data

5.6.1 Discussion of Flexure and Shear Interaction

The overall deflected shapes of reinforced concrete shafts have both flexural and shear deformation components. However, in the analysis of drilled shafts the shear deformation component has traditionally been neglected (a reasonable assumption if shear demand is low). In configurations where shear demand is significant compared to capacity, neglecting this component could introduce bias into the results. Therefore, the ability to characterize the flexural and shear deformations of the shaft and their relative contributions to the overall deformation is examined in this section.

5.6.2 Shear deformations

Shear deformations in the 2 ft flagpole and 2 ft fixed-head shafts were measured by diagonal DC LVDTs embedded in the shafts in an “X” configuration. Shear deformations, decoupled from flexural deformations, in the shaft can be determined from these diagonal measurements and vertical measurements by using a method described by Massone, et al. (2006). Schematic representations of a concrete element under pure flexural and shear deformations are shown in Figure 5.19. For an element with pure flexural deformation, and a center of rotation at the element center, there is no displacement in the diagonal sensors, and so any readings from these sensors would be due to the shear contribution. However, since the center of rotation for concrete elements is often not at the center of the element, a correction must be applied. The corrected average shear displacement of the element is given as (Massone, et al., 2006):

$$\overline{U_s} = \frac{\sqrt{D_1^{meas\,2} - (h+V_2)^2} - \sqrt{D_2^{meas\,2} - (h+V_1)^2}}{2} - U_f \tag{5.5}$$

where $\overline{U_s}$ is the average shear displacement; h is the element height; D_1^{meas} and D_2^{meas} are the diagonal lengths for the undeformed element; V_1 and V_2 are the vertical displacements at the top of the element; and U_f is the flexural lateral displacement.

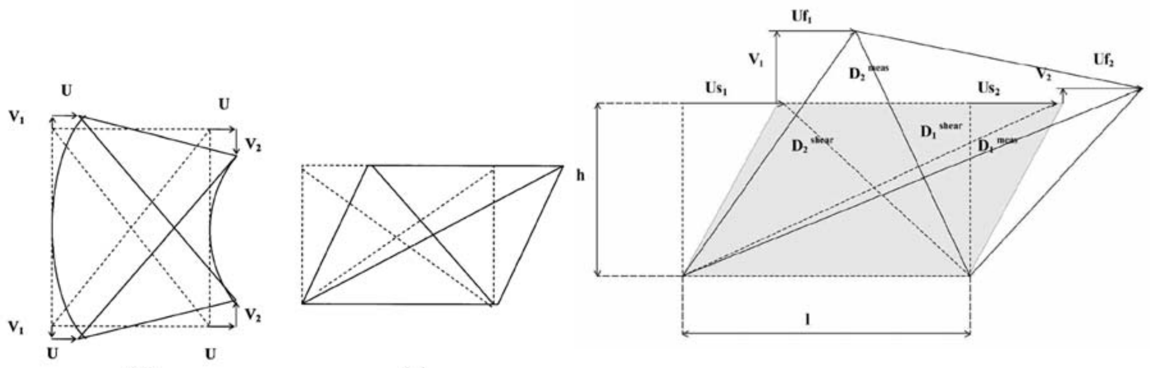

(a) (b) (c)

Figure 5.19. Schematic (a) shear and (b) flexural deformed shapes and (c) measured values for shear displacement calculation

Figure 5.20 shows the corrected average shear displacement for each “X” pair over the shaft profile and also shows the cumulative shear displacement of the fixed-head shaft (data for the flagpole shaft is not available to do failure of the diagonal LVDTs during concrete placement as explained in Section 4.1.2). The cumulative shear is calculated by assuming zero shear displacement below the deepest “X” pair and then summing the corrected average shear displacements as depth decreases. Figure 5.20 includes the element displacements (indicated by symbols), cumulative displacement of the shaft (indicated by the solid lines) and project displacement above the top sensor pair (indicated by the dotted lines) for each displacement level in both loading directions. The projected shear displacements are extrapolated by extending a line between the two top most values to the ground surface.

Shear Deformations for +/-0.25" Head Displacement

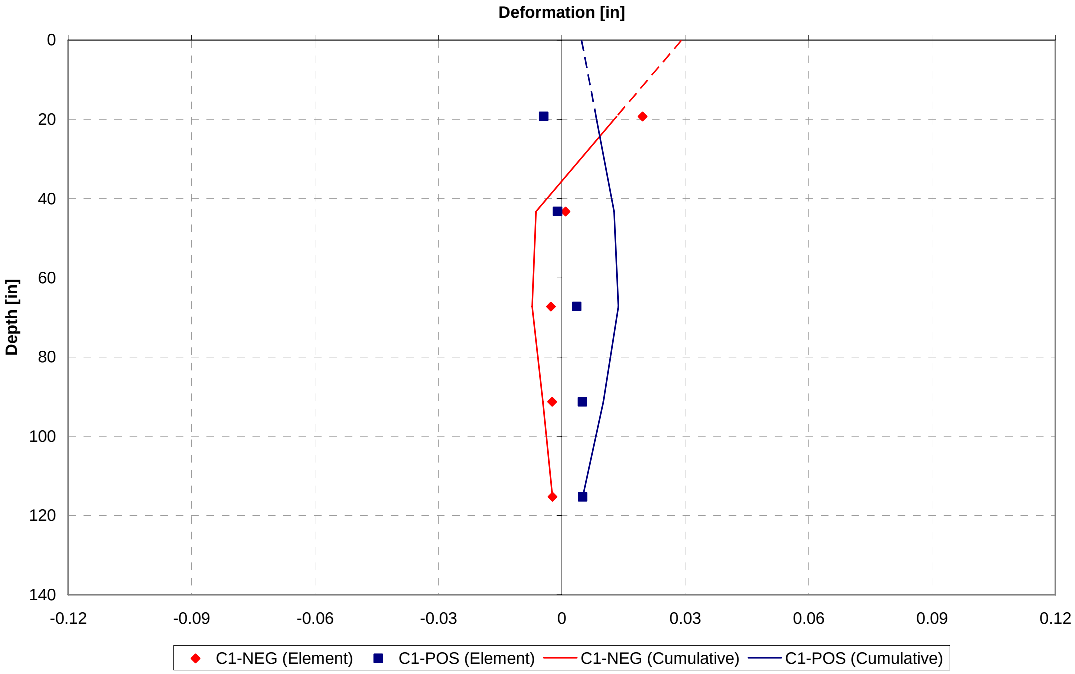

Shear Deformations for +/-0.375" Head Displacement

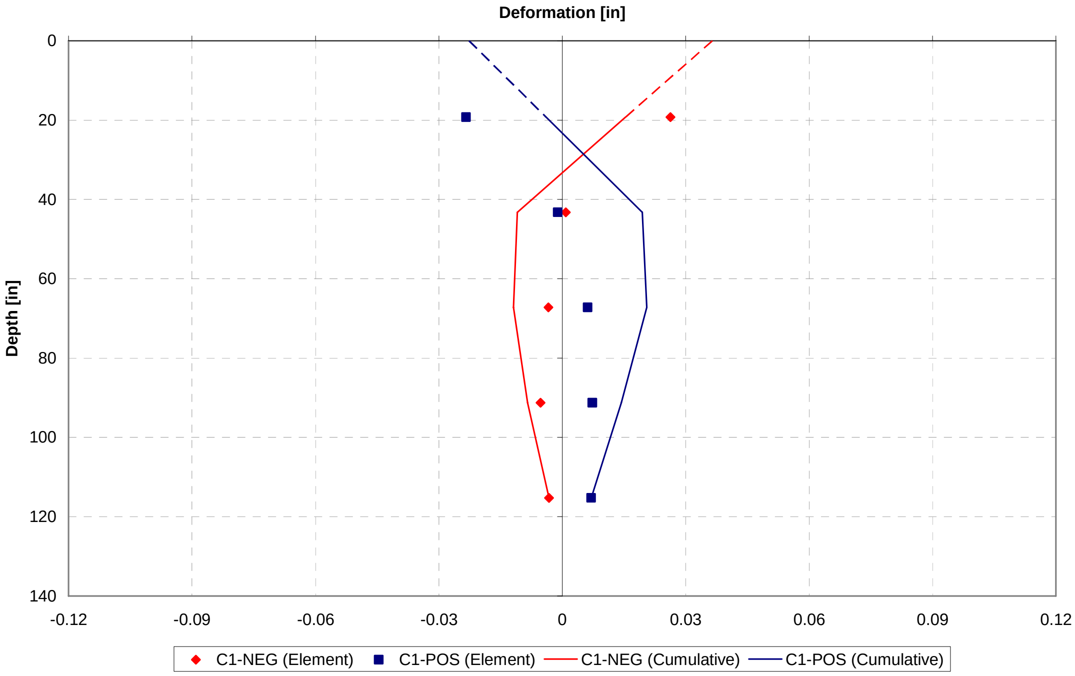

Figure 5.20. Corrected average shear element displacements, cumulative displacements and projected ground line displacements for the fixed-head shaft.

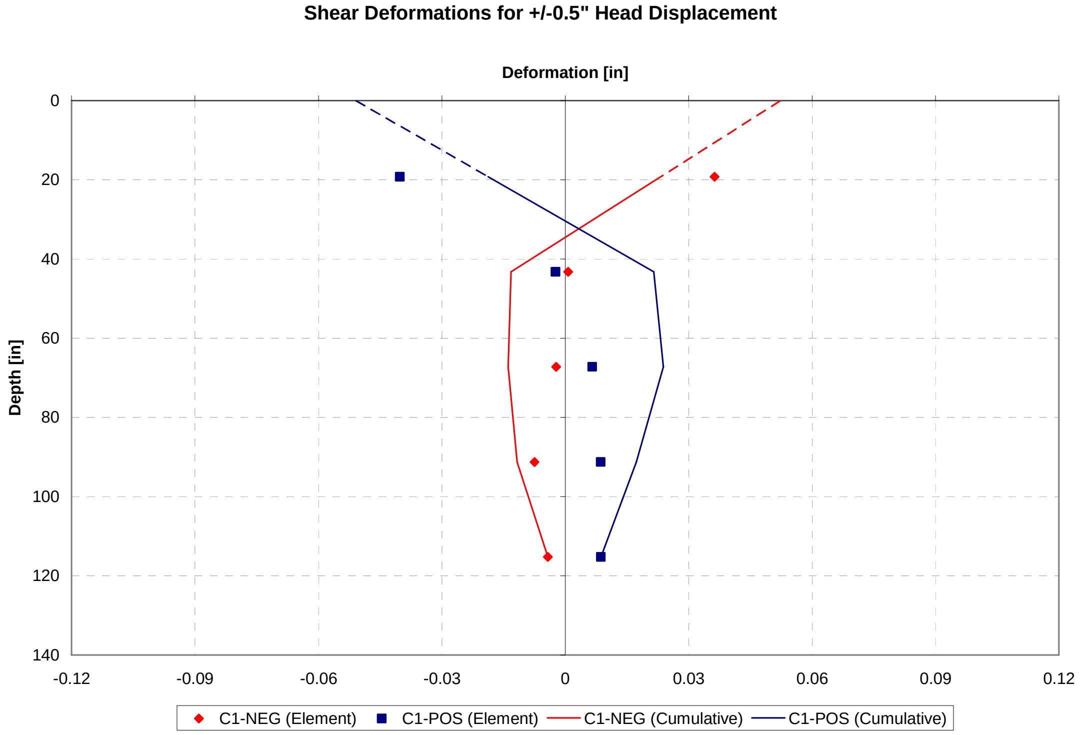

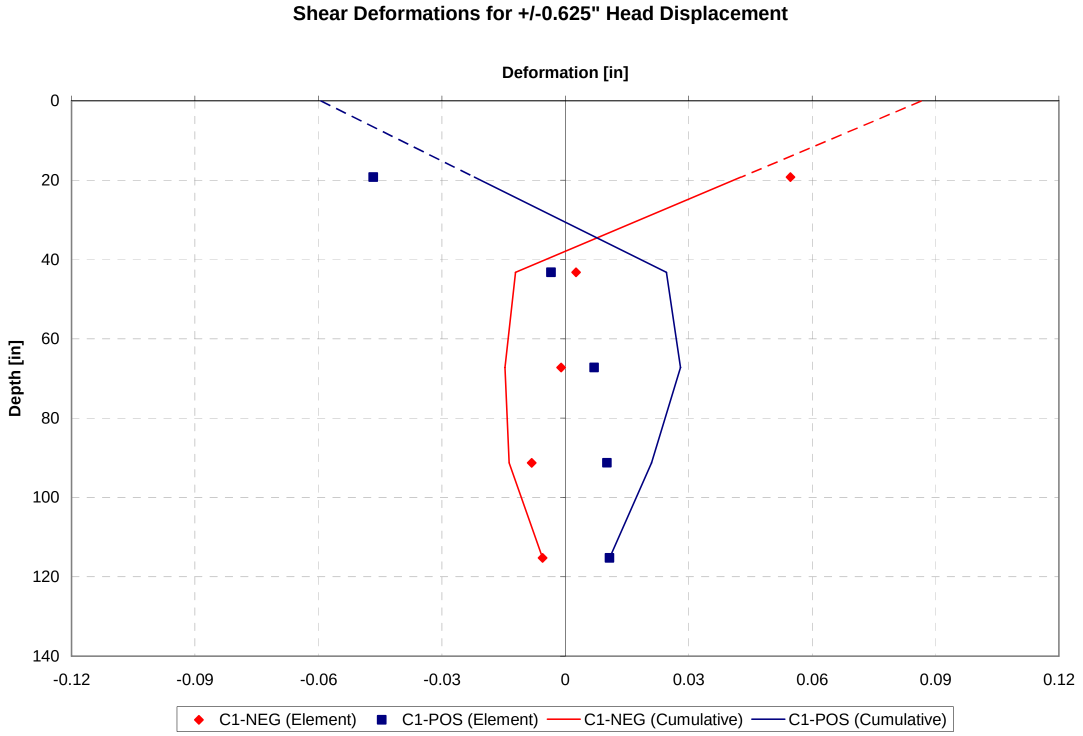

Figure 5.20 (continued). Corrected average shear element displacements, cumulative displacements and projected ground line displacements for the fixed-head shaft.

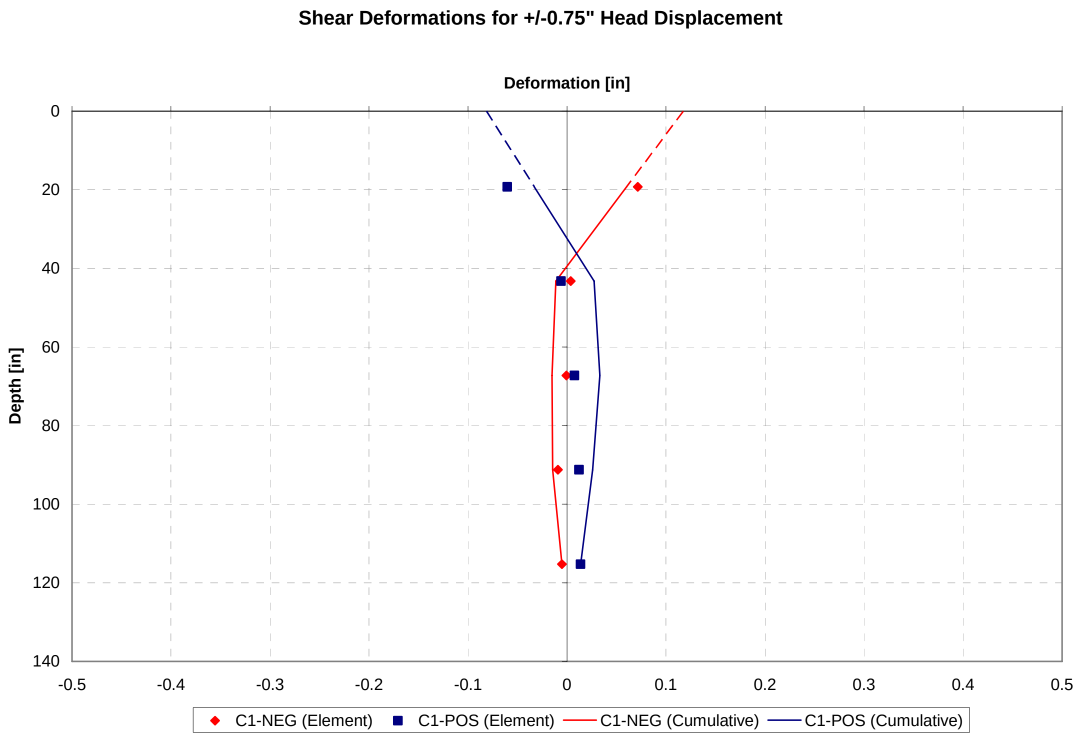

Shear Deformations for +/-0.75" Head Displacement

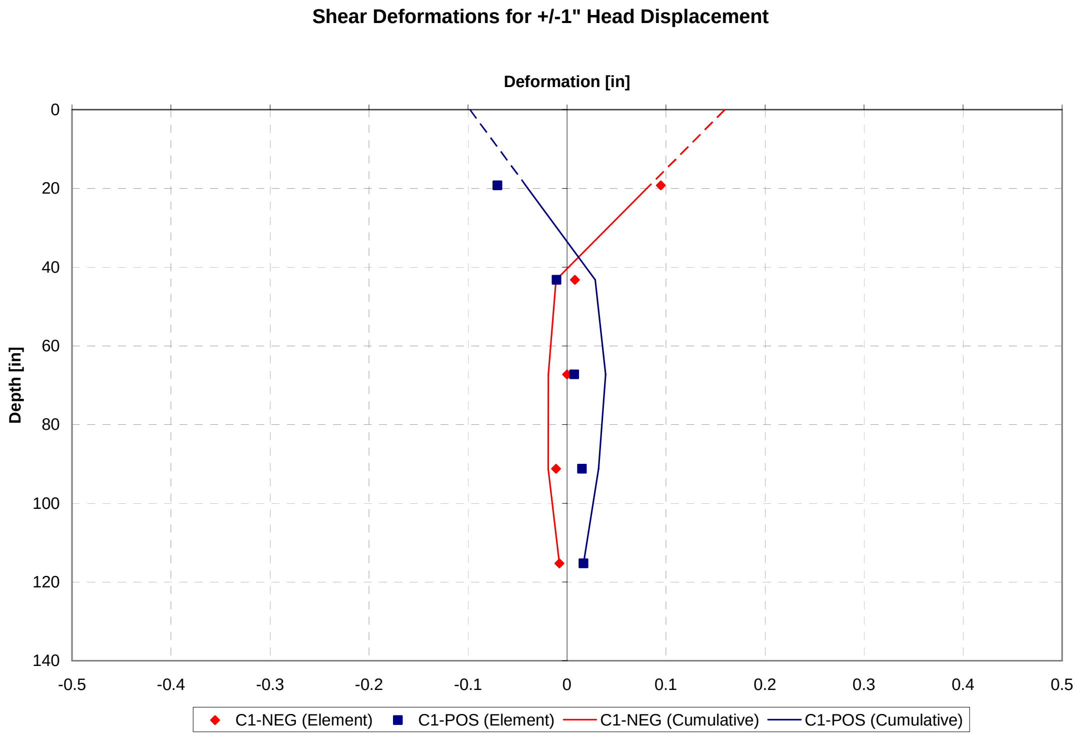

Shear Deformations for +/-1" Head Displacement

Figure 5.20 (continued). Corrected average shear element displacements, cumulative displacements and projected ground line displacements for the fixed-head shaft.

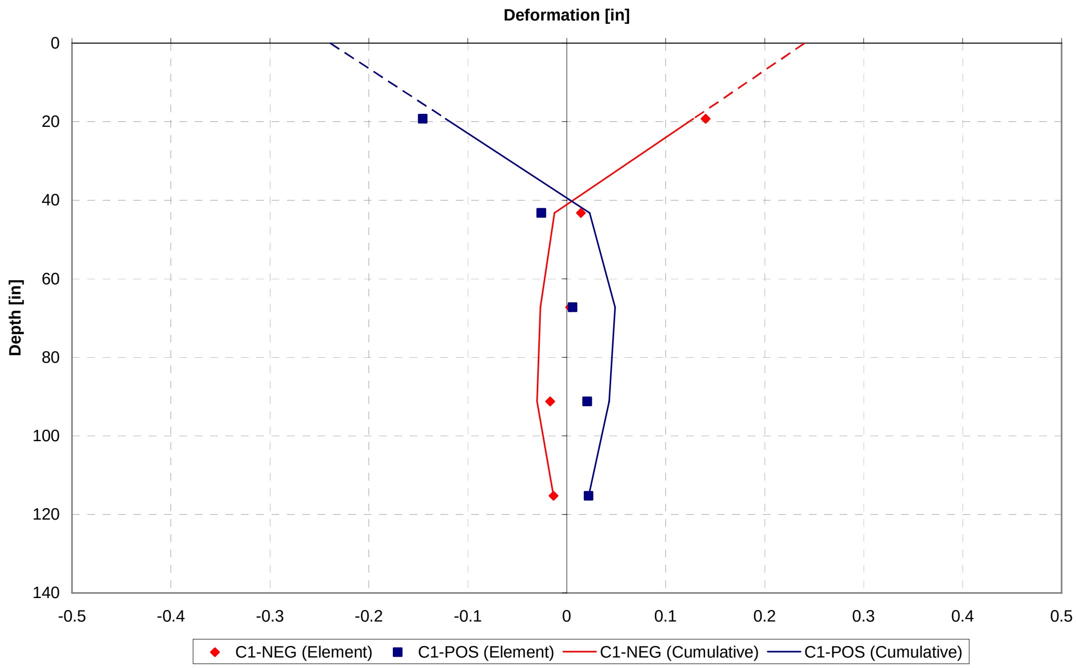

Shear Deformations for +/-1.5" Head Displacement

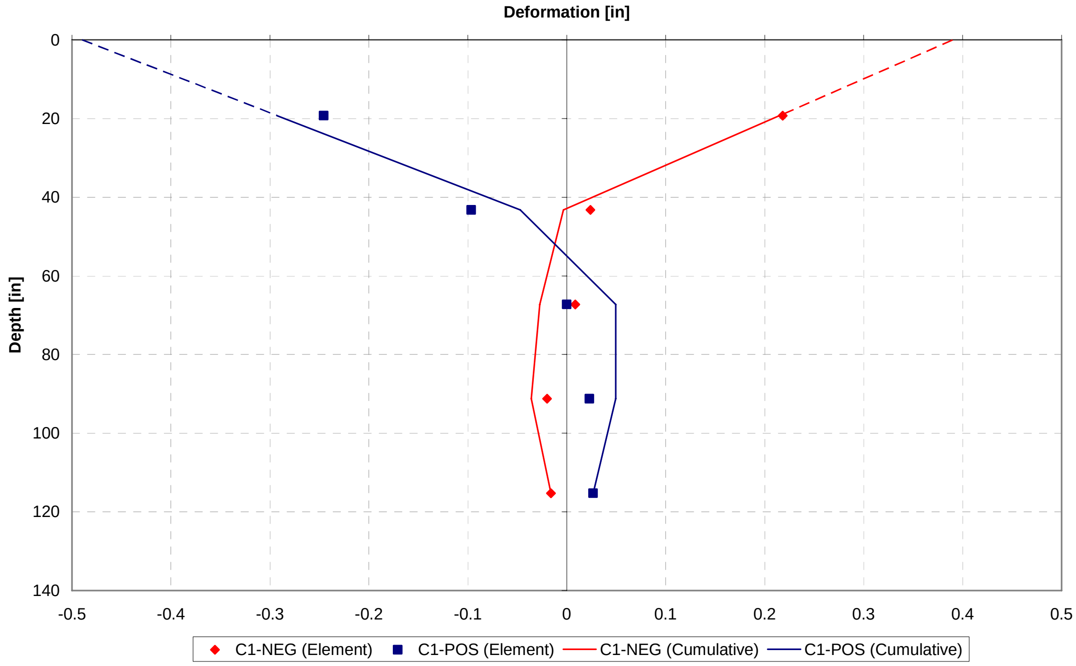

Shear Deformations for +/-2" Head Displacement

Figure 5.20 (continued). Corrected average shear element displacements, cumulative displacements and projected ground line displacements for the fixed-head shaft.

5.6.3 Shear Deformation Influence on *P-y* curves

As can be seen from the shear deformation profiles presented in the previous section, and from the predicted shear profiles in Figure 5.21 from Rha, et al. (2005), shear significantly contributes to the response of the fixed-head shaft, and less significantly to the response of the flagpole shaft. For the 2 ft flagpole configuration test, the shear demand on the shaft is predicted to be low (V = 60 kips @ head Δ = 10 in, see Figure 5.21) compared to capacity (V_n = 306 kips), so the influence of shear on shaft deformation should be small. However, for the 2 ft fixed-head test, the shear demand is predicted to be significant (V = 240 kips @ head Δ = 0.6 in, see Figure 5.21).

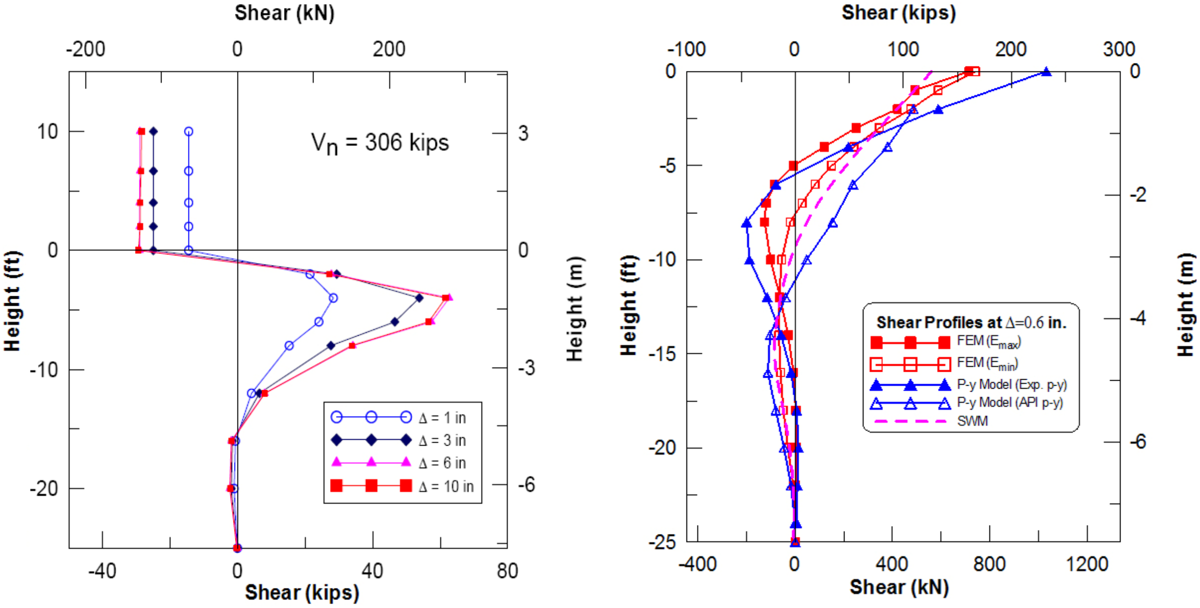

(a)

(b)

Figure 5.21. Predicted shear profiles for (a) 2 ft flagpole and (b) 2 ft fixed-head tests (Rha, et al., 2005)

High shear demands on the 2ft fixed-head specimen can affect the *p-y* curves generated by increasing the deflection of the shaft in soil and by decreasing the moment capacity of the shaft. The deflected shape profiles used to find the *y*-ordinates for *p-y* curves are derived by double integrating the measured curvature profile for the shaft. However, the curvature measurements only capture the flexural response of the shaft and do not account for shaft displacements due to shear deformations. As an example, for the first cycle in the positive loading direction for the 2 inch displacement level, the projected cumulative shear displacement at the ground surface is 0.5 inches, which is 25% of the overall ground surface displacement.

Shear demands near the shear capacity of the shaft can decrease the moment capacity of the section (Massone, et al., 2006). Figure 5.22 shows the experimental load-deflection relationship for a reinforced concrete wall with shear demand near the shear capacity of the wall. Also shown on the figure is the expected load-deflection relationship considering only flexure. The experimental curve has a significant drop in stiffness, strength, and residual strength from the flexure-only curve. While concrete walls have different geometries than that of drilled shafts, it is inferred that the drilled shaft section will also have a similar drop in load capacity (and subsequently moment capacity). This is indicated by the decreased moment capacity for the 2 ft fixed-head shaft reported in Section 5.3.4. The analysis of a moment curvature relationship that accounts for shear is non-trivial and was beyond the scope of this research. A conceptual framework for adapting the work of Massone, et al. (2006) for drilled shaft section characteristics is described in Chapter 6.

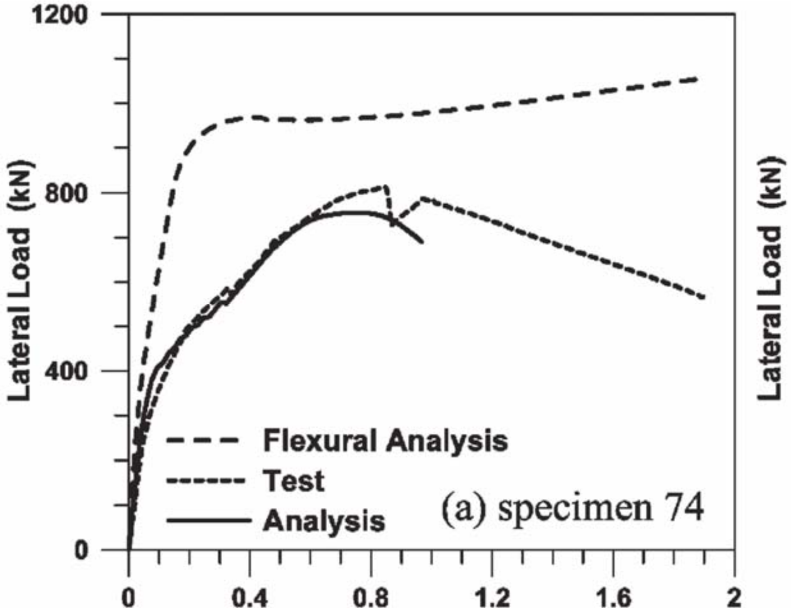

Figure 5.22. Experimental, analytical and flexural load-deflection response of a reinforced concrete wall with shear demand near capacity (Massone, et al., 2006).

5.6.4 P-y Curves from Fixed-head Test Including Shear Deformations

Since the diagonal LVDT sensors can measure shear deformations independent of flexural deformations, displacement profiles generated by double integration of curvature and displacement profiles generated by summing average shear displacements can be combined to produce profiles of the overall displacement of the shaft. Once the overall displacement profiles are generated and associated with soil reaction profiles, *p-y* curves that account for shear-flexure interaction can be developed. *P-y* curves with shear deformations included are shown in Figure 5.23 (flexure only curves are shown as dashed lines for reference).

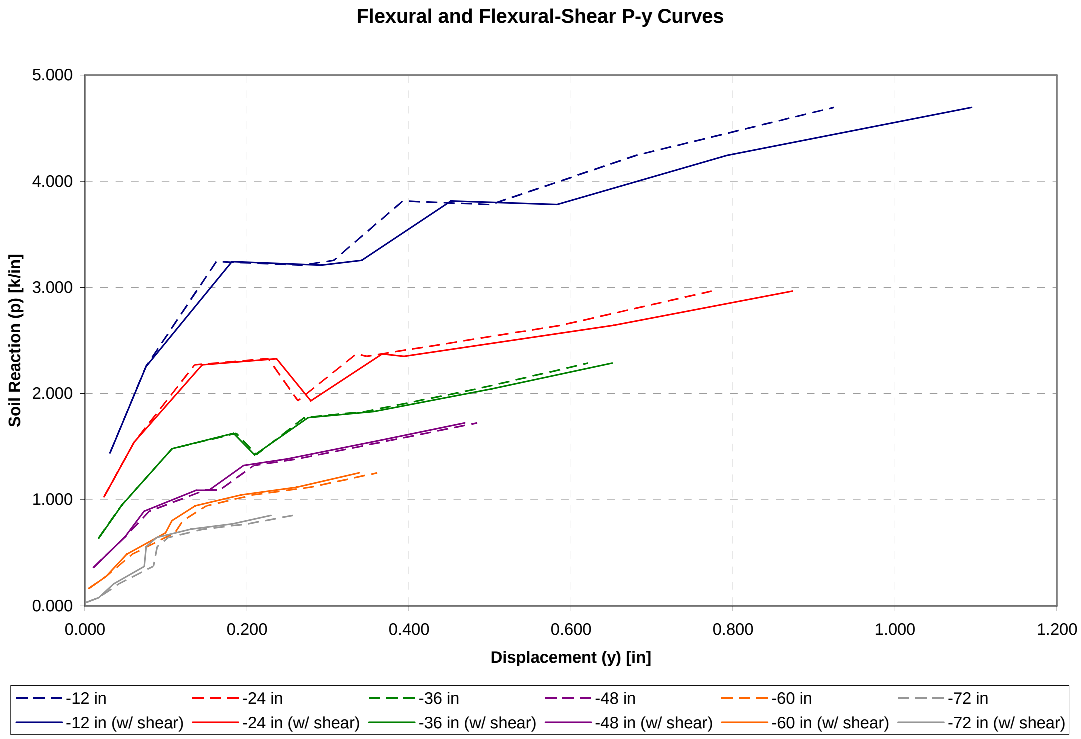

Figure 5.23. P-y curves including shear and flexural deformations (solid), and curves including flexural deformations only (dashed), at various depths.

The effect of shear on the *p-y* curves was largest near the surface, with the shear accounting for 16% of the overall deflection for the curve at 12 inches below the ground surface. Shear deformations for the 72 inch deep curve were in the opposite direction of the flexural deformations, causing the combined shear-flexural deformation to be 12% less that the flexural deformation alone. Overall, including the effects of shear created more flexible curves at the 12, 24 and 36 inch depths and stiffer curves at the 48, 60 and 72 inch depths.

It should be noted that the effects of shear on the generation of *p-y* curves are two fold: (1) increased shaft deflection because of shear, as described above; (2) modified moment-curvature relationship. Only the first of these effects has been formally considered here. The effect of shear on the moment-curvature relationship has been only approximately considered by the reduced ordinates shown in Figure 5.8. To more accurately gauge the effect of shear-flexure interaction on *p-y* curves, a more detailed analysis, such as is outlined in Chapter 6, is required.

6 ANALYSES OF TEST RESULTS

6.1 Overview

The processing of the raw test data and the initial determination of lateral soil resistance versus displacement (i.e., *p*-*y*) profiles based on direct interpretation of the curvature data has been discussed in Chapter 5. In this chapter, we use the experimental data to calibrate the backbone curve parameters of a macroelement described in Taciroglu *et al.* (2006) and to obtain experimentally calibrated *p*-*y* curves. The calibrated *p*-*y* springs are then used to simulate the field tests, and comparisons are made with the predictions obtained via existing API backbone curves for stiff clay.

6.2 API curves and the Macroelement Behavior

The backbone curve of the macroelement described in Taciroglu *et al.* (2006) is devised to have the same parametric form as API (1993) curves for clay. Pertinent formulation details of this macroelement and its relationship to the API model are provided in the following subsections.

6.2.1 Macroelement behavior under monotonic loading

The macroelement of Taciroglu *et al.* (2006) admits an additive form for the total displacement under monotonic loading; and thus, the lateral soil resistance (F) is given by

$$F = E\delta^{e} = E\left(\delta - \delta^{p}\right) \tag{6.1}$$

where E represents the elastic stiffness of the soil. The parameters δ, δ^{e}, δ^{p} are the total, elastic and plastic displacements. The yield function for the macroelement is defined as

$$f_{py} = -F - \left(F_{Y} + \alpha\right) \leq 0 \tag{6.2}$$

where $F_Y \geq 0$ is the yield force and $\alpha > 0$ is the hardening variable. The evolution equations for the force and the hardening variable (F, α) are stated as

$$\left(\dot{F}, \dot{\alpha}\right) = \begin{cases} \left(C(\delta)\,\dot{\delta}, \quad \left|\dot{F}\right|\right) & \text{if } f_{py} = 0, \\ \left(E\dot{\delta}, \quad 0\right) & \text{if } f_{py} < 0. \end{cases} \tag{6.3}$$

Consequently, the elastoplastic (continuum) material tangent stiffness is

$$\frac{\partial \dot{F}}{\partial \dot{\delta}} = \begin{cases} C\left(\delta\right), & \text{if } f_{py} = 0, \\ E, & \text{if } f_{py} < 0. \end{cases} \tag{6.4}$$

where E and $C(\delta)$ are the elastic and the plastic tangent stiffnesses, respectively. Any well-defined envelope curve (i.e., one that has a continuous slope) obtained from field tests (or from analytical models) may be used for constructing the constitutive model of the macroelement. Here, the functional form of the p-y curve for stiff clay (API, 1993) is chosen, which may be stated in a generic form as follows

$$F = \eta \ \text{sign}\left(\delta\right)\left(\frac{|\delta|}{\beta}\right)^{n} \ \text{and} \ \dot{\alpha} = \left|\dot{F}\right| \ \text{when} \ f_{py} = 0.. \tag{6.5}$$

The values of material parameters η, β, and n generally depend on depth. The plastic tangent stiffness may be obtained from Eq. (6.5) as

$$C\left(\delta\right) \equiv \frac{\eta n}{\beta^{n}}\left|\delta\right|^{n-1}. \tag{6.6}$$

It is useful to note that the yield force F_Y for the elastic portion is not an independent parameter, and is related to the rest of the material parameters via

$$F_Y = E \sqrt[(1-n)]{\eta / \left(E\beta^{n}\right)}. \tag{6.7}$$

6.2.2 API Envelope Curves for Clay

The p-y envelope curves for stiff clay—described in API guidelines (1993)—are parameterized using the undrained shear strength c, unit weight of the soil γ, pile/pier diameter D, an empirical constant J, and depth z as displayed in Figure 6.1. The solid curve in Figure 6.1 denotes the p-y envelope for static lateral load. The vertical and horizontal axes in this figure denote the normalized lateral resistance (p / p_u) and deflection (y / y_c) respectively where the parameters p_u and y_c denote ultimate resistance and the deflection at one-half of the ultimate resistance.

The parameter z_r denotes the depth below soil surface to bottom of reduced resistance zone where p_u decreases. API (1993) provides the dependency of z_r, y_c, and p_u on c, γ, D, and J as

$$z_r = 6D \Big/ \left(\frac{\gamma D}{c} + J \right), \quad y_c = 2.5\varepsilon_c D, \text{ and } \; p_u = \begin{cases} \left(3 + \dfrac{\gamma z}{c} + \dfrac{Jz}{D} \right) cD & \text{if } 0 < z \le z_r, \\ 9c & \text{if } z \ge z_r, \end{cases} \tag{6.8}$$

where the strain ε_c is that which occurs at one-half of the maximum stress (i.e., $p = 0.5\, p_u$) on the laboratory stress-strain curve. Consequently, the equivalencies $\eta = 0.5 p_u L_{tr}$ and $\beta = y_c = 2.5\varepsilon_c D$ hold between the API parameters and the parameters used in Eq. (6.5) that defines the macroelement envelope curve. The parameter L_{tr} is the tributary length for each of the soil-pile interaction elements. The exponent *n* is identical in either descriptions of the *p*-*y* envelope.

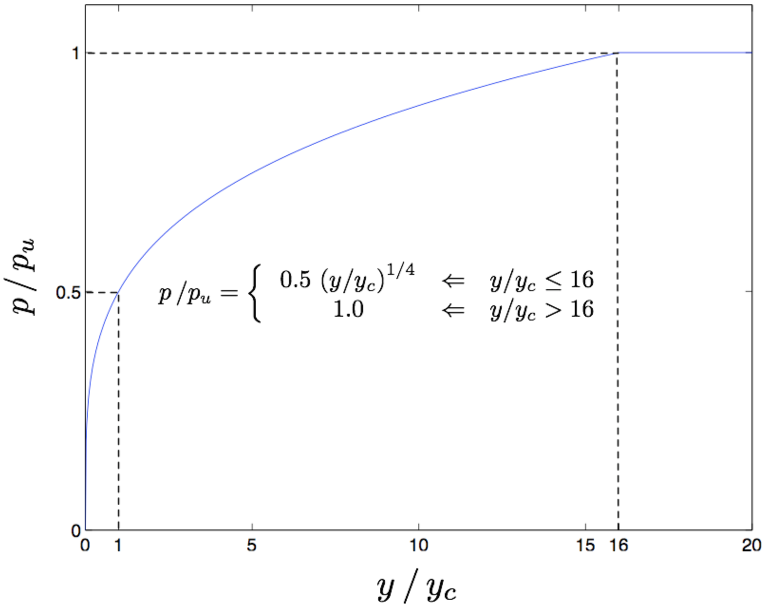

Figure 6.1. The API (1993) envelope curves for stiff clay.

6.3 Experimental *p-y* Curves— the “Mathematical Fit”

In Chapter 5, the fixed-head and flagpole shaft raw test data collected at different sensors had been processed to obtain curvature profiles for each specific top displacement level. Subsequently, these curvature profiles were converted (through double integrations and differentiations) into *p* versus *y* data sampled at various load-levels for different depths (see,

Figure 5.10). These "experimental," albeit processed, *p*-*y* data are not directly useable in a numerical analysis. Here, we describe a methodology for fitting a curve—that possesses the functional form of an API curve—to the aforementioned experimental data. Details of this "mathematical fitting" procedure are provided below.

6.3.1 Calibration of Macroelements

The lateral soil pressure-displacement data (respectively denoted here as p_i and δ_i) obtained at different depths are used here for calibrating the macroelement's backbone curve parameters (i.e., η, β, and n).

6.3.2 Error Function and the Minimization Procedure

The objective function per each depth for this process is defined as

$$S(\tilde{\eta}, \beta, n) = \sum_{i=1}^{M} w_i \left[p_i - \hat{p}_i(\tilde{\eta}, \beta, n, \delta_i) \right]^2 \qquad (6.9)$$

where $\hat{p}_i$ denotes the backbone curve defined in Eq. (6.5) ($\hat{p}_i = F$ per unit length of pile); and w_i and *M* denote the weights and the number of data points. The parameter $\tilde{\eta}$ in Eq. (6.9) is not a new and independent parameter, but is simply defined through the equivalency $\eta = \tilde{\eta} L_{tr}$. The optimal values of the backbone curve parameters are obtained by solving

$$\underset{\{\tilde{\eta}, \beta, n\}}{\text{minimize}} \, S(\tilde{\eta}, \beta, n) \quad \text{subject to} \quad 0 \le \text{n} \le 1 \quad \text{and} \quad 0 \le \beta \le 1. \qquad (6.10)$$

We solved this nonlinear least-squares minimization problem using the "Trust Region" algorithm, implemented in MATLAB's curve fitting toolbox `cftool`. The weights in Eq. (6.9) were chosen to be "bi-square weights" as described in MATLAB 6.5 User's Manual.

6.3.3 Calibration Results and "Mathematically" Fitted *p-y* Curves for the Fixed-Head Shaft

The results of the calibration procedure for the fixed-head shaft are given in Table 6.1. The table also contains the calibrated equivalent API parameters. These values are different from those recommended in API guidelines (1993), which were used in the pre-test model predictions (also provided in the Table 6.1). Based on these results, a new macroelement model of the fixed head shaft is created as illustrated in Figure 6.2. In this model, the macroelements are placed at 1ft intervals within the first 10 ft from the ground level. This spacing matches the locations where the field measurements were made, except for the ground level where measurements were unavailable (for which we have used standard/original API parameters).

Table 6.1. Calibrated and pre-test backbone curve parameters for the fixed-head shaft.

	Macroelement Parameters			Equivalent API Parameters			Pre-test Model Parameters		
z (in)	$\hat{\eta}$ (kips/in)	β (in)	n	p_u	y_c	n	p_u	y_c	n
-12	2.4560	0.1865	0.1078	4.9120	0.1865	0.1078	2.0452	0.4200	0.3333
-24	2.2700	0.3499	0.1723	4.5400	0.3499	0.1723	2.1463	0.4200	0.3333
-36	1.7020	0.2633	0.3063	3.4040	0.2633	0.3063	2.2475	0.4200	0.3333
-48	1.1150	0.1539	0.4395	2.2300	0.1539	0.4395	2.3486	0.4200	0.3333
-60	2.3890	0.7890	0.6070	4.7780	0.7890	0.6070	2.4498	0.4200	0.3333
-72	1.1500	0.2669	0.7854	2.3000	0.2669	0.7854	2.5510	0.4200	0.3333
-84	1.0530	0.2634	0.8759	2.1060	0.2634	0.8759	2.6521	0.4200	0.3333
-96	1.4010	0.7480	0.6700	2.8020	0.7480	0.6700	2.7533	0.4200	0.3333
-108	0.7226	0.3520	1.0000	1.4452	0.3520	1.0000	2.8544	0.4200	0.3333
-120	0.0834	0.5070	0.0757	0.1668	0.5070	0.0757	2.9556	0.4200	0.3333

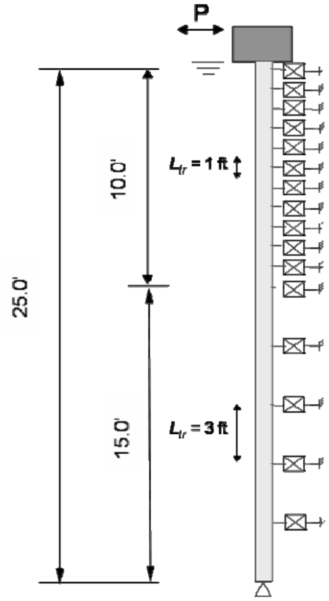

Figure 6.2. The new macroelement model of the fixed-head shaft.

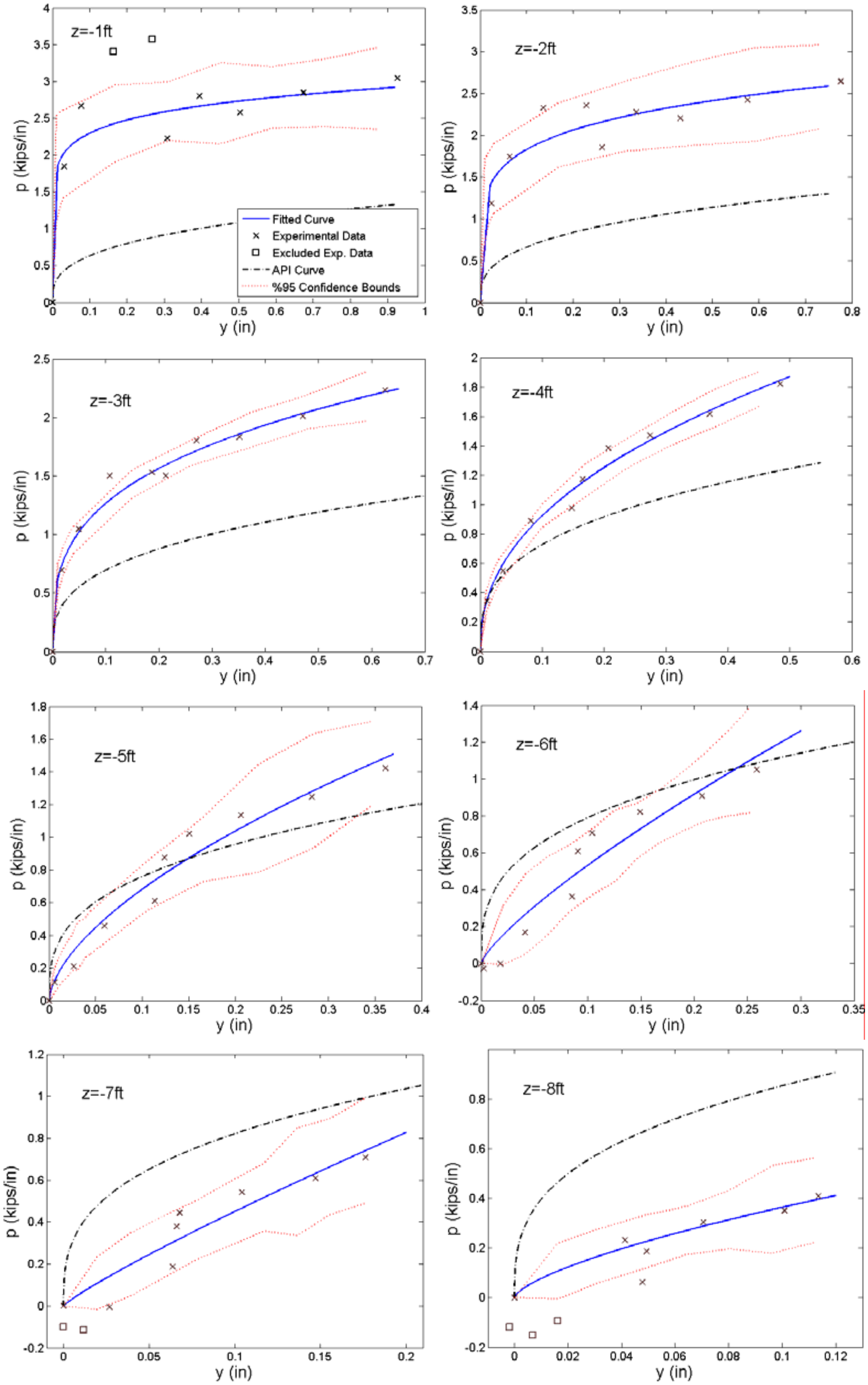

Figure 6.3. Calibrated *p-y* curves for the fixed-head shaft at 1 ft trough 8 ft.

The calibrated *p*-*y* curves for the fixed-head shaft down to 8 ft depth are shown in Figure 6.3. As this figure indicates, the confidence intervals on the calibrated *p*-*y* curves become wider with depth. This is expected because signal-to-noise ratio in the curvature measurements—from which the *p*-*y* data are deduced—reduces with depth. The API curves imply a more flexible soil response than what is actually measured from the ground level to 4 ft (i.e., two pile diameters) below. At depths greater than 5 ft, the API curves are too strong and stiff. Curvature profiles and the top load-displacement responses from the pre-test (i.e., API) macroelement model, the calibrated macroelement model, and the field measurements are shown in Figure 6.4. This figure reveals that the macroelement model with calibrated *p*-*y* curves approximates the measured response better than the standard API *p*-*y* curves.

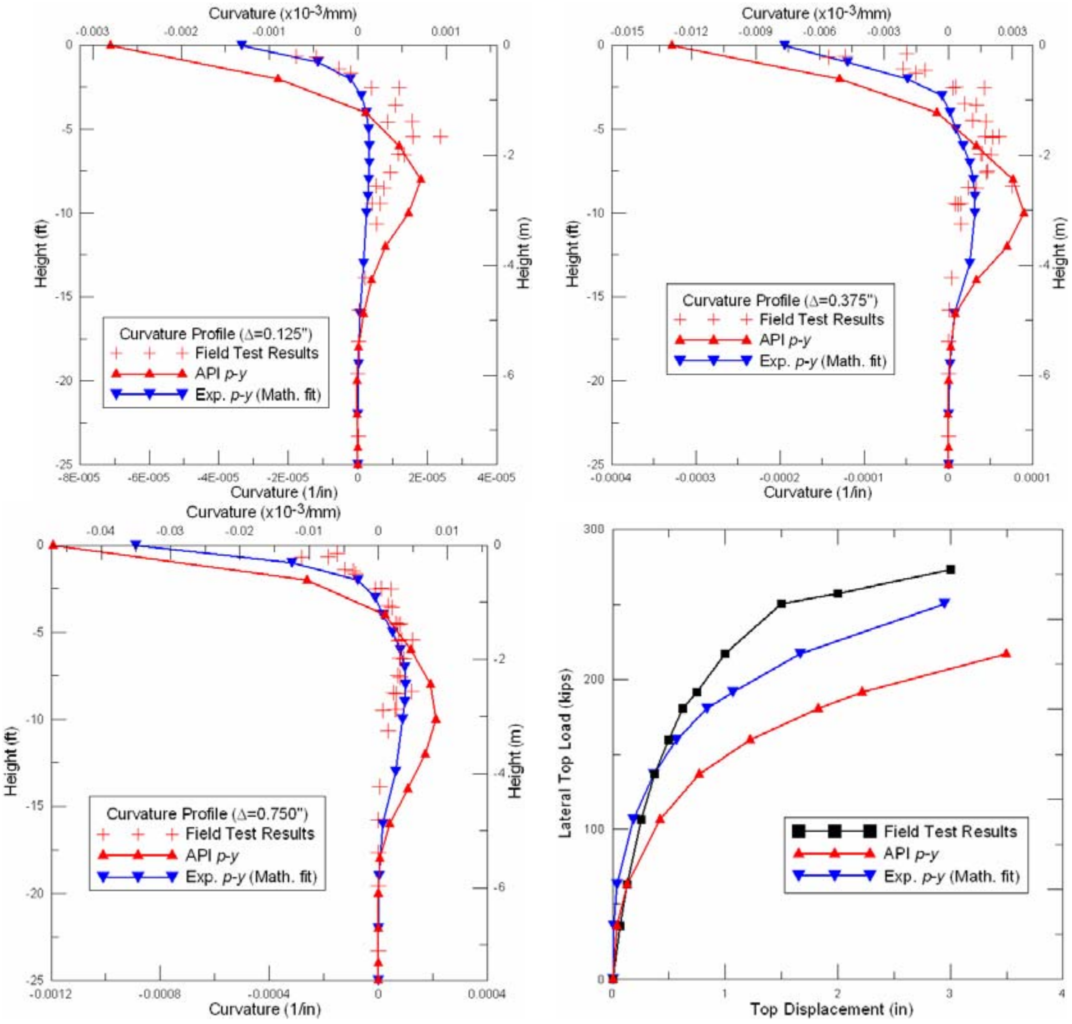

Figure 6.4. Curvature profiles and top load-displacement response of the fixed-head shaft obtained through calibrated (experimental) and API *p*-*y* models.

6.3.4 Calibration Results and “Mathematically” Fitted *p-y* Curves for the Flagpole Shaft

The results of the calibration procedure for the flagpole shaft are given in Table 6.2. The calibrations could only be made with data from measurements at 2 ft, 3 ft, and 4 ft, because at larger depth it was not possible to perform the piecewise polynomial fitting described in Chapter 5 due to shaft curvature levels that generally fell below the sensor noise threshold. The table also contains the calibrated equivalent API parameters. Again, these values are different from those recommended in API guidelines (1993), which were used in the pre-test model predictions (also provided in the Table 6.2).

Table 6.2. Calibrated and pre-test backbone curve parameters for the flagpole shaft.

	Macroelement Parameters			Equivalent API Parameters			Pre-test Model Parameters		
z (in)	$\hat{\eta}$ (kips/in)	β (in)	n	p_u	y_c	n	p_u	y_c	n
-24	3.213	0.3046	0.8956	6.426	0.3046	0.8956	2.1463	0.4200	0.3333
-36	2.968	0.3937	0.6938	5.936	0.3937	0.6938	2.2475	0.4200	0.3333
-48	0.8202	0.2008	0.4192	1.6404	0.2008	0.4192	2.3486	0.4200	0.3333

The calibrated *p-y* curves for the flagpole shaft down to 4 ft depth are shown in Figure 6.5. In this figure, similar to the fixed-head shaft, the API curves imply a more flexible soil response than what is actually measured from the ground level to 3 ft (i.e., one-and-a-half pile diameters) below. The trend appears to reverse somewhere between 3 and 4 ft depth.

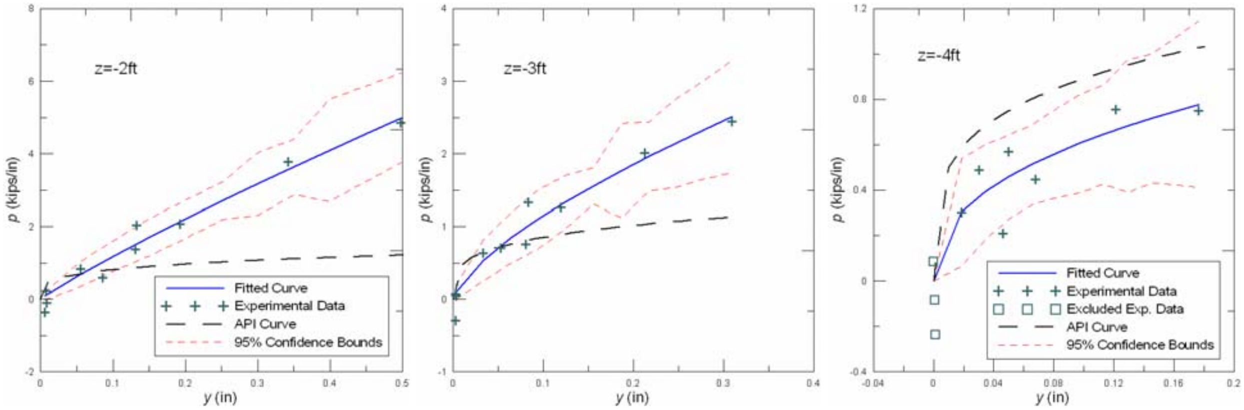

Figure 6.5. Calibrated *p-y* curves for the flagpole shaft at 2 ft trough 4 ft.

Based on these results, a new macroelement model of the flagpole shaft is created. In this model, the macroelements are placed at 2 ft intervals throughout the shaft. The parameters of the macroelement at the ground level were deduced from the one at $z = -24$ in, and by using the explicit depth-dependence of the original API formulation (cf. Eq. 6.8). Thus, the ground-level macroelement parameters were set at $\hat{\eta} = 2.91 = 0.9\hat{\eta}\big|_{z=-24"}$, $\beta = 0.3046$, and $n = 0.8956$. The standard API curves were employed for $z < -48$ in. Curvature profiles and the top load-displacement responses from the pre-test (i.e., API) macroelement model, the calibrated macroelement model, and the field measurements are shown in Figure 6.6. This figure reveals that the macroelement model with calibrated *p-y* curves approximates the measured response better than the standard API *p-y* curves.

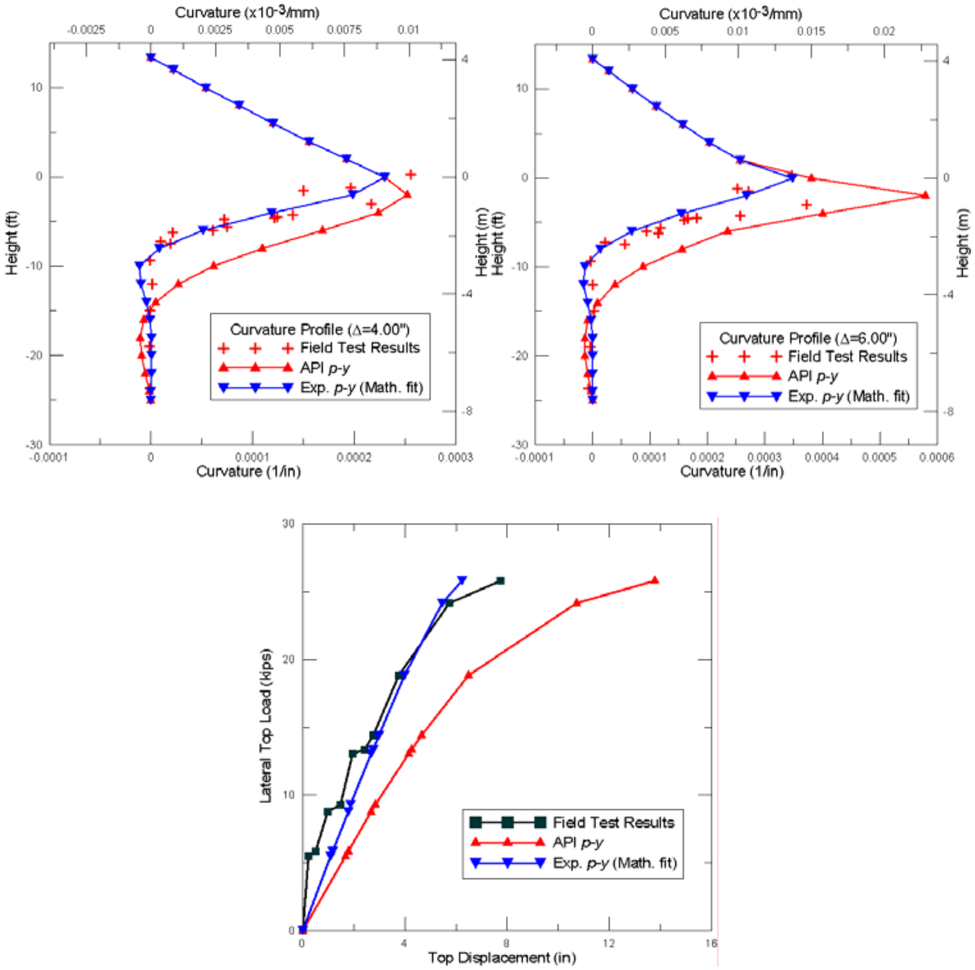

Figure 6.6. Curvature profiles and top load-displacement response of the flagpole shaft obtained through calibrated (experimental) and API *p-y* models.

6.4 Experimental *p-y* Curves—the “Mechanical Fit”

In this section, we pursue an alternative approach in calibrating the macroelement parameters from experimental data. Dubbed as the “mechanical fit,” this approach relies on the determination of “optimal” macroelement backbone curve parameters that directly minimizes the discrepancy between measured and predicted response measures, namely curvature profiles and the load-displacement values at the top of the shaft. As such, this approach is distinct from that presented above, which simply provided a smooth fit through the *p*-*y* curves developed in Chapter 5.

First, we define five new scaling coefficients—namely, C_η, C_E , C_β, C_n and C_{E_c}. We use the first four of these coefficients to control the response of macroelements, as follows:

$$\frac{\partial \dot{F}}{\partial \dot{\delta}} = \begin{cases} C(\delta), & \text{if } f_{py} = 0, \\ C_E E, & \text{if } f_{py} < 0, \end{cases} \qquad F = C_\eta\, \eta \left(\frac{|\delta|}{\beta\, C_\beta} \right)^{(C_n\, n)} . \tag{6.11}$$

We use the fifth coefficient (C_{E_c}) for scaling the stiffness of the concrete fiber elements of the shaft. The aim is to determine the “optimal” values of these parameters such that the measured and the predicted response discrepancies are minimized. Because of the complexity of the ensuing algebra, and the high cost of computations, we opted to employ a systematic trial-and-error method for solving this five-dimensional optimization problem.

We used four different error measures based on pile curvature measurements by three different types of sensors (strain gauges, LVDT’s, and fiber-optics). Two distinct error measures were used for the fiber optic sensors—one for shallow depths (FO1) and another for deeper measurements (FO2). These error measures are defined through

$$E_{SG} = \sum_{i=1}^{N} (\phi_{SGi} - \hat{\phi}_i)^2,\ E_{LVDT} = \sum_{i=1}^{N} (\phi_{LVDTi} - \hat{\phi}_i)^2,\ E_{FO(1,2)} = \sum_{i=1}^{N} (\phi_{FO(1,2)i} - \hat{\phi}_i)^2 \tag{6.12}$$

where N is the number of curvature measurements for a specific sensor type, ϕ is the field-measured shaft curvature, and $\ddot{\phi}$ is the shaft curvature computed using a specific set of values for the model parameters. We calculate a weighted average error value as follows:

$$E_{TOTAL} \equiv \sum_{i=1}^{4} w_i E_i \Bigg/ \sum_{i=1}^{4} w_i \tag{6.13}$$

where w_i are scalar weights, and $E_1 = E_{SG}$, $E_2 = E_{LVDT}$, $E_3 = E_{FO1}$, $E_4 = E_{FO2}$. Different weight combinations were used in order to account for differences in sensor reliabilities, as shall be described later in the following subsections.

6.4.1 Calibration Results and "Mechanically" Fitted *p-y* Curves for the Fixed-Head Shaft

Our first suite of analyses was performed assuming the undrained shear strength at the site remains constant with depth (*c* = 3900 psf). The dependence of the results on details of the strength profile is demonstrated subsequently. Ultimately, the best weight combination for the fixed-head shaft was the one in which we used equal weights for all sensor measurements and a weight of zero for E_{FO1}. This outcome was consistent with our *a priori* observations, which indicated that the fiber-optic sensors at shallow depths were not reliable. Upon selecting the weights, we employed a basic trial-and-error searching procedure for minimizing E_{TOTAL}. This task was simplified through sequential observations. For example, in the initial phases of this study, we realized that the curvature profiles were the least sensitive to the stiffness of the concrete fibers, so C_{E_c} was fixed to 1.0 (i.e., the originally presumed concrete stiffness was kept constant).

In the fitting process, a number of plots were prepared for studying the effect of each parameter on the residual behavior. For example, the plot of the overall residual versus 480 different combinations of the scaling coefficients for the fixed-head shaft at the top displacement level $\delta_{top} = 0.75''$ is shown in Figure 6.7. In this initial phase of trial-and-error searches, we carried out analyses for all combinations of C_η = {1.1, 1.2, 1.3, 1.5, 1.75, 2.0, 2.5, 3.0}, C_E = {1.0, 1.2, 1.4, 1.6, 2.0}, C_β = {0.78, 0.86, 1.0, 1.07}, n = {0.33, 0.50, 0.66}, and C_{E_c} = {1.0}.

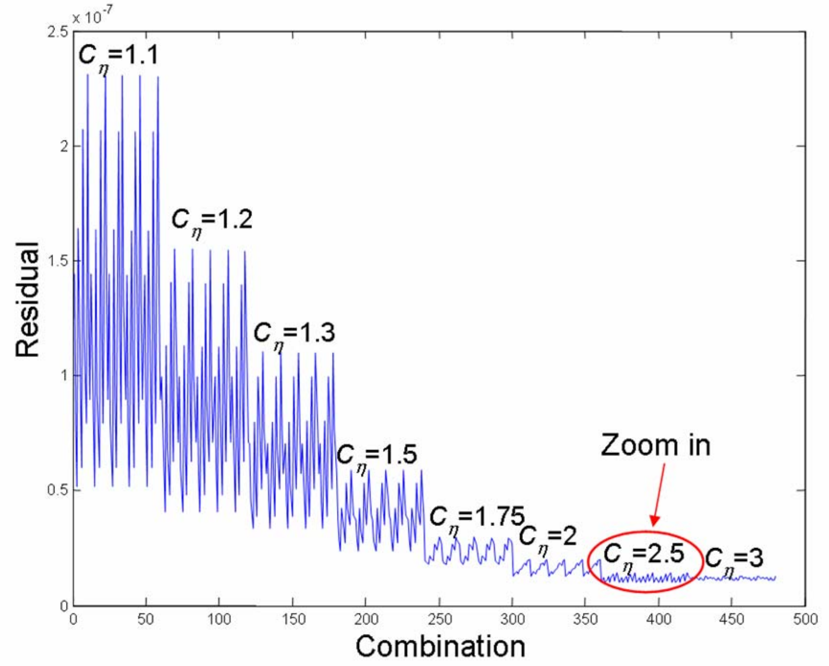

Figure 6.7. The effect of C_η on the curvature residual behavior of the fixed-head shaft.

As shown in Figure 6.7, C_η has the largest effect on minimizing residuals and $C_\eta = 2.5$ minimizes the total weighted curvature error. Because $C_\eta = 1.0$ corresponds to the API recommendation, this result suggests that the standard API *p-y* curves underestimate the fixed-head shaft capacity.

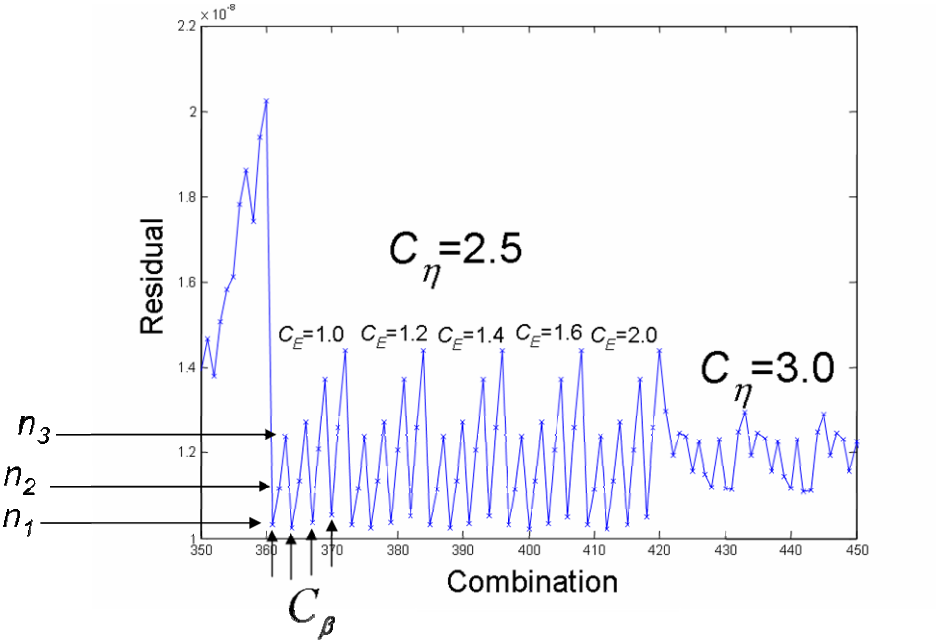

Figure 6.8. The effects of all of the scaling parameters on the fixed-head shaft residual behavior.

In order to see the effect of other parameters on the fit residual behavior, we zoomed in on the $C_\eta = 2.5$ segment of the residual profile, as shown in Figure 6.8. We observe from this figure that the residual is not affected by variations in the values of C_E. Therefore, it is reasonable to assume that the original values of the initial slope of the *p*-*y* curves (i.e., $C_E = 1.0$) are acceptable with respect to minimizing the total weighted curvature error. Additionally, we observe from Figure 6.8 that, within the $C_\eta = 2.5$ segment, the coefficient C_β affects the residual behavior more for larger values of n (in other segments the converse was true). Consequently, we concluded that the effects of these two parameters on the residual are coupled, which should be expected because of the form of Eq. (6.11).

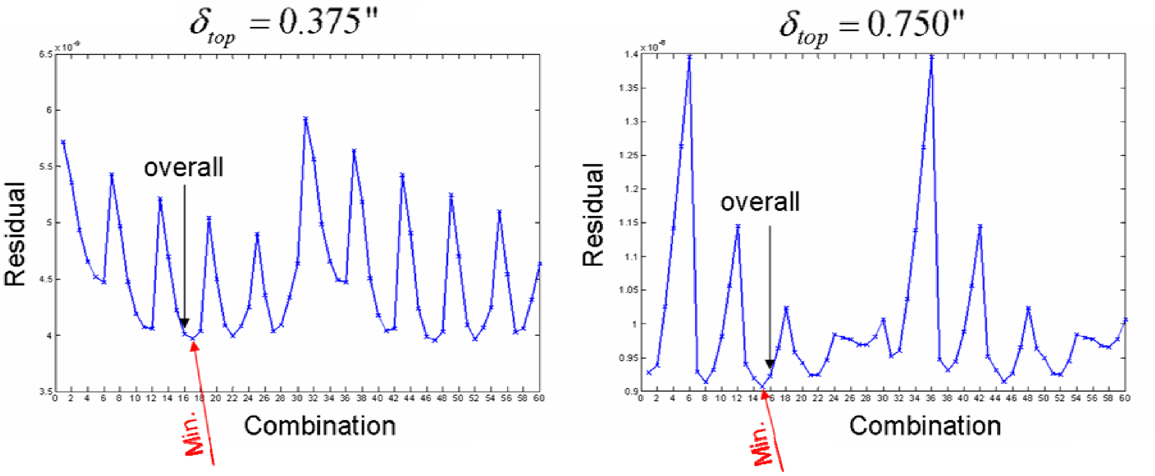

Figure 6.9. Finding the overall best fit for curvature profiles of all top displacement levels of the fixed-head shaft.

By following the introduced procedure, very good curvature fits for all top displacement levels were obtained by fixing the values of C_{E_c}, C_E, and C_η and at the same time by varying the values of C_β and C_n. Since we had to decide on a single set of values for C_β and n for all top displacement levels, we defined a combination error—at the very final step—for all δ_{top} values by taking a weighted average of all curvature residuals obtained for each δ_{top}. The residuals at the top displacement levels of $\delta_{top} = \{1.00", 0.75", 0.375", 0.25"\}$ were respectively assigned with the weights $\{4.0, 4.0, 2.0, 1.0\}$. We assigned larger weights to the residuals of the larger top displacement values because we know that for the larger δ_{top}, there is a larger signal to noise ratio in the measurements. This last process was a compromise among different fits for different top displacement levels to reach to a single set of parameters, as shown schematically in the Figure 6.9.

Ultimately, the best-fit parameters that minimize the combined curvature residual (which was doubly weighted—once among different sensor readings, and a second time among different top displacement levels) for the fixed-head shaft were $C_E^{OPT} = 1.0$, $C_\eta^{OPT} = 2.2$, $C_\beta^{OPT} = 0.36$, and $n^{OPT} = 0.3$. It should be noted that the depth-dependence of the *p-y* curves was hardwired into the aforementioned analyses, and this dependence is identical to API formulae (see, Eq. 6.8). In other words, we did not fit independent *p-y* curves for different depths in the trial-and-error process; thus, the scaling coefficients discussed above affect all macroelements along the shaft simultaneously. It is noteworthy that despite this restriction, we obtained good curvature fits for all top displacement levels. This suggests that depth-dependence of the API p-y curves is generally reasonable. The calibrated *p-y* curves for the fixed head shaft obtained via the described method are shown in Figure 6.10. Also included in Figure 6.10 are the standard API *p-y* curves for comparison. As may be observed from this figure, the specimen (i.e., the fixed-head shaft plus the soil) exhibits a stronger response than the API curves.

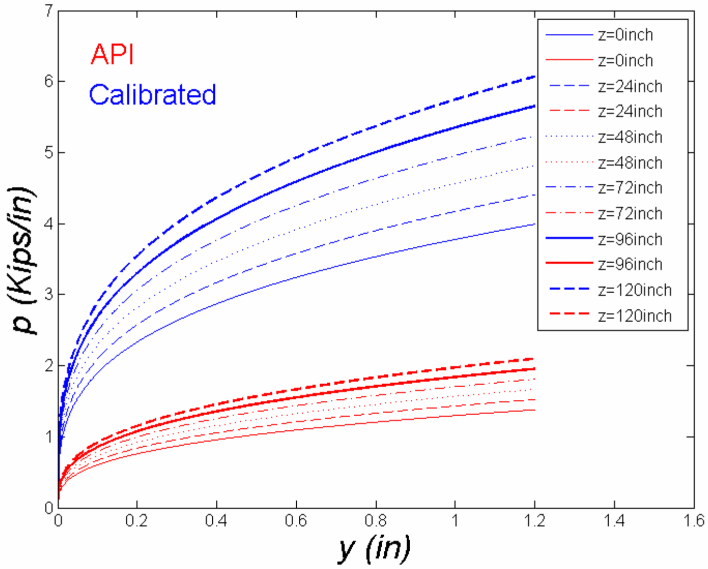

Figure 6.10. API and mechanically fitted *p-y* curves for fixed-head shaft at various depths.

6.4.2 Assessment of Calibrated *p-y* Curves for the Fixed-Head Shaft

In this section, we compare various responses of the fixed-head shaft obtained using different sets of *p-y* curves to the field measurements; The three different sets used in the re-analyses are the standard API, the mathematically fitted and the mechanically fitted *p-y* curves.

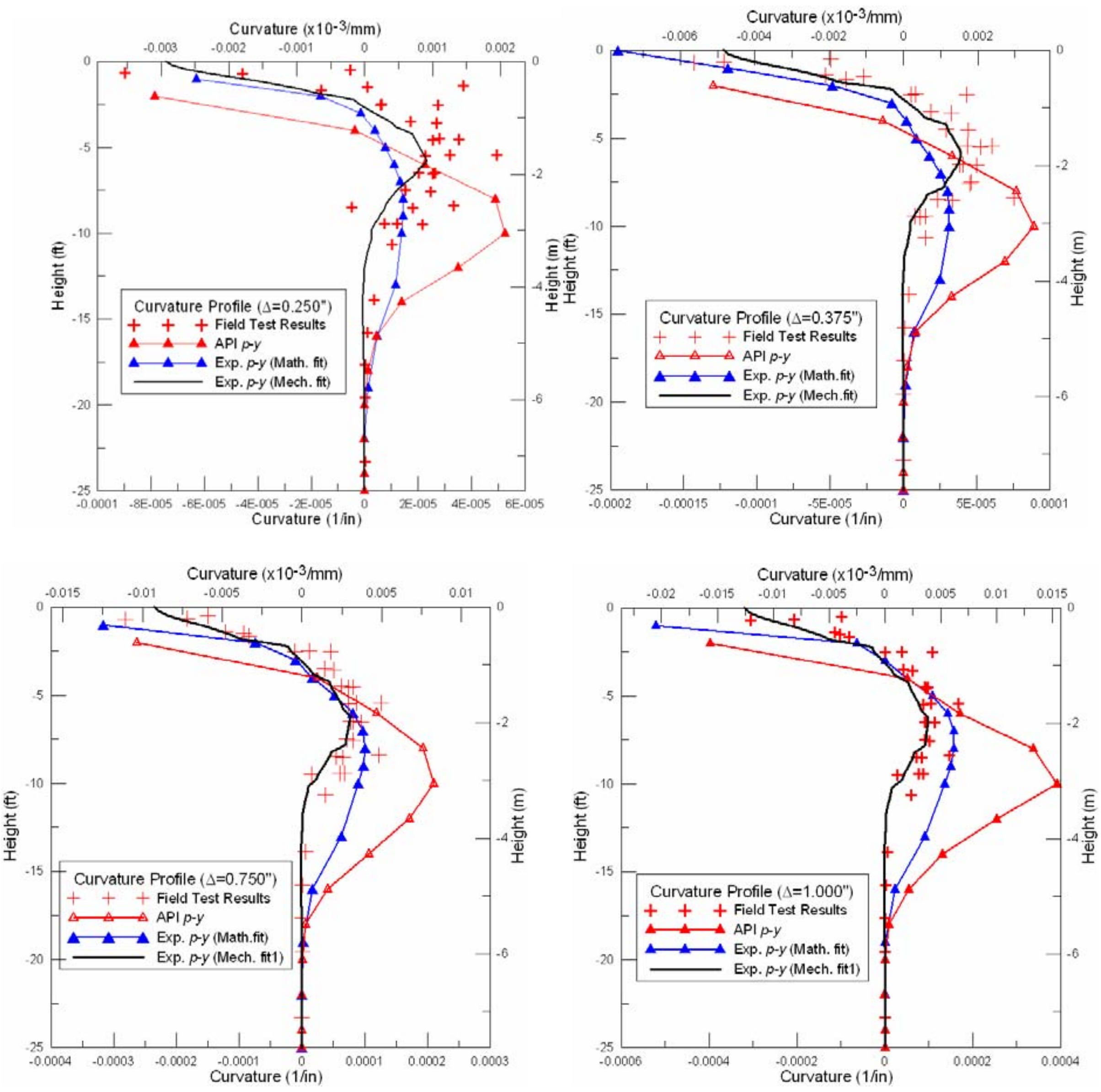

Figure 6.11. Curvature profiles of the fixed-head shaft obtained through API, "mathematically" fitted and "mechanically" fitted *p-y* curves, and the field test results.

The curvature profiles obtained via the aforementioned three different *p-y* models are compared with field test results for four different levels of the shaft top displacements in Figure 6.11. As this figure reveals, the API *p-y* curves are over-predicting both the negative and the positive maximum curvatures of the shaft, which can result in unnecessarily conservative pile designs. The mathematically fitted *p-y* curves yield good predictions, especially in comparison to the responses obtained via the API curves. The best fits are obtained with the "mechanical" fitting approach, which is expected because this approach is specifically targeted at minimizing curvature residuals. The top load-displacement response of the fixed head shaft using the aforementioned methods of analysis is presented in Figure 6.12. The API and mathematically fitted *p-y* curves underestimate the lateral capacity of the shaft whereas the mechanically fitted curves over-estimate both the initial stiffness and the capacity of the shaft. This reveals a limitation of the "mechanical fitting" procedure, which may be remedied as described below.

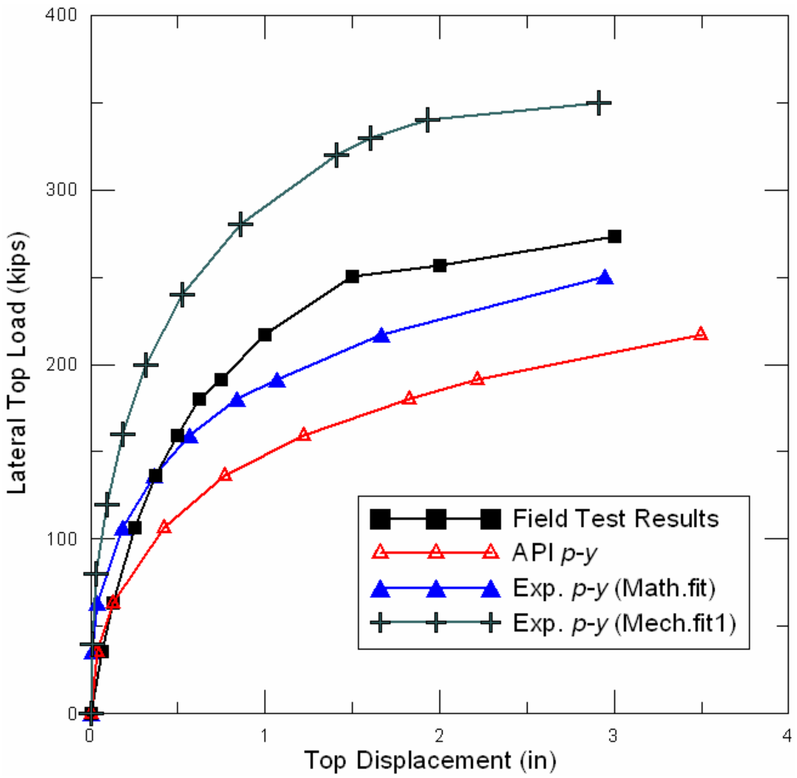

Figure 6.12. Top load-displacement response of the fixed head shaft predicted by *p-y* model with different *p-y* curves in comparison to field measured values.

In order to overcome the shortcomings exposed in Figure 6.12, we modified the mechanically fitted *p-y* curves. First, we reduced the initial stiffness of the calibrated *p-y* curves through trial-and-error, ultimately settling at the value $C_E = 0.1$. Second, for correcting the capacity prediction, we refined the finite element model of the shaft near the top, and looked for a better representation of the undrained shear strength profile of the soil, instead of the constant value that was previously used. As we demonstrate in the following subsection, the undrained shear strength of the soil has a significant effect on the lateral capacity of the fixed-head shaft, and not necessarily on its curvature profile. In the end, this parameter must be carefully selected in any analytical model used for predicting the lateral response of the shafts. Details of the selection of this parameter for the test site and other improvements to the "mechanical fitting" procedure are discussed in the following subsection.

6.4.3 Improving the Accuracy of the "Mechanically Fitted" Model of the Fixed-Head Shaft

Our numerical experiments suggested that the success of the "mechanical fit" depends critically on an accurate accounting of the soil profile at the site. As described by Gabr *et al*. (1994), many attempts have been made to adjust the bearing capacity parameter near the surface to predict p_u. Herein, we opted to represent the depth variation of p_u via the API expression provided in Eq. (6.8). In that API equation, p_u varies with depth—first explicitly through *z*, then implicitly through the undrained shear strength of the soil (*c*). We re-examined the field and laboratory shear strength data to develop a more accurate undrained shear strength profile.

We used all available CPT and SCPT data from Janoyan *et al*. (2001) to determine the average cone tip resistance (q_c) for different depths. Then, we simply calculated the vertical effective stress of the soil using a moist unit weight of $\gamma_m = 120 \text{ pcf}$ (from laboratory tests). By having the tip resistance and the effective vertical stress in the soil, the undrained shear strength of the soil can be obtained through the relationship

$$S_u = (q_c - \sigma'_v)/N_k \tag{6.14}$$

where S_u is the undrained shear strength of the soil (i.e., same as the parameter '*c*' in Eq. (6.8)), N_k is an empirical factor varying in the range of $10 \le N_k \le 30$. Shear strength bounds inferred from the CPT data and this N_k range are shown in Figure 6.13(a). Using laboratory UU triaxial test data along with shear strengths estimated from in situ pressuremeter tests (also shown in Figure 6.13a; Janoyan *et al.*, 2001), we estimate that the calibrated N_k value for this site should be taken as $N_k = 12$ for shallower depths and $N_k = 10$ at depth.

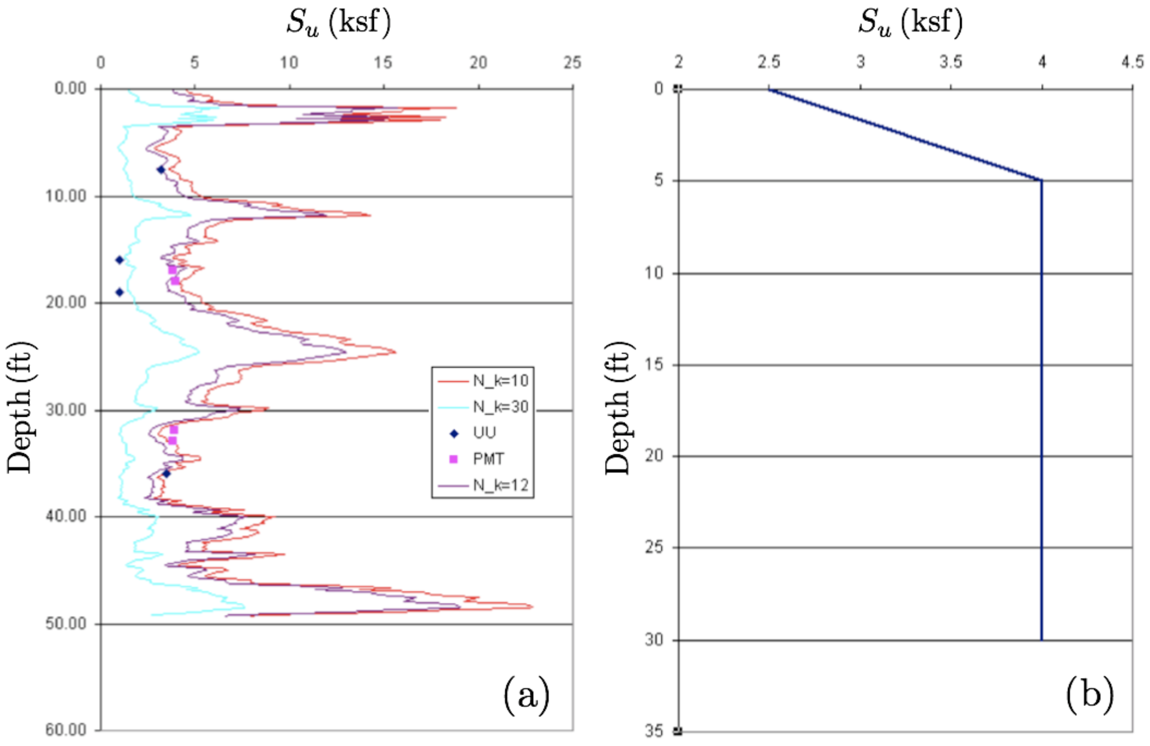

Figure 6.13. The measured undrained shear strength profile of the soil at the test site (a), and the approximate strength profile used for modeling (b).

Based on the results in Figure 6.13(a), we constructed the S_u profile shown in Figure 6.13(b), and used it in the macroelement model of the fixed-head shaft. It should also be noted that the top 3-4ft layer of the soil at the site had been excavated prior to testing of the shafts, because it contained an asphalt layer from prior activity. Therefore, the zero-depth in Figure 6.13(b) corresponds nearly to 4ft depth in Figure 6.13(a), with $S_u = 2.5$ psf.

After recalibrating the macroelement *p-y* curves by taking the aforementioned depth variation of the shear strength at shallower depths into account, we incorporated two additional improvements into the numerical model of the fixed head shaft. First, we reduced the macroelement spacing from 2ft to 1ft for the first 10ft from the ground level. Second, we reduced the initial stiffness of the mechanically calibrated *p-y* curves as suggested by the results displayed in Figure 6.12. Thus, the scaling coefficients of the mechanically fitted *p-y* curves became $C_E^{OPT} = 0.1$, $C_\eta^{OPT} = 2.0$, $C_\beta^{OPT} = 0.36$, and $n^{OPT} = 0.3$. These final *p-y* curves are depicted in Figure 6.14.

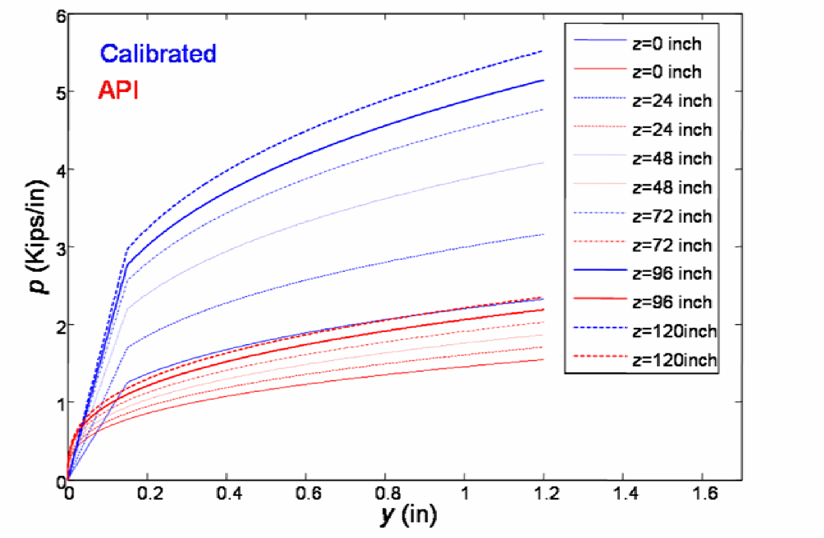

Figure 6.14. Improved mechanically fitted *p-y* curves for the fixed-head shaft.

The aforementioned improvements arguably led to a numerical model that better represents the actual pile/soil conditions at the site, as the new model predicts both curvature profiles and top lateral load-displacement responses quite well. The predictions using the improved model are superposed to those provided earlier in Figure 6.11 and Figure 6.12, and are shown in Figure 6.15 and Figure 6.16.

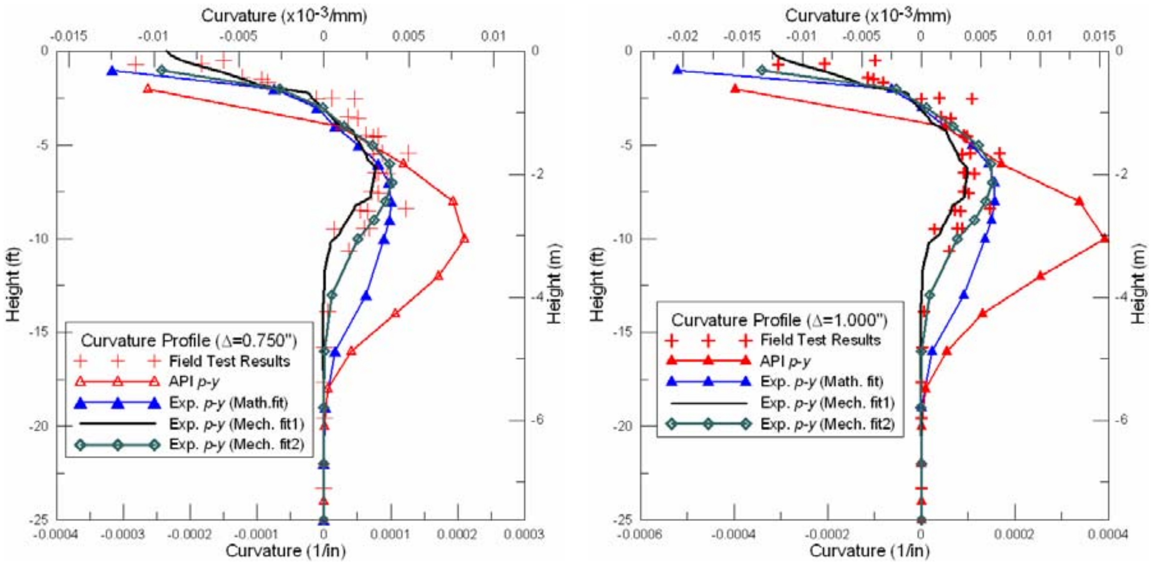

Figure 6.15. Curvature profiles of the fixed-head shaft, including the improved "mechanical" fit results (indicated with "Mech. fit2" in the figure legend).

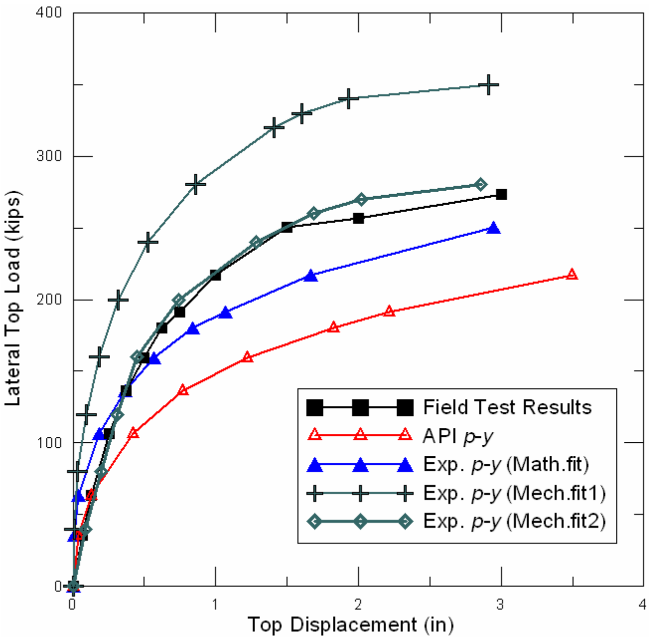

Figure 6.16. Top load-displacement response of the fixed-head shaft, including the improved "mechanical" fit results (indicated with "Mech. fit2" in the figure legend).

As indicated by the figures above, the fitted *p-y* curves introduced in Figure 6.14 not only do still represent the curvature profiles reasonably well, but also an excellent agreement is obtained between the field measured top load-displacement response and that predicted by the improved numerical model, which incorporates the new set of *p-y* curves. These new backbone curves are used in Section 6.5 for comparing the response predictions of the *p-y* and the strain-wedge methods.

6.4.4 Calibration Results and "Mechanically" Fitted *p-y* Curves for the Flagpole Shaft

Following the "mechanical fitting" procedure described earlier, and by using the same soil shear strength profile shown in Figure 6.13(b), we obtained a new set of calibrated *p-y* curves for the 2ft-diameter flagpole shaft. The procedure led to sets of results (details omitted here for brevity), which indicated that without adjusting the reinforced concrete shaft's properties, the measured curvature profiles could not be matched. The top load-displacement response displayed good agreement with data, and appeared to be somewhat less sensitive to the shaft's properties. Therefore, we performed a trial-and-error search to improve the curvature fits by varying a concrete parameter, which was chosen to be the "concrete strain at peak stress" (cf. Figure 3.6). Ultimately, the best curvature fits were obtained when this critical strain parameter was increased

18 times is nominal value. This result is believed to have been caused by a soft construction joint at ground line, the possibility of which was mentioned previously in Section 2.2.1. The calibrated coefficients for the flagpole specimen were taken as $C_E^{OPT} = 0.5$, $C_\eta^{OPT} = 3.0$, $C_\beta^{OPT} = 0.36$, and $n^{OPT} = 0.3$. The resulting *p-y* curves for the flagpole shaft are shown in Figure 6.17. Again, the calibrated *p-y* curves are stronger and stiffer than the API curves.

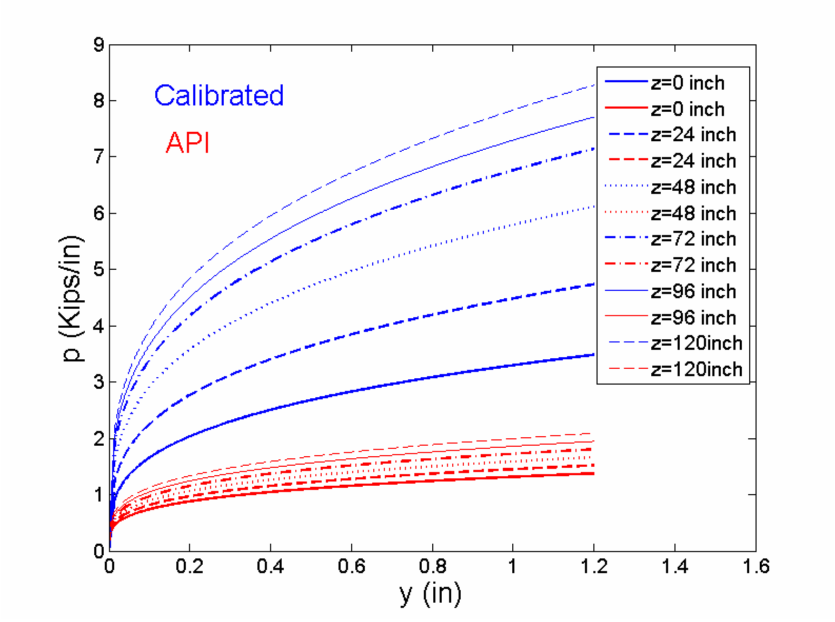

Figure 6.17. Mechanically fitted *p-y* curves for the flagpole shaft.

The comparisons of the curvature profiles and the top load-displacement responses of the flagpole shaft using the calibrated *p-y* curves to the field measurements, API models, and SWM are deferred to Section 6.5.2.

6.4.5 Comparison of Experimentally Calibrated *p-y* Curves for Fixed-Head and Flagpole Shafts to API Curves

The derived *p-y* curves for the flagpole and the fixed-head shafts obtained through the "mechanical fitting" procedure are shown together with the standard API curves in Figure 6.18 for various depths (up to two times the shaft diameter). The fitted *p-y* curves for the two head fixity conditions do not match. However, our opinion is that the available data at this time does not support the notion that the *p-y* curves for these two head fixity conditions are distinct. There are two reasons for this – one having to do with the large scatter in the *p-y* curves (especially for the flagpole configuration and the other having to do with the preliminary nature of these *p*-*y* curves.

Those confidence intervals in Figure 6.18.were derived by (*i*) plotting residuals of the top displacements versus top load; (*ii*) fitting a straight line to the residuals, which was nearly zero (as expected); (*iii*) evaluating 95% confidence intervals about the fitted line from *ii*, which are sensitive to the scatter of the data and the number of data points; (*iv*) evaluating the range of C_η that maintain a mean residual fit line within the confidence intervals from *iii*; (*v*) the range of *p*-*y* curves produced by the range of C_η from *iv* is taken as the confidence interval on *p*-*y*, as shown in Figure 6.18. Our preliminary view is that the differences between the *p*-*y* curves may not be statistically significant, given the scatter in the data as reflected by the confidence intervals shown in the figure.

Final judgment on this issue of compatibility of *p*-*y* curves should be reserved until additional research can be done to better constrain these curves. For the flagpole shaft, this future work needs to more carefully consider the weakened concrete in the construction joint without softening concrete in other areas. For the fixed-head shaft, this future work needs to account for shear deformation effects on the *p*-*y* curves, which could significantly change their shape.

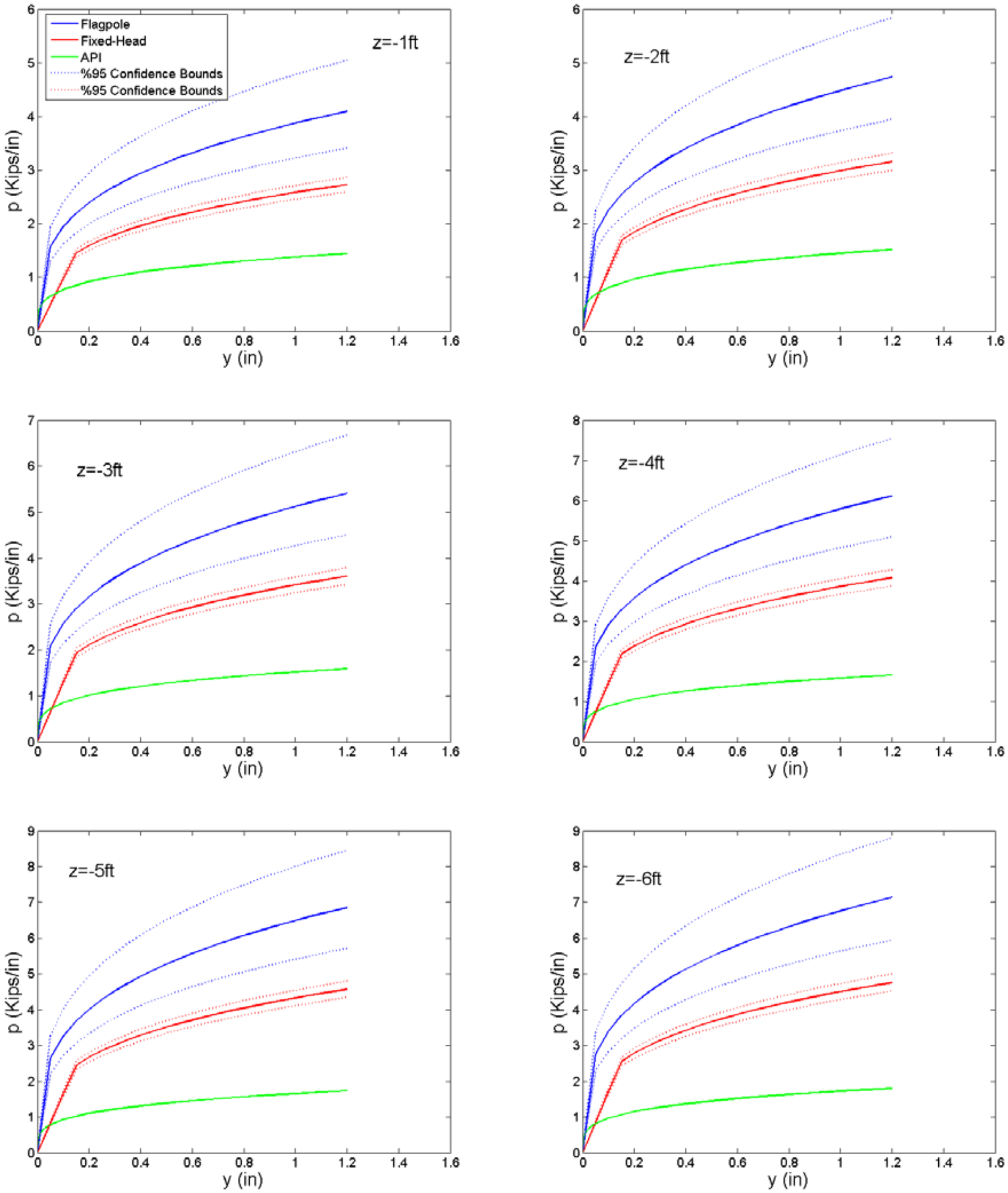

Figure 6.18. Mechanically fitted *p-y* curves of the flagpole and the fixed-head shafts in comparison to the standard API curves.

6.5 SWM and Calibrated *p-y* Model Response Predictions in Comparison to Measured Data

6.5.1 Fixed-Head Shaft Response Comparisons

The curvature profiles of the shaft obtained from different models for two large top displacement levels—i.e., $\delta_{top} = 0.75$ in. and $\delta_{top} = 1.00$ in.—are shown in Figure 6.19. As this figure indicates, the strain-wedge model predicts the shaft response well—indicative of the appropriateness of the kinematic hypotheses employed in the formulation of SWM, at least for this site's soil profile). This is impressive because the inputs to this model are fundamental soil and reinforced concrete material properties that may be obtained from standard tests.

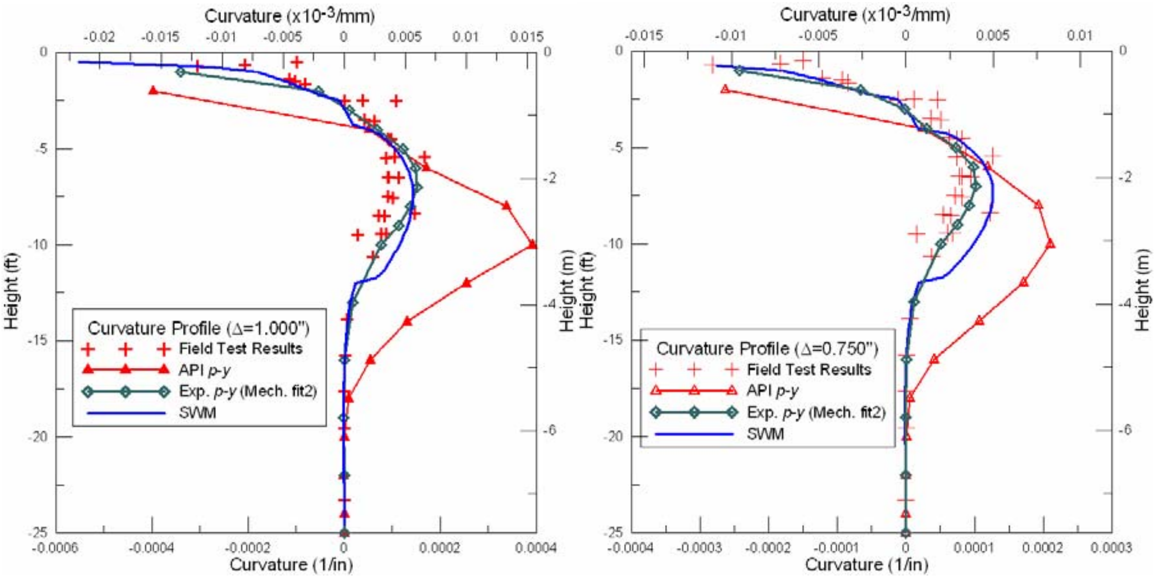

Figure 6.19. Fixed-head shaft curvature profiles from field-test results, *p-y* methods, and SWM.

The top load-displacement responses of the fixed-head shaft obtained from different models are shown in Figure 6.20. The strain-wedge model predicts the initial stiffness and the soil-shaft interaction up to nearly 1 inch of top displacement quite well, at which point the SWM software terminates and predicts that the capacity is reached. As such, SWM underestimates the top load capacity of the shaft. Perhaps by coincidence, the capacity predicted by SWM is very close to the API *p-y* model prediction.

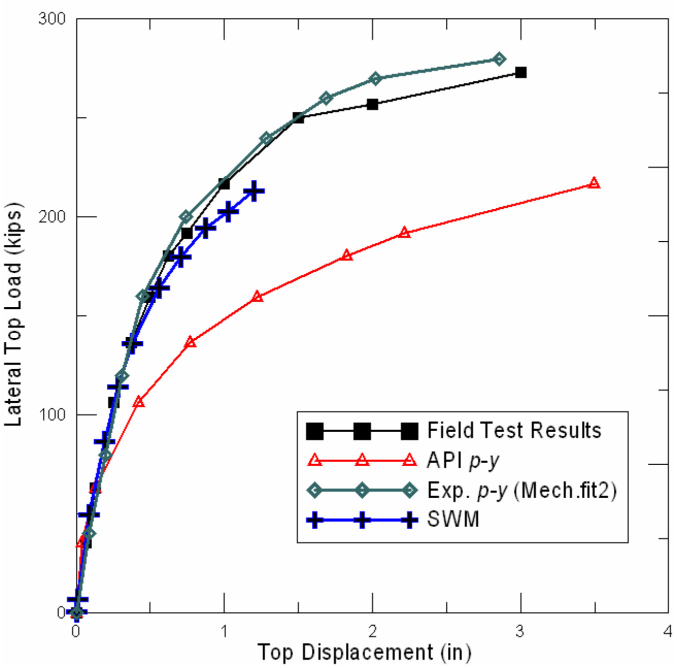

Figure 6.20. Fixed-head shaft top load-displacement response from field test results, *p-y* methods, and SWM.

6.5.2 Flagpole Shaft Response Comparisons

The curvature profile of the flagpole shaft obtained from different models for two top displacement levels ($\delta_{top} = 4.00''$ and $\delta_{top} = 6.00''$) are compared in Figure 6.21. As indicated by this figure, analyses using the API *p-y* curves are unable to capture the sharp curvature change that occurs approximately one foot below ground level. Moreover, it over-predicts the maximum curvature of the shaft for $\delta_{top} = 6.00''$. SWM predicts the shaft curvature profiles reasonably well, but underestimates the maximum curvature of the shaft near the ground surface for $\delta_{top} = 6.00''$. The mechanically fitted *p-y* curves provide the best predictions for the flagpole shaft.

The top load-displacement response of the flagpole specimen obtained from different models are compared to the field measurements in Figure 6.22. The data and the results obtained via mechanically fitted *p-y* curves terminate at 8 in. top displacement, because the curvature data becomes too sparse to support these analyses at larger displacement levels. As this figure reveals, strain wedge model and the mechanically fitted *p-y* curves replicate the test results well. The API model underestimates both the stiffness and the capacity of the shaft, which would result in a conservative design, as was the case for the fixed-head specimen.

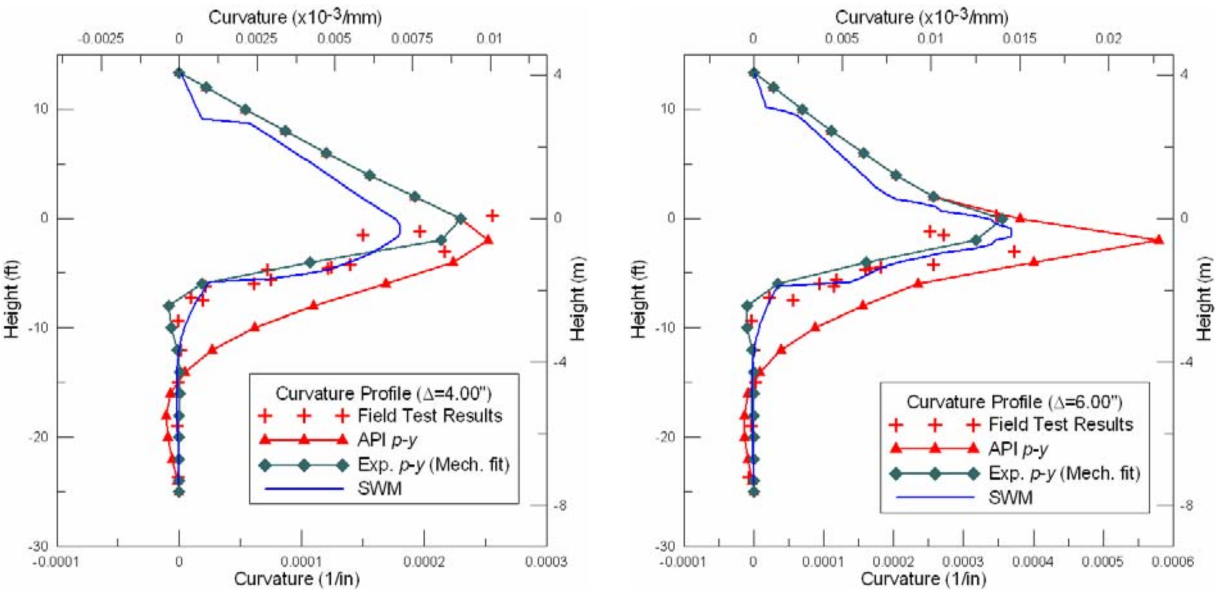

Figure 6.21. Flagpole shaft curvature profiles from field test results, p-y methods, and SWM.

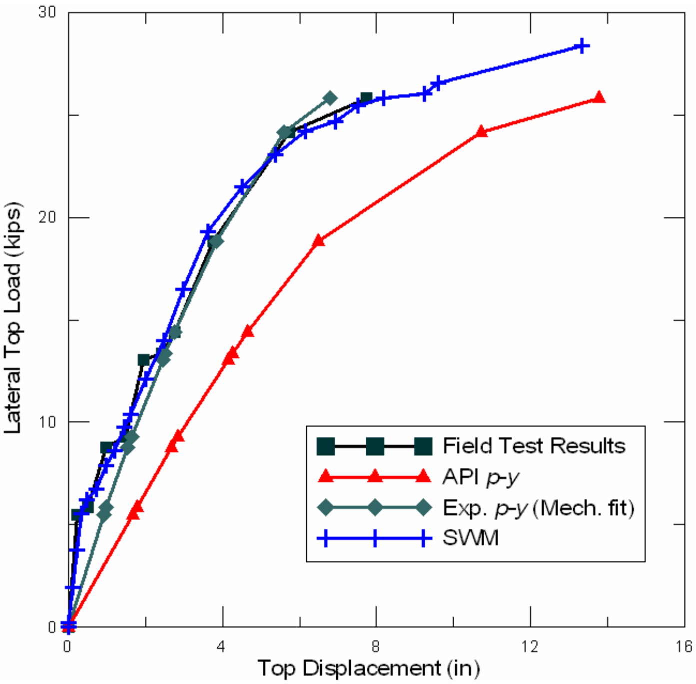

Figure 6.22. Flagpole shaft top load-displacement response from field test results, p-y methods, and SWM.

6.5.3 Comparison of *p-y* curves Inferred from the Strain-Wedge Method to Test Results

It is possible to infer *p*-*y* curves from the strain-wedge model. Herein, we first compare these *p*-*y* curves for the fixed-head shaft to the experimentally calibrated and the standard API *p*-*y* curves for three different depths (1ft, 3ft and 5ft) in Figure 6.23. The *p*-*y* curves inferred from SWM appear to agree with the experimentally calibrated *p*-*y* curves for shallower depths where the effect of these curves are important for the lateral response of the pile; but as we go deeper, the discrepancy increases between the two sets of *p*-*y* curves.

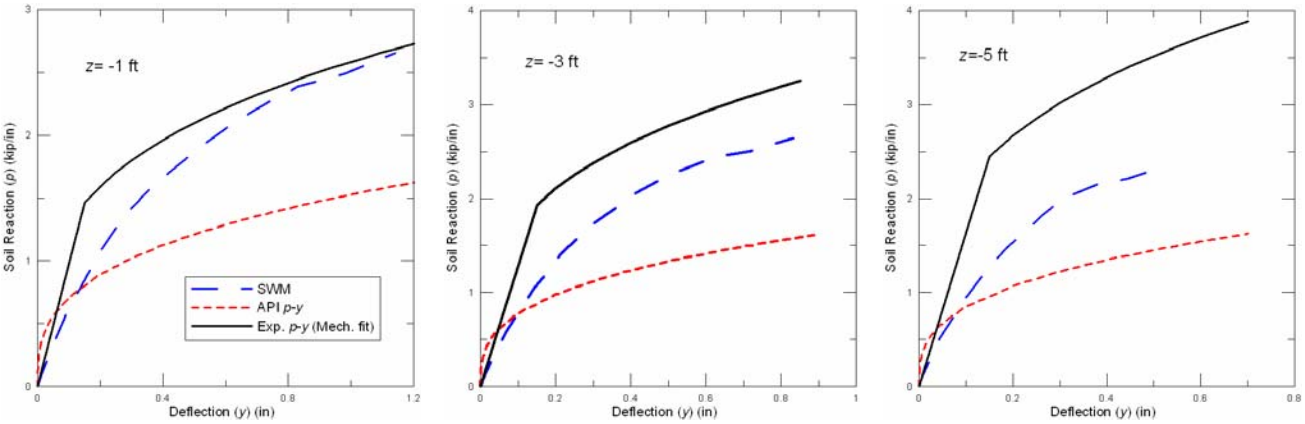

Figure 6.23. The API, and SWM, experimentally calibrated *p-y* curves for the fixed-head shaft.

Next, we compare the *p*-*y* curves for the flagpole shaft to those obtained from SWM for three different depths (0ft, 1ft, 2ft) in Figure 6.24. Again, the comparisons are made for shallow depths where the soil-pile interaction most affects the flagpole shaft response. This time, the *p*-*y* curves from SWM are similar to the API *p*-*y* curves, except for their smaller initial stiffness. The mechanically fitted *p*-*y* curves are significantly stiffer and stronger than both sets of *p*-*y* curves.

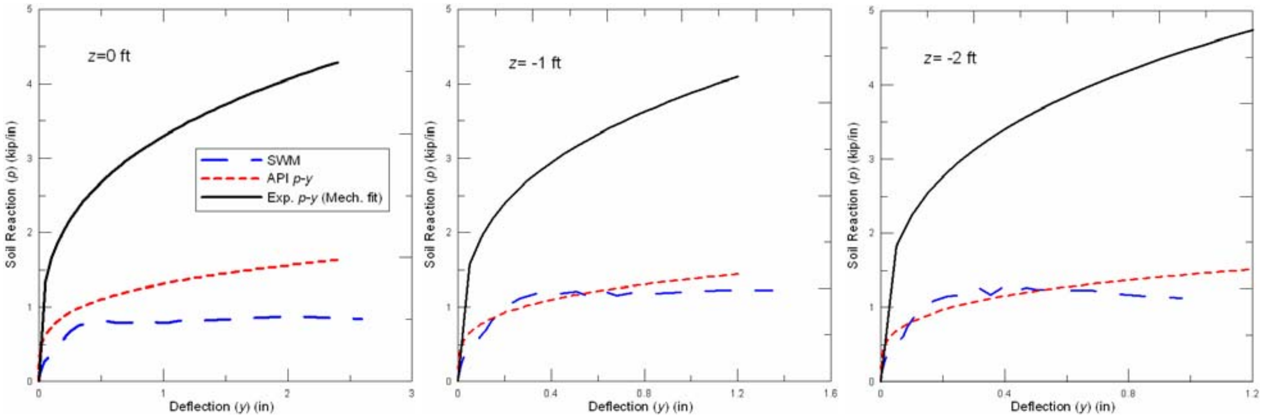

Figure 6.24. The API, and SWM, experimentally calibrated *p-y* curves for the flagpole shaft.

6.5.4 Comparison of *p-y* curves from Six Foot Flagpole Shaft to Results of Current Test

Janoyan et al. (2001) describe the results of a previous flagpole test on a six foot diameter shaft that is otherwise very similar in configuration to the flagpole shaft tested in the present research. Figure 6.25 shows *p-y* curves for the 6 ft diameter flagpole shaft at a depth of 36 inches using the API (1993) formulation, using experimentally derived curves inferred from test data (Janoyan et al., 2001), and using curves experimentally derived from a 2 ft diameter flagpole shaft, multiplied by the API diameter scaling factor. The API diameter scaling factor was calculated by dividing the magnitude coefficients of the 6 ft diameter and 2 ft diameter p-y functions. The scaling factor at a depth of 36 inches was calculated as 2.2.

The API curves are again shown to be biased toward underprediction of soil resistance at shallow depths. The p-y curve for the scaled 2 foot test lies within the confidence intervals for the 6 ft curve. Hence, the data does not indicate a bias in the diameter scaling implied by the API model for stiff clay.

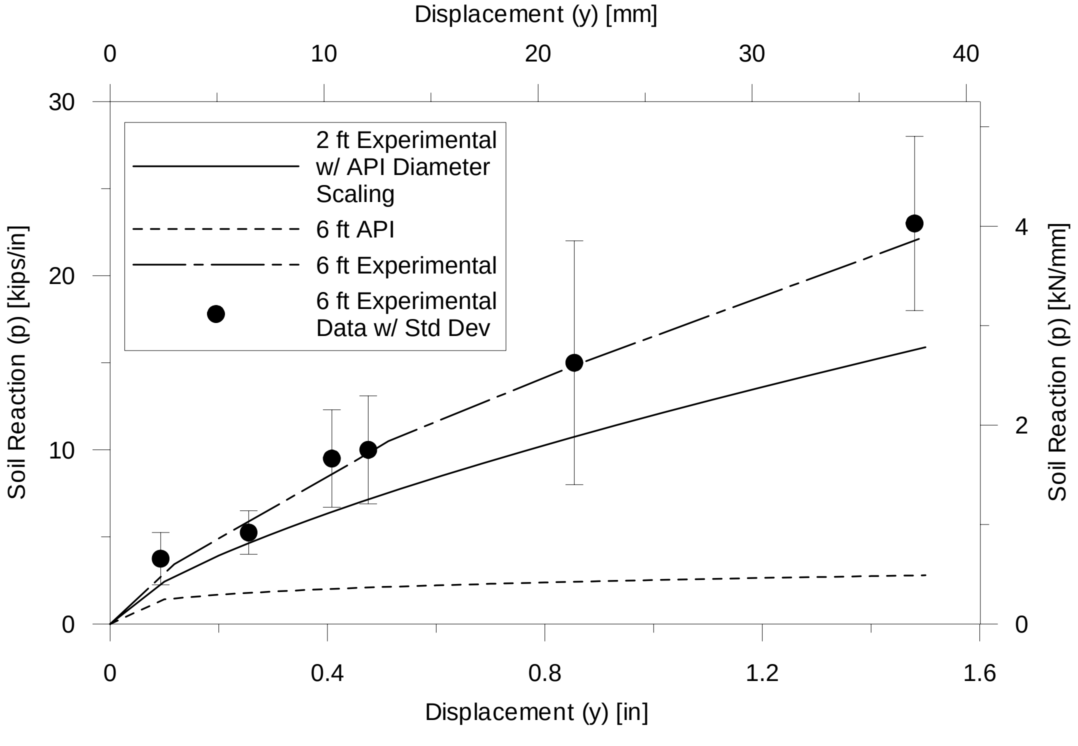

Figure 6.25. *p-y* curves for 6 foot diameter shafts – inferred from data (Janoyan et al., 2001); API (API, 1993); modified from 2 foot diameter result from this study per the diameter scaling implied by the API model for stiff clay.

6.6 Calibration Results for the 9-Pile Group

We can simulate the pile group response by using the experimentally calibrated *p-y* curves for the fixed-head shaft presented previously in Figure 6.14, and by assuming that the same *p-y* curves identically hold for every pile within the group. Thus, we assume that neighboring piles are unaffected by each others presence, and hence, the "group efficiency factor (G_e)" is equal to one. The predicted capacity can therefore be estimated as being nine times the capacity of the calibrated fixed-head shaft model.

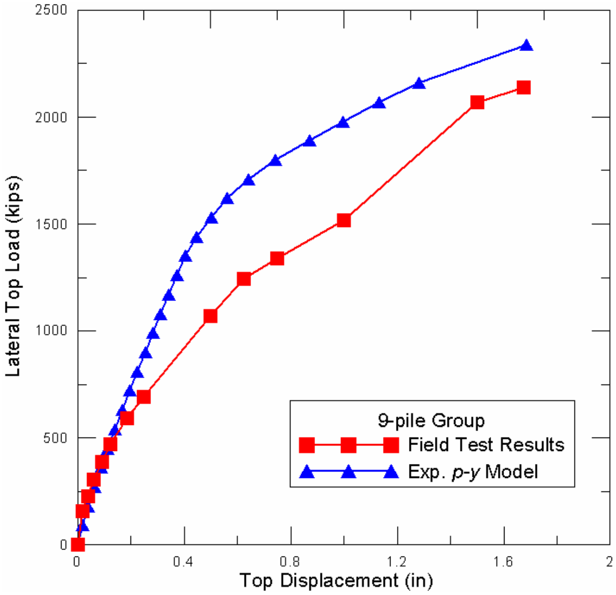

Figure 6.26. Top load-displacement response of the 9-pile group (measured), and of the single fixed-head shaft obtained using calibrated (experimental) *p-y* curves.

The ensuing computed top load-displacement response of the pile group—using the calibrated *p-y* curves—along with the field-measured response of the 9-pile group in the field is shown in Figure 6.26. By evaluating the ratio of these two response curves, we obtain the group efficiency factor (G_e) as a function of lateral head-displacement or head-load. These results are shown in Figure 6.27. Here, it can be seen that the group efficiency factor ranges between 0.7 and 1.6.

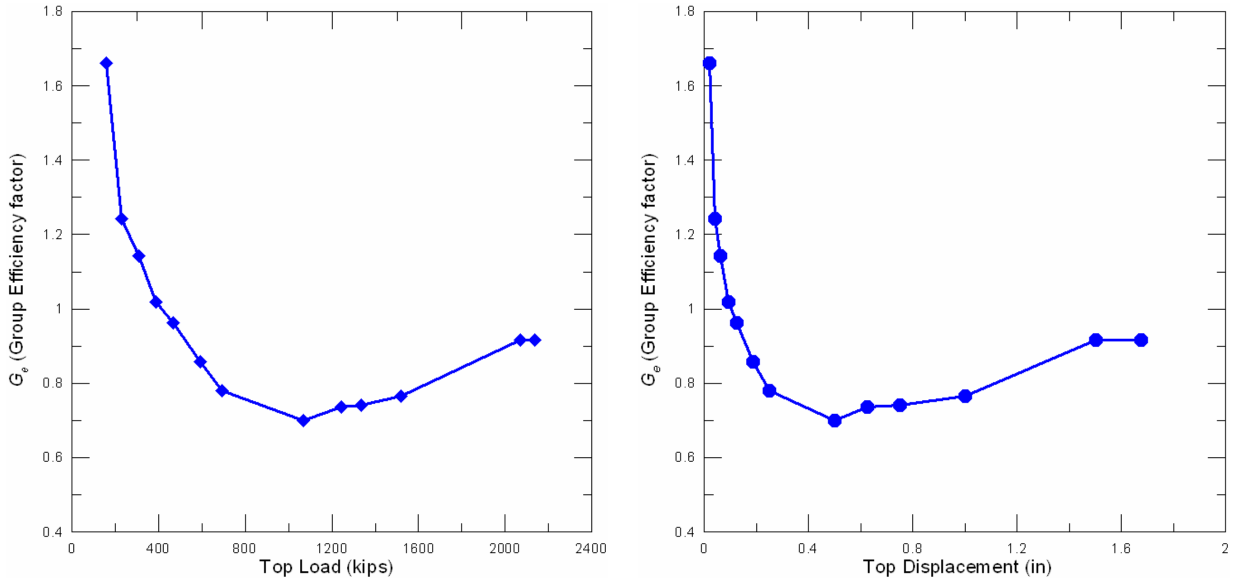

Figure 6.27. Group efficiency factors versus lateral top load (left) or displacement (right) as deduced from the single fixed-head shaft and the 9-pile group experiments.

An alternative approach to obtaining the group efficiency factors is to use the field-measured backbone curve of the fixed-head shaft's lateral top load-displacement response. Figure 6.28 displays this backbone curve. The same figure also provides a curve indicating the group capacity that is equal to nine times the experimental single fixed-head shaft capacity, together with the field-measured backbone curve of the 9-pile group. Again, by evaluating the ratio of these two latter curves, we can obtain a second estimate of the group efficiency factor.

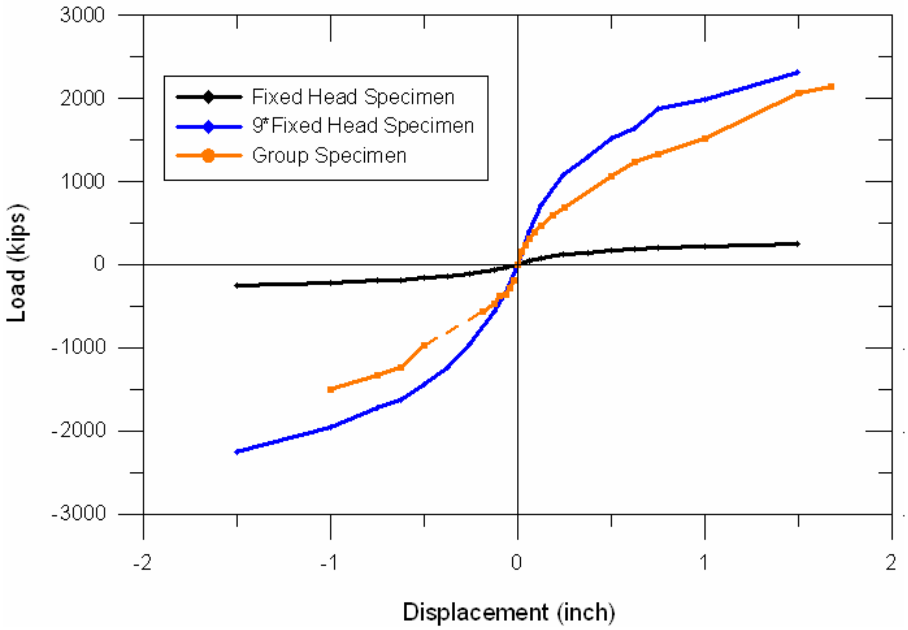

Figure 6.28. Load-displacement responses of the single fixed-head shaft and the 9-pile group.

The group efficiency factors obtained through the two different methods described above are shown in Figure 6.29. As previously mentioned, the first method relies on fixed-head shaft lateral response, which is computed with calibrated *p-y* curves; whereas the second directly utilizes field-measured lateral response. As such, the first method is arguably less accurate, because it embodies additional errors contained in the *p-y* curve fitting procedures described in Section 6.4. The G_e from the first and the second methods are labeled as "computed" and "experimental" in Figure 6.29, respectively. The presumably more accurate "experimental" values range between 0.64 and 0.89. Eventually, both values appear destined to converge to an expected value of 1.0 with increasing head-displacement levels.

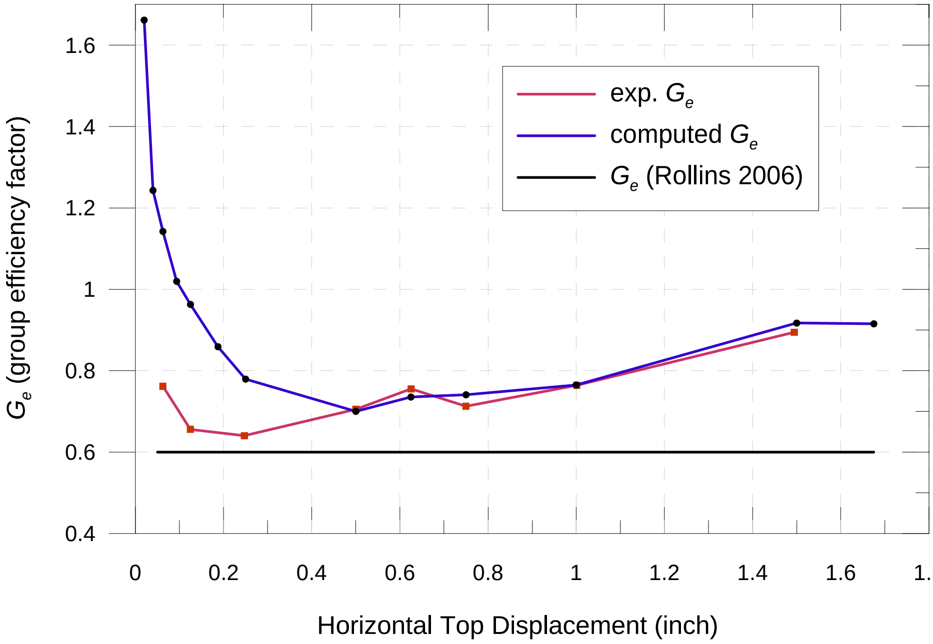

Figure 6.29. Comparison of group efficiency factors deduced from experimental data with two different methods to values by Rollins et al. (2006).

The same figure contains results obtained in previous experiments by Rollins *et al*. (2006a, b), who obtained *p*-multiplier values for pile groups. By averaging the *p*-multipliers, the group efficiency factor is found to be 0.6 by averaging the *p*-multiplier values for all piles in the group. This value does not vary with top load/displacement level. Comparisons with present results suggest that Rollins' value is a conservative lower bound on the group efficiency factors. Moreover, our data suggests a significant dependence of the group multiplier on the displacement level, an effect not reflected in current models.

7 CONCLUSIONS AND RECOMMENDATIONS

7.1 Overview

This research has investigated important attributes of shaft-soil interaction with implications for Caltrans seismic design practice. In this chapter, we do not strive to summarize the scope and the full suite of findings from this research. Rather, we distill the results to key findings that we anticipate will be useful in Caltrans' design practice and in the organization of future research programs.

7.2 Recommendations Related to Shaft-Soil Interaction

Current Caltrans' practice related to shaft-soil interaction for seismic applications is to use the beam on nonlinear Winkler foundation paradigm for modeling. The nonlinear interaction is simulated with *p-y* curves recommended by API (1993). There has been some suggestion from past research that *p-y* curves should depend on the head fixity condition, but this is not currently taken into consideration. Diameter effects on *p-y* curves are built into the model formulation, but due to the lack of empirical validation for large diameters, there is a lack of confidence in their application. When piles or drilled shafts are installed in groups, the *p* component of the *p-y* curves is reduced using empirical group reduction factors similar to those provided by Rollins et al. (2006). Those group interaction factors depend on pile spacing and the configuration of piles in a group, but not on load level.

This research has addressed many issues related to the use of *p-y* curves for seismic design. Our main findings and recommendations are summarized in the following:

- The API formulation for *p-y* curves at shallow depths in stiff clay appears to be significantly too soft and to have a peak capacity that is too low. As a preliminary recommendation, it appears that within the current API formulation, the capacity can be increased by factors ranging from two to three at shallow dephts, which affects both the stiffness and the ultimate capacity of the nonlinear backbone *p*-*y* curve.

- At the present stage of our work, we are unable to find a distinct variation in *p*-*y* curves for an unrestrained (flagpole) and fixed head condition. Accordingly, we see no reason to recommend changing current Caltrans practice in this respect at the present time.
- We do not find evidence of bias in the diameter effect built into the API *p*-*y* curve model for stiff clay.
- The current practice of using group interaction factors that are independent of load level (or displacement level) can significantly underestimates group resistance. We find that for a drilled shaft group, the interaction factor is essentially unity at small displacement levels (elastic condition), then drops to values near those currently recommended as displacements increase towards and past the yield displacement. As the group displacement continues beyond yield towards ultimate structural failure, group factors rise and again approach unity. Hence, increases in current group interaction factors are recommended for the common condition of groups designed for small displacements (elastic conditions) or the less common condition of groups expected to be loaded significantly beyond yield.

7.3 Recommendations Related to Future Testing

In this section we would like to convey a number of lessons learned over the course of this research that could benefit future research programs and ultimately Caltrans' seismic design practice. The first set of lessons concerns instrumentation types that have been found to be effective for lateral load testing of drilled shafts. The second set of lessons concerns additional testing that is needed to further advise Caltrans engineers on critical issues affecting the seismic design of bridges.

Regarding the instrumentation issue, we find that sensor performance is affected by the head fixity condition. For an unrestrained head condition (flagpole), fiber-optic sensors seem to provide the best means of monitoring changes of length on opposite sides of the shaft for the evaluation of curvature. DCDT and strain gauge sensors were significantly less effective. On the other hand, for a restrained head condition, fiber-optic sensors fail rapidly during the test, and DCDT and strain gauges performed relatively well. For both types of head fixity, inclinometers perform well, although they provide data that is less directly related to curvature. Regardless of the type of sensor used, close spacing of the sensors within the zone of significant curvature is vital to extracting meaningful information on soil-shaft interaction and the nonlinear response of the shaft section in shear and moment.

There are significant opportunities for future testing that can advance Caltrans' seismic design procedures. In the area of drilled shaft foundations, testing of the quality presented here (sufficient to robustly define *p-y* curves) is needed for shafts installed in a variety of soil types to confirm the trends established in this program for stiff clay. There is also significant opportunity to extend the testing to faster loading rates to more accurately simulate seismic response conditions. Field testing capabilities enabled by the *nees@UCLA* field equipment site provide the opportunity for the establishment of a highly cost-effective research program in this area. Specific issues that could be addressed by such a testing program include the calibration of models for damping associated with pile-soil interaction and the rate-dependence of *p-y* curves.

References

ABAQUS, User’s Manual (2003). ABAQUS, Inc., Version 6.4.

Alsiwat, J.M. and Saatcioglu, M. (1992). “Reinforcement Anchorage Slip under Monotonic Loading,” *J. Struct. Eng.*, ASCE, 118 (9), 2421-2438.

American Petroleum Institute (1993). “Recommended Practice for Planning, Designing, and Constructing Fixed Offshore Platforms - Working Stress Design,” *Report RP 2A-WSD*, 20th Edition.

Applied Technology Council (ATC) (1996). “Improved Seismic Design Criteria for California Bridges: Provisional Recommendations,” *Report ATC-32*, California Department of Transportation.

Ashour, M. and Norris, G. (2000). “Modeling Lateral Soil-Pile Response Based on Soil-Pile Interaction,” *J. Geotech. and Geoenv. Eng.*, ASCE, 126 (5), 420-428.

Ashour, M., Norris, G., and Pilling, P. (1998). “Lateral Loading of a Pile in Layered Soil Using the Strain Wedge Model,” *J. Geotech. and Geoenv. Eng.*, ASCE, 124(4), 303-315.

Ashour, M., Norris, G., and Pilling, P. (2002). “Strain Wedge Model Capability of Analyzing Behavior of Laterally Loaded Isolated Piles, Drilled Shafts, and Pile Groups,” *J. Bridge Eng.*, ASCE, 7 (4), 245-254.

Brown, D.A., Reese, L.C., and O'Neill, M.W. (1987). “Behavior of a Large Scale Pile Group Subjected to Cyclic Lateral Loading,” *J. Geotech. Eng.*, ASCE, 113(11), 1326-1343.

Cook, R.D., Malkus, D.S., and Plesha, M.E. (1989). *Concepts and Applications of Finite Element Analysis*, John Wiley & Sons, Inc., New York

Coutinho, A. (2006). “Data Reduction of Horizontal Load Full-Scale Tests on Bored Concrete Piles and Pile Groups,” *J. Geotech. And Geoenv. Eng.*, ASCE, 132(6), 752-769.

Federal Emergency Management Agency (2000). “Prestandard and Commentary for the Seismic Rehabilitation of Buildings” *FEMA-356*, Washington, D.C.

Filippou, F.C., Popov, E.P. and Bertero, V.V. (1983). “Effects of Bond Deterioration on Hysteretic Behavior of Reinforced Concrete Joints.” *Rep. No. UCB/EERC-83/19*, Earthquake Engrg. Res. Ctr., University of California, Berkeley, Calif.

Gabr, M., Lunne, T., and Powell, J. J. (1994). “P–y Analysis of Laterally Loaded Piles in Clay Using DMT,” *J. Geotech. Eng.*, ASCE, 120 (5), 816-837.

Janoyan, K., Stewart, J.P., and Wallace, J.W. (2001). "Analysis of *p-y* curves from lateral load test of large diameter drilled shaft in stiff clay," *Caltrans* 6^{th} *Seismic Design Workshop*, Sacramento, CA. Paper 5-105.

Kramer, S. L. (1991). "Behavior of piles in full-scale field lateral loading tests," *Report No. WA-RD 215.1*, Washington State Dept. of Transportation, Va.

Lin, S.-S. and Liao, J-C. (2006). "Lateral Response Evaluation of Single Piles Using Inclinometer Data," *J. Geotech. and Geoenv. Eng.*, ASCE, 132 (12), 1566-1573.

Lowther, J. and Shene, C.K. (2003). "Teaching B-Splines Is Not Difficult!," *SIGCSE Bulletin*, ACM, 35(1), 381-385.

Massone, L. M. and Wallace, J. W. (2006). "Load-Deformation Responses of Slender Reinforced Concrete Walls," *ACI Structural Journal*, 101 (1), 103-113.

Matlock, H. (1970). "Correlations for Design of Laterally Loaded Piles in Soft Clay," *Proc. 2nd Offshore Technology Conf.*, OTC 1204, Houston, Vol. 1, 577-594.

Menegotto, M. and Pinto, P.E. (1973). "Method of Analysis for Cyclically Loaded Reinforced Concrete Plane Frames Including Changes in Geometry and Non-Elastic Behavior of Elements under Combined Normal Force and Bending." *Proc., IABSE Symp. on Resistance and Ultimate Deformability of Struct. Acted on by Well-Defined Repeated Loads*, Lisbon.

Mohd-Yassin, M.-H. (1994). "Nonlinear Analysis of Prestressed Concrete Structures under Monotonic and Cyclic Loads." *PhD. Thesis*, University of California, Berkeley.

Norris, G. M. (1986). ''Theoretically based BEF laterally loaded pile analysis.'' *Proc., 3rd Int. Conf. on Numerical Methods in Offshore Piling*, TECHNIP Ed., Paris, 361–386.

OpenSees, http://opensees.berkeley.edu/OpenSees/developer.html

Park, R., Priestley M. J. and Gill, W.D. (1982). "Ductility of Square-Confined Concrete Columns." *J. Struct. Div.*, ASCE, 108(ST4), 929-950.

Reese, L. and Van Impe, W. (2001). *Single Piles and Pile Groups under Lateral Loading*, A. A. Balkema, Rotterdam.

Rha, C., Taciroglu, E., Ahlberg, E., Wallace, J.W., Stewart, J.P. (2005). "Response of a reinforced concrete embedded pile under lateral loading. II: Numerical studies," *2005 Caltrans Bridge Research Conference*, Sacramento, CA, Paper 8-504.

Rha, C.S., Wallace, J.W., and Taciroglu, E. (2004), "Analytical Modeling of Soil-Structure Interaction for Bridge Columns." *13th World Conference on Earthquake Engineering*, Vancouver, B.C. Canada.

Rollins, K.M., Olsen, R.J., Egbert, J.J., Jensen, D.H., Olsen, K.G., and Garrett, B.H. (2006a). "Pile Spacing Effects on Lateral Pile Group Behavior: Load Tests", *J. Geotech. and Geoenv. Eng.*, ASCE, 132(10), 1262-1271.

Rollins, K.M., Olsen, K.G., Jensen, D.H, Garrett, B.H., Olsen, R.J., and Egbert, J.J. (2006b). "Pile Spacing Effects on Lateral Pile Group Behavior: Analysis", *J. Geotech. and Geoenv. Eng.*, ASCE 132(10), 1272-1283.

Spacone, E., Filippou, F.C. and Taucer, F.F. (1996). "Fiber Beam-Column Model for Nonlinear Analysis of R/C Frames: Part I. Formulation." *Earthquake Eng. and Struct. Dyn.*, 25, 711-725.

Taciroglu, E., Rha, C., Wallace, J. W. (2006). "A Robust Macroelement Model for Soil–Pile Interaction under Cyclic Loads," *J. Geotech. and Geoenv. Eng.*, ASCE, 132(10), 1304-1314.

Taciroglu, E., Rha, C.S., Stewart, J.P., and Wallace, J.W. (2003). "Robust Numerical Models for Cyclic Response of Columns Embedded in Soil." *Proc., 16th ASCE Eng. Mech. Conf.*, University of Washington, Seattle.

Wallace, J.W. and Ibrahim, Y.A. (1996). Biax for MS Windows.

Wallace, J.W., Fox, P.J., Stewart, J.P., Janoyan, K., Qiu, T., and Lermitte, S. (2001). "Cyclic large deflection testing of shaft bridges. Part I-Background and field test results," Report to California Department of Transportation, December.

Wilson, D. (1998). "Soil-Pile-Superstructure Interaction in Liquefying Sand and Soft Clay," Ph.D. Dissertation, University of California at Davis.